

# Development of an Unstructured CFD Solver for External Aerothermodynamics and Nano/Micro flows

Ashwani Assam

A Thesis Submitted to  
Indian Institute of Technology Hyderabad  
In Partial Fulfillment of the Requirements for  
The Degree of Doctor of Philosophy



भारतीय प्रौद्योगिकी संस्थान हैदराबाद  
Indian Institute of Technology Hyderabad

Department of Mechanical and Aerospace Engineering

December 2018

© Copyright by Ashwani Assam, 2019.

All Rights Reserved

## Declaration

I declare that this written submission represents my ideas in my own words, and where ideas or words of others have been included, I have adequately cited and referenced the original sources. I also declare that I have adhered to all principles of academic honesty and integrity and have not misrepresented or fabricated or falsified any idea/data/fact/source in my submission. I understand that any violation of the above will be a cause for disciplinary action by the Institute and can also evoke penal action from the sources that have thus not been properly cited, or from whom proper permission has not been taken when needed.

*Ashwani Assam*

(Signature)

**Ashwani Assam**

(Student Name)

**ME12M14P000004**

(Roll Number)

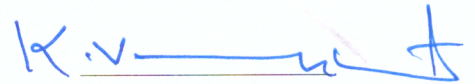


## Approval Sheet

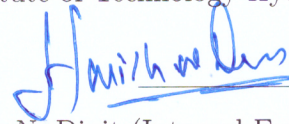
This Thesis entitled Development of an Unstructured CFD Solver for External Aerothermodynamics and Nano/Micro flows by Ashwani Assam is approved for the degree of Doctor of Philosophy from IIT Hyderabad.



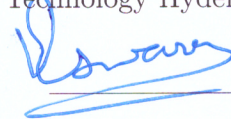
Prof. Amit Agrawal (Examiner)  
Department of Mechanical Engineering  
Indian Institute of Technology Bombay



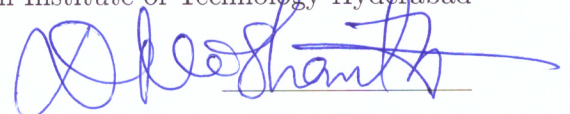
Dr. K. Venkatasubbaiah (Internal Examiner)  
Department of Mechanical and Aerospace Engineering  
Indian Institute of Technology Hyderabad



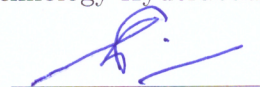
Dr. Harish N. Dixit (Internal Examiner)  
Department of Mechanical and Aerospace Engineering  
Indian Institute of Technology Hyderabad



Prof. Vinayak Eswaran (Adviser/Guide)  
Department of Mechanical and Aerospace Engineering  
Indian Institute of Technology Hyderabad



Dr. Nishanth Dongari (Co-Adviser)  
Department of Mechanical and Aerospace Engineering  
Indian Institute of Technology Hyderabad



Dr. Saptarshi Majumdar (Chairman)  
Department of Chemical Engineering  
Indian Institute of Technology Hyderabad



## Acknowledgements

I would like to thank my teacher who has tried to imbibe in me a value system which has made me to become qualified to stand where I am today.

I would like to express my sincere gratitude to my advisor Prof. Vinayak Eswaran who gave me a vision and motivation to work on such a large computer code from scratch. I also thank him and my co-advisor Dr Nishanth Dongari for their valuable guidance, support and encouragement throughout my research. Dr Nishanth had helped to understand and has given that initial thrust for me to pursue the field of the rarefied gas dynamics which forms a major portion of this thesis.

I thank my doctoral committee members, Dr K. Venkatasubbaiah, Dr Harish N. Dixit and Dr Saptarshi Majumdar for their insightful comments and valuable suggestions during my research.

I am grateful to the Indian Institute of Technology, Hyderabad and our department for providing a good research environment and excellent facilities. I would also like to acknowledge the fellowship assistance provided by the Department of Higher Education, Ministry of Human Resource Development, Government of India.

I would like to acknowledge Dr Amaresh Dalal, Department of Mechanical Engineering, IIT Guwahati, for providing the unstructured solver framework *Anupravaha-2* over which the current compressible flow solver was developed. Also, a sincere thanks goes to his students for providing great hospitality and suggestions whenever required. I thank Mr Venkata P.P.K. of computer division, Bhabha Atomic Research Centre, Mumbai who helped in initial hiccups we faced related to the code.

A special thanks go to Dr Ganesh Natarajan, Department of Mechanical Engineering, IIT Guwahati who gave us initial inputs regarding the development of a compressible CFD solver when we visited IITG in 2014. I would like to express my gratitude to Dr Yair Mor-yossef, Israel CFD centre, Zikhron, Yaakov, Israel for his valuable advice in implementing his implicit scheme for turbulent equations and also for providing valuable suggestions to improve our code. I would like to thank Dr Debashis Chakraborty, who first told us of the SLAU2 scheme, and Dr Keiichi Kitamura, Yokohama National University, Japan for the discussion on his SLAU2 scheme which gave us the confidence to attempt the work that forms the final chapter of this thesis.

My heartfelt gratitude to all my instructors who guided me to many to new frontiers of knowledge, Dr Raja Banerjee, Dr Ashok Kumar Pandey, Dr CP Vyasarayani, Dr Pankaj Kolhe, Dr Viswanath Chinthapenta and all those who are part of my doctoral committee, during my course work.

I thank Dr Narendra Gajbhiye and Dr Praveen Throvagunta for their valuable suggestions at various points of the thesis work.

I would like to thank Mr Madhu P Joshua, for his valuable time and help in many software installing issues and at the moments when our system crashed with unknown problems.

I thank all my friends who made my stay in IITH educative and enjoyable, especially Anil B. Wakale, Neelapu Sathish, Varun Jadon, Nikhil R, Mohammed Ali, Surendra Soni, Rakesh Kale, Mahesh, Abhinash Biswal, Harshal R Gijare, Apurva Bahgat, Praveen Sharma.

It was a great opportunity to be a part of the project for the “Development of a General Purpose Compressible CFD Solver”. And this whole code is made possible because of efforts of many students under the supervision of Prof. Vinayak Eswaran. I would like to especially thank Nikhil K Narayan, Vatsalya Sharma, Saketh A Chandra, Nived MR, Amit, Ashutosh. I am thankful to every one of them for providing a friendly and supportive working environment in the lab.

I would like to express my deep regard and gratitude to my wife Aparna, who has helped to streamline my life in many ways and whose cooperation and support was indeed very helpful in completing my PhD work.

The good wishes and blessings from my parents and in-laws and members of both our families have always been a support. Their understandings when we have not been able to go home when our presence would have given them much joy will always be remembered.

Finally, I would like to thank all my friends and other helpful persons whom I have met in my life through various mediums. I shall always remain grateful to all those whom I have not explicitly named here. Thank You!

December-2018

**Ashwani Assam**  
IIT Hyderabad

## Dedication

*To my Teacher without whom I would never even  
qualify to start...*



# Abstract

Computational aerothermodynamics is the branch of science which focuses on the computation of the effect of thermodynamic and transport models on aerodynamics and heating. They are widely used for external flow cases. On the other hand, the computation of heat and stress in the design of Nano/Micro Electronic Mechanical Systems from the point of view of a fluid mechanics engineer is also an important area of study. A generalized computational tool which can simulate the low and high speed flows at both the macro and micro levels is desirable from the perspective of industry, academics and research. For a developing nation, it is extremely important to have such a solver developed indigenously to create self-sufficiency and self-reliance.

In this work, a robust three-dimensional density-based general purpose computational fluid dynamics solver was developed in house by our research group. The cell-centred finite volume discretization method is used on an unstructured grid, which is more desirable for computation on a complex geometry from the perspective of pre-processing (meshing). Compressible flow solutions obtained from density-based solvers usually do not work well at low speeds where the flow is close to incompressible, unless special schemes and/or special treatments are used. An all-speed algorithm was incorporated using two different methods: (a) preconditioning of the governing equations or (b) through the use of the recently developed SLAU2 all-speed convective scheme. The time-stepping discretization is done implicitly, using the lower-upper symmetric-Gauss-Seidel method, which allows us to take a high CFL number during computations. Throughout this work, we have used a second-order accurate reconstruction with limiters to accurately capture the shocks without dispersive error. Turbulence modelling is done using Favre- and Reynolds- Averaged Navier-Stokes equations using the Spalart Allmaras turbulence model.

The developed solver is used to solve external flow problems at low and high speeds (hypersonic regimes). In these problems, the thesis focus is on the implementation and testing of an automatic wall function treatment for the Spalart-Allmaras turbulence model.

The applicability of the solver is extended to rarefied gas flow regimes in the following manner. Thermal non-equilibrium which exists in the rarefied flow regime is tackled using non-equilibrium boundary conditions in the slip flow regime. The use of non-equilibrium boundary conditions allows the applicability of the Navier-Stokes equation to be extended beyond the continuum to the slip regime. This approach is used to solve problems of hypersonic rarefied flows and nano/micro flows; and for testing and validation of several recently proposed boundary conditions for several

problems in the slip flow regime.

The main focus of this work is in developing newer numerical methods and on testing and improving other recently proposed numerical techniques that are used for solving the problems covered in this thesis. In the following paragraphs we present the major outcomes of the thesis.

The Spalart-Allmaras (SA) is one of the most popular turbulence models in the aerospace CFD community. In its original (low-Reynolds number) formulation it requires a very tight grid (with  $y^+ \simeq 1$ ) spacing near the wall to resolve the high flow gradients. The use of fine grids increases the computational cost of the solutions. However, the use of wall functions with an automatic feature of switching from the wall function to the low-Reynolds number approach is an effective solution to this problem. We have extended Menter's automatic wall treatment (AWT), devised for the  $K - \omega$  SST, to the SA model. It is shown, for both momentum and energy equations, that the formulation gives excellent predictions with low sensitivity to the grid spacing near the wall, and allows the first grid point to be placed at  $y^+$  as high as 150 without loss of accuracy, even for curved walls. In practical terms, this means a near-wall grid 10-30 times as coarse as that required in the original model would be sufficient for the computations.

Extending the solver capability for rarefied flows, we have incorporated various non-equilibrium wall boundary conditions to extend the applicability of the Navier-Stokes equation to the slip flow regime,  $0.001 \leq Kn \leq 0.1$ . A new type of Smoluchowski temperature jump condition considering the viscous heat generation (sliding friction) has been recently proposed as an alternative jump condition for the accurate prediction of the surface gas temperature at solid interfaces for high-speed non-equilibrium gas flows. It extends the concept of including the effect of sliding friction in the calculation of surface heat flux to the temperature jump condition. The effect of the new jump condition on temperature and heat flux has been reported for various flow situations in the literature. However, this jump conditions seems to adversely affect the prediction of surface pressure. Hence, there is therefore a need for a more comprehensive evaluation of the new jump condition taking into account its effect on the other flow properties such as pressure and slip velocity, the effect of various inlet flow conditions and the effect on the convergence. We evaluate the jump condition for various cases of hypersonic rarefied gas flows over a flat plate. The results are compared with the experimental data in addition to direct simulation Monte Carlo results. It is found that for the cases considered the pressure is over-predicted using the new temperature jump condition. We then revisit a previously

derived but largely neglected pressure jump boundary condition and find an optimal way for its implementation. The use of the new temperature jump with the pressure jump boundary condition circumvents the problem of over-prediction of pressure without affecting other flow parameters. We also report a possible limitation of the new temperature jump boundary condition.

In order to further analyse the new temperature and the pressure jump condition, we carry out a numerical study using these boundary conditions for four cases of nano/micro flows: 1) 90° bend Microchannel pressure driven flow, 2) Nanochannel backward facing step with a pressure driven flow, 3) Nanoscale flat plate and 4) NACA 0012 Microairfoil. The results are compared with the available DSMC results. We have also demonstrated the capability of the low-speed preconditioned density-based algorithm for rarefied gas flows. The algorithm captured flows at even very low Mach numbers of  $2.12 \times 10^{-5}$ . Based on this study, we conclude that the effect of inclusion of sliding friction in improving the thermodynamic prediction is case-dependent. It is shown that its performance depends not only on the slip velocity at the surface but also on the mean free path of the gas molecule and the shear stress at the surface.

Finally, we have carried out a numerical study to understand the effect of rarefaction in external hypersonic computations using the case of flow over cylinder. We have proposed a modification to the SLAU2 convective scheme to improve the accuracy of flow predictions in the presence of strong shocks. We then perform the numerical simulation of hypersonic viscous flow over a cylinder at Mach 8 and 16.34 at different Knudsen numbers. We carry out the study using the modified SLAU2 and the classical Roe schemes. The numerical computation of hypersonic flows over blunt bodies is challenging due to the difficulty in robust and accurate wall heat flux prediction and proper capturing of shock waves free from the “carbuncle” phenomenon and other shock anomalies. We study how the shock anomalies found in the continuum hypersonic flows behave with the degree of rarefaction. It is found that the modified SLAU2 captures the shock free from the shock anomalies at all  $Kn$ , while the Roe scheme lacks robustness for  $Kn \lesssim 10^{-3}$ . The variation of different flow properties such as heat flux, wall shear stress and the Mach number is investigated. The peak heating value was observed to decrease with the degree of rarefaction.



# Contents

Declaration . . . . .	iii
Approval Sheet . . . . .	iv
Acknowledgements . . . . .	v
Abstract . . . . .	viii
<b>List of Figures</b>	<b>8</b>
<b>List of Tables</b>	<b>9</b>
<b>Nomenclature</b>	<b>11</b>
<b>1 Introduction</b>	<b>17</b>
1.1 Background . . . . .	17
1.2 Development of an All-Speed Density-Based Navier-Stokes Solver for Unstructured grid . . . . .	18
1.3 Turbulence Modeling . . . . .	19
1.4 Automatic Wall Treatment . . . . .	20
1.5 Non-Equilibrium Boundary Conditions . . . . .	22
1.6 Applications to Micro/Nano Flows . . . . .	23
1.7 Hypersonic Flow over a Cylinder . . . . .	24
1.8 Thesis Outline . . . . .	26
<b>2 Governing Equations and Discretization</b>	<b>29</b>
2.1 Introduction . . . . .	29
2.2 Navier-Stokes Equations . . . . .	29
2.3 Spatial Discretization . . . . .	35
2.3.1 Convective Flux . . . . .	35
2.3.2 Viscous Flux . . . . .	44
2.3.3 Solution Reconstruction . . . . .	45
2.3.4 Green-Gauss Method . . . . .	46

2.3.5	Limiters . . . . .	47
2.4	Temporal Discretization . . . . .	49
2.4.1	Explicit Scheme ( $\beta = 0, \omega = 0$ ) . . . . .	49
2.4.2	Implicit Schemes ( $\beta \neq 0$ ) . . . . .	50
2.4.3	Courant number . . . . .	51
2.5	Initial and Boundary Conditions . . . . .	53
2.5.1	Inviscid wall . . . . .	53
2.5.2	No-Slip Wall . . . . .	54
2.5.3	Non-Equilibrium wall . . . . .	54
2.5.4	Pressure Farfield . . . . .	54
2.5.5	Pressure Inlet . . . . .	56
2.5.6	Symmetry Plane . . . . .	56
2.6	Closure . . . . .	57
<b>3</b>	<b>Turbulence Modeling</b>	<b>59</b>
3.1	Overview . . . . .	59
3.2	Governing Differential Equation . . . . .	60
3.2.1	Reynolds and Favre averaging . . . . .	60
3.2.2	Favre- and Reynolds-Averaged Navier-Stokes Equations . . . . .	61
3.3	Turbulence models . . . . .	63
3.3.1	Spalart-Allmaras (SA) . . . . .	63
3.3.2	Standard $K - \epsilon$ model . . . . .	66
3.3.3	Menter's SST $K - \omega$ Model . . . . .	67
3.4	Near Wall Physics . . . . .	68
3.5	Time Integration Method . . . . .	69
3.5.1	Theoretical Motivation . . . . .	70
3.6	Constructing the $\mathcal{M}$ matrix . . . . .	71
3.6.1	Convective-Diffusion and Source Jacobian . . . . .	73
3.7	Closure . . . . .	75
<b>4</b>	<b>Automatic Wall Treatment for Spalart-Allmaras Turbulence Model</b>	<b>77</b>
4.1	Overview . . . . .	77
4.2	Automatic Wall Treatment . . . . .	78
4.2.1	Algorithm for implementing the AWT . . . . .	79
4.3	Boundary and initial conditions . . . . .	81
4.4	Results and Discussion . . . . .	81
4.4.1	Case 1: Turbulent flow over a flat plate . . . . .	81

4.4.2	Case 2: Forced Convection Over a Flat Plate. . . . .	83
4.4.3	Case 3: Turbulent flow over a bump in channel . . . . .	86
4.4.4	Case 4: Turbulent flow over 2D NACA 0012 Airfoil . . . . .	93
4.5	Closure . . . . .	96
<b>5</b>	<b>Non-Equilibrium Boundary Conditions</b>	<b>99</b>
5.1	Overview . . . . .	99
5.2	Direct Simulation Monte Carlo (DSMC) . . . . .	100
5.3	Interactions of Gas with the Surface . . . . .	100
5.4	Different types of Boundary Conditions . . . . .	101
5.4.1	Maxwell slip boundary condition . . . . .	102
5.4.2	Smoluchowski temperature jump boundary condition . . . . .	103
5.4.3	The Le Temperature Jump boundary Condition . . . . .	104
5.4.4	Pressure Jump Boundary Condition . . . . .	105
5.5	Heat transfer in a rarefied gas flow simulations . . . . .	107
5.6	Hypersonic Flat Plate Case . . . . .	107
5.7	Boundary and initial conditions . . . . .	108
5.8	Numerical Verification and Validations . . . . .	108
5.9	Results and Discussion . . . . .	108
5.9.1	Case 1: Metcalf <i>et al.</i> 's, $M_\infty = 6.1$ and $T_w = 77\text{K}$ . . . . .	111
5.9.2	Case 2: Metcalf <i>et al.</i> 's, $M_\infty = 6.1$ and $T_w = 294\text{K}$ . . . . .	113
5.9.3	Case 3: Becker's, $M_\infty = 12.7$ and $T_w = 292\text{K}$ . . . . .	118
5.9.4	Convergence Study . . . . .	119
5.9.5	Effect of $\zeta$ used for the pressure jump wall boundary condition. . . . .	119
5.10	Closure . . . . .	123
<b>6</b>	<b>Investigation of non-equilibrium boundary conditions considering sliding friction for micro/nano flows</b>	<b>127</b>
6.1	Overview . . . . .	127
6.2	General Problem Setup . . . . .	128
6.3	Boundary and initial conditions . . . . .	128
6.4	Results and Discussion . . . . .	129
6.4.1	Case 1: Pressure driven flow in a Microchannel with $90^\circ$ bend . . . . .	129
6.4.2	Case 2: Pressure driven flow over a backward facing step in a Nanochannel . . . . .	136
6.4.3	Case 3: Nanoscale flat plate . . . . .	139
6.4.4	Case 4: NACA 0012 Microairfoil . . . . .	140



6.5	Closure . . . . .	145
<b>7</b>	<b>Effect of rarefaction in hypersonic computation using two different convective schemes - Roe and modified SLAU2</b>	<b>151</b>
7.1	Overview . . . . .	151
7.2	General Problem Setup . . . . .	152
7.3	Boundary and initial conditions . . . . .	152
7.4	Modified SLAU2 . . . . .	152
7.5	Results and Discussion . . . . .	156
7.5.1	Grid Sensitivity study . . . . .	156
7.5.2	Effect of Rarefaction . . . . .	157
7.6	Closure . . . . .	168
<b>8</b>	<b>Conclusions and Future Work</b>	<b>171</b>
8.1	Conclusions . . . . .	171
8.2	Scope for Future Work . . . . .	173
<b>A</b>	<b>Modified SLAU2: Validation &amp; Verification</b>	<b>175</b>
A.1	Formulation of M-SLAU2 . . . . .	175
A.2	Validation & Verification . . . . .	176
A.2.1	Laminar flow over a flat plate ( $Ma_\infty = 0.2$ ) . . . . .	177
A.2.2	Inviscid flow over airfoil with transonic free-stream condition ( $Ma_\infty = 0.8$ ) . . . . .	177
<b>B</b>	<b>Hypersonic Flow over a cylinder: Using Pressure and Le Temperature Jump condition</b>	<b>181</b>
	<b>References</b>	<b>185</b>
	<b>List of publications</b>	<b>185</b>

# List of Figures

2.1	A finite control volume (non-moving). . . . .	30
2.2	Gradient Computation on a tetrahedral grid. The cross denotes the location where the gradients are evaluated in order to compute the viscous fluxes (mid-point of the face ABC). . . . .	45
2.3	Piecewise linear reconstruction. . . . .	46
3.1	Turbulence boundary layer u-velocity profile. . . . .	70
3.2	Flowchart summarizing the construction of $\mathcal{M}$ matrix. . . . .	74
4.1	Case 1: Flow domain and conditions for turbulent flow over a flat plate. . . . .	82
4.2	Case 1: The $y^+$ variation of the first grid point for the four different meshes considered. . . . .	82
4.3	Case 1: Turbulent flat plate with an inlet $M_\infty = 0.2$ with the four mesh configurations. . . . .	84
4.4	Case 2: Flow conditions for forced convection over a flat plate. . . . .	85
4.5	Case 2: $y^+$ variation of the first grid point for the four different meshes considered. . . . .	85
4.6	Case 2: Forced convection over a flat plate with four different mesh configurations. . . . .	87
4.7	Case 3: Flow domain for turbulent flow over a bump in a channel. . . . .	88
4.8	Case 3: The $y^+$ variation of the first grid point for the three different meshes considered. . . . .	88
4.9	Case 3: Surface Pressure Coefficient for three mesh configurations and the reference. . . . .	90
4.10	Case 3: Contours of eddy viscosity (normalized by free-stream laminar viscosity = $1.846 \times 10^{-5}$ ) for the three different mesh configuration compared with the fine grid results obtained using CFL3D. . . . .	91

4.11	Case 3: Flow over bump in a channel with inlet $Ma = 0.2$ , with the three mesh configurations and the reference. . . . .	92
4.12	Case 4: Flow domain for turbulent flow over the NACA 0012 airfoil with a zoomed view of the nose of the airfoil. . . . .	93
4.13	Case 4: The $y^+$ variation of the first grid point for the three different meshes considered. . . . .	94
4.14	Case 4: Flow over the NACA 0012 airfoil with $Ma = 0.15$ with the three mesh configurations and reference. . . . .	95
4.15	Case 4: Flow over the NACA 0012 airfoil with $Ma = 0.15$ with on Mesh-3 with and without AWT. . . . .	97
5.1	Flat plate problem. . . . .	109
5.2	Code Verification: The profile of surface temperature and heat flux over the flat-plate surface. . . . .	110
5.3	Metcalf et al.'s case: $T_w = 77K$ . Comparison of temperature and pressure over the flat plate surface. . . . .	114
5.4	Metcalf et al.'s case: $T_w = 77K$ . Slip velocity, wall heat flux and shear work per unit area (measure of sliding friction) distribution over the flat plate surface. . . . .	115
5.5	Metcalf et al.'s case: $T_w = 294K$ . Comparison of temperature and pressure over the flat plate surface. . . . .	116
5.6	Metcalf et al.'s case: $T_w = 294K$ . Slip velocity, wall heat flux and shear work per unit area (measure of sliding friction) distribution over the flat plate surface. . . . .	117
5.7	Becker's case: Comparison of temperature and pressure over the flat plate surface. . . . .	120
5.8	Becker's case: Slip velocity, wall heat flux and shear work per unit area (measure of sliding friction) distribution over the flat plate surface. . . . .	121
5.9	Convergence history of the scaled residue of pressure for Case-1. . . . .	122
5.10	Effect of $\zeta = 0$ and clipped $\zeta$ using Eq. 5.13, used for the pressure jump wall boundary condition for predicting the surface pressure. Comparison of PC3 (with the sliding friction and the pressure jump BC using Eq. 5.8 and Eq. 5.12 respectively.) with the DSMC and experiment results. . . . .	124
6.1	Grid Independence and Convergence study for the case of a pressure driven microchannel. . . . .	131



---

6.2	Pressure driven flow in a Microchannel with 90° bend. . . . .	132
6.3	Flow distributions along the channel centerline. . . . .	133
6.4	Variation of various flow properties along the lower/right wall of 90° microchannel, normalised by its entire length. . . . .	134
6.5	Temperature distributions along the channel centerline. . . . .	135
6.6	Backward facing step nanochannel with a pressure driven flow. . . . .	137
6.7	Variation of various flow properties along the wall 3 (lower wall after step). . . . .	138
6.8	Nanoscale flat plate problem (L=100 nm). . . . .	139
6.9	Flow profile at $x = 80$ nm from the plate tip. . . . .	141
6.10	Density contour computed using PC1 for the nanoscale flat plate problem, showing the formation of boundary layer and diffusive shock at free stream Mach number of 4.38. . . . .	142
6.11	Variation of various flow properties along the surface of the flat plate. . . . .	143
6.12	Schematic of flow domain. . . . .	144
6.13	Variation of temperature along the lower and upper wall of the airfoil. . . . .	146
6.14	Variation of surface pressure coefficient along the lower and upper wall of the airfoil. . . . .	147
6.15	Variation of slip velocity distribution along the lower and upper wall of the airfoil. . . . .	148
6.16	Variation of heat transfer distribution along the lower and upper wall of the airfoil. . . . .	149
7.1	Flow domain and mesh used for the flow over the half cylinder (R=38.1 mm). . . . .	153
7.2	Heat flux prediction using SLAU2 and M-SLAU2 for two Mach numbers. The heat flux at the surface of wall is plotted over the whole half cylinder. We have, however, shown the variation at the top and bottom of the cylinder together in order to observe the presence of asymmetry, if present. . . . .	154
7.3	Grid independence study using four meshes with different first grid point spacing. . . . .	158
7.4	Heat flux prediction at different Knudsen number for the case A ( $M_\infty = 8.0$ ). . . . .	161
7.5	Heat flux prediction at different Knudsen number for the case B ( $M_\infty = 16.34$ ). . . . .	162

7.6	Wall Shear stress prediction at different Knudsen number for the case A ( $M_\infty = 8.0$ ). . . . .	164
7.7	Wall Shear stress prediction at different Knudsen number for the case B ( $M_\infty = 16.34$ ). . . . .	165
7.8	Mach number line contour using (a) Roe and (b) M-SLAU2 scheme at different Knudsen number for the case A ( $M_\infty = 8.0$ ). . . . .	166
7.9	Mach number line contour using (a) Roe and (b) M-SLAU2 scheme at different Knudsen number for the case B ( $M_\infty = 16.34$ ). . . . .	167
A.1	Flow domain for the case of laminar flow over flat plate. . . . .	177
A.2	Plot for the velocity profile at $Re_x = 1.059 \times 10^6$ . . . . .	178
A.3	Computational domain and mesh for the case of inviscid flow over airfoil. . . . .	179
A.4	Pressure Coefficient along the wall: Comparison for $M = 0.8$ and $\alpha = 1.25^\circ$ with the reference solution [1]. . . . .	179
B.1	Wall heat flux and temperature jump calculated for the case B ( $M_\infty = 16.34$ ) using three different boundary conditions. PC3 is not plotted for the case of (a), (b) and (c) as it leads to unstable results. . . . .	183
B.2	Pressure and slip velocity at the wall calculated for the case B ( $M_\infty = 16.34$ ) using three different boundary conditions. PC3 is not plotted for the case of (a), (b) and (c) as it leads to unstable results. . . . .	184

# List of Tables

5.1	Different experimental flow conditions for flat plate cases considered.	111
5.2	Coefficients of transport properties of the different gases considered. .	111
5.3	Different studies performed based on the wall BC's for velocity, temperature and pressure. . . . .	111
6.1	Coefficients of transport properties of the different gases considered. .	129
6.2	Different studies performed based on the wall BC's for velocity, temperature and pressure. . . . .	129
7.1	Different cases considered for the parametric study. . . . .	159
7.2	Peak heating computed using various cases considered. A1 and B1 experimental results is also tabulated. . . . .	167





# Nomenclature

## Roman Symbols

$\hat{A}$	Approximate Jacobian Matrix
$c$	speed of sound
$C$	Courant number
$C_f$	skin friction coefficient
$C_p$	surface Pressure coefficient
$c_p$	specific heat capacity at constant pressure
$c'$	chord length
$c_v$	specific heat capacity at constant volume
$d$	distance; diameter
$\Delta\hat{S}^x$	projections of the control volume on the yz
$\Delta\hat{S}^y$	projections of the control volume on the xz
$\Delta\hat{S}^z$	projections of the control volume on the xy
$\Delta t$	global time-step
$E$	total specific energy
$\mathbf{F}$	convective flux vector
$\mathbf{G}$	viscous flux vector
$H$	total specific enthalpy
$\underline{J}$	Jacobian Matrix
$A$	Jacobian Matrix
$k$	thermal conductivity
$k_B$	Boltzmann constant = $1.38 \times 10^{-23}$ J/K

---

$Kn$	Knudsen number
$L$	characteristic length scale
$l$	length
$M$	Mach number
$\bar{M}$	modal matrix
$\dot{m}$	mass flux
$h$	specific enthalpy
$m$	mass of a molecule
$\mathbf{N}$	unit normal vector
$Nu$	Nusselt Number
$n_x$	x-component of unit normal
$n_y$	y-component of unit normal
$n_z$	z-component of unit normal
$p$	pressure
$Pr$	laminar Prandtl number
$Pr_T$	Turbulent Prandtl number
$\mathbf{Q}$	Primitive variables vector
$R$	specific gas constant
$Re_{cell}$	grid Reynolds number
$Re$	Reynolds number
$\mathbf{R}$	residual
$\mathbf{S}_W$	source term vector
$S$	boundary
$s_b$	entropy
$\mathbf{S}$	tensor
$\mathbf{q}$	heat flux
$S_x$	x-component of face surface area vector
$S_y$	y-component of face surface area vector
$S_z$	z-component of face surface area vector

$T$	static temperature
$t$	time
$u$	x-component of velocity
$U_p$	velocity magnitude at the cell adjacent to the wall
$U^+$	$= U_p/u_\tau$ , non-dimensional speed for wall functions
$U_r$	reference velocity
$\mathbf{u}_S$	slip velocity $= \mathbf{u} - \mathbf{u}_w$
$u_\tau$	friction speed
$v$	y-component of velocity
$V_n$	contra-variant velocity
$\vec{v}$	velocity vector with u, v and w as the component
$\mathbf{W}$	conserved variables vector
$w$	z-component of velocity
$x, y, z$	cartesian coordinates
$y_0$	bump height
$y_p$	distance from the centroid of the cell adjacent to the wall
$y^+$	$= yu_\tau/\nu$ , dimensionless normal-to-wall distance for wall functions or grid generation

### Greek Symbols

$\Delta l$	first cell height normal to the wall
$\epsilon_{vk}$	Venkarkrishnan's limiter controlling parameter
$\Gamma$	preconditioning matrix
$\gamma$	specific heat ratio
$\lambda$	molecular mean free path
$\Lambda_c$	eigenvalue of the convective flux Jacobian
$\hat{\Lambda}_c$	spectral radius of the convective flux Jacobian
$\hat{\Lambda}_v$	spectral radius of the viscous flux Jacobian
$\mu$	dynamic viscosity
$\Omega$	volume

---

$\bar{\omega}$	VHS temperature exponent
$\Psi$	used in definition of convective componet of flux vector of SLAU2 scheme
$\Psi$	limiter
$\rho$	density
$\sigma$	fraction or accomodation coefficient
$\sigma_T$	thermal accomodation coefficient
$\sigma_u$	tangential momentum accomodation coefficient
$\tau$	viscous stress
$\tau_{ij}$	components of viscous stress
$\zeta$	ratio of the normal viscous stresses to pressure
<b>Superscripts</b>	
$n$	previous time step
$n + 1$	new time step
<b>Subscripts</b>	
0	values related to cell0
1	values related to cell1
b	boundary value
$f$	related to the face of control volume
$i, j, k$	nodal point index
$\infty$	at infinity (free-stream)
$L$	left state of the face; laminar
$nb$	neighboring cell
o	stagnant (or total) value
$\vec{r}$	position vector
$ref$	reference value
$R$	right state of the face
$T$	turbulent
$w$	wall

**Acronyms / Abbreviations**

AUSM	Advection Upstream Splitting Method
CFD	Computational Fluid Dynamics
CFL	CourantFriedrichsLewy (number)
DNS	Direct Numerical Simulation
DSMC	Direct Simulation Monte Carlo
FRANS	Favre and Reynolds Averaged Navier-Stokes Equations
HRN	high-Reynolds-number
LES	Large Eddy Simulation
LRN	low-Reynolds-number
RANS	Reynolds Averaged Navier-Stokes Equations
RHS	right-hand-side
SA	Spalart-Allmaras
SLAU	Simple Low-dissipation AUSM
UPC	Unconditional positive-convergent
VHS	Variable Hard Sphere





# Chapter 1

## Introduction

### 1.1 Background

Aerothermodynamics is the branch of fluid mechanics that focuses on the effect of the thermodynamic and transport models on aerodynamics and heating [2]. The aerothermodynamics challenge requires [3]:

1. Providing an optimal design which satisfies the mission requirements, and
2. Reducing design margin and thus the design costs.

External aerothermodynamics refers to the study of the aerothermodynamic characteristic of an object in an open environment, such that the boundary layer develops freely without the constraints imposed by the adjacent surfaces. The investigation of such fluid flow and heat transfer problems would require the use of experimental or theoretical analysis. However, these have the limitation of being complicated, expensive and in some cases nearly impossible to perform. The advent of advanced numerical techniques and high-speed computation has allowed us to study such flow dynamics using numerical methods. Computational fluid dynamics (CFD) is the branch of fluid mechanics in which numerical simulation of the flow-field is performed by solving the governing partial differential equations for mass, momentum and energy conservation while coupling them with the appropriate relations for thermodynamic and transport properties.

A general purpose CFD solver is a preferred choice for many researchers as it gives the freedom to work on different applications and geometry using a common framework. For a developing nation, it is beneficial to have such a solver developed

indigenously to develop much needed expertise. This thesis is partially a result of the effort being put to develop a 3D unstructured grid density-based solver at Indian Institute of Technology, Hyderabad, India. This solver is designed to tackle external flow problems at both low-speed (incompressible) and very high speed (hypersonic) regimes. Unstructured finite volume method is used for this purpose. Also, nano/micro flows can be solved using the same CFD code. The main focus of this work has been on testing and improving recently proposed numerical methods for solving the class of problems covered in this thesis.

## **1.2 Development of an All-Speed Density-Based Navier-Stokes Solver for Unstructured grid**

Many industrial applications would require us to solve the three-dimensional fluid flow problems with an all-speed feature [4, 5, 6, 7]. The governing fluid flow equations, the Navier-Stokes equations, are commonly solved using either pressure-based or density-based solvers [8]. Pressure-based solvers are used for incompressible flows, while density-based solvers are generally used for compressible flows. However, for flows that involve both low-Mach number essentially incompressible flow along with high-speed compressible flow it is required that the solver should have an all-speed computation capacity. This is generally obtained using preconditioning methods [9, 10] or else by using an all-speed convective scheme [11, 12].

In the first part of this work, we present the development of the robust three-dimensional density-based solver on an unstructured grid to solve flow problems involving complex geometry. The finite volume discretization method is used, wherein the whole flow domain is divided into a number of small control volumes (or cells). The numerical solution is obtained at the center of these cells. The discretization of the temporal, convective and diffusive terms of the Navier-Stokes equations are discussed in this thesis. The various convective schemes used in this work – such as Roe [13], preconditioned Roe [9] and SLAU2 [12] are then explained. The solution in the finite volume framework requires the solution values at the face of the cells (to be obtained by interpolation). In this work, we have used second-order accurate reconstruction flux with limiters to obtain the face value. The diffusion term is discretized using a central order approximation. The various forms of boundary conditions which are used in this work are also explained.

The developed laminar solver has been validated for various regimes of the flow [14, 15, 16, 17] but these test cases have not been presented in this thesis<sup>1</sup>, as this work deals primarily with turbulent and rarefied gas flow computations.

## 1.3 Turbulence Modeling

Computational aerodynamics also plays a key critical role in aircraft and missile aerodynamic design. An accurate prediction of flow-fields even for complex (w.r.t geometry) flow simulations with low computational cost is always desirable. Turbulence adds further difficulty in such predictions. As a step further into the development of the solver, the incorporation of the turbulence models is also discussed in this work.

A laminar Navier-Stokes code could be used to obtain the complete turbulent flow through the method which is known as the direct numerical simulation (DNS) [18, 19]. But the accuracy, computational power and memory requirements to do this are exorbitant. The use of DNS is limited to simple flows at low Reynolds number (Re) ( $\sim 10^4 - 10^5$ ) [8]. For complex flows or flows at higher Re, the DNS computation is limited by the huge computational requirements. Therefore, the researchers usually use an approximate modeling method to obtain the statistically averaged flow quantities.

As compressible flow involves variation in density, the governing equations are obtained by performing a time and mass averaging of the Navier-Stokes equations, to obtain the Favre- and Reynolds- Averaged Navier-Stokes equations [20, 21]. The set of governing equations is then “closed” using different approaches [8]. One commonly used closure is the Boussinesq eddy-viscosity hypothesis [22] which then requires the computation of an effective or turbulent viscosity,  $\mu_T$ . The method to obtain  $\mu_T$  is through the use of turbulence models.

Principally, there are five classes of turbulence models [8]:

1. algebraic
2. one-equation
3. multiple-equations
4. Reynolds-Stress models

---

<sup>1</sup>except, for the case of hypersonic laminar flow over the cylinder, for which the validation case will be presented in Chapter 7 and for the M-SLAU2 scheme for which validation case is presented in Appendix A

of which the first three use the Boussinesq hypothesis.

In this work, the one-equation Spalart Allmaras model [23] is used to find the eddy viscosity. However, we have also incorporated the two multiple-equations model, Standard  $K - \epsilon$  model [24] and Menter's SST  $K - \omega$  Model [25] in the solver. These are discussed in brief/detail in Section 3.3.

A challenge for these models is the computation of the flow near walls, where the strongest gradients of flow variables are found. The near-wall modeling strategies are briefly discussed in Chapter 3. Later, we separately present a major discussion on how we have developed a novel method to perform the near-wall modeling when using the Spalart-Allmaras turbulence model.

The turbulent model equations are convective-diffusive with stiff non-linear source terms for the production, dissipation and diffusion of turbulent energy and other quantities. These terms change the flow variables very rapidly, at a much smaller time-scales as compared to the mean flow. This causes significant stiffness in the governing equations, which in turn stalls their convergence. Also, non-physical solutions can be obtained, with positive turbulent quantities, like energy, taking negative values, as the solution evolves over time. These lead to numerical instability. Positive preserving and convergence issues being the focus of many researchers [26, 27, 28]. In this work, we have used the unconditional positive convergent implicit time integration procedure for the turbulence model equations developed by Mor-Yossef and Levy [29, 30]. They have a general implicit time integration procedure that guarantees the positivity of two-equation turbulence model dependent variables, that is applicable on both structured and unstructured grids.

## 1.4 Automatic Wall Treatment

In industrial cases, most of the fluid dynamic applications involve turbulent bounded flows. This requires flow behavior to be captured accurately and efficiently near walls. The presence of a wall causes the mean velocity to reduce to zero. Also, near to the wall, viscous damping and kinematic blocking cause the velocity to reduce and the turbulence to be considerably modified. However, in the outer part of the near-wall region, due to the presence of strong mean velocity gradients, the production of turbulence kinetic energy and turbulence increase rapidly [31, 32].

The standard procedure to accurately capture the near wall region is to have a very

fine mesh close to the wall. This procedure is known as the integration method and requires a low-Reynolds-number (LRN) type of turbulence model. This approach becomes computationally expensive as the cell count of the mesh becomes large. To counter this, we can alternatively use the log law of wall to model the flow very near the wall, and place the first grid point further from the wall. This latter approach is known as the wall function method, which commonly is used with a high-Reynolds-number (HRN) type of the turbulence model [33].

In this work, we have chosen to use one-equation Spalart-Allmaras [23] because of its accurate predictions of a wide range of aerodynamic flow problems [34, 35, 36] even in comparison with the two-equation RANS based turbulence models. However, this model is a low-Reynolds number model and hence would require very tight grid spacing near the wall. The use of the wall function method with SA is therefore desirable. The wall function method requires the first-grid point to be placed optimally to get accurate results [33] with less computational effort, at  $y^+$  around 30. This placement is difficult to do a-priori during grid generation, as it depends on the yet-unknown flow variables. This has led to developments of ‘automatic wall’ treatment (AWT, also called ‘adaptive’ or ‘enhanced’ by different researchers) which allows for a wider range of first-grid-point placement as it switches between the wall functions to the low-Re formulation depending on the grid spacing [37, 38, 39, 40]. Craft et al. [41] developed a wall function which solves boundary-layer type transport equation across a locally defined sub-grid. Segunda et al. [42] have used the AWT available in commercial solvers for the  $K - \omega$  SST turbulence models for predicting flow over a wavy wall. Recently, Berger and Aftosmis [43] have developed an ODE-based subgrid wall model that is valid even vary far from the wall and into the boundary layer’s wake region ( $y^+ > 500$ ). They also reviewed, Spalding’s classic formula and the analytic Spalart-Allmaras wall function model [44, 45]. Goldberg and Batten [46] have recently used wall functions over rough walls with a one-equation turbulence model and obtained results close to those from two-equation models.

Menter et al. [47, 48] applied an AWT with the SST turbulent model [49, 50], a two-equation turbulent model. We use, and modify, this AWT to obtain an automatic wall treatment for the low-Re SA model. It allows for consistent modeling of eddy viscosity in the inner and outer layers of the near-wall region. This approach allows the desired automatic switching, between a low-Re formulation and the wall function approach, based on the grid density. The detailed description of this work along with

validation and verification will be presented in Chapter 4

## 1.5 Non-Equilibrium Boundary Conditions

The simulation of rarefied gas flow in hypersonic aerodynamics is important for the design of space and re-entry vehicles. Computer simulations can provide the necessary aerodynamic data at less cost and for cases where experiments are difficult to conduct. Therefore, there is a constant effort to develop newer numerical methods and to improve the existing ones based on appropriate physical modeling to bring the computer simulations closer to reality.

In compressible flows, the regimes based on the rarefaction effect of gas molecules can be classified as continuum, slip, transition and free molecular flow. These different regimes are characterized by the Knudsen number ( $Kn$ ), defined as [51]:

$$Kn = \frac{\lambda}{L} \quad (1.1)$$

where  $\lambda$  and  $L$  are the molecular mean free path and characteristic length scale of the flow, respectively. For high gas density,  $Kn$  is small; gas flows can be simulated by solving the Euler ( $Kn \leq 0.0001$ ) or the Navier-Stokes (NS) equation with no-slip boundary conditions ( $0.001 \leq Kn \leq 0.01$ ). As the Knudsen number increases further, there is a corresponding decrease in collisions among the molecules, and the assumptions of the fluid as a continuum begin to fail. The range  $0.001 \leq Kn \leq 0.1$  is called the slip regime, where the no-slip conditions are no longer applicable. For  $0.1 \leq Kn \leq 10$  called the transition regime, the NS equation cannot be used, as the near-equilibrium assumptions for flows breaks down. Flow with  $Kn > 10$  is called the free molecular regime. Hypersonic rarefied flows come under the category of non-equilibrium gaseous flows. High velocities, high temperatures and low gas density are major contributors for non-equilibrium [52, 53].

There have been many studies for rarefied gas flows using Direct Simulation Monte Carlo (DSMC) and Computational Fluid Dynamics (CFD) [54, 55]. The DSMC method is computationally more viable for higher  $Kn$  regimes and has been shown to converge to solutions of the Boltzmann equation [56, 57]. However, the DSMC method is an order of magnitude costlier than the CFD methods for flows in the continuum and slip flow regime [57]. Thus, efforts are made to improve the validity of CFD methods beyond the continuum regime. One such method, used in the slip regime, is to replace

the typically used no-slip boundary conditions with slip velocity and temperature-jump boundary conditions [58]. This allows us to capture the non-equilibrium effects near the surface and helps in a more accurate prediction of heat transfer and flow stresses at the surface which are very important for the design of high altitude vehicles. Non-equilibrium velocity slip and temperature jump boundary conditions have been proposed by several researchers such as Maxwell [59], Smoluchowski [60], Myong [61], Le [55, 62], etc..

Surface temperature and heat flux are very important design considerations for hypersonic vehicles. In the CFD methods, the wall heat transfer is computed using the temperature gradient and the Fourier heat conduction law, whereas in the DSMC method it is computed using the particle velocities [63]. The absence of a velocity contribution causes the result obtained from CFD to differ considerably from the DSMC results for heat transfer. Maslen [64] overcame this problem by adding a sliding friction term to the heat transfer calculation that is obtained from the slip velocity boundary condition applied to the surface. This slip results in a higher heat transfer between the gas molecules and the surface. Recently, Le et al. [65] revisited the formulation proposed by Maslen [64] for a planar surface and extended it for a curved geometrical surfaces. In another recent work [62] they modified the Smoluchowski temperature jump condition by considering the sliding friction viscous heat generation and derived a new temperature jump condition (referred to as the Le temperature jump condition, henceforth) which gives good agreement, for the surface gas temperature and heat transfer, with DSMC results. However, they did not investigate the effect of the jump condition on the prediction of other flow properties. There is a need for more comprehensive analysis of the effect of the Le temperature jump boundary condition on all relevant flow properties for different flow conditions. The detailed study on this is performed in the Chapter 5 using the case of hypersonic flow over a flat plate.

## 1.6 Applications to Micro/Nano Flows

Accurate prediction of temperature and heat is crucial for the design of various nano/micro devices in engineering. Non-equilibrium effects such as rarefaction and gas-surface interactions have an important influence on fluid mechanics and heat transfer for nano/micro gas flows in Nano/Micro Electronic Mechanical Systems



(NEMS/MEMS). These find many applications in areas such as microprocessor cooling and biomedical analyses, etc., and have led to certain common terminologies such as micropumps, micro-ducts, micro-heat-exchangers and micro-sensors [66, 67]. Rarefaction effects are present in various NEMS/MEMS devices. In the Chapter 5, as discussed in the previous section, we will present the recently proposed Le temperature jump boundary condition considering the viscous heat generation (sliding friction) as an alternative jump condition for the prediction of the surface gas temperature at solid interfaces. Through the study of hypersonic flow over a flat plate [68, 69] in Chapter 5, it will be shown that the Le temperature jump boundary condition should be complemented with a pressure jump boundary condition at the wall, [70, 53]. An over-prediction of pressure, especially at the leading edge of the flat plate, that is seen when using the Le temperature jump condition alone can be corrected by the pressure jump condition.

Le et al. [62] have investigated the flow over a micro-airfoil and have studied the temperature and heat flux distribution over the airfoil surface using their jump condition considering, sliding friction. It would be interesting to study the effect of the jump conditions considering sliding friction, on the other flow properties as well and for different types of nano/micro devices. The detailed study is performed in the Chapter 6.

## 1.7 Hypersonic Flow over a Cylinder

The design of a thermal protection system for hypersonic vehicles is highly dependent on the accurate prediction of the aero-thermal characteristics [71, 72]. CFD, being a cheaper and more accessible design tool, is used extensively in the design of such hypersonic vehicles. However, the computation of hypersonic flows in the continuum regime has been found to be surprisingly difficult, with the standard methods seldom achieving accurate and robust prediction of the wall heat flux. Another problem is the robust capture of shocks free from the “carbuncle” phenomena [73, 74, 75, 76]. These predictions are dependent on the mesh geometry, mesh size, near wall grid spacing, the choice of the convective scheme, etc. [77].

Kitamura et al. [78] have stated that a numerical scheme must have the property of shock stability, enthalpy conservation and accurate capture of the boundary layer to be used for such problems. Hoffmann et al. [79] have shown that the wall heat flux

value is highly dependent on the chosen first grid point near the wall. In a separate study, Kitamura [12] have defined the shock related anomalies as “shock oscillations” and “shock instabilities”. Shock oscillations refer to the oscillating nature of the shock in time or space. It is usually found to be confined to two cells only and in grids which are not aligned with the shock. The shock in such cases jumps from one cell to another. Shock instabilities called as “carbuncles” appear only for multi-dimensional cases. However, it is worth noting that shock-fitting methods do not report such anomalies [12], but they are algorithmically difficult, although researchers are still developing more efficient algorithms [80]. These studies are in general confined to the flow at normal atmospheric conditions.

Knowledge of how existing convective schemes behave with the degree of rarefaction is required to better understand the above shock anomalies. How serious is the problem of “shock oscillations” and “shock instabilities” in a rarefied regime? Does the convective scheme used for hypersonic flows behave differently in the rarefied regime, as compared to the continuum regime? These questions are needed to be looked upon to better understand numerical modeling of rarefied gas flows.

Ivanov et al. [81] have shown that the Navier-Stokes equations yield a qualitatively correct solution up to  $Kn = 0.5$  in their study of rarefaction effects over a blunt body. Panda and Moulic [82] have shown in their study of buoyancy-induced (natural convective) gas microflow using the Navier-Stokes equation with the first-order slip and jump boundary condition that the Nusselt number decreases with the increase in Knudsen number, i.e. rarefaction. Shoja-Sani et al. [83] studied the effect of increase in Knudsen number from slip to transition regime on the aerodynamic characteristics of the NACA 0012 airfoil. Huang and Agarwal [84] have analyzed the effect of rarefaction on heat transfer and drag prediction to simulate the hypersonic flow around a blunt body. They have used the commercial solver ANSYS FLUENT and have carried out a shape-optimization study to minimize the drag and heat flux. However, they have not taken into consideration the behavior of different convective schemes with regards to the shock anomalies.

In the continuum regime, a new all-speed convective scheme SLAU (Simple Low-dissipation AUSM [Advection Upstream Splitting Method]) and its extension SLAU2 is gaining popularity [85, 12, 86]. The SLAU2 scheme is designed to reduce the numerical dissipation for the low speed computations and to improve the robustness of the SLAU scheme in case of strong shocks [12]. However, they still suffer from

shock anomalies under certain test conditions as shown in references [87, 88]. The original idea of the SLAU2 has been to add dissipation to the numerically captured shock according to the shock strength. But, as noted by Kitamura et al. [12] SLAU2 still showed discrepancies in the prediction of heat flux for the case of hypersonic flow over a blunt body. We have proposed a modification to the SLAU2 scheme by altering the calculation method for interfacial speed of sound and have found it to improve the prediction of heat flux in the presence of strong shocks, in comparison with the SLAU2 scheme.

Also, to the authors' knowledge, these schemes have not been tested for rarefied flows. Therefore, there is need to study how does these schemes behave with the degree of rarefaction. The nature of shock and its related anomalies with rarefaction is required to be studied in order to understand the shock related phenomena in the hypersonic regime better.

To meet this objective, we have carried out the hypersonic flow simulation over a cylinder at two hypersonic Mach numbers,  $M_\infty = 8.0$  and  $M_\infty = 16.34$ , using the proposed modified SLAU2 and Roe convective schemes. By reducing the free-stream pressure, we increase the degree of rarefaction ( $Kn$ ), and study how these two schemes behave at various  $Kn$  by studying the predicted flow parameters such as wall heat flux, wall shear stress, the flow Mach number and the peak heating value. Also, the relationship of nature of the shock with degree of rarefaction is studied. The detailed study on this is performed in Chapter 7.

## 1.8 Thesis Outline

The present dissertation deals with the development of an unstructured three-dimensional density-based all-speed computational fluid dynamics solver for the application of external aerothermodynamics and micro/nano flows. The thesis is organized into a total of eight chapters including this introduction chapter.

- Chapter 2 describes the governing equations and boundary conditions along with their discretization method which is used to develop the laminar CFD solver.
- Chapter 3 describes the procedure through which turbulence is incorporated into the solver.

- 
- Chapter 4 describes the necessity of the near-wall treatment and our development of an automatic wall function for the Spalart-Allmaras turbulence model.
  - Chapter 5 describes the nature of rarefied gas flows and the different types of non-equilibrium wall boundary conditions which are studied in this work. In this chapter, we perform a comprehensive analysis of a recently developed temperature jump condition and have proposed a possible correction for the observed anomaly in the results.
  - Chapter 6 further investigates the recently developed temperature jump condition along with the possible correction suggested in the previous chapter for various cases of micro/nano flows.
  - Chapter 7 presents the modification to the SLAU2 convective scheme and the parametric study of the effect of rarefaction in hypersonic computations using the case of hypersonic flow over a cylinder at two hypersonic Mach numbers.
  - Chapter 8 summarizes the conclusions of the complete dissertation and highlights possible future work.



# Chapter 2

## Governing Equations and Discretization

### 2.1 Introduction

In this chapter, we present a numerical procedure for solving the Navier-Stokes equation using a density-based algorithm. The discretization is done using the finite volume method on an unstructured grid. The Navier-Stokes equation is derived from the conservation of momentum while the commonly referred system of Navier-Stokes equations also includes the laws of conservation for mass and energy. They consist of four terms classified as temporal, convection, diffusion and source. The discretization of these terms is also discussed in this chapter. A computational domain in a finite volume approach consists of interior cells and boundary faces. The governing equations are numerically solved at the interior cell-center points, and appropriate boundary conditions are applied at the boundary faces.

### 2.2 Navier-Stokes Equations

The study of the behavior of fluids is termed “*fluid dynamics*”. The principal mathematical equations governing the study of fluid dynamics are determined using the following conservation laws:

1. Conservation of mass,
2. Conservation of momentum,

## 3. Conservation of energy.

The details of these conservation laws can be found in any popular fluid dynamics text-book e.g. Ref. [89, 8]. The complete system of equations derived using the above conservation laws assuming Newton's law of viscosity is called the *Navier-Stokes Equations*. They can be used both in a differential form or in integral form. In their integral form, they describe the flow based on the exchange of mass, momentum and energy across the boundary  $S$  of a control volume  $\Omega$  as shown in Fig. 2.1.

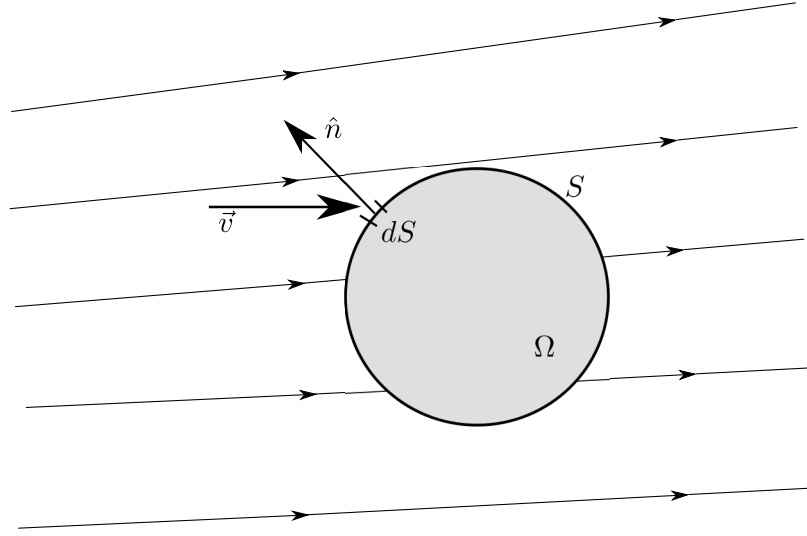


Figure 2.1: A finite control volume (non-moving).

The complete system of Navier-Stokes equations for conservation flow is shown below:

$$\frac{\partial}{\partial t} \int_{\Omega} \mathbf{W} d\Omega + \oint_S [\mathbf{F} - \mathbf{G}] dS = \int_V \mathbf{S}_W d\Omega \quad (2.1)$$

where,

$$\mathbf{W} = \begin{pmatrix} \rho \\ \rho u \\ \rho v \\ \rho w \\ \rho E \end{pmatrix} \quad (2.2)$$



The vector of convective fluxes is written as

$$\mathbf{F} = \begin{pmatrix} \rho V_n \\ \rho V_n u + p n_x \\ \rho V_n v + p n_y \\ \rho V_n w + p n_z \\ \rho V_n H \end{pmatrix} \quad (2.3)$$

where,  $V_n$  is the *contravariant velocity* - the velocity normal to the surface element  $dS$  with unit normal,  $\hat{n}$ - being defined as

$$V_n \equiv \vec{v} \cdot \hat{n} = n_x u + n_y v + n_z w \quad (2.4)$$

and the total specific energy,  $E$  is:

$$E = c_v T + \frac{u^2 + v^2 + w^2}{2}$$

and the total specific enthalpy,  $H$  is:

$$H = E + \frac{p}{\rho}$$

The viscous fluxes vector is written as

$$\mathbf{G} = \begin{pmatrix} 0 \\ n_x \tau_{xx} + n_y \tau_{xy} + n_z \tau_{xz} \\ n_x \tau_{yx} + n_y \tau_{yy} + n_z \tau_{yz} \\ n_x \tau_{zx} + n_y \tau_{zy} + n_z \tau_{zz} \\ n_x \theta_x + n_y \theta_y + n_z \theta_z \end{pmatrix} \quad (2.5)$$

where,

$$\begin{aligned} \theta_x &= u \tau_{xx} + v \tau_{xy} + w \tau_{xz} + k \frac{\partial T}{\partial x} \\ \theta_y &= u \tau_{yx} + v \tau_{yy} + w \tau_{yz} + k \frac{\partial T}{\partial y} \\ \theta_z &= u \tau_{zx} + v \tau_{zy} + w \tau_{zz} + k \frac{\partial T}{\partial z} \end{aligned}$$

The  $\theta$ 's are the terms relating to the heat influx due to viscous stresses and to the

heat conduction in the fluid. The shear (or viscous) stress terms are defined as:

$$\begin{aligned}\tau_{xx} &= \frac{2}{3}\mu\left(2\frac{\partial u}{\partial x} - \frac{\partial v}{\partial y} - \frac{\partial w}{\partial z}\right), & \tau_{yy} &= \frac{2}{3}\mu\left(2\frac{\partial v}{\partial y} - \frac{\partial u}{\partial x} - \frac{\partial w}{\partial z}\right), & \tau_{zz} &= \frac{2}{3}\mu\left(2\frac{\partial w}{\partial z} - \frac{\partial u}{\partial x} - \frac{\partial v}{\partial y}\right) \\ \tau_{xy} &= \mu\left(\frac{\partial u}{\partial y} + \frac{\partial v}{\partial x}\right) = \tau_{yx}, & \tau_{xz} &= \mu\left(\frac{\partial u}{\partial z} + \frac{\partial w}{\partial x}\right) = \tau_{zx}, & \tau_{yz} &= \mu\left(\frac{\partial v}{\partial z} + \frac{\partial w}{\partial y}\right) = \tau_{zy}\end{aligned}$$

The right-hand side term of Eq. 2.1,  $\mathbf{S}_W$  is the source term which is set equal to zero in this work. To close the entire system of equation, we need to specify the viscosity coefficient  $\mu$  and the thermal conductivity  $k$  as functions of the thermodynamic state of the system. Following are the additional equations which are derived on the assumption that the working fluid behaves like a calorically perfect gas, as is generally taken in the literature [90, 8] for the study of pure aerodynamic flows.

The ideal gas law is:

$$p = \rho RT \quad (2.6)$$

where  $R$  denotes the specific gas constant. The specific enthalpy is given as,

$$h = c_p T \quad (2.7)$$

The pressure is then conveniently expressed in terms of conservative variables using  $R = c_p - c_v$ ,  $\gamma = \frac{c_p}{c_v}$  as,

$$p = (\gamma - 1)\rho\left[E - \frac{u^2 + v^2 + w^2}{2}\right] \quad (2.8)$$

The viscosity coefficient for a perfect gas has a strong dependence on temperature but is nearly independent of pressure. The commonly used relationship between dynamic viscosity ( $\mu$ ) and the absolute temperature (T) is the Sutherland's formula [91], which is shown below:

$$\mu = A_s \frac{T^{1.5}}{T + T_s} \quad (2.9)$$

where  $A_s = 1.45 \times 10^{-6} \text{ Pa} \cdot \text{s} \cdot \text{K}^{-1/2}$  and  $T_s = 110 \text{ K}$  for air.

The other commonly used viscosity relation, especially for some cases of rarefied

flows is the variable hard sphere (VHS) model [92, 57]. It is given as:

$$\mu = \mu_{ref} \left( \frac{T}{T_{ref}} \right)^{\bar{\omega}} \quad (2.10)$$

where,

$$\mu_{ref} = \frac{15\sqrt{\pi m k_B T_{ref}}}{2\pi d_{ref}^2 (5 - 2\bar{\omega})(7 - 2\bar{\omega})} \quad (2.11)$$

where  $\bar{\omega}$  is the VHS temperature exponent,  $m$  is the mass of one molecule of the gas,  $d_{ref}$  is the diameter of the molecule,  $T_{ref}$  is the reference temperature and  $k_B$  is the Boltzmann constant. For air,  $m = 4.81 \times 10^{-26}$  kg,  $d_{ref} = 4.19 \times 10^{-10}$  m,  $T_{ref} = 273.0$  K and  $\bar{\omega} = 0.77$ .

Assuming, the Prandtl number  $Pr$  is constant in the entire flow field, we get,

$$k = c_p \frac{\mu}{Pr} \quad (2.12)$$

Popularly, there are two classes of numerical methods for solving the Navier-Stokes Equation, which are as follows:

1. Pressure-Based solvers [93]
2. Density-Based solvers [8]

Traditionally, the pressure-based solvers were used for low-speed incompressible flows while the density-based solvers were used for high-speed compressible flows. However, in recent times both have been extended to solve for a wide range of flow conditions [94]. The density-based solver solves the continuity, momentum and energy equations simultaneously. The continuity equation is solved to obtain the flow density while pressure is calculated using the equation of state. The accuracy and convergence of a density-based algorithm are reduced at low-speed [95, 96]. Time-derivative preconditioning provides a methodology for making the convergence and accuracy independent of the Mach number. For this preconditioning, we pre-multiply the temporal term by a suitable preconditioning matrix. This helps to obtain a well-conditioned system by scaling the eigenvalues of the system to similar orders of magnitude [95]. This is done by changing the acoustic speed of the system such that we get a system of equations with eigenvalues of similar magnitudes, to improve the convergence. In the research literature, several approaches to preconditioning have been proposed [97, 98, 99]. Low-speed preconditioning [100] enables simulation of incompressible

flow by a compressible (density-based) solver. The present study uses this algorithm in an indigenous unstructured three-dimensional cell-based finite volume CFD solver [14].

An integral form of the preconditioned compressible Navier-Stokes equation for an arbitrary control volume  $\Omega$  with an elemental surface area  $dS$  is written as [8],

$$\Gamma \int \frac{\partial}{\partial t} \mathbf{Q} d\Omega + \int [\mathbf{F} - \mathbf{G}] dS = 0 \quad (2.13)$$

where  $\mathbf{Q}$  is the vector of primitive variables and  $\mathbf{F}$  and  $\mathbf{G}$  are convection and viscous flux vectors at the cell-face, respectively given as:

$$\mathbf{F} = \begin{pmatrix} \rho V_n \\ \rho V_n u + p n_x \\ \rho V_n v + p n_y \\ \rho V_n w + p n_z \\ \rho V_n H \end{pmatrix} \quad \mathbf{G} = \begin{pmatrix} 0 \\ n_x \tau_{xx} + n_y \tau_{xy} + n_z \tau_{xz} \\ n_x \tau_{yx} + n_y \tau_{yy} + n_z \tau_{yz} \\ n_x \tau_{zx} + n_y \tau_{zy} + n_z \tau_{zz} \\ n_x \theta_x + n_y \theta_y + n_z \theta_z \end{pmatrix}$$

$$\mathbf{Q}^T = \begin{pmatrix} p & u & v & w & T \end{pmatrix}$$

where  $n_x, n_y, n_z$  are the components of the outward unit vector at the cell boundaries, and  $V_n, \theta_x, \theta_y, \theta_z$  are defined as,

$$\begin{aligned} V_n &= n_x u + n_y v + n_z w \\ \theta_x &= u \tau_{xx} + v \tau_{xy} + w \tau_{xz} + k \frac{\partial T}{\partial x} \\ \theta_y &= u \tau_{yx} + v \tau_{yy} + w \tau_{yz} + k \frac{\partial T}{\partial y} \\ \theta_z &= u \tau_{zx} + v \tau_{zy} + w \tau_{zz} + k \frac{\partial T}{\partial z} \end{aligned} \quad (2.14)$$

Using the Gauss divergence theorem, the Navier-Stokes equation is discretized for a general multi-hydral element as,

$$\Gamma \frac{\partial}{\partial t} \mathbf{Q}^{n+1} + \frac{1}{\Omega} \Sigma_f (\mathbf{F}_f - \mathbf{G}_f)^{n+1} dS_f = 0 \quad (2.15)$$

where  $\Gamma$  is the preconditioning matrix which helps in getting accurate solutions of both compressible and incompressible flows at low speeds [100] when using the density-

based algorithm.

$$\Gamma = \begin{bmatrix} \Phi & 0 & 0 & 0 & \rho_T \\ u\Phi & \rho & 0 & 0 & u\rho_T \\ v\Phi & 0 & \rho & 0 & v\rho_T \\ w\Phi & 0 & 0 & \rho & w\rho_T \\ H\Phi - 1 & u\rho & v\rho & w\rho & \rho_T H + \rho c_p \end{bmatrix} \quad (2.16)$$

where  $\Phi$  is defined as

$$\Phi = \frac{1}{U_r^2} - \frac{\rho_T}{\rho c_p} \quad (2.17)$$

and  $U_r$  is the reference velocity whose definition can be found in [100, 14] and  $\rho_T$  is the temperature derivative of density at constant pressure. The quantity  $U_r$  is chosen so that the eigenvalues are of similar magnitude and the system remains well conditioned for the time-scale for the convective and diffusive terms [9]. In the above formulation, the non-preconditioned system is retrieved by setting  $\Phi = \rho_p = \frac{\rho}{p}$ , in Eq. 2.16.

The above system of governing equations is solved numerically. In this work, we have used the finite volume method to discretize the governing equations. We shall now see how the various terms of Eq. 2.15 are discretized.

## 2.3 Spatial Discretization

The numerical approximation of the convective and viscous terms is called the spatial discretization of the Navier-Stokes equations. In the governing equation Eq. 2.15 there are two separate flux terms – convective flux ( $\mathbf{F}$ ) and viscous flux ( $\mathbf{G}$ ). In this section, we see in detail the methodology adopted for their discretization.

### 2.3.1 Convective Flux

The convective flux, to be evaluated, would require the information at the faces of the cell. This has to be obtained by interpolation from the cell-centered values. In compressible flows, the following points has to be considered so as to have a viable numerical method to discretize the convective term.

1. For a supersonic flows, the convective flux assumes a hyperbolic nature based on the theory of characteristics where all the information travels from upstream

to downstream. Hence for these flows, the flux calculations should ensure that only (or mainly) the cell-center values on the upstream side of the face are considered in the interpolation.

2. For a subsonic flow, the convective flux discretization assumes an elliptic nature, wherein the information can move from upstream to downstream and vice versa. The flux calculation for a subsonic flow should therefore ensure that it uses the cell-center values on both sides of the face in the interpolation.
3. A shock wave has both a supersonic and subsonic region on either side; and also creates a mathematical discontinuity in the flow variables. The convective flux term should be able to capture the shock properly.

The convective flux is discretized in this work by using one of three upwind formulations viz., Roe's flux difference splitting [13], or Preconditioned Roe<sup>1</sup> [9], or the SLAU2<sup>2</sup> scheme [12]. The Roe scheme is a classical method and most popular. Preconditioned Roe is an extension of the Roe scheme which is used in a preconditioned Navier-Stokes equation and allows for low-speed calculations even while using the density-based algorithm. The SLAU2 scheme is an extension of the SLAU ((Simple Low-dissipation AUSM (Advection Upstream Splitting Method))) scheme. It allows all-speed calculations even without using a preconditioned system [12, 101]. Also, it is proven to capture hypersonic flows accurately as will be seen later in this thesis.

### 2.3.1.1 Roe's flux difference splitting

Roe's scheme belongs to the group of flux-difference splitting methods. It is based on the solution of the Riemann problem for each wave speed. The Riemann problem for a wave requires the solution of the Euler equation in the neighborhood of a point across which there is initially a discontinuity in the solution variables. Mathematically, it is expressed as a hyperbolic PDE with a discontinuous initial condition. For the one-dimensional Euler equations, it is represented as [102, 103, 104]:

$$\frac{\partial \mathbf{W}}{\partial t} + A \frac{\partial \mathbf{W}}{\partial x} = 0, \quad t > 0 \quad (2.18)$$

<sup>1</sup>The coding for preconditioning was done by Vatsalya Sharma and the final implementation of the method was done in collaboration with the author.

<sup>2</sup>The coding for SLAU2 was done independently by Nikhil Kalkote and Saketh Chandra and the final version used in this thesis is done in collaboration with them and Nived MR.

$$\mathbf{W}(x, 0) = \begin{cases} \mathbf{W}_L, & \text{for } x < 0 \\ \mathbf{W}_R, & \text{for } x > 0 \end{cases} \quad (2.19)$$

where  $\mathbf{W}$  is the vector of the conserved variables and L and R indicate the left and right initial state of the interface across which the solution is to be obtained, here it is  $x = 0$ . Here,  $A$  is the Jacobian matrix of the conserved variables  $\mathbf{W}$ , given as:

$$A(\mathbf{W}) = \frac{\partial \mathbf{F}}{\partial \mathbf{W}} \quad (2.20)$$

where  $\mathbf{F}$  is the convective flux vector. As  $A$  depends on  $\mathbf{W}$ , the solution of the above Riemann problem requires iterations and a large computational effort. A complete Euler solution in an entire domain would require solution of the Riemann problem for each cell for each time-step, making it computationally very intensive [104]. Thus, an approximate non-iterative solution is usually used for the Riemann problem, for computational efficiency.

An approximate Riemann solver developed by Roe [13] is the most widely used convective scheme today. It has the advantage of higher accuracy in boundary layer flows and has a good resolution of shocks. We show below how the Roe scheme is derived from Eqs. 2.18–2.20 [103].

The Jacobian matrix  $A(\mathbf{W})$  is approximated as:

$$A(\mathbf{W}) \simeq \hat{A}(\mathbf{W}_L, \mathbf{W}_R) \quad (2.21)$$

where the approximate flux Jacobian matrix  $\hat{A}$  is represented as a function of the left and right states at  $t = 0$ . The approximate Riemann problem then becomes:

$$\frac{\partial \mathbf{W}}{\partial t} + \hat{A} \frac{\partial \mathbf{W}}{\partial x} = 0, \quad t > 0 \quad (2.22)$$

$$\mathbf{W}(x, 0) = \begin{cases} \mathbf{W}_L, & \text{for } x < 0 \\ \mathbf{W}_R, & \text{for } x > 0 \end{cases} \quad (2.23)$$

Eq. 2.22 is now a linear system with constant coefficients. An approximate Jacobian has to satisfy [104] the property of hyperbolicity of the system, consistency with the

exact Jacobian and conservation across discontinuities. Hyperbolicity of the system requires  $A$  to have real eigenvalues and the corresponding eigenvectors to be linearly independent. Consistency of the Jacobian requires the approximate and the exact Jacobian to become identical for  $\mathbf{W}_L = \mathbf{W}_R$ , such that  $\hat{A}(\mathbf{W}, \mathbf{W}) = A(\mathbf{W})$ . The property of conservation across discontinuity requires the convective flux to be conserved across the discontinuity, i.e.  $\mathbf{F}(\mathbf{W}_R) - \mathbf{F}(\mathbf{W}_L) = \hat{A}(\mathbf{W}_R - \mathbf{W}_L)$ .

Using the above properties, the Roe flux formula is derived. The detail derivation can be found in [13], [104] (Chapter 11) and [103] (Chapter 2, Page 15-16). The final form of the flux is split into three parts. The first two correspond to the two directions along which information is traveling (along the characteristic lines) at the face, and the third part is upwind differencing of the flux split consistent with their corresponding eigenvalues, which is expressed as [8]:

$$\mathbf{F}_R - \mathbf{F}_L = |\hat{A}|_f(\Delta\mathbf{W}) \quad (2.24)$$

The final expression for the flux at each face being:

$$\mathbf{F} = \frac{1}{2} \left[ \mathbf{F}_R + \mathbf{F}_L - |\hat{A}|_f(\Delta\mathbf{W}) \right] \quad (2.25)$$

Here,  $\Delta\mathbf{W} = \mathbf{W}_R - \mathbf{W}_L$ ,  $\mathbf{F}_R = \mathbf{F}(\mathbf{W}_R)$  and  $\mathbf{F}_L = \mathbf{F}(\mathbf{W}_L)$ ; where  $\mathbf{W}_R$  and  $\mathbf{W}_L$  are the reconstructed conservative vectors on the “right” and “left” side of the face. The product of  $|\hat{A}|_f(\nabla\mathbf{W})$  is written as [8]

$$|\hat{A}|_f(\mathbf{W}_R - \mathbf{W}_L) = |\Delta\mathbf{F}_1| + |\Delta\mathbf{F}_{2,3,4}| + |\Delta\mathbf{F}_5| \quad (2.26)$$

where

$$|\Delta\mathbf{F}_1| = |\tilde{V}_n - \tilde{c}| \left( \frac{\Delta p - \tilde{\rho}\tilde{c}\Delta V_n}{2\tilde{c}^2} \right) \begin{bmatrix} 1 \\ \tilde{u} - \tilde{c}n_x \\ \tilde{v} - \tilde{c}n_y \\ \tilde{w} - \tilde{c}n_z \\ \tilde{H} - \tilde{c}\tilde{V}_n \end{bmatrix} \quad (2.27)$$



$$|\Delta \mathbf{F}_{2,3,4}| = |\tilde{V}_n| \left\{ \left( \Delta \rho - \frac{\Delta p}{\tilde{c}^2} \right) \begin{bmatrix} 1 \\ \tilde{u} \\ \tilde{v} \\ \tilde{w} \\ \frac{\tilde{q}^2}{2} \end{bmatrix} + \tilde{\rho} \begin{bmatrix} 0 \\ \Delta u - \Delta V_n n_x \\ \Delta v - \Delta V_n n_y \\ \Delta w - \Delta V_n n_z \\ \tilde{u} \Delta u + \tilde{v} \Delta v + \tilde{w} \Delta w - \tilde{V}_n \Delta V_n \end{bmatrix} \right\} \quad (2.28)$$

$$|\Delta \mathbf{F}_5| = |\tilde{V}_n + \tilde{c}| \left( \frac{\Delta p + \tilde{\rho} \tilde{c} \Delta V_n}{2\tilde{c}^2} \right) \begin{bmatrix} 1 \\ \tilde{u} + \tilde{c} n_x \\ \tilde{v} + \tilde{c} n_y \\ \tilde{w} + \tilde{c} n_z \\ \tilde{H} + \tilde{c} \tilde{V}_n \end{bmatrix} \quad (2.29)$$

The term  $\Delta(\bullet) = (\bullet)_R - (\bullet)_L$ , is defined as the jump condition. The Roe-averaged variables are defined following [13, 8], using the left and the right state of the face (the reconstructed value of left and right cell at the current face):

$$\begin{aligned} \tilde{\rho} &= \sqrt{\rho_L \rho_R} \\ \tilde{u} &= \frac{u_L \sqrt{\rho_L} + u_R \sqrt{\rho_R}}{\sqrt{\rho_L} + \sqrt{\rho_R}} \\ \tilde{v} &= \frac{v_L \sqrt{\rho_L} + v_R \sqrt{\rho_R}}{\sqrt{\rho_L} + \sqrt{\rho_R}} \\ \tilde{w} &= \frac{w_L \sqrt{\rho_L} + w_R \sqrt{\rho_R}}{\sqrt{\rho_L} + \sqrt{\rho_R}} \\ \tilde{w} &= \frac{H_L \sqrt{\rho_L} + H_R \sqrt{\rho_R}}{\sqrt{\rho_L} + \sqrt{\rho_R}} \\ \tilde{c} &= \sqrt{(\gamma - 1) \left( \tilde{H} - \frac{\tilde{q}^2}{2} \right)} \\ \tilde{V}_n &= \tilde{u} n_x + \tilde{v} n_y + \tilde{w} n_z \\ \tilde{q} &= \tilde{u}^2 + \tilde{v}^2 + \tilde{w}^2 \end{aligned} \quad (2.30)$$

Eq. 2.24 will produce unphysical solutions for the case of expansion waves, as  $\mathbf{F}_L = \mathbf{F}_R$ , but  $\Delta \mathbf{W} \neq 0$ . It will cause a discontinuity in the solution for an expansion wave, which should have a smooth solution. It may also lead to the ‘‘carbuncle phenomena’’ where a perturbation occurs ahead of a strong bow shock along the

stagnation line. The underlying problem is that the scheme does not model the sonic point. This anomaly is corrected by modifying the modulus of eigenvalues  $|\Lambda_c| = |\tilde{V} + \tilde{c}|$ , using the Harten's entropy correction [105, 106] given as:

$$|\Lambda_c| = \begin{cases} |\Lambda_c|, & \text{if } |\Lambda_c| > \delta \\ \frac{\Lambda_c^2 + \delta^2}{2\delta} & \text{if } |\Lambda_c| \leq \delta \end{cases} \quad (2.31)$$

where  $\delta$  is a small value, generally taken as 1/10 of the local speed of sound [8], or a value between 0 and 0.125 [107, 8]. In this work, we have used the former definition of  $\delta$ , unless otherwise mentioned.

### 2.3.1.2 Preconditioned Roe

The inviscid flux expression given by Eq. 2.25 can be defined as a second-order central difference with an additional dissipation term. However, for nearly incompressible flows, unphysical results are obtained because the pressure term is not scaled properly; as is shown by an asymptotic analysis of pressure fluctuation with respect to Mach number [108]. This leads to inaccuracy in the result. In order to overcome the above difficulty, preconditioning is applied to the Roe scheme which then shows correct asymptotic behavior even at very low Mach number.

Furthermore, at very low Mach number the system of governing equation becomes stiff, because the flow velocity magnitude is very low compared to the acoustic speed. This reduces the scheme's convergence to the steady state. Preconditioning changes the acoustic speed of the system such that we get a system of equations with eigenvalues of similar magnitude. This helps to improve the rate of convergence.

In this section, we show how we obtain the preconditioned Roe flux, following the derivation given by Weiss and Smith[9]. The flux difference Roe scheme presented in Sec. 2.3.1.1 needs to be adapted to be compatible with the preconditioned system [109]. The matrix  $\hat{A}_f$  can also be written in terms of flux Jacobian  $\partial(F)/\partial(W)$  and  $|\hat{A}|_f$  as:

$$|\hat{A}|_f = \bar{M}|\Lambda_c|\bar{M}^{-1}$$

where  $\Lambda_c = \text{diag}(V_n, V_n, V_n, V_n + c, V_n - c)$ ,  $\bar{M}$  is the modal matrix that is used to diagonalize  $\hat{A}_f$  in the non-preconditioned system.

The preconditioned eigenvalues are used to transform Eq. 2.25 in terms of primitive

variables. The reconstructed primitive variables  $\mathbf{Q}_R$  and  $\mathbf{Q}_L$  on either side of the face are used to recompute the fluxes  $F_L$  and  $F_R$ . The dissipative term on the right hand side of Eq. 2.25 is transformed as follows [9]:

$$\begin{aligned}
|\hat{A}|_f \Delta W &\simeq \hat{A}_f \Delta W \\
&= \Gamma \Gamma^{-1} \frac{\partial F}{\partial W} \Delta W \\
&= \Gamma \left( \Gamma^{-1} \frac{\partial F}{\partial Q} \right) \Delta Q \\
&= \Gamma |\hat{A}_\Gamma|_f \Delta Q
\end{aligned} \tag{2.32}$$

where  $\Delta Q = \mathbf{Q}_R - \mathbf{Q}_L$ . The term  $|\hat{A}_\Gamma|_f$  is defined as:

$$|\hat{A}_\Gamma|_f = \bar{M}_\Gamma |\Lambda_\Gamma| \bar{M}_\Gamma^{-1} \tag{2.33}$$

The modal matrix in Eq. 2.33 is derived based on the preconditioned system, with  $\Lambda_\Gamma = \text{diag}(V_n, V_n, V_n, V_n' + c', V_n' - c')$ .

where,

$$\begin{aligned}
V_n &= \vec{v} \cdot \hat{n} \\
V_n' &= V_n (1 - \alpha) \\
c' &= \sqrt{\alpha^2 V_n^2 + U_r^2} \\
\alpha &= (1 - \beta U_r^2) / 2 \\
\beta &= \left( \rho_P + \frac{\rho_T}{\rho C_p} \right)
\end{aligned}$$

The resultant preconditioned flux can be written in the following form:

$$\Gamma |\hat{A}_\Gamma|_f \Delta Q = |V_n| \begin{Bmatrix} \Delta(\rho) \\ \Delta(\rho u) \\ \Delta(\rho v) \\ \Delta(\rho w) \\ \Delta(\rho E) \end{Bmatrix} \hat{n} + \delta V_n \begin{Bmatrix} \rho \\ \rho u \\ \rho v \\ \rho w \\ \rho H \end{Bmatrix} \hat{n} + \delta p \begin{Bmatrix} 0 \\ n_x \hat{i} \\ n_y \hat{j} \\ n_z \hat{k} \\ V_n \end{Bmatrix} \tag{2.34}$$

where,

$$\delta V_n = M^* \Delta V_n + [c^* - (1 - 2\alpha)|V_n| - \alpha V_n M^*] \frac{\Delta p}{\rho U_r^2}$$

$$\delta p = M^* \Delta p + [c^* - |V_n| + \alpha V_n M^*] \rho \Delta V_n$$

$$\Delta V_n = \Delta v \cdot \hat{n}$$

$$c^* = \frac{|u' + c'| + |u' - c'|}{2}$$

$$M^* = \frac{|u' + c'| - |u' - c'|}{2c'}$$

The above preconditioned system reduces to Roe's flux difference for  $\alpha = 0$ ,  $V'_n = V_n$  and  $c' = U_r = c$ . For preconditioning, we have not used Roe-averaged values. Instead, we have used simple averaging of left and right variables values at the face. For more details of the above formulation, the interested readers can refer to [9].

### 2.3.1.3 SLAU2

Although preconditioned Roe helps to overcome the difficulty associated in the low-speed computation with a density-based solver, it inherits the shortcomings associated with the original Roe scheme. The preconditioned Roe suffers from the lack of accuracy and robustness for high Mach number flows with shocks, as does the original Roe scheme [85]. Also, preconditioning destroys the temporal accuracy of the system. So, it can be directly used only for steady-state problems.

Kitamura and Shima [12] have recently proposed the SLAU2 scheme which is an extension of their previous SLAU scheme. This scheme can be used without preconditioning even at low Mach number and it was designed so as to be robust and accurate for the high Mach number flows and unsteady computations. This scheme reduces the numerical dissipation in low Mach number flows. At high Mach number, it is supposed to add a proper amount of dissipation to the numerically captured shock according to the shock strength. Both these features will make it a more general all-speed scheme in comparison to the preconditioned Roe. The inviscid flux using the SLAU2 scheme is mentioned below. We have used the same notation as used in the original paper of Kitamura et al. [12, 11].

$$\mathbf{F}_{1/2} = \frac{\dot{m} + |\dot{m}|}{2} \boldsymbol{\Psi}^+ + \frac{\dot{m} - |\dot{m}|}{2} \boldsymbol{\Psi}^- + \tilde{p} \mathbf{N} \quad (2.35)$$

where,

$$\boldsymbol{\Psi} = (1, u, v, w, H)^T \quad (2.36)$$

$$\mathbf{N} = (0, n_x, n_y, n_z, 0)^T \quad (2.37)$$

The mass flux can be written as:

$$\dot{m} = \frac{1}{2} \left\{ \rho_L (V_{nL} + |\bar{V}_n|^+) + \rho_R (V_{nR} - |V_n|^-) - \frac{\chi}{c_{1/2}} \Delta p \right\} \quad (2.38)$$

where,

$$|\bar{V}_n| = \frac{\rho_L |V_{nL}| + \rho_R |V_{nR}|}{\rho_L + \rho_R} \quad (2.39)$$

where,

$$|\bar{V}_n|^+ = (1 - g) |\bar{V}_n| + g |V_{nL}|$$

$$|\bar{V}_n|^- = (1 - g) |\bar{V}_n| + g |V_{nR}|$$

$$g = -\max[\min(M_L, 0), -1] \cdot \min[\max(M_R, 0), 1] \in [0, 1]$$

The pressure flux can be written as:

$$\begin{aligned} \tilde{p} = & \frac{p_L + p_R}{2} + \frac{f_{pL}^+ - f_{pR}^-}{2} (p_L - p_R) \\ & + \sqrt{\frac{u_L^2 + v_L^2 + w_L^2 + u_R^2 + v_R^2 + w_R^2}{2}} (f_{pL}^+ + f_{pR}^- - 1) \frac{\rho_L + \rho_R}{2} c_{1/2} \end{aligned} \quad (2.40)$$

where,  $c_{1/2}$  is the inter-facial speed of sound given as:

$$c_{1/2} = \frac{c_L + c_R}{2} \quad (2.41)$$

and other terms are defined as:

$$\chi = (1 - \hat{M})^2 \quad (2.42)$$

$$\hat{M} = \min\left(1.0, \frac{1}{c_{1/2}} \sqrt{\frac{u_L^2 + v_L^2 + w_L^2 + u_R^2 + v_R^2 + w_R^2}{2}}\right) \quad (2.43)$$

$$f_p^\pm = \begin{cases} \frac{1}{2}(1 \pm \text{sign}(M)), & \text{if } |M| \geq 1 \\ \frac{1}{4}(M \pm 1)^2(2 \mp M), & \text{otherwise} \end{cases} \quad (2.44)$$

$$M = \frac{V_n}{c_{1/2}} = \frac{un_x + vn_y + wn_z}{c_{1/2}} \quad (2.45)$$

The third term in the Eq. 2.40, is the dissipation term. It causes the numerical dissipation in the pressure flux term to be proportional to the Mach number at supersonic speed. This correction is intended to help remove the shock anomalies in presence of strong shocks.

However, we shall show in Chapter 7 that the SLAU2 scheme still shows shock anomalies leading to decrease accuracy in the heat flux prediction in presence of strong shocks. We have proposed a simple modification to the SLAU2 scheme, which will help to improve the robustness in flow prediction in the presence of strong shocks. This will be discussed in detail in Chapter 7.

### 2.3.2 Viscous Flux

To evaluate the diffusive fluxes ( $\vec{F}_v$ ) we need to know the values of flow variables and their gradient at the face centers of the control volume. The viscous term has a non-convective nature which allows the values of velocity components ( $u$ ,  $v$  and  $w$ ), the dynamic viscosity ( $\mu$ ) and the heat conduction coefficient ( $k$ ) to be computed as simple average at a face. Taking  $U$  as any of these flow variables we get,

$$U_f = \frac{U_0 + U_1}{2} \quad (2.46)$$

To evaluate the gradient of the velocity components and temperature we follow the following two steps:

1. Simple average of the cell gradients on either side of the face center.

$$\overline{\nabla U}_f = \frac{1}{2}[\nabla U_0 + \nabla U_1] \quad (2.47)$$

where  $\nabla U_0$  and  $\nabla U_1$  are the gradient computed in cell0 and cell1 respectively, using the Green Gauss method.

2. The Green Gauss method has a very wide stencil and does not use nearby information effectively. So, we incorporate local information by replacing the component of the gradient along the line joining the adjacent cell centers (named here as cell0 and cell1) by the directional derivative using the cell-center values. This involves modifying the gradient calculated to allow for use of the two

nearest cell centers [110]:

$$\nabla U_f = \overline{\nabla U}_f - \left[ \overline{\nabla U}_f \cdot \vec{t}_f - \left( \frac{\partial U}{\partial l} \right)_f \right] \vec{t}_f \quad (2.48)$$

where  $\vec{t}_f$  is the unit vector along the line connecting cell0 and cell1; and  $l_f$  is the distance between the cell-centroids of cell0 and cell1.

$$\vec{t}_f = \frac{\vec{r}_f}{l_f} \quad (2.49)$$

and the directional derivative along the line between the cell-centroids,  $\left( \frac{\partial U}{\partial l} \right)_f$  is given as

$$\left( \frac{\partial U}{\partial l} \right)_f \approx \frac{U_1 - U_0}{l_f} \quad (2.50)$$

It is to be noted that this procedure is in the spirit of Rhie-Chow interpolation which is to add and subtract the same quantity but evaluate them in two different ways to the linearly interpolated gradient.

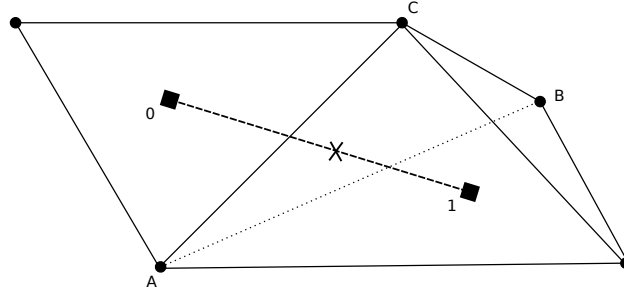


Figure 2.2: Gradient Computation on a tetrahedral grid. The cross denotes the location where the gradients are evaluated in order to compute the viscous fluxes (mid-point of the face ABC).

### 2.3.3 Solution Reconstruction

As seen earlier, the convective term discretization requires the flow states to be defined on the left and right side of the face of a cell. A finite volume cell stores only the cell center value and therefore the solution variation within the cell is lost [111]. Therefore, it is required to approximately represent the solution variation within the cell using the cell center value. This process is termed as reconstruction. We choose to reconstruct the primitive variable, as its gradient is also required for the viscous

flux computation and thus makes it computationally cheaper. In this work, we follow the reconstruction procedure of Barth and Jespersen [112], called the piecewise linear reconstruction. The assumption underlying this procedure is that the solution is piecewise linearly distributed over the control volume. Thus, the face value from the left and right side of a face  $f$  of a cell0 (see Fig. 2.3) is obtained using the following formulation:

$$\begin{aligned} U_L &= U_0 + \Psi_0 \nabla U_0 \cdot \vec{r}_L \\ U_R &= U_1 + \Psi_1 \nabla U_1 \cdot \vec{r}_R \end{aligned} \quad (2.51)$$

where  $\nabla U_0$  and  $\nabla U_1$  is the gradient of  $U$  at the cell center of cell0 and cell1,  $\Psi_0$  and  $\Psi_1$  is the limiter function corresponding to cell0 and cell1, respectively,  $\vec{r}_L$  and  $\vec{r}_R$  are the distance vectors from the cell-center to the face-midpoint as shown in Fig. 2.3. The above formulation is based on the Taylor series expansion about the cell-center and gives second-order accuracy in space. The gradient computation can be accomplished using either least-squares or the Green-Gauss approach. In this work we have used the Green-Gauss approach, owing to its simple form of implementation, which we shall explain below:

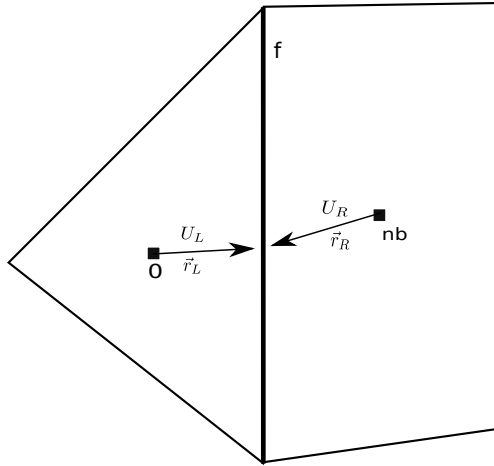


Figure 2.3: Piecewise linear reconstruction.

### 2.3.4 Green-Gauss Method

This method approximates the gradient of a scalar function  $U$ , by using the special form of the Gauss divergence theorem:

$$\iiint_{V_0} \nabla U d\Omega = \iint_S U d\vec{S} \quad (2.52)$$



This yields the discretized form for the cell-center gradient as:

$$\nabla U_0 \approx \frac{1}{\Omega_0} \sum_f \frac{1}{2} (U_0 + U_{nb}) \vec{S}_f \quad (2.53)$$

where  $nb$  denotes the neighboring cell at each face  $f$  and the summation is over all the faces of the cell0 with the volume  $V_0$ , and  $\vec{S}_f$  denotes the face area vector.

### 2.3.5 Limiters

In the regions where the solution has large gradients, e.g. at shocks, high-order schemes (more than 1st order accurate) will suffer from loss in monotonicity; leading to spurious oscillations in the solution. The reason for this is explained based on Godunov theorem, which states: “All linear monotone scheme schemes for the convection equation are necessarily first order accurate” [113]. In other words, high-order linear schemes will always generate numerical solutions which violate the principle of monotonicity. The way around this problem has been to move to nonlinear schemes and make them to be monotonic with high-order accuracy. Limiters are defined as a non-linear fix that enforces monotonicity [111]. A limiter must have the following properties:

1. At strong discontinuities, the limiter function must obtain a first-order upwind scheme to guarantee monotonicity.
2. The gradient should not be limited in the region of smooth flow regions.
3. The concept is - *Within a given cell the interpolated state at the face using the reconstructed gradients must not take values outside the range specified by the cell-averaged states in its neighbours. (ref. Pg. No.25 [111])*

Consider a cell ‘0’ with  $N$  neighbors cell with index ‘ $nb$ ’. Let  $U_0$  and the  $U_{nb}$  denote the cell-center values of the concerned variables at these cells. We define

$$\Delta_{\max} = \max(U_{nb}) - U_0 \quad (2.54)$$

$$\Delta_{\min} = \min(U_{nb}) - U_0 \quad (2.55)$$

where the subscripts max and min indicate the maximum and minimum differences using all the neighbours of Cell0.

To denote the spatial change of a variable in the direction of face  $f$  (at  $\vec{r}_f$ ) of cell0, we first use the component of cell-gradient in the required direction.

$$\Delta = \nabla U_0 \cdot \Delta \vec{r} \quad (2.56)$$

where,

$$\Delta \vec{r} = \vec{r}_f - \vec{r}_0$$

However, this value of  $\Delta$  is not directly used but is multiplied by  $\Psi_0$  (cell0 limiter) before use (Eq. 2.51) in the solution reconstruction. It is also used as switch indicator for varying the value of limiter from 0 to 1. We present below the two popularly used limiters for unstructured meshes which are implemented in our solver, viz. the Max-Min and Venkatakrishnan limiters.

### 2.3.5.1 Max-Min Limiter

The Max-Min limiter [114] for the cell0 is given as

$$\Psi_0 = \min_f \begin{cases} \min(1, \frac{\Delta_{max}}{\Delta}) & \text{if } \Delta > 0 \\ \min(1, \frac{\Delta_{min}}{\Delta}) & \text{if } \Delta < 0 \\ 1 & \text{if } \Delta = 0 \end{cases} \quad (2.57)$$

where  $\min_f$  means the minimum of the values at the faces forming cell0. This limiter not being continuously differentiable, may lead to convergence problems for steady flows. Furthermore, the limiter is active even in the smooth flow regions thus hampering the accuracy of the solution [111].

### 2.3.5.2 Venkatkrishnan's Limiter

The limiter of Venkatkrishnan [115, 116] is widely used for its better convergence properties. The limiting factor for cell0 is given as

$$\Psi_0 = \min_f \begin{cases} \frac{1}{\Delta} \left[ \frac{(\Delta_{max}^2 + \epsilon_{vk}^2)\Delta + 2\Delta^2\Delta_{max}}{\Delta_{max}^2 + 2\Delta^2 + \Delta_{max}\Delta + \epsilon_{vk}^2} \right] & \text{if } \Delta > 0 \\ \frac{1}{\Delta} \left[ \frac{(\Delta_{min}^2 + \epsilon_{vk}^2)\Delta + 2\Delta^2\Delta_{min}}{\Delta_{min}^2 + 2\Delta^2 + \Delta_{min}\Delta + \epsilon_{vk}^2} \right] & \text{if } \Delta < 0 \\ 1 & \text{if } \Delta = 0 \end{cases} \quad (2.58)$$

where  $\epsilon_{vk}^2$  is a limiter controlling parameter. It controls the effect of limiting and preventing the limiter to get active in smooth flow regions. A value of  $\epsilon_{vk} \rightarrow 0$

indicates more limiting and  $\epsilon_{vk} \rightarrow \infty$  indicates no limiting. An ad hoc expression for  $\epsilon_{vk}$  [8] is given as

$$\epsilon_{vk}^2 = (K * h_{vk})^3 \quad (2.59)$$

where  $K$  is a constant of  $\mathcal{O}(1)$  (taken as 2 in this work [8]) and  $h_{vk}$  represents the characteristic length of the scale, taken here  $h_{vk} = (\Omega_0)^{\frac{1}{3}}$ ,  $\Omega_0$  being the volume of the cell. In order to avoid division by zero in the Eq. 2.58 we set the denominator as  $\Delta + 1e^{-15}$

## 2.4 Temporal Discretization

The governing equation, Eq. 2.15 can be written for cell0 as:

$$\frac{d(\Omega\Gamma\mathbf{Q})_0}{dt} = -\mathbf{R}_0 \quad (2.60)$$

Here,  $\Omega$  denotes the control volume.  $\mathbf{R}_0$  stands for the spatial discretization terms (also called the residual) in Eq. 2.15, that serve to couple the system of differential equations for the cells in the domain.

For a static grid, the time derivative is approximated through a non-linear scheme [117], given as

$$\frac{(\Omega\Gamma)_0}{\Delta t} \Delta \mathbf{Q}_0^n = -\frac{\beta}{1+\omega} \mathbf{R}_0^{n+1} - \frac{1-\beta}{1+\omega} \mathbf{R}_0^n + \frac{\omega\Omega\Gamma}{(1+\omega)\Delta t_0} \Delta \mathbf{Q}_0^{n-1} \quad (2.61)$$

with

$$\Delta \mathbf{Q}_0^n = \mathbf{Q}_0^{n+1} - \mathbf{Q}_0^n \quad (2.62)$$

where  $\Delta t$  is the time step. By specifying different values for  $\beta$  and  $\omega$ , we get explicit or implicit schemes with different order of accuracy in time.

### 2.4.1 Explicit Scheme ( $\beta = 0, \omega = 0$ )

Eq. 2.61 becomes

$$\Gamma_0 \Delta \mathbf{Q}_0^n = -\frac{\Delta t_0}{\Omega} \mathbf{R}_0^n \quad (2.63)$$

The following points can be noted down for an explicit scheme:

- Eq. 2.63 is a first order accurate *single-stage* scheme.

- However explicit *multistage* time-stepping schemes (Runge-Kutta schemes) can be implemented.
- It is numerically cheap.
- $\Delta t$  is extremely restricted, particularly for viscous flows.
- For stiff systems (e.g. real gas simulation, turbulence models),  $\Delta t$  becomes very small and the computations required to reach the steady state can be very large.
- An explicit scheme can become unstable and also may have spurious steady solutions. [118]
- For accelerating the convergence, several techniques have been proposed:
  - (a) local-time stepping
  - (b) characteristic time-stepping
  - (c) Jacobi preconditioning
  - (d) Implicit residual smoothing or residual averaging
  - (e) Implicit-explicit residual smoothing
  - (f) Multigrid Method

### 2.4.2 Implicit Schemes ( $\beta \neq 0$ )

In spite of the acceleration techniques mentioned previously an explicit scheme still suffers from small  $\Delta t$  restrictions. This motivates us to use implicit time-stepping methods<sup>3</sup>. Various forms of implicit time stepping can be developed by using  $\beta \neq 0$  in Eq. 2.61. An implicit scheme can be formed by setting  $\omega = 0$  and is best suited for stationary flow problems [8]. Eq. 2.61 can then be written as:

$$\frac{(\Omega\Gamma)_0}{\Delta t} \Delta \mathbf{Q}_0^n = -\beta \mathbf{R}_0^{n+1} - (1 - \beta) \mathbf{R}_0^n \quad (2.64)$$

The solution of Eq. 2.64 is cumbersome as it is a non-linear equation involving the unknown flow variables at the time  $(t + \Delta t)$ . It requires calculating  $\mathbf{R}_0^{n+1}$ , which

---

<sup>3</sup>The conception and initial testing for this was done by Nikhil Kalkote and the final implementation of the method was done in collaboration with the author.

cannot be done as  $Q_0^{n+1}$  is unknown. In order to solve this problem we expand the residual  $\mathbf{R}_0^{n+1}$  around the known residual flux  $\mathbf{R}^n$ , we get

$$\mathbf{R}_0^{n+1} = \mathbf{R}_0^n + \left( \frac{\partial \mathbf{R}}{\partial \mathbf{Q}} \right)_0^n \Delta \mathbf{Q}_0^n + \text{H.O.T} \quad (2.65)$$

where  $\frac{\partial \mathbf{R}}{\partial \mathbf{Q}}$  is the *flux Jacobian*.

The parameter  $\beta$  in Eq. 2.64 is set to 1 for a first order temporal accuracy [8]. Thus, using  $\beta = 1$  and Eq. 2.65, we can rewrite the Eq. 2.64 as:

$$\left[ \frac{\Omega}{\Delta t} \Gamma + \Sigma_f \underline{J}_{f,0} S_f \right] \Delta \mathbf{Q}_0^n - \Sigma_f \underline{J}_{f,nb} \Delta \mathbf{Q}_{nb}^n = -\mathbf{R}_0^n \quad (2.66)$$

where  $0, nb$  refers to centers of the cell and its neighbors, respectively,  $\underline{J}_{f,0/nb}$  is the flux Jacobian matrix of the discretized flux ( $\mathbf{F}^n - \mathbf{G}^n$ ) with respect to variables at the  $0$  or  $nb$  cell-centres. The discretized flux at face  $f$  is a function of the  $0^{th}$  cell value as well as the neighboring cell values, thus the neighboring  $nb$  term appears in the equation above. Rearranging Eq. 2.66 for the whole domain, we get

$$[\underline{I} - \Sigma_f \underline{J}_{f,nb} S_f] \Delta \mathbf{Q}_{global}^n = -\mathbf{R}_{global}^n \quad \text{or} \quad [\underline{A}]_{global} \Delta \mathbf{Q}_{global}^n = -\mathbf{R}_{global}^n \quad (2.67)$$

where

$$\underline{I} \equiv \left[ \frac{\Omega}{\Delta t} \Gamma + \Sigma_f \underline{J}_{f,0} S_f \right] \quad (2.68)$$

is a diagonal matrix and the equation set Eqs. 2.67 is solved using the symmetric Gauss-Seidal procedure [119, 120]. The Jacobian used is the exact Jacobian of the approximate flux. We have used the direct method for the inner iteration (while LU preconditioner takes care of the outer iterations) since the matrix involved is only  $5 \times 5$ . More details can be found in [8] and in the upcoming Nikhil Kalkote's PhD Thesis.

### 2.4.3 Courant number

In order to have the time-stepping choice based on the flow solution at the end of each time-step, we determine the overall time-step size using the user-specified constant CFL number. For the case of explicit schemes the choice of CFL is restricted based on von Neumann Stability analysis (usually  $< 1$ ), however implicit schemes being

much more stable allow for the use of large CFL number ( even  $10^9$  and more<sup>4</sup> [17]). However, in this work, we have limited to a maximum CFL of 500 as, there is not much change in the convergence rate at large CFL. It has been reported in literature [8] that the time-stepping method of Vijayan [121] gives a more accurate time-step estimation:

$$\Delta t_{\text{local}} = \frac{\Omega}{(\hat{\Lambda}_c^x + \hat{\Lambda}_c^y + \hat{\Lambda}_c^z) + C(\hat{\Lambda}_v^x + \hat{\Lambda}_v^y + \hat{\Lambda}_v^z)} \quad (2.69)$$

where C is the chosen Courant number, and the convective spectral radii are defined as:

$$\begin{aligned} \hat{\Lambda}_c^x &= (|u| + c)\Delta\hat{S}^x \\ \hat{\Lambda}_c^y &= (|v| + c)\Delta\hat{S}^y \\ \hat{\Lambda}_c^z &= (|w| + c)\Delta\hat{S}^z \end{aligned} \quad (2.70)$$

and assuming the eddy-viscosity turbulence model, the viscous spectral radii are defined as:

$$\begin{aligned} \hat{\Lambda}_v^x &= \max\left(\frac{4}{3}, \frac{\gamma}{\rho}\right) \left(\frac{\mu_L}{Pr_L} + \frac{\mu_T}{Pr_T}\right) \frac{(\Delta\hat{S}^x)^2}{\Omega} \\ \hat{\Lambda}_v^y &= \max\left(\frac{4}{3}, \frac{\gamma}{\rho}\right) \left(\frac{\mu_L}{Pr_L} + \frac{\mu_T}{Pr_T}\right) \frac{(\Delta\hat{S}^y)^2}{\Omega} \\ \hat{\Lambda}_v^z &= \max\left(\frac{4}{3}, \frac{\gamma}{\rho}\right) \left(\frac{\mu_L}{Pr_L} + \frac{\mu_T}{Pr_T}\right) \frac{(\Delta\hat{S}^z)^2}{\Omega} \end{aligned} \quad (2.71)$$

where  $\Delta\hat{S}^x$ ,  $\Delta\hat{S}^y$  and  $\Delta\hat{S}^z$  are the projections of the control volume on the  $y - z$ ,  $x - z$  and  $x - y$  plane. They are given as:

$$\begin{aligned} \Delta\hat{S}^x &= \frac{1}{2} \sum_{i=1}^{N_F} |S_x|_F \\ \Delta\hat{S}^y &= \frac{1}{2} \sum_{i=1}^{N_F} |S_y|_F \\ \Delta\hat{S}^z &= \frac{1}{2} \sum_{i=1}^{N_F} |S_z|_F \end{aligned} \quad (2.72)$$

where  $S_x$ ,  $S_y$  and  $S_z$  denotes the component of surface area vector at the face of the cell, in the  $x$ ,  $y$  and  $z$ -directions respectively. Eq. 2.69 represents the local time-step calculated for one particular cell. The global time-step used for the computation is taken as the minimum of all the local time-step in the entire zone.

<sup>4</sup>This statement obviously cannot be generalized as it will be problem-dependent.

$$\Delta t = \min(\Delta t_{local}) \quad (2.73)$$

This method is used to calculate the  $\Delta t$  for all the simulations in this work that are done using a fixed Courant number  $C$ .

## 2.5 Initial and Boundary Conditions

In order to solve the governing equation Eq. 2.1 we need to specify appropriate *initial* and *boundary conditions*. The simulations in this thesis are false-transient solutions of steady-state flow. Hence, the initial conditions given can be arbitrary. Throughout this work we have used the free-stream or the inlet values to initialize the entire flow-field. The simulations in this thesis are mostly of external flows, that have at least some open boundaries where the flow domain is artificially truncated. The following are the types of boundaries which are implemented in our solver and are discussed below.

- Inviscid wall
- No-Slip wall
- Non-Equilibrium wall
- Pressure Far-field
- Pressure inlet
- Symmetry

### 2.5.1 Inviscid wall

This boundary condition is used when the inviscid Euler equations are being solved. It is assumed that the velocity vector remains tangential to the surface. This implies that there is no flow perpendicular to the surface. It is given as:

$$\vec{v} \cdot \hat{n} = 0 \quad (2.74)$$

where  $\hat{n}$  is the unit normal vector at the surface. Eq. 2.74 implies that the contravariant velocity  $V_n$  (Eq. 2.4) is zero at the wall and thus the convective flux (Eq. 2.3)

at the wall has only the pressure terms:

$$\mathbf{F} = \begin{pmatrix} 0 \\ p_w n_x \\ p_w n_y \\ p_w n_z \\ 0 \end{pmatrix} \quad (2.75)$$

where  $p_w$  is the pressure at the wall.

### 2.5.2 No-Slip Wall

This boundary condition is used for the Navier-Stokes equation. In case of a viscous fluid passing over a solid wall, the relative velocity between the wall and the fluid is taken to be zero. Therefore, for a stationary surface, this boundary condition becomes

$$u = v = w = 0 \quad (2.76)$$

Since, the velocity component is zero at the wall, in this case also Eq. 2.75 applies for the convective flux calculation.

### 2.5.3 Non-Equilibrium wall

In non-equilibrium flows, when the mean free path of the molecules of the working fluid is of the order of the characteristic length of the flow domain, the gaseous molecules slip over the surface, and we have to use non-equilibrium boundary conditions. The details of these will be discussed separately later in this thesis.

### 2.5.4 Pressure Farfield [111]

When the flow field is truncated by an artificial boundary, we require that the boundary condition minimizes the artificial reflections of outgoing disturbances (such boundary conditions are called *non-reflecting*). At the farfield we can assume the flow is isentropic. Riemann invariants, are formed by assuming the flow to be locally one-dimensional, in the normal direction to the boundary face. Based on these considerations, we define two Riemann invariants (i.e. characteristic variables), corresponding



to incoming (fixed) and outgoing (extrapolated) waves [111, 122]:

$$R_\infty = v_{n_\infty} - \frac{2c_\infty}{\gamma - 1} \quad (2.77)$$

$$R_i = v_{n_i} + \frac{2c_i}{\gamma - 1} \quad (2.78)$$

where,

$$v_{n_i} = \vec{v}_i \cdot \hat{n} \quad \vec{v}_i = [u_i, v_i, w_i]^T \quad c_i^2 = \gamma RT_i \quad (2.79)$$

$$v_{n_\infty} = \vec{v}_\infty \cdot \hat{n} \quad \vec{v}_\infty = [u_\infty, v_\infty, w_\infty]^T \quad c_\infty^2 = \gamma RT_\infty \quad (2.80)$$

$$M_i = \frac{|v_{n_i}|}{c_i} \quad (2.81)$$

If the flow is locally supersonic ( $M_i > 1$ ) and is leaving the domain (i.e. **supersonic outflow**), it means there is no incoming characteristic waves and thus  $R_\infty$  is modified as,

$$R_\infty = v_{n_i} - \frac{2c_i}{\gamma - 1} \quad (2.82)$$

while  $R_i$  remains the same as Eq. 2.78.

Similarly, if the flow is supersonic and entering the domain (i.e. **supersonic inflow**), then there is no outgoing characteristic waves and thus  $R_i$  is modified as,

$$R_i = v_{n_\infty} + \frac{2c_\infty}{\gamma - 1} \quad (2.83)$$

while  $R_\infty$  remains the same as Eq. 2.77.

Thus, in terms of these Riemann invariants, we can obtain the normal velocity and local speed of sound at the boundary  $b$  as follows:

$$v_{n_b} = \frac{1}{2}(R_i + R_\infty) \quad (2.84)$$

$$c_b = \frac{\gamma - 1}{4}(R_i - R_\infty) \quad (2.85)$$

Using the above values, we obtain the velocity vector and entropy on the farfield boundary as follows:

$$\vec{v}_b = \begin{cases} \vec{v}_\infty + (v_{n_b} - v_{n_\infty})\hat{n}, & \text{if } v_{n_b} \leq 0 \text{ (inflow)} \\ \vec{v}_i + (v_{n_b} - v_{n_i})\hat{n}, & \text{if } v_{n_b} > 0 \text{ (outflow)} \end{cases} \quad (2.86)$$

$$s_b = \begin{cases} \frac{c_\infty^2}{\gamma\rho_\infty^{\gamma-1}} & \text{if } v_{n_b} \leq 0 \text{ (inflow)} \\ \frac{c_i^2}{\gamma\rho_i^{\gamma-1}} & \text{if } v_{n_b} > 0 \text{ (outflow)} \end{cases} \quad (2.87)$$

Using the above expressions, the density and pressure is calculated as:

$$\rho_b = \left( \frac{c_b^2}{\gamma s_b} \right)^{1/(\gamma-1)}, p_b = \frac{\rho_b c_b^2}{\gamma} \quad (2.88)$$

### 2.5.5 Pressure Inlet

This boundary condition is generally used for internal flows. This is used to provide a loss-free transition from the inlet flow conditions to the stagnation region. For the ideal gas assumptions, this allows the use of the isentropic flow relations. It requires specification of total pressure ( $P_o$ ), total temperature ( $T_o$ ) and the static pressure ( $P_b$ ) at the inlet.

$$p_o = p_b \left( 1 + \frac{\gamma-1}{2} M^2 \right)^{\frac{\gamma}{\gamma-1}} \quad (2.89)$$

$$T_o = T_b \left( 1 + \frac{\gamma-1}{2} M^2 \right) \quad (2.90)$$

We then use the isentropic relation for total pressure, Eq. 2.89 to determine the Mach number at the inlet. Then using the temperature isentropic relation, Eq. 2.90 we determine the static temperature ( $T_b$ ) at the inlet using the computed Mach number ( $M$ ). Using the temperature, we obtain the sonic speed at the inlet and thus, the velocity based on the Mach number is obtained.

### 2.5.6 Symmetry Plane

For symmetry, there should be no flux across the plane. It is required that the velocity normal to the symmetry plane is zero. A zero gradient is applied to all the flow variables at the symmetry plane.

## 2.6 Closure

In this chapter, we have presented the basic governing equations which can be used for simulating laminar compressible flows. We have presented the all-speed framework of our solver using the preconditioned Roe and the SLAU2 convective schemes. The basic boundary conditions which will be used have been explained. A detailed methodology for the spatial and temporal discretization of the governing Navier-Stokes equations has been discussed.



# Chapter 3

## Turbulence Modeling

### 3.1 Overview

As we have earlier mentioned, in the absence of an exact theory, many heuristic turbulence models compete for the attention of the CFD analyst. The most common approach is to use the Reynolds averaged Navier-Stokes equations (RANS) with a “closure” model for the effective, or turbulent, “eddy viscosity”. These require the governing equations to be the Favre- (for compressible flows) or Reynolds-averaged Navier-Stokes (for incompressible flows) equations with an appropriate turbulence model. The formulation is based on the time or ensemble averaged instantaneous transport equations for mass, momentum and reactive scalars. The primary complexity introduced by averaging is that non-linear terms in the governing equations result in unclosed terms, which cannot be fully determined by the quantities being computed. Thus a closure model is needed to represent the unresolved physics. Most of the closure models involve the Boussinesq assumption that the Reynolds stresses obtained from the convective terms of the governing equations can be represented in a pseudo-Newtonian stress-strain rate relationship, with the constant laminar viscosity being replaced by a variable turbulent viscosity which is computed by the turbulence model.

In this chapter, we present the statistically averaged governing equations and show how it is derived, the particular turbulence models that has been used, and the near wall modeling and the unconditional positive convergent implicit scheme for solving the turbulent equations.

## 3.2 Governing Differential Equation

Theoretically speaking, the Navier-Stokes equations discussed in the previous chapter can be used to obtain the complete turbulent flow by solving for the *instantaneous* velocity and pressure fields. The procedure to do so is known as the *direct numerical simulation* (DNS) [18] of the flow. However, the amount of storage and computational time required is very huge due to the fact that all spatial and time scales, down to the smallest, have to be adequately resolved by taking appropriately small grid intervals and time-steps. However, for engineering applications, merely accounting of turbulence in an appropriate manner so as to obtain the gross flow characteristics is looked upon as being more practicable and accessible. It is done by solving the Navier-Stokes equation for *statistically averaged* flow quantities instead of the instantaneous flow variables directly.

### 3.2.1 Reynolds and Favre averaging

The instantaneous Navier-Stokes equations are averaged to solve them, along with turbulence models, in order to obtain the *mean* turbulent flow. Let  $\Phi$  be any dependent variable. It is convenient to define two different types of averaging of  $\Phi$ :

**Classical time averaging (Reynolds averaging):** In this approach the flow variables are divided into two parts – mean and fluctuating. Then, the Eq. 2.13 is solved using the mean values. The variables are decomposed as:

$$\Phi = \bar{\Phi} + \Phi' \quad (3.1)$$

where,  $\bar{\Phi}$  denotes the mean value while, the  $\Phi'$  denotes the turbulent fluctuation of the variable  $\Phi$ . For, stationary turbulence (Steady turbulence), the mean value is determined using time-averaging as shown below:

$$\bar{\Phi} = \lim_{\bar{T} \rightarrow \infty} \frac{1}{\bar{T}} \int_t^{t+\bar{T}} \Phi(t) dt \quad (3.2)$$

For flow where the temperature and density fluctuations can be neglected, using the above Reynold's averaging method leads to a closure problem (i.e. insufficient number of equations for all the unknowns in the governing equations). Using, Eq. 3.1 to obtain RANS equation from Eq. 2.13, leads to additional unknown quantities. These are then solved using additional equations, i.e. the turbulence model.

**Density weighted time averaging (Favre Reynolds averaging):**

The above approach works well for constant density flows. But for compressible flows, it yields additional unknown quantities related to the statistical moments of the density. Favre [123] proposed to use density-weighted averaging procedure, which reduces this problem. Favre averaging for velocity can be obtained as:

$$\tilde{v} = \frac{1}{\bar{\rho}} \lim_{\bar{T} \rightarrow \infty} \frac{1}{\bar{T}} \int_t^{t+\bar{T}} \rho v dt \quad (3.3)$$

where  $\bar{\rho}$  is the Reynolds-averaged density. The decomposition of instantaneous velocity into mass-averaged component ( $\tilde{v}$ ) and a fluctuating component ( $v''$ ) is shown below:

$$v = \tilde{v} + v'' \quad (3.4)$$

**3.2.2 Favre- and Reynolds-Averaged Navier-Stokes Equations**

For hypersonic flows, compressible free shear layers, combustion or flow with significant heat transfer, density fluctuation cannot be neglected. We present in this section the compressible flow equations obtained by performing the Reynold's averaging for density and pressure, and Favre averaging for the other flow variables. A detailed derivation of the *Favre- and Reynolds-averaged Navier-Stokes* equations can be found in many textbook such as Ref. [20, 113]. The final form of the equations can be written as:

$$\begin{aligned} \frac{\partial \bar{\rho}}{\partial t} + \frac{\partial}{\partial x_i} [\bar{\rho} \tilde{v}_i] &= 0 \\ \frac{\partial}{\partial t} (\bar{\rho} \tilde{v}_i) + \frac{\partial}{\partial x_j} (\bar{\rho} \tilde{v}_j \tilde{v}_i) &= -\frac{\partial}{\partial x_j} (\bar{p}) + \frac{\partial}{\partial x_j} (\widetilde{\tau_{ij}} - \bar{\rho} \widetilde{v_i'' v_j''}) \\ \frac{\partial}{\partial t} (\bar{\rho} \tilde{E}) + \frac{\partial}{\partial x_j} (\bar{\rho} \tilde{v}_j \tilde{H}) &= \frac{\partial}{\partial x_j} \left( k \frac{\partial \tilde{T}}{\partial x_j} - \bar{\rho} \widetilde{v_j'' h''} + \widetilde{\tau_{ij}'' v_i''} - \bar{\rho} \widetilde{v_j'' K} \right) \\ &\quad + \frac{\partial}{\partial x_j} [\tilde{v}_i (\widetilde{\tau_{ij}} - \bar{\rho} \widetilde{v_i'' v_j''})] \end{aligned} \quad (3.5)$$

where

$$\tilde{H} = \tilde{E} + \frac{\bar{p}}{\bar{\rho}}$$

The *Favre-averaged Reynolds-stress* tensor is defined as:

$$\tau_{ij}^F = -\bar{\rho} \widetilde{v_i'' v_j''} \quad (3.6)$$

Boussinesq [22] observed that the momentum transfer in the case of turbulent flow is dominated by the fluctuating component of the flow (large energetic turbulent eddies). This leads to the notion that the turbulent shear stress is proportional to the mean strain rate, as is the case in laminar flow. This is known as the Boussinesq eddy-viscosity hypothesis. This further leads to the idea that the Reynolds stress can be modeled by an equation similar to the laminar viscous stress, with the molecular viscosity being replaced by a similar “eddy viscosity”. Mathematically, it is written as:

$$\tau_{ij}^F = 2\mu_T \tilde{S}_{ij} - \left(\frac{2\mu_T}{3}\right) \frac{\partial \tilde{v}_k}{\partial x_k} \delta_{ij} - \frac{2}{3} \bar{\rho} \tilde{K} \delta_{ij} \quad (3.7)$$

where  $\mu_T$ ,  $\tilde{S}_{ij}$  and  $\tilde{K}$  respectively denote the turbulent viscosity, Favre-averaged strain rate and turbulent kinetic energy. Almost all the RANS based models use the Boussinesq approximations as their basis. The different models differ only in the way they find the eddy-viscosity  $\mu_T$ , using either an algebraic prescription or one or two partial differential equations - which are thereby called zero-, one- or two equation models.

Following the Reynolds analogy, i.e. the heat flux in a turbulent system is treated as analogous to the shear stress, and the turbulent heat-flux vector is modeled as:

$$\bar{\rho} \widetilde{v_j'' h''} = -k_T \frac{\partial T}{\partial x_j} \quad (3.8)$$

where the turbulent thermal conductivity coefficient  $k_T$  is approximated and obtained from  $\mu_T$ , using a prescribed constant value of  $Pr_T$ , the so-called turbulent Prandtl number:

$$k_T = c_p \frac{\mu_T}{Pr_T} \quad (3.9)$$

For the turbulence case, Eq. 2.13 is interpreted as the Favre- and Reynolds-averaged Navier Stokes equations and all the flow variables are taken to be the corresponding Favre-averaged quantities except the pressure and density which are taken to be Reynolds averaged, as seen through Eq. 3.5. We use the Boussinesq hypothesis discussed above and replace the dynamic viscosity used for stress term definition and thermal conductivity in Eq. 2.13 with the following expression [8]:

$$\mu = \mu_L + \mu_T \quad (3.10)$$

$$k = k_L + k_T = c_p \left( \frac{\mu_L}{Pr_L} + \frac{\mu_T}{Pr_T} \right) \quad (3.11)$$



where  $\mu_L$  and  $\mu_T$  are respectively the laminar dynamic and turbulent viscosities (the latter being obtained from the turbulence model, as seen later in Eq. 3.13), while  $c_p$ ,  $Pr_L$  and  $Pr_T$  are the specific heat coefficient, laminar Prandtl number ( $\approx 0.71$ ) and turbulent Prandtl number (assumed to be a constant between 0.7-0.9 [124]) respectively. It is to be noted that we include the  $\frac{2}{3}\bar{\rho}\tilde{K}\delta_{ij}$  term in Eq. 3.7 (which is often dropped), as it is generally considered for supersonic flows [125].

### 3.3 Turbulence models

The above Favre-averaged equation requires additional equations to model the turbulent viscosity. This is achieved using any one of the various turbulence models.

A turbulence model, in general, is expected to have local behavior independent of the grid or dimensions of the flow, insensitivity to the free-stream values, smooth transition from laminar to turbulence, in terms of grid resolution requirement. Further, its predictions in different problems with separated flows, wakes or free vortices, shock-boundary layer interaction reveal the strengths and weaknesses of a model. In the 50 years or so from the start of RANS based turbulence modelling many different models have been proposed, and a vast literature exists on their comparative strengths and weaknesses.

We have chosen three commonly used turbulence models which are popular and well-regarded for implementations in the solver. However, we discuss below in detail only the Spalart-Allmaras model which is primarily used in this thesis, while the other two turbulence model are discussed in brief<sup>1</sup>.

#### 3.3.1 Spalart-Allmaras (SA)

The Spalart-Allmaras (SA) one-equation model [23] uses a transport equation for an eddy-viscosity variable  $\tilde{\nu}$ : The salient features of this model are [8]:

- Accurate predictions of turbulent flow in adverse pressure gradients leading to flow separation.
- It is designed especially for aerospace applications and performs well for wall-bounded flows.

---

<sup>1</sup> The turbulence modeling was done by the author in collaboration with Vatsalya Sharma for the explicit code and later with Nikhil Kalkote for the implicit version of the solver.

- It is “local,” which implies that the equation at any one point does not depend on the solution at the other points, which allows for greater grid independence and applicability of the model in three dimensions also.
- It is robust, converges fast to the steady-state, and requires only moderate grid resolution in the near-wall region. However, it is a “low-Reynolds” number model that requires the grid to extend very close to the wall (unlike, “high-Re” models that allow a coarse grid near the wall, by fitting the log-law of the wall in the near-wall regions).

The governing equation for the model is

$$\begin{aligned} \frac{\partial}{\partial t}(\rho\tilde{\nu}) + \frac{\partial}{\partial x_i}(\rho\tilde{\nu}u_i) = G_\nu + \\ \frac{1}{\sigma_{\tilde{\nu}}} \left[ \frac{\partial}{\partial x_j} \left\{ (\mu + \rho\tilde{\nu}) \frac{\partial \tilde{\nu}}{\partial x_j} \right\} + C_{b2}\rho \left( \frac{\partial \tilde{\nu}}{\partial x_j} \right)^2 \right] - Y_\nu \end{aligned} \quad (3.12)$$

where  $G_\nu$  is the production of turbulent viscosity, and  $Y_\nu$  is the destruction of turbulent viscosity that occurs in the near-wall region due to wall blocking and viscous damping. The parameters  $\sigma_{\tilde{\nu}}$  and  $C_{b2}$  are model constants.

The turbulent viscosity is modeled as:

$$\mu_T = \rho\tilde{\nu}f_{v1} \quad (3.13)$$

where the viscous damping function  $f_{v1}$  is given as:

$$f_{v1} = \frac{\chi^3}{\chi^3 + C_{v1}^3} \quad (3.14)$$

where

$$\chi \equiv \frac{\tilde{\nu}}{\nu} \quad (3.15)$$

The production term,  $G_\nu$  is modeled by:

$$G_\nu = C_{b1}(1.0 - f_{t2})\rho\tilde{S}\tilde{\nu} \quad (3.16)$$

where

$$f_{t2} = C_{t3}e^{-C_{t4}\chi^2} \quad (3.17)$$

and

$$\tilde{S} \equiv S' + \frac{\tilde{\nu}}{\kappa^2 d^2} f_{v2} \quad (3.18)$$

and

$$f_{v2} = 1 - \frac{\chi}{1 + \chi f_{v1}} \quad (3.19)$$

Here,  $C_{b1}$  and  $\kappa$  are two more model constants,  $d$  is the distance from the nearest wall,  $\nu = \mu_L/\rho$  is the molecular kinematic viscosity and  $S'$  is a scalar measure of the vorticity magnitude. The formulation for  $S'$  is written as follows [126, 127]:

$$S' \equiv |\Omega_{ij}| + C_{prod} \min(0, |S_{ij}| - |\Omega_{ij}|) \quad (3.20)$$

where  $C_{prod} = 2.0$ ,  $\Omega \equiv \sqrt{2\Omega_{ij}\Omega_{ij}}$ , where  $\Omega_{ij}$  is the mean rate-of-rotation tensor defined by:

$$\Omega_{ij} = \frac{1}{2} \left( \frac{\partial u_i}{\partial x_j} - \frac{\partial u_j}{\partial x_i} \right) \quad (3.21)$$

and  $S \equiv \sqrt{2S_{ij}S_{ij}}$  where  $S_{ij}$  is the mean strain rate tensor defined by:

$$S_{ij} = \frac{1}{2} \left( \frac{\partial u_j}{\partial x_i} + \frac{\partial u_i}{\partial x_j} \right) \quad (3.22)$$

The destruction term  $Y_\nu$  is modeled by:

$$Y_\nu = \left( C_{w1} f_w - \frac{C_{b1}}{\kappa^2} f_{t2} \right) \rho \left( \frac{\tilde{\nu}}{d} \right)^2 \quad (3.23)$$

where

$$f_w = g \left[ \frac{1 + C_{w3}^6}{g^6 + C_{w3}^6} \right]^{1/6} \quad (3.24)$$

and

$$g = r + C_{w2}(r^6 - r) \quad (3.25)$$

where

$$r = \min \left[ \frac{\tilde{\nu}}{\tilde{S}\kappa^2 d^2}, 10 \right] \quad (3.26)$$

### Model Constants

The above formulation has a number of model constants that are given the standard values [23, 128]:  $C_{b1} = 0.1355$ ,  $C_{b2} = 0.622$ ,  $\sigma_{\tilde{\nu}} = \frac{2}{3}$ ,  $C_{v1} = 7.1$ ,  $C_{t3} = 1.2$ ,  $C_{t4} = 0.5$ ,  $C_{w1} = \frac{C_{b1}}{\kappa^2} + \frac{(1+C_{b2})}{\sigma_{\tilde{\nu}}}$ ,  $C_{w2} = 0.3$ ,  $C_{w3} = 2.0$  and  $\kappa = 0.4187$

### Initial and boundary conditions

The inflow boundary condition for the Spalart-Allmaras turbulence model is set to the free-stream turbulent viscosity ratio ( $\mu_T/\mu_L$ ) obtained from the relevant reference. For most of the external flows, it is small; it is generally taken between  $1 < \mu_T/\mu_L < 10$ . At outflow and symmetry boundaries the turbulent variables are extrapolated from interior values. At the wall, for low-Reynolds number modeling,  $\tilde{\nu} = 0$  and hence  $\mu_T = 0$ . The uniform free-stream inflow condition is used to set the initial conditions throughout the flow-field, for the pseudo-transient solution.

### 3.3.2 Standard $K - \epsilon$ model

The standard  $K - \epsilon$  model was proposed by Launder and Spalding [24]. It is a two-equation model. The  $K - \epsilon$  model is derived considering the flow is fully turbulent and the effect of laminar viscosity can be neglected. The standard  $K - \epsilon$  model is therefore valid only for fully turbulent flows. It is the most widely used two-equation model and is most suited for free-shear flows.

The governing equations for the model are

$$\frac{\partial}{\partial t}(\rho K) + \frac{\partial}{\partial x_i}(\rho K u_i) = \frac{\partial}{\partial x_j} \left[ \left( \mu + \frac{\mu_T}{\sigma_k} \right) \frac{\partial K}{\partial x_j} \right] + G_k + G_b - \rho \epsilon - Y_M \quad (3.27)$$

$$\frac{\partial}{\partial t}(\rho \epsilon) + \frac{\partial}{\partial x_i}(\rho \epsilon u_i) = \frac{\partial}{\partial x_j} \left[ \left( \mu + \frac{\mu_T}{\sigma_\epsilon} \right) \frac{\partial \epsilon}{\partial x_j} \right] + C_{1\epsilon} \frac{\epsilon}{K} (G_k + C_{3\epsilon} G_b) - C_{2\epsilon} \rho \frac{\epsilon^2}{K} \quad (3.28)$$

where:

- $G_k$  represents the generation rate of turbulence kinetic energy due to the mean velocity gradients.
- $G_b$  is the generation rate of turbulence kinetic energy due to buoyancy.
- $Y_M$  represents the contribution of the fluctuating dilatation in compressible turbulence to the overall dissipation rate.
- $C_{1\epsilon}$ ,  $C_{2\epsilon}$ , and  $C_{3\epsilon}$  are constants.
- $\sigma_k$  and  $\sigma_\epsilon$  are the turbulent Prandtl numbers for  $K$  and  $\epsilon$ , respectively.

### Modelling of $\mu_T$

The turbulent (or eddy) viscosity,  $\mu_T$ , is computed by combining  $K$  and  $\epsilon$  as follows:

$$\mu_T = \rho C_\mu \frac{K^2}{\epsilon} \quad (3.29)$$

where  $C_\mu$  is a constant.

**Model Constants:**  $C_{1\epsilon} = 1.44$ ,  $C_{2\epsilon} = 1.92$ ,  $C_\mu = 0.09$ ,  $\sigma_k = 1.0$ ,  $\sigma_\epsilon = 1.3$

### 3.3.3 Menter's SST $K - \omega$ Model

Shear-stress transport (SST) [49]  $K - \omega$  model includes a blend between the  $K - \omega$  model (robust and accurate in the near wall region) and  $K - \epsilon$  model (free-stream independence). For this, the  $K - \epsilon$  is transformed into a  $K - \omega$  formulation. This model has the advantage of accurately predicting flows with strong adverse pressure gradients and boundary layer separation.

The governing equation for the model is

$$\frac{\partial}{\partial t}(\rho K) + \frac{\partial}{\partial x_i}(\rho K u_i) = \frac{\partial}{\partial x_j} \left[ \Gamma_k \frac{\partial K}{\partial x_j} \right] + \widetilde{G}_k - Y_k + S_k \quad (3.30)$$

$$\frac{\partial}{\partial t}(\rho \omega) + \frac{\partial}{\partial x_i}(\rho \omega u_i) = \frac{\partial}{\partial x_j} \left[ \Gamma_\omega \frac{\partial \omega}{\partial x_j} \right] + G_\omega - Y_\omega + D_\omega + S_\omega \quad (3.31)$$

where:

- $\widetilde{G}_k$  represents the generation rate of turbulence kinetic energy due to the mean velocity gradients.
- $G_\omega$  is the generation rate of  $\omega$ .
- $\Gamma_k$  and  $\Gamma_\omega$  represent the effective diffusivity of  $K$  and  $\omega$ , respectively.
- $Y_k$  and  $Y_\omega$  represents the dissipation rate of  $K$  and  $\omega$  due to turbulence.
- $D_\omega$  is the cross-diffusion term.

### Modelling of $\mu_T$

The turbulent (or eddy) viscosity,  $\mu_T$ , is computed based on the description given in [25]

$$\mu_T = \frac{\rho a_1 K}{\max(a_1 \omega, S F_2)} \quad (3.32)$$

where  $S = \sqrt{2S_{ij}S_{ij}}$ , is strain rate magnitude, given as

$$S = \left| \frac{1}{2}(\partial_j u_i + \partial_i u_j) \right| \quad (3.33)$$

$F_2$  is a blending function that is equated to 1.0 for the boundary-layer flows and 0.0 for free shear flows, and  $a_1$  is a model constant given the value of 0.31. This modification is done so as to keep the Bradshaw's assumption that the shear stress is proportional to the turbulent kinetic energy  $k$  ( $\tau = \rho a_1 K$ ) satisfied in adverse gradient flows, where the ratio of production to dissipation can be significantly large [129]. It leads to an over-prediction of turbulent shear stress  $\tau$ . The blending function  $F_2$  is used to recover the turbulent viscosity formulation of  $\mu_T = \rho K/\omega$  for free shear layers (where the Bradshaw's assumption does not hold).

### 3.4 Near Wall Physics

One of the major problem encountered in turbulence is to accurately compute flows near walls. Turbo-machinery, external flows over vehicles and internal flows in pipe are some of the examples of flow influenced by turbulence near the wall. The wall causes two effects [33]:

1. Turbulent flow becomes anisotropic due to damping of the wall normal components.
2. Because of shear introduced by the wall, the production of turbulence increases.

An important requirement in the accurate modelling of turbulent flows is the proper treatment of the equations near the wall. This is called near-wall treatment and is important as the flow variables have strong gradients with momentum and turbulent transport occurring most vigorously near the wall. The near-wall zone (see Fig. 3.1) is generally subdivided into three regions: the innermost layer is called the viscous sublayer ( $y^+ < 5$ ), where the turbulence is suppressed by viscosity, the outer layer is the fully-turbulent layer and is called log-law region ( $y^+ > 30$ ) and the in-between layer is called the buffer region ( $5 < y^+ < 30$ ). Here,  $y^+$  is the non-dimensional normal to the wall given as:

$$y^+ = \sqrt{\left(\frac{\tau_w}{\rho}\right)} \quad (3.34)$$

where  $\tau_w$  is the wall shear-stress.

The wall-function treatment and the low Reynolds number method are two alternate approaches for modeling the near-wall region. The wall function treatment employs a semi-theoretical formula to avoid computations in the sublayer region and thus provides the boundary conditions for the mean flow and turbulent variables directly in the buffer layer. This method reduces the computational cost by allowing a coarser grid near the wall. However, its predictive accuracy usually deteriorates if the first grid point, where the boundary conditions are prescribed, does not fall within the buffer region. This region depends on the wall stress, which again is not known a priori at the time of grid generation. As the semi-theoretical formulation used for the wall treatment is obtained from flow over a flat plate, this method cannot be used for predicting accurately decelerating flows and boundary-layer separations.

On the other hand, the low Reynolds number method employs a very fine grid near the wall to resolve the viscous sublayer. This approach, thus, uses significantly more computation due to the fine grid involved. So, for efficient computation in flows where the low-Re approach is not strictly necessary, we would like to use a wall function treatment that would automatically switch from the wall-function to a low-Re formulation depending on the grid-spacing near the wall. Menter et al. [48] proposed an AWT for the SST turbulence model, and we have extended that AWT formulation to the SA model, which we shall discuss in detail in the next chapter.

## 3.5 Time Integration Method

Eq. 2.67 shows the algebraic equation for the mean flow equations. A similar simplified form of the algebraic equation for turbulence can be written as [30]:

$$\left[ \frac{\Omega}{\Delta t} I - \frac{\partial \mathbf{R}}{\partial \mathbf{U}} \right]^n \Delta \mathbf{U}^{n+1} = \mathbf{R}^n \quad (3.35)$$

For this, we use the same LU-SGS method used for solving the mean flow equations. However, direct use of the exact Jacobian  $\frac{\partial \mathbf{R}}{\partial \mathbf{U}}$ , would usually lead to instability, showing convergence and positive preserving<sup>2</sup> difficulties. We have used the unconditional positive-convergent (UPC) time-integration implicit scheme developed by Mor-Yossef and Levy [30] for turbulence transport equations.

<sup>2</sup>Certain turbulent quantities, e.g.  $\mu_T$  and  $K$ , etc., need to be always positive, otherwise they can cause a catastrophic failure of the computations.

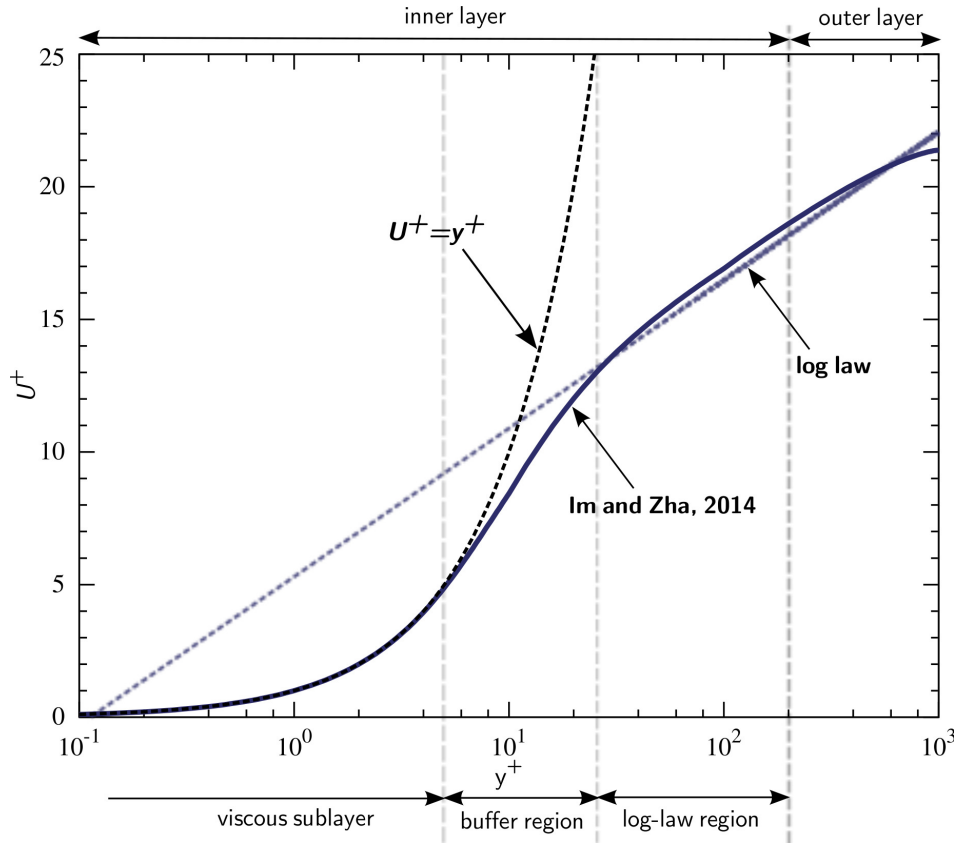


Figure 3.1: Turbulence boundary layer u-velocity profile. (The velocity profile obtained by [130] is also shown.)

### 3.5.1 Theoretical Motivation

The turbulence model equations are convective-diffusive-source equations. The inclusion of a source term causes instability when it becomes dominant. This is generally observed when using turbulence or chemistry models. A large source term changes the flow variables rapidly in space and time, and needs a very small time-step size (*stiffness*) for stable computations. This can be avoided by using temporal linearization of the negative part of the source term [29]. This method allows for the calculation of Jacobian which is close to the true Jacobian so that one gets a rapid convergence when the residuals are small while at the same time it retains the unconditional positivity condition [23].

Mor-Yossef and Levy [30] have given the following definition for an unconditional positive implicit scheme of a discretized form of the turbulence model equations (TME):

**Definition** (Unconditional positive scheme) For a numerical scheme to be uncondi-



tionally positive,  $U^{n+1} > 0$  for any given  $U^n > 0$  and for any time step  $\Delta t$ .

The convective part of TME is discretized using the first order upwind to allow for stability. For an implicit scheme to be unconditionally positive-convergent, the concept of M-matrix<sup>3</sup> is used [131]. An M-matrix has many properties out of which the following is important for the design of an UPC scheme. The Jacobian,  $-\frac{\partial \mathbf{R}}{\partial \mathbf{U}}$  in Eq. 3.35 is approximated by a matrix  $\mathcal{M} \approx -\frac{\partial \mathbf{R}}{\partial \mathbf{U}}$  such that it follows the following two conditions [132]:

1.  $\mathcal{M}$  is an M-matrix.
2.  $\mathbf{R} + \mathcal{M}\mathbf{U}$  is a non-negative vector.

Eq.3.35 can be written in terms of  $\mathcal{M}$  as follow:

$$\left[ \frac{\Omega}{\Delta t} \mathcal{I} - \mathcal{M} \right]^n \Delta \mathbf{U}^{n+1} = \mathbf{R}^n \quad (3.36)$$

Eq. 3.36 is a representation of the UPC scheme. It is solved uncoupled from the mean flow equations. The complete algorithm will be presented in the next chapter while discussing the implementation of the wall function with the SA turbulence model. The detail of the proof and derivation is mentioned in the work of Mor-Yossef and Levy [30].

## 3.6 Constructing the $\mathcal{M}$ matrix

Below we demonstrate using the Spalart-Allmaras turbulence model as an example of how we construct the implicit Jacobian, following references [30, 133]. The Jacobian  $\mathcal{M}$  is split into the convective-diffusive implicit Jacobian and the source term Jacobian. It is defined as:

$$\mathcal{M} = \mathcal{N} + \mathcal{J} \quad (3.37)$$

In the first step, we show how the  $R$  in Eq. 3.36 is constructed. The motivation is to have the residual vector ( $\mathbf{R}$ ) as a product of the matrix with the solution vector ( $\mathbf{U}$ ). This helps in constructing the desired residual Jacobian easily and shows that the implicit Jacobian depends on the residual vector. For a cell  $i$ , let  $\mathbf{R}_i$  denotes the

---

<sup>3</sup>M-matrix is a Z-matrix having the eigenvalues whose real part is nonnegative. Z-matrix is the matrix whose off-diagonal terms are non-positive.

turbulence model residual with  $\mathbf{C}_i$ ,  $\mathbf{D}_i$  and  $\mathbf{S}_i$  being the convective residual, diffusive residual and source term residual, respectively.

$$\mathbf{R}_i = \mathbf{C}_i + \mathbf{D}_i + \mathbf{S}_i \quad (3.38)$$

The convective residual vector  $\mathbf{C}_i$  is written as:

$$\mathbf{C}_i = - \sum_{j \in N(i)} \mathbf{F}_{c_{ij}} S_{ij} = \sum_{j \in N(i)} C_{ij}^i \mathbf{U}_i + \sum_{j \in N(i)} C_{ij}^j \mathbf{U}_j \quad (3.39)$$

where,  $S_{ij}$  is the face area of interface  $ij$ , between the cell  $i$  and its neighbor cell  $j$ . Using HLLC flux discretization [134],  $C_{ij}^i$  is written as:

$$C_{ij}^i = -S_{ij} \mathcal{I} \begin{cases} V_{n_i} & \text{if } S_i > 0, \\ \frac{S_i - V_{n_i}}{S_i - S_M} S_M & \text{if } S_i \leq 0 < S_M, \\ 0 & \text{otherwise.} \end{cases} \quad (3.40)$$

Similarly,  $C_{ij}^j$  is written as:

$$C_{ij}^j = -S_{ij} \mathcal{I} \begin{cases} \frac{S_j - V_{n_j}}{S_j - S_M} S_M & \text{if } S_M \leq 0 \leq S_j, \\ V_{n_j} & \text{if } S_j < 0, \\ 0 & \text{otherwise.} \end{cases} \quad (3.41)$$

where for the SA model  $\mathcal{I}$  is a unit matrix of size 1. The choice of using the HLLC scheme is due to its positive characteristics [29]. Also, we use first order accuracy for the turbulent convective term so as to allow for a positive and stable spatial discretization. The diffusive term is also discretized accordingly as:

$$\mathbf{D}_i = \sum_{j \in N(i)} \mathbf{F}_{d_{ij}} S_{ij} = \sum_{j \in N(i)} D_{ij}^i \mathbf{U}_i + \sum_{j \in N(i)} D_{ij}^j \mathbf{U}_j \quad (3.42)$$

where,

$$D_{ij}^i = -S_{ij} \frac{1}{\rho_i \sigma} \left( \frac{(\mu + \rho \tilde{\nu}) \mathbf{r} \cdot \hat{\mathbf{n}}}{|\mathbf{r}|^2} \right)_{ij} \quad (3.43)$$

and

$$D_{ij}^j = S_{ij} \frac{1}{\rho_j \sigma} \left( \frac{(\mu + \rho \tilde{\nu}) \mathbf{r} \cdot \hat{\mathbf{n}}}{|\mathbf{r}|^2} \right)_{ij} \quad (3.44)$$

In the same way the source term can be written as:

$$\mathbf{S}_i = S^i \mathbf{U}_i \quad (3.45)$$

where  $S^i = \frac{S^i}{\rho \bar{\nu}}$  for SA equation, Eq. 3.12. The complete residual vector as a matrix multiplied with the turbulence solution vector can now be written as using Eq. 3.39-3.45:

$$\mathbf{R}_i = \sum_{j \in N(i)} C_{ij}^i \mathbf{U}_i + \sum_{j \in N(i)} C_{ij}^j \mathbf{U}_j + \sum_{j \in N(i)} D_{ij}^i \mathbf{U}_i + \sum_{j \in N(i)} D_{ij}^j \mathbf{U}_j + S^i \mathbf{U}_i \quad (3.46)$$

### 3.6.1 Convective-Diffusion and Source Jacobian

The construction of the convective-diffusive Jacobian ( $\mathcal{N}$ ) is simplified by splitting each of the matrices  $C_{ij}^i$ ,  $C_{ij}^j$ ,  $C_{ij}^i$ ,  $C_{ij}^j$  into their positive and negative parts as shown below using matrix  $\mathcal{A}$ .

$$\mathcal{A} = \mathcal{A}_P - \mathcal{A}_N \quad (3.47)$$

where

$$\mathcal{A}_P = \left( (a_P)_{kl} \in \mathbf{R}^{2 \times 2} \right)$$

and

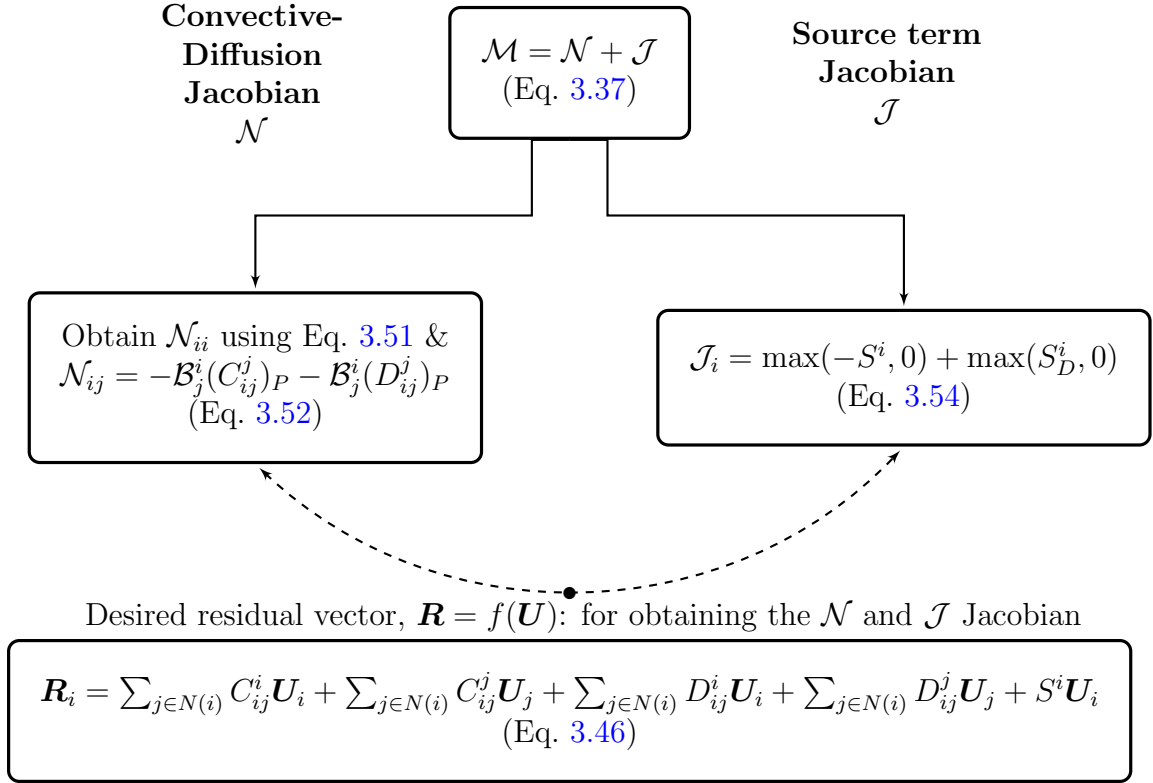
$$\mathcal{A}_N = \left( (a_N)_{kl} \in \mathbf{R}^{2 \times 2} \right)$$

where

$$\begin{aligned} (a_P)_{kl} &= \frac{1}{2} (|a_{kl}| + a_{kl}) \\ (a_N)_{kl} &= \frac{1}{2} (|a_{kl}| - a_{kl}) \end{aligned} \quad (3.48)$$

Using the above notation we can re-write the convective (Eq. 3.39) and diffusion (Eq. 3.42) residual vector as shown below:

$$\begin{aligned} \mathbf{C}_i &= \sum_{j \in N(i)} \left[ (C_{ij}^i)_P - (C_{ij}^i)_N + (\mathcal{I} - \mathcal{B}_j^i) (C_{ij}^j)_P \mathcal{T}_j^i - (C_{ij}^j)_N \mathcal{T}_j^i \right] \mathbf{U}_i \\ &\quad + \sum_{j \in N(i)} B_j^i (C_{ij}^j)_P \mathbf{U}_j \end{aligned} \quad (3.49)$$

Figure 3.2: Flowchart summarizing the construction of  $\mathcal{M}$  matrix.

$$\begin{aligned} \mathbf{D}_i = & \sum_{j \in N(i)} \left[ (D_{ij}^i)_P - (D_{ij}^i)_N + (\mathcal{I} - \mathcal{B}_j^i)(D_{ij}^j)_P \mathcal{T}_j^i - (D_{ij}^j)_N \mathcal{T}_j^i \right] \mathbf{U}_i \\ & + \sum_{j \in N(i)} \mathcal{B}_j^i (D_{ij}^j)_P \mathbf{U}_j \end{aligned} \quad (3.50)$$

where  $\mathcal{T}_j^i$  is the diagonal matrix with the diagonal element  $= \frac{(\rho \bar{v})_j}{(\rho \bar{v})_i}$  for SA. The above formulation is the exact convective-diffusive residual and is best suited to construct the desired Jacobian. The quantities  $\mathcal{N}_{ii}$  and  $\mathcal{N}_{ij}$  shown below are the diagonal and off-diagonal block matrices of row  $i$  of the matrix  $\mathcal{N}$ , respectively.

$$\begin{aligned} \mathcal{N}_{ii} = & \sum_{j \in N(i)} \left[ (C_{ij}^i)_N + (C_{ij}^j)_N \mathcal{T}_j^i - (\mathcal{I} - \mathcal{B}_j^i)(C_{ij}^j)_P \frac{\partial \mathcal{T}_j^i}{\partial \mathbf{U}_i} \mathbf{U}_i \right] \\ & + \sum_{j \in N(i)} \left[ (D_{ij}^i)_N + (D_{ij}^j)_N \mathcal{T}_j^i - (\mathcal{I} - \mathcal{B}_j^i)(D_{ij}^j)_P \frac{\partial \mathcal{T}_j^i}{\partial \mathbf{U}_i} \mathbf{U}_i \right] \end{aligned} \quad (3.51)$$

$$\mathcal{N}_{ij} = -\mathcal{B}_j^i(C_{ij}^j)_P - \mathcal{B}_j^i(D_{ij}^j)_P \quad (3.52)$$

where

$$\mathcal{B}_j^i = \mathcal{T}_j^i[\mathcal{I} + \mathcal{T}_j^i]^{-1} \quad (3.53)$$

The **source term Jacobian**  $\mathcal{J}_i$  is approximated as follows:

$$\mathcal{J}_i = \max(-S^i, 0) + \max(S_D^i, 0) \quad (3.54)$$

where  $S_D^i = -\frac{\partial S^i}{\partial U_i} U_i$ . Figure 3.2 shows the flowchart summarizing the construction of the  $\mathcal{M}$  matrix.

## 3.7 Closure

In this chapter, we have presented the method to model the mean turbulent flow for the case of compressible flows wherein the density fluctuations cannot be neglected. Favre- and Reynolds averaged Navier-Stokes equations together with the Boussinesq hypothesis along with the appropriate turbulence model equations form the complete system of governing equations required to solve the mean turbulent flow. We briefly presented the near-wall modeling which will be discussed in more detail in the next chapter. The condition of the matrices that are solved to obtain the turbulent quantities for the next time-step was demonstrated. It is to be noted that in the construction of  $\mathcal{M}$  matrix for the convective part of turbulent flows, a HLLC discretization is assumed. However, the mean flow equation uses Roe and SLAU2 for the convective term discretization. This inconsistency however does not matter since the turbulence model is solved decoupled from the rest of the variables.



# Chapter 4

## Automatic Wall Treatment for Spalart-Allmaras Turbulence Model

### 4.1 Overview

In the previous chapter we discussed three popular turbulence models – the one equation Spalart-Allmaras (SA) and the two-equation standard  $K - \epsilon$  and Menter’s SST  $K - \omega$  turbulence models. The one-equation Spalart-Allmaras (SA) [23] has become popular for its reasonably accurate predictions of a wide range of aerodynamic flow problems [34, 35, 36] even in comparison with the two-equation RANS based turbulence models.

However, as discussed previously the standard SA is a low-Reynolds number model that requires very tight grid spacing near the wall to resolve the large gradients in flow and turbulent variables and would thus require the use of a good wall function which can work equally well for a wider range of grid point placements near the wall. In this chapter, we demonstrate how we have developed an automatic wall treatment (AWT) for the SA turbulence model, for predicting the wall shear stress and heat flux. We have validated and verified [135] the proposed formulation for four cases involving adiabatic and constant temperature wall boundary conditions, thus validating the wall function modeling for both energy and momentum equations. To demonstrate the power of the AWT with SA, results are presented for grids with significantly different grid spacing at the wall, and their accuracy is reported.

## 4.2 Automatic Wall Treatment

As noted previously in Sec. 1.4 and in Sec. 3.4, the need is to model the wall function such that it switches automatically from the wall-function to a low-Re formulation depending on the grid-spacing near the wall. This would prevent the deterioration in the solution which happens when using a low-Reynolds model on an under-resolved mesh. Menter [48] while applying the automatic wall treatment to the  $K - \omega$  turbulence model took the advantage of the fact that the analytical equation for  $\omega$  is available in the viscous sublayer and the log-law region. He developed a formulation which blended these analytical equations as a function of  $y^+$  to achieve automatic (or smooth) switching for a given grid. Using, the Menter [48] notation, the analytical equations for  $\omega$  in the viscous sublayer and log-law region is given as:

$$\begin{aligned}\omega_{vis} &= \frac{6\nu}{\beta y^2} \\ \omega_{log} &= \frac{u_\tau}{C_\mu^{1/4} \kappa y}\end{aligned}\quad (4.1)$$

The above Eq. 4.1 is written in terms of  $y^+$  and a smooth blending is achieved by:

$$\omega_{wall}(y^+) = \sqrt{\omega_{vis}^2(y^+) + \omega_{log}^2(y^+)} \quad (4.2)$$

Menter's similarly used the formulation for the friction speed near the wall to obtain the velocity profile near the wall:

$$u_\tau^{vis} = \frac{U_p}{y^+} \quad (4.3)$$

$$u_\tau^{log} = \frac{U_p}{\frac{1}{\kappa} \ln(y^+) + C}$$

$$u_\tau = \sqrt[4]{(u_\tau^{vis})^4 + (u_\tau^{log})^4} \quad (4.4)$$

The above Eqs. 4.3-4.4 provide the relation between the velocity at the wall-adjacent cell ( $U_p$ ) and the friction speed ( $u_\tau = \sqrt{\frac{\tau_w}{\rho}}$ ). Menter has shown [48] that the grid dependency is reduced significantly when using automatic wall treatment compared to the standard low-Re formulation and the standard wall function approach.

In the low-Re SA formulation, the boundary conditions for  $\tilde{\nu}$  is homogeneous Dirichlet that is applied at the wall. However, a homogeneous Dirichlet condition for  $\tilde{\nu}$  will not be applicable for a coarser grid that does not adequately resolve the viscous



sublayer; however, a homogeneous Neumann condition will make the results relatively insensitive to the coarseness of the grid. We employ a homogeneous Neumann boundary condition for  $\tilde{\nu}$  in our AWT (instead of employing an automatic switch as done for the  $\omega$  term by Menter [48] for  $K - \omega$  SST turbulence model as shown earlier). The friction speed is blended as in Menter's method discussed above. It is to be noted that the AWT does not "switch" abruptly between the low-Re and wall function procedures at some prescribed  $y^+$  of the first point. Rather, as  $y^+$  decreases  $u_\tau^{vis}$  dominates the value of  $u_\tau$ , hence implicitly applying the low-Re condition.

For the energy equations a similar automatic wall function was employed by Menter [48] following Kader [136]:

$$T^+ \equiv \frac{(T_w - T_p)\rho_w c_p u_\tau}{\dot{q}} = e^\Gamma T_{lam}^+ + e^{1/\Gamma} T_{turb}^+ \quad (4.5)$$

$$\Gamma = -\frac{a(Pr y^+)^4}{1 + bPr^3 y^+} \quad (4.6)$$

$$T_{lam}^+ = Pr \left( u_{lam}^+ + \frac{\rho u_\tau}{2\dot{q}} V^2 \right) \quad (4.7)$$

$$T_{turb}^+ = Pr_T \left\{ u_{turb}^+ + p + \frac{\rho u_\tau}{2\dot{q}} \left[ U_p^2 - \left( \frac{Pr}{Pr_T} - 1.0 \right) (u_c^+)^2 (u_\tau)^2 \right] \right\} \quad (4.8)$$

where  $u_c^+$  is the value of  $u^+$  ( $\equiv u/u_\tau$ ) at the intersection point of the logarithmic and the linear law of the wall for momentum,  $T_p$  is the temperature at the wall-adjacent cell,  $\dot{q}$  is the wall heat flux, and the constants  $a = 0.01$  and  $b = 5$ . However, in the present work, we have not used the above formulation but instead, find the turbulent heat flux by employing a turbulent Prandtl number between 0.7-0.9. We have found the results to be quite insensitive to the actual value of the turbulent Prandtl number within this range. This method of calculating the turbulent heat flux is explained in the following subsection which describes the algorithm used.

### 4.2.1 Algorithm for implementing the AWT

The following steps are taken for every time-step in order to implement the AWT formulation:

1. Solve for (a) the mean flow equations (Eq. 3.5) and (b) the SA equation (Eq. 3.12) uncoupled from each other, based on the previous time-step values of the flow

variables and turbulent viscosity.

2. Calculate the new values of  $\mu_T$  at all the interior cell-centers using the new values of  $\tilde{\nu}$ .
3. At the wall  $\tilde{\nu}$  and  $\mu_T$  are obtained based on AWT in the following manner:
  - (a) Solve Eq.4.3-4.4 to obtain the shear velocity ( $u_\tau$ ).
  - (b) Using  $u_\tau = \sqrt{\frac{\tau_w}{\rho}}$  we obtain shear stress value  $\tau_w$ .
  - (c) Following references [33, 137]:

$$\frac{\tau_w}{\rho} = u_\tau^2 = (\nu + \mu_T/\rho) \frac{U_p}{y_p} \quad (4.9)$$

where  $U_p$  is the magnitude of velocity at the cell adjacent to the wall and  $y_p$  is the normal distance from the centroid of that cell, i.e., the “first cell-center” or “first grid point” from the wall. This distance is calculated as the magnitude of the component of the vector joining the cell-center to the face-center of the boundary face in the direction of the face unit normal. More details for this can be found in the PhD Thesis of Dalal (2008) [138]. The last part of the equation seems to suggest that we assume the velocity profile to be linear, and so Eq. 4.9 apparently can be applied only in the viscous sublayer. This is however not true as is seen in step 3(3d) below.

- (d) Obtain  $\mu_T$  and  $k_T$  at the wall using the following relation:

$$\mu_T = \rho(u_\tau^2 \frac{y_p}{U_p} - \nu) \quad (4.10)$$

$$k_T = \mu_T \frac{c_p}{Pr_T} \quad (4.11)$$

Note that, following [33, 137], in Eq. 4.10, the turbulent viscosity is prescribed at the wall by inverting Eq. 4.9. That is, the effective viscosity at the wall is modified so that the Eq. 4.9 gives the correct wall shear stress even if  $y_p$  lies outside the linear region, i.e., the viscous sublayer.

4. Repeat steps 1-3 till convergence is achieved.

## 4.3 Boundary and initial conditions

For the inlet and outlet, the characteristic boundary conditions based on Riemann invariants are used for the mean flow equations [139, 8] (Sec. 2.5). The inflow boundary condition for the Spalart-Allmaras turbulence model is set to the free-stream turbulent viscosity ratio obtained from the experimental data or relevant reference. At outflow and symmetry boundaries, the turbulent variables are extrapolated from interior values. At the wall, the AWT wall function is applied and is used to compute the turbulent variables. The uniform free-stream inflow condition is used to set the initial conditions throughout the flow-field, for the pseudo-transient solution.

## 4.4 Results and Discussion

The automatic wall function treatment presented in this chapter is validated using four test cases involving (a) turbulent flow over a flat plate, (b) forced turbulent convection over a flat plate, (c) turbulent flow over a bump in a channel and (d) turbulent flow over a NACA 0012 airfoil. In these cases, the results are computed on a series of meshes with different  $y^+$  values at the wall-adjacent cell in order to demonstrate the accuracy of AWT on different grids. To solve the mean flow equations we have used low-speed preconditioning with Roe flux [9] (Sec. 2.3.1.2). The time-stepping has been done implicitly using LU-SGS (Sec. 2.4.2) with the turbulent equation being discretized using the unconditionally positive convergent (UPC) scheme (Sec. 3.5) [29, 133] as discussed in the previous chapters.

### 4.4.1 Case 1: Turbulent flow over a flat plate

The first case considered is the turbulent flow over a flat plate [140] at  $M = 0.2$  with Reynolds number  $Re = 5 \times 10^6$  and  $T_\infty = 540 \text{ }^\circ\text{R} = 300 \text{ K}$ . The Reynolds number is calculated based on the half-length of the plate. The flow domain and boundary conditions are shown in Fig. 4.1. The turbulent inflow boundary condition uses a turbulent viscosity ratio of 3 [125]. The turbulent Prandtl number is taken to be 0.9. The main aim of this case is to verify the AWT formulation for momentum by comparing the surface skin friction coefficient and the velocity profile with those results given on the Turbulence Modeling Resource (TMR) web-page [125].

Four different meshes are studied with different first cell-center distance from the

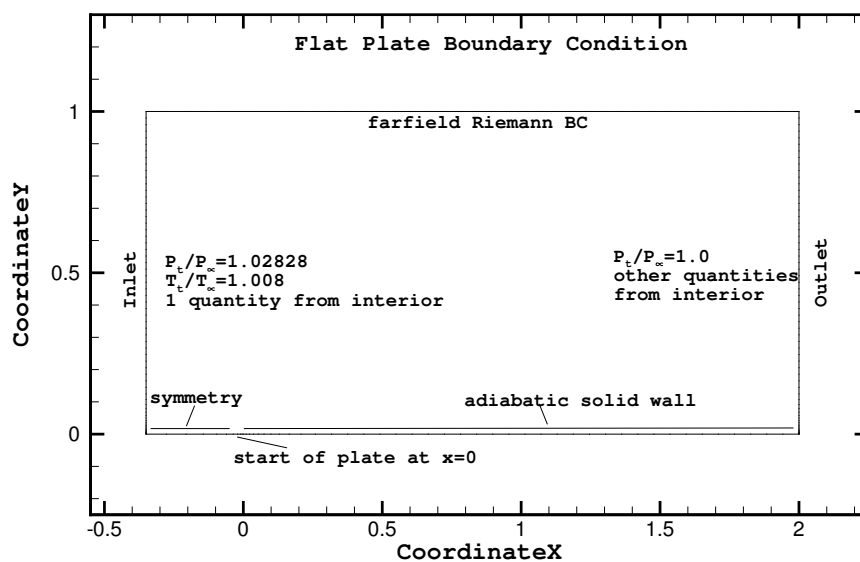


Figure 4.1: Case 1: Flow domain and conditions for turbulent flow over a flat plate.

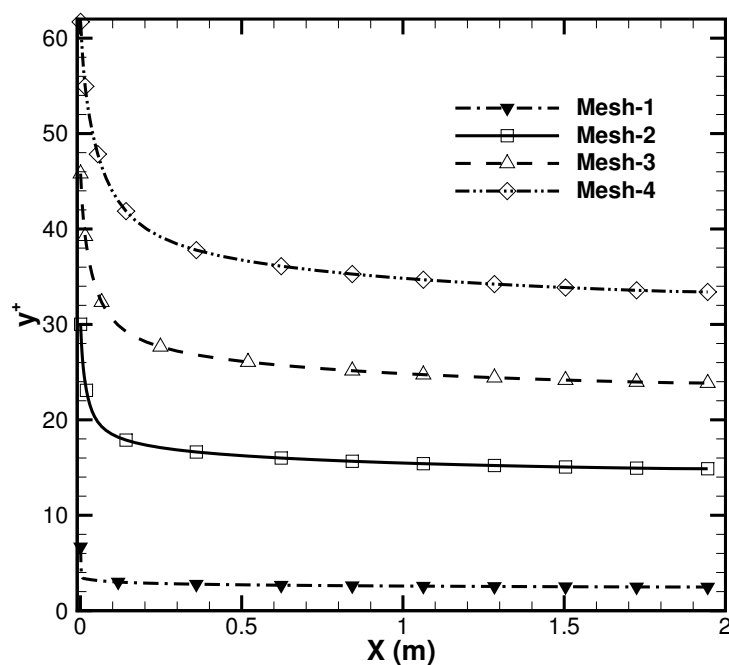


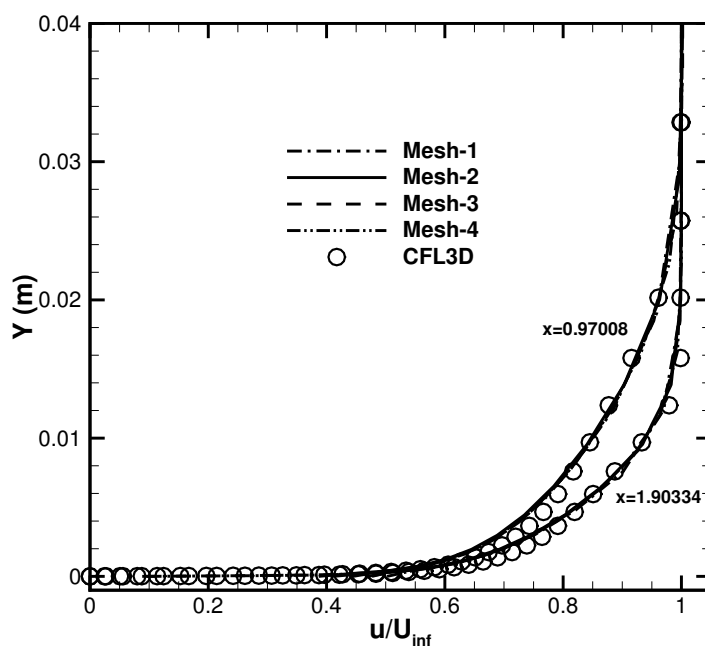
Figure 4.2: Case 1: The  $y^+$  variation of the first grid point for the four different meshes considered.

wall which in the final solution (see Fig. 4.2) corresponds to  $y^+$  ranging from 2-7 (Mesh-1, the first point is in the border region between sublayer and buffer layer), 15-30 (Mesh-2, completely in buffer layer), 24-46 (Mesh-3, in between the buffer layer and log region) and 33-62 (Mesh-4, completely in the log region). Figure 4.3(a) shows the velocity profile at two locations ( $x = 0.97008$  and  $x = 1.90334$ ) over the flat plate with the results being compared with CFL3D [141] results. The CFL3D results used  $545 \times 385$  ( $= 209825$ ) cells with the viscous sublayer fully resolved (i.e. no wall-function) and are considered a benchmark for this case. The present computation has been done using only  $50 \times 70$  ( $=3500$ ) cells. All the four meshes give nearly identical and accurate profiles, thereby showing the capability of the AWT. The corresponding result for the skin-friction coefficient ( $C_f$ ) compared against experiment [142] is shown in Fig. 4.3(b). A slight deviation is observed at the leading edge of the plate for Mesh-1 which corresponds to  $5 < y^+ < 7$ . The result shows that while the AWT gives accurate results for different coarser grid-spacings, a grid with first cell-centre  $5 < y^+ < 15$  in the present results show slight inaccuracy. However, it is also known that the standard SA model gives inaccuracy if the first grid point is in the buffer regions [143]; the computation on this finest mesh will correspond most closely with the standard SA model. The wall function treatment, unexpectedly, seems to remedy this inaccuracy. The main purpose of wall functions, however, is to allow a coarser grid near the wall and thus reduce the computational cost. This purpose is well-served by the current implementation, judging by these results.

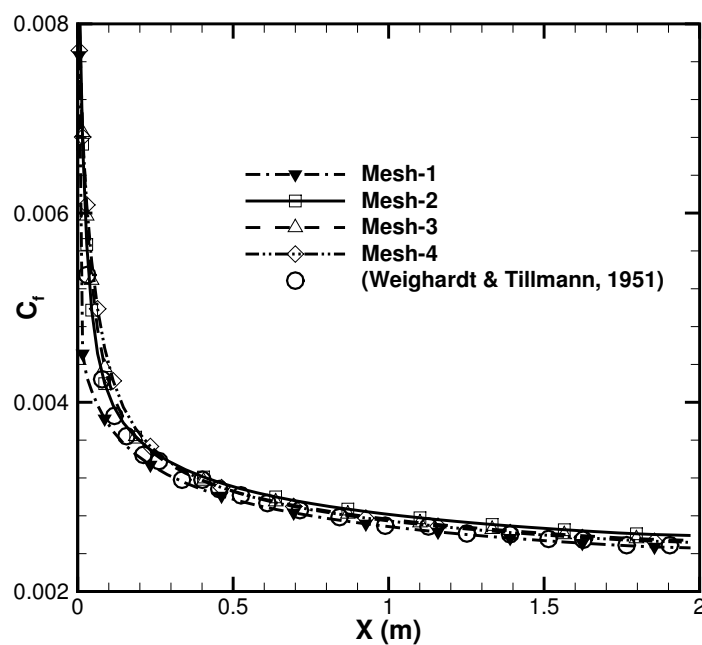
#### 4.4.2 Case 2: Forced Convection Over a Flat Plate.

In Case 2, we simulate forced convection over a flat plate with  $U_\infty = 1m/s$ ,  $T_\infty = 353$  K,  $P_\infty = 101325.0$  Pa,  $T_w(= T_p) = 413$  K,  $Re_L = 1.5 \times 10^6$  and  $Pr = 0.71$ . The turbulent viscosity ratio for the SA model at the inlet is chosen to be 1 [144]. The turbulent Prandtl number is taken to be 0.85. The flow domain is shown in Fig. 4.4. Four different meshes are studied with different first cell-center distance from the wall which, in the final solution (see Fig. 4.5), corresponds to  $y^+$  ranging from 2-4 (Mesh-1, first point is completely in the sublayer), 13-23 (Mesh-2, completely in the buffer layer), 23-37 (Mesh-3, in between the buffer layer and log region) and 32-52 (Mesh-4, completely in the log region).

Figure 4.6(a) shows the velocity profile at the outlet with the results being compared with a fully resolved (no wall-function) computation on a  $30 \times 100$  grid [144].



(a) The  $u$ -velocity profile at  $x = 0.97008$  &  $x = 1.90334$  vs  $y$ .



(b) Surface skin friction coefficient.

Figure 4.3: Case 1: Turbulent flat plate with an inlet  $M_\infty = 0.2$  with the four mesh configurations.

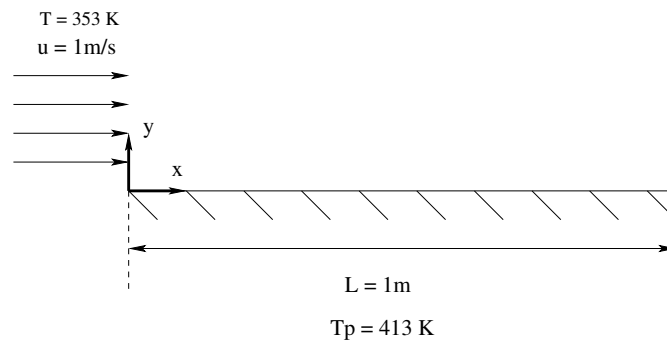


Figure 4.4: Case 2: Flow conditions for forced convection over a flat plate.

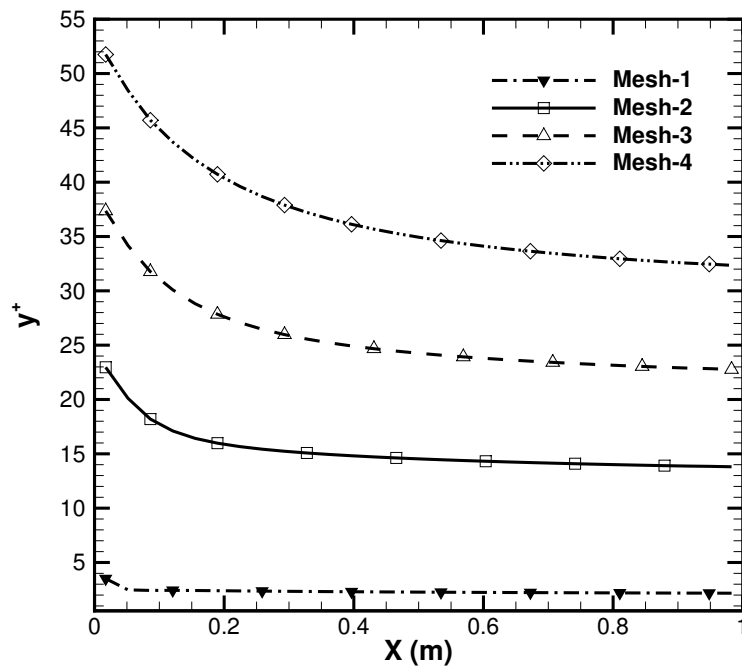


Figure 4.5: Case 2:  $y^+$  variation of the first grid point for the four different meshes considered.

The present AWT computation used a  $29 \times 40$  grid. The corresponding result for the local Nusselt number is validated in Fig. 4.6(b) against Reynolds correlation [145] and experiments [146]. It is observed that the numerical solutions on all all grids are very accurate.

The above results demonstrate the capability of AWT for both momentum and energy equations near the wall with the four mesh configurations with their first point locations ranging from the viscous sublayer to well within the log layer. In this case, we have not used the law of wall for energy equation of Kader [136] shown in Eq. 4.5-4.8, but have instead used the algorithm presented in this work, i.e. a constant  $Pr_t$  is prescribed to find the turbulent thermal conductivity.

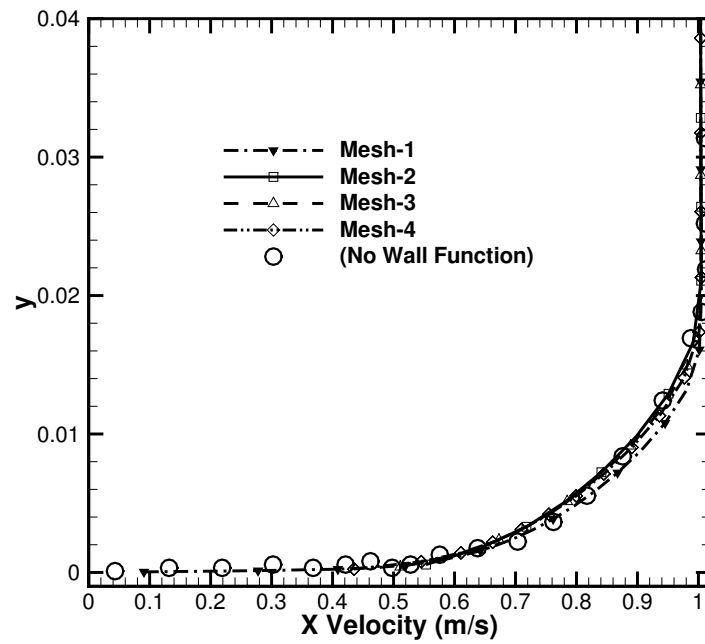
### 4.4.3 Case 3: Turbulent flow over a bump in channel

The third case is the turbulent flow over a bump in a channel at  $M_\infty = 0.2$  with Reynolds number  $Re = 3 \times 10^6$  and  $T_\infty = 540 \text{ }^\circ\text{R} = 300 \text{ K}$ . The flow domain and boundary conditions applied are shown in Fig. 4.7. The lower wall from  $x = 0$  to 1.5 is a viscous adiabatic wall. The maximum bump height is 0.05 ( $= y_0$ ) at  $x = 0.75$ . The Reynolds number mentioned above is based on the unit length of the bump between  $x = 0.2$  to  $x = 1.2$ , which is also used as the nondimensionalizing length scale. The turbulent inflow boundary condition used a turbulent viscosity ratio of 3 [125]. The turbulent Prandtl number is taken to be 0.9. This case is to verify the AWT formulation for momentum by comparing the surface skin friction coefficient and the velocity profile with the results on the Turbulence Modeling Resource (TMR) webpage [125]. Other quantities such as pressure coefficient  $C_p$  and  $\mu_T$  are also verified. This case involves wall curvature which causes pressure gradients and thus is a good test for the verification of AWT formulation for SA. The bump height is given as:

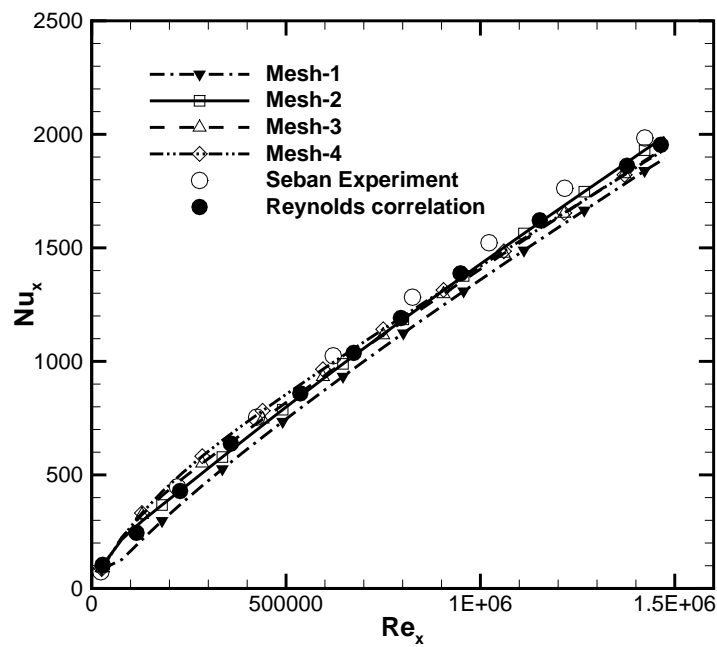
$$\begin{aligned} y &= \frac{1}{20} \sin^4\left(\frac{\pi x}{0.9} - \frac{\pi}{3}\right) & \text{for } 0.3 \leq x \leq 1.2 \\ y &= 0 & \text{for } 0 \leq x < 0.3 \text{ and } 1.2 < x \leq 1.5 \end{aligned} \quad (4.12)$$

Three different meshes are studied with different first cell-centre distance from the wall which in the final solution (see Fig. 4.8) corresponds to  $y^+$  ranging from 2-8 (Mesh-1), 13-40 (Mesh-2) and 18-55 (Mesh-3). As against the previous two cases here the  $y^+$  variation first decreases and then increases upstream of the bump, then





(a) The u-velocity profile at the outlet.



(b) Plot of Reynolds number Vs Nusselt number along the wall.

Figure 4.6: Case 2: Forced convection over a flat plate with four different mesh configurations.

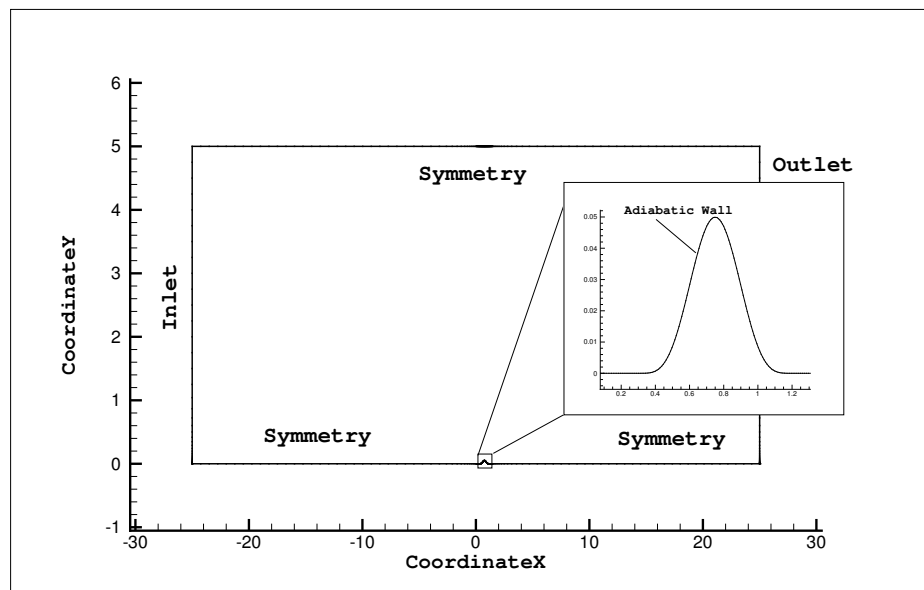


Figure 4.7: Case 3: Flow domain for turbulent flow over a bump in a channel.

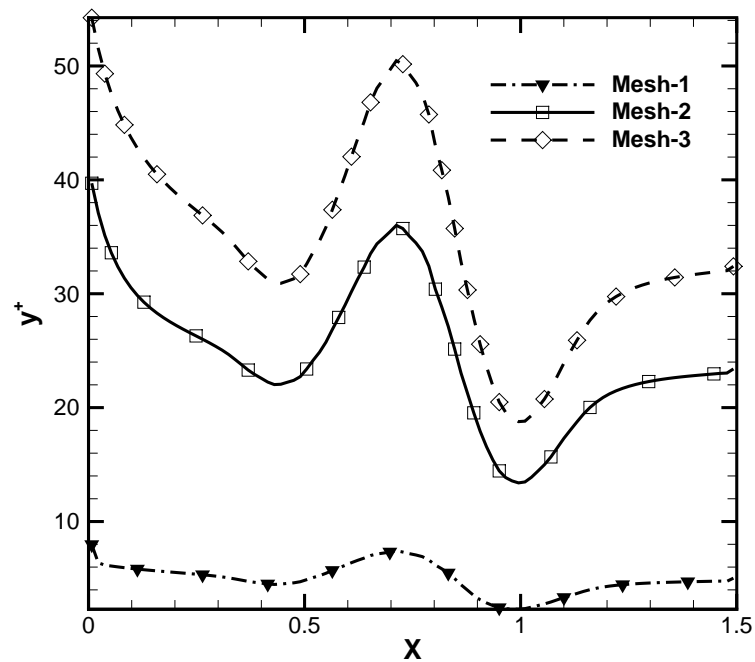


Figure 4.8: Case 3: The  $y^+$  variation of the first grid point for the three different meshes considered.

decreases downstream and then increases again over the downstream flat plate. The reference solution chosen for the verification is provided by CFL3D [141] using a fine grid with  $1409 \times 641$  ( $= 903169$ ) cells, with the viscous sublayer being fully resolved, that is considered a benchmark for this case. The present AWT computation used a grid with  $180 \times 50$  ( $=9000$ ) cells. Figure 4.9 shows the plot for the computed pressure coefficient along the wall for the various mesh configurations compared against the CFL3D results. The results are very good. Figure 4.10 shows the normalized eddy viscosity obtained for the three different meshes. Once again the contours match well with those obtained by the CFL3D computation on the much finer mesh. Throughout the boundary layer, there is good agreement with the reference solution in the prediction of eddy viscosity. A slight inaccuracy in the sharpness of eddy-viscosity contours can be attributed to the fact that the present meshes are much coarser than that used in the CFL3D computations.

Figure 4.11(a) shows the velocity profile at two locations: one being at the mid-plane of the bump and the other being at the downstream of the bump ( $x = 0.75$  and  $x = 1.20148$ ) with the results being compared with CFL3D results. These results from all the three meshes show very good agreement with the fully resolved solution obtained from CFL3D. The corresponding results for the skin-friction coefficient ( $C_f$ ) are shown in Fig. 4.11(b). All the predictions are in good agreement with the CFL3D results over the bump except for mesh-1. However, mesh-1, the finest grid of the three used, shows the best accuracy at the leading edge. The largest error on meshes 2 and 3 is found near the leading edge ( $x \lesssim 0.15$ ) where the boundary layer is beginning to form and so is extremely thin and the eddy viscosity is still developing. This region is most challenging [43] to capture and is known to remain under-resolved by the wall function approach. For mesh-1 we can see this error is least as the mesh is fine near the wall ( $4 < y^+ \leq 8$ ). The inaccuracy observed for Mesh-1 compared to other meshes over the bump reinforces the observation in Case-1, i.e., the AWT seems to give more accurate results for the coarser grid-spacings of  $y^+ > 15$ . We conclude that a grid with  $5 < y^+ < 15$  may lead to slight inaccuracy with AWT since there is no buffer layer treatment.

We can also note that  $y^+$  (Fig. 4.8) which is obtained as part of the solution follows a similar trend as  $C_f$  (Fig. 4.11(b)), the reason being is for this incompressible case is that  $y^+$  is proportional to  $\tau_w$  (or  $C_f$ ).

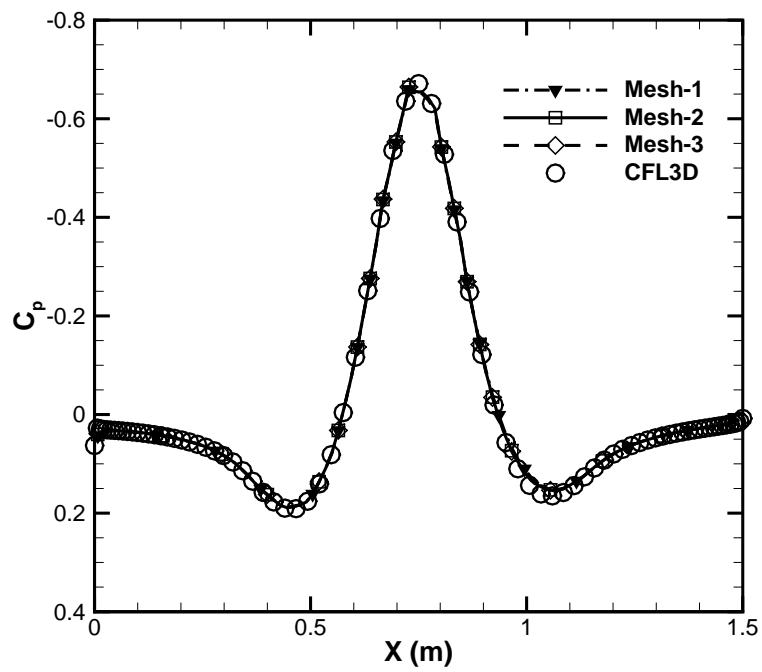


Figure 4.9: Case 3: Surface Pressure Coefficient for three mesh configurations and the reference [125].

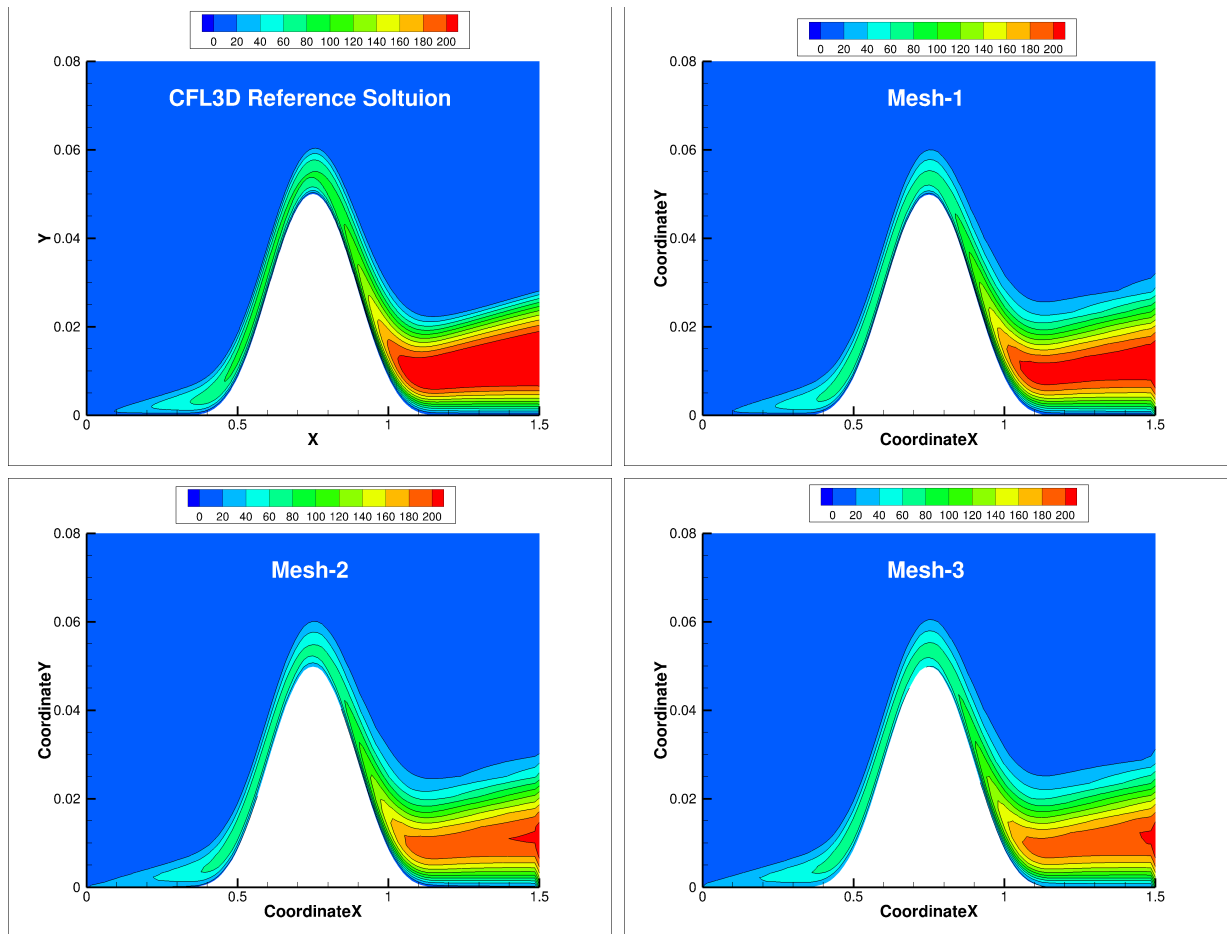
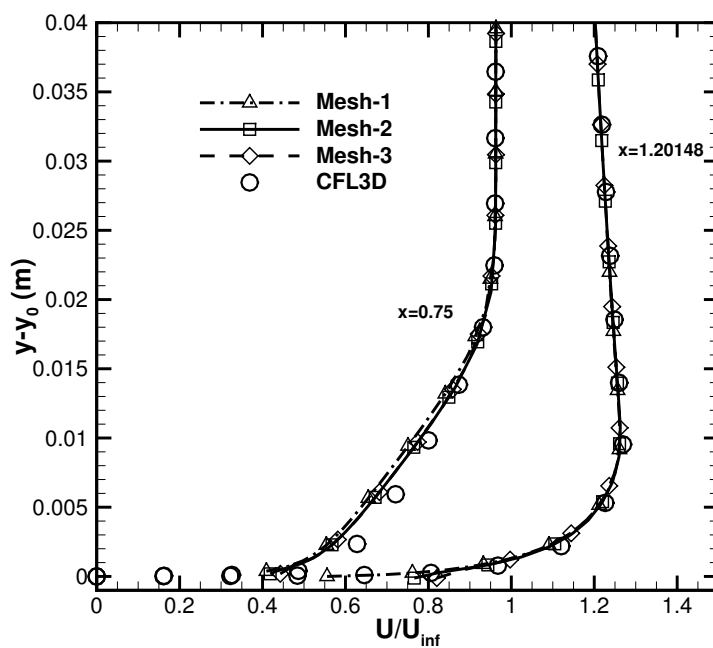
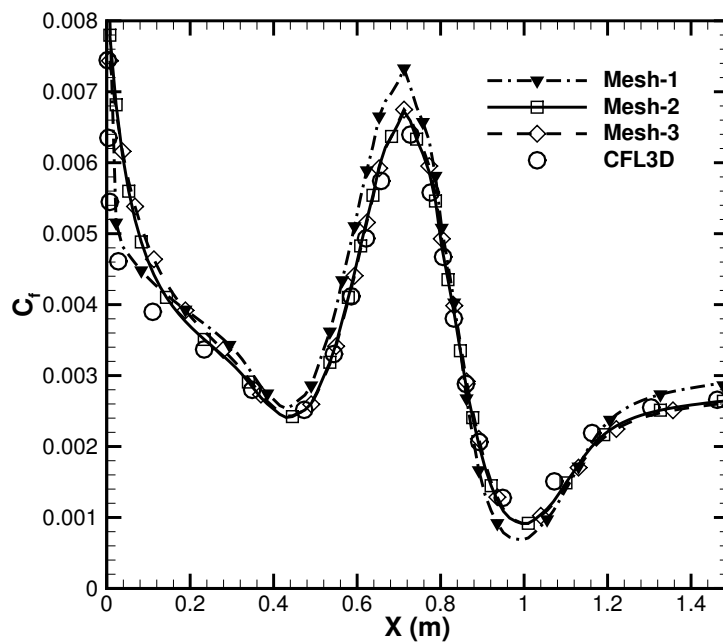


Figure 4.10: Case 3: Contours of eddy viscosity (normalized by free-stream laminar viscosity =  $1.846 \times 10^{-5}$ ) for the three different mesh configuration compared with the fine grid results obtained using CFL3D.



(a) The u-velocity profile at  $x=0.75$  &  $x=1.20148$ .



(b) Surface skin friction coefficient.

Figure 4.11: Case 3: Flow over bump in a channel with inlet  $Ma = 0.2$ , with the three mesh configurations and the reference [125].

#### 4.4.4 Case 4: Turbulent flow over 2D NACA 0012 Airfoil

The fourth case considered is the turbulent flow over a NACA 0012 airfoil with angle of attack of  $\theta = 10^\circ$  at  $M_\infty = 0.15$  with Reynolds number  $Re = 6 \times 10^6$ ,  $T_\infty = 540$  °R = 300 K and adiabatic wall conditions. The Reynolds number is calculated based on the chord length of the airfoil (here taken as unity). The far-field boundary in the grid is located almost 500 chords away from the airfoil, in order to avoid the issues associated with the effect of far-field boundary conditions. The flow domain and boundary conditions applied are shown in Fig. 4.12. The turbulent inflow boundary condition assumes a turbulent viscosity ratio of 3 [125]. The turbulent Prandtl number is taken to be 0.9. This case is to validate and verify the AWT formulation for SA for the NACA 0012 airfoil [43] by comparing the results with experiment and CFL3D numerical benchmark given on the Turbulence Modelling Resource (TMR) webpage [125]. The results are compared for surface pressure coefficient ( $C_p$ ) both with experiment and CFD (CFL3D) while the skin friction coefficient ( $C_f$ ) results are compared only with CFL3D as there are no corresponding experimental data available.

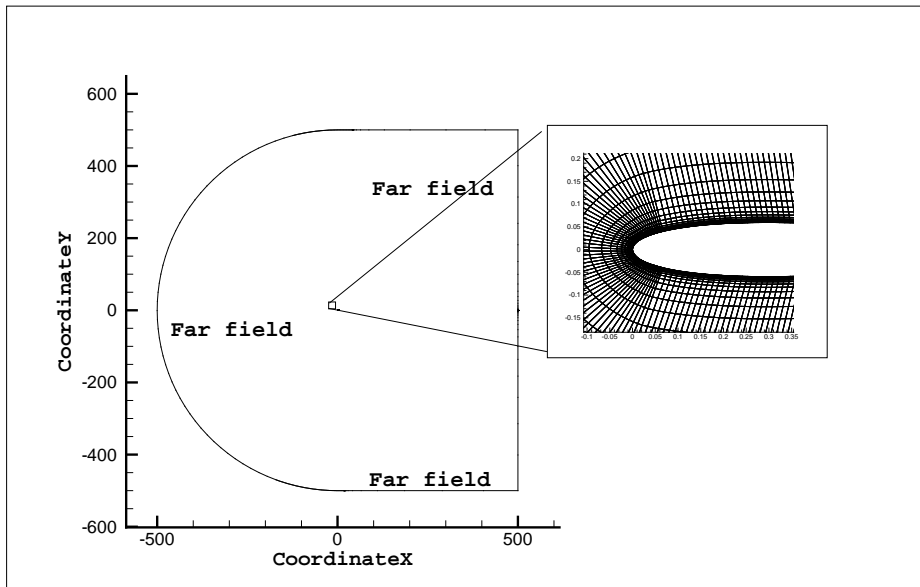
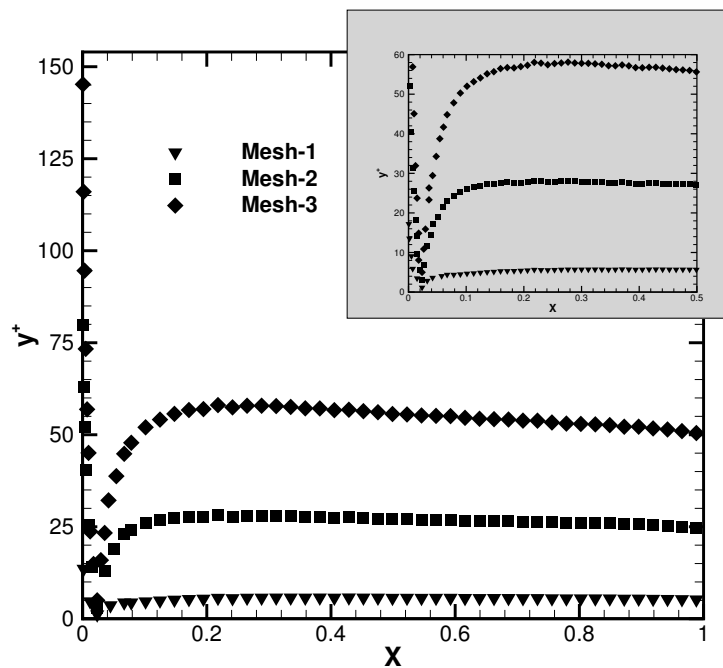
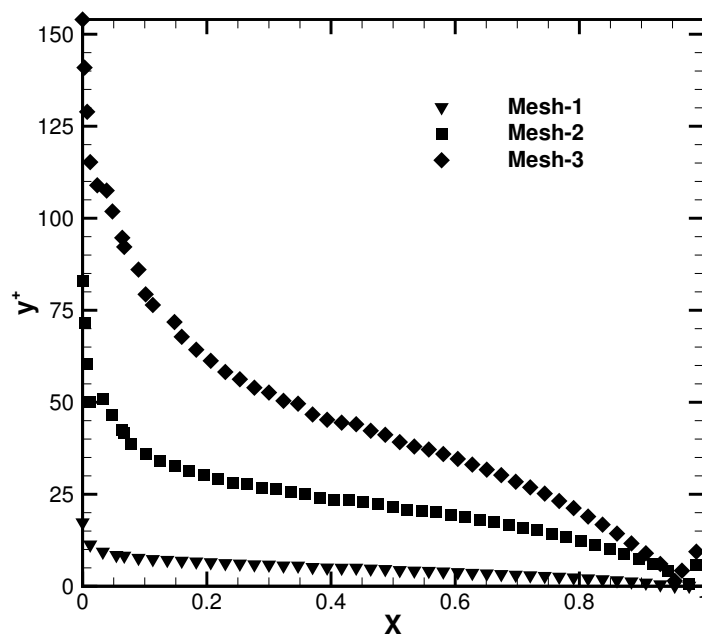


Figure 4.12: Case 4: Flow domain for turbulent flow over the NACA 0012 airfoil with a zoomed view of the nose of the airfoil.

Three meshes are studied with different first cell-centre distance from the wall which in the final solution (see Fig. 4.13) correspond to different  $y^+$  ranges at both the upper and lower walls of the airfoil. Figure 4.13 shows  $y^+$  ranges from 0.001-18



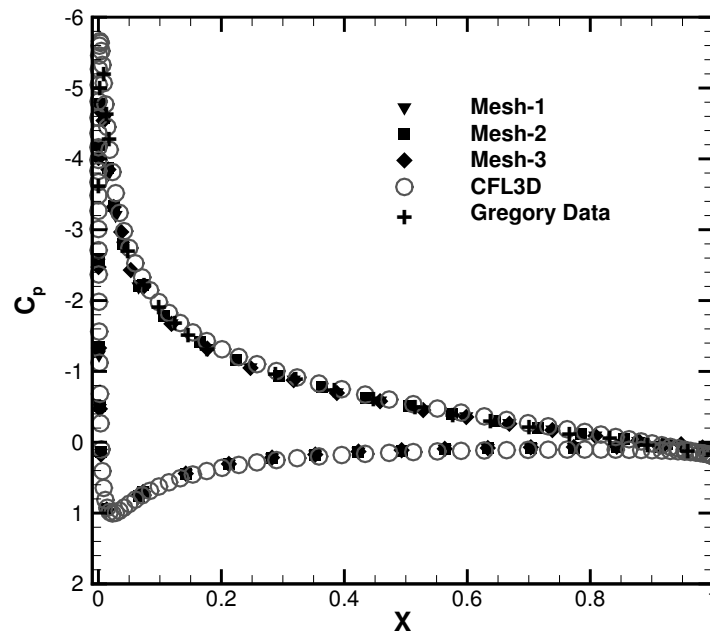
(a) The  $y^+$  plot along the lower surface of the airfoil with a zoom view to show its variation in the first half of the airfoil.



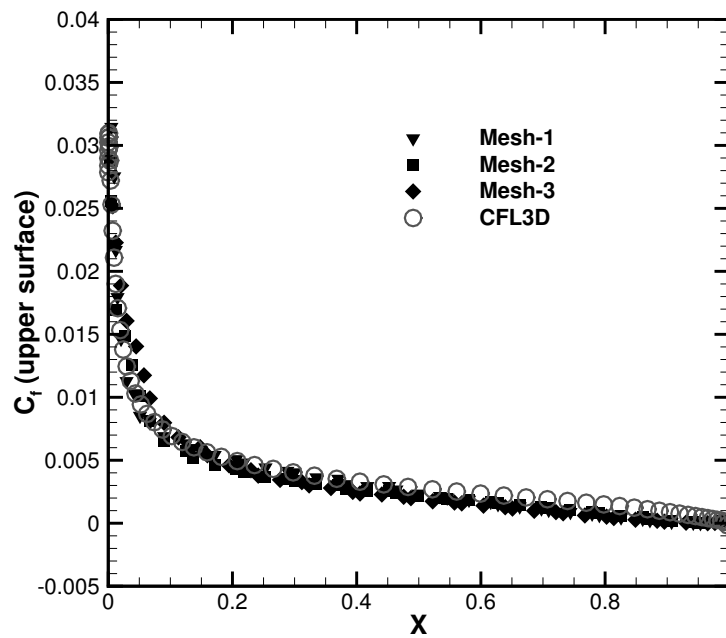
(b) The  $y^+$  plot along the upper surface of the airfoil.

Figure 4.13: Case 4: The  $y^+$  variation of the first grid point for the three different meshes considered.





(a) Surface Pressure Coefficient.



(b) Surface skin friction coefficient for the upper surface.

Figure 4.14: Case 4: Flow over the NACA 0012 airfoil with  $Ma = 0.15$  with the three mesh configurations and reference.

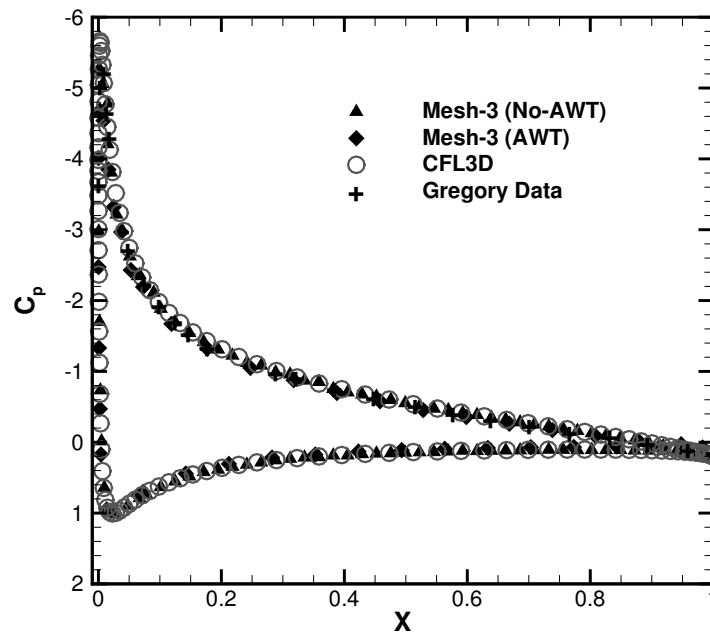
(Mesh-1), 0.7-83 (Mesh-2) and 1.4-154 (Mesh-3). The  $y^+$  variation is smoother for the upper wall. However, over the lower airfoil the  $y^+$  value shows a dip especially at  $x \sim 0.04m$  and then it increases followed by a very gradual monotonic decrease in the  $y^+$  value. Since, the flow is at an angle of attack of  $10^\circ$ , the sudden dip is due to the formation of the stagnation region at the beginning of the airfoil lower surface. The reason for a gradual monotonic decrease in the  $y^+$  value is because of the presence of more favorable pressure gradient to the flow in comparison with the upper surface. These plots show, as against the previous cases, here the  $y^+$  variation is spread over a larger range of  $y^+$  values, far beyond what would be considered acceptable in conventional CFD practice, especially for the Mesh-3 considered here. The reference solution chosen for the verification is provided by CFL3D [141] using a fine grid with 230529 cells with the viscous sublayer being fully resolved. In contrast, the meshes used in this study have 10000 cells.

Figure 4.14 (a) shows the plots for the pressure coefficient along the wall against the CFL3D results and the experiment results [147] available for the upper surface. The results from all meshes are in good agreement with the references. Figure 4.14(b) shows the plot of skin friction coefficient along the wall of the airfoil. The results are in very good agreement with those of CFL3D for all three mesh configurations. This completes our validation of the present AWT formulation for the SA turbulence model.

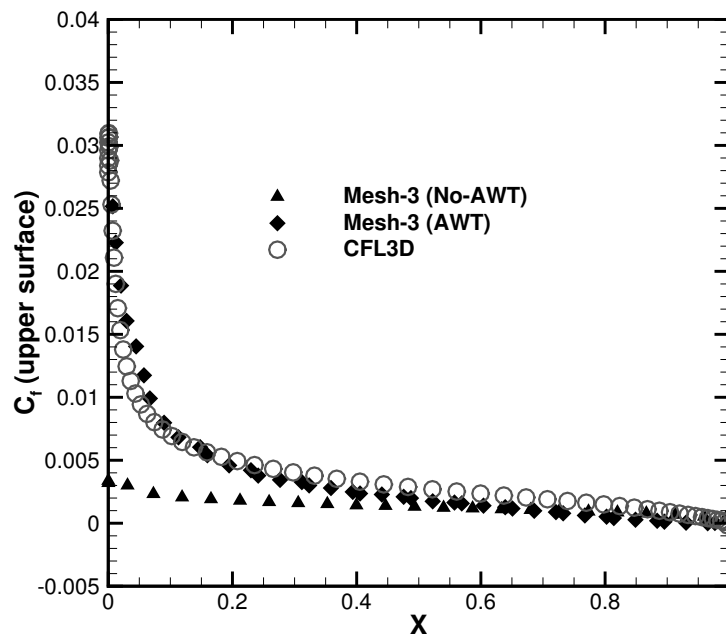
In order to highlight the role played by AWT we compare in Fig. 4.15 the results, on coarsest mesh (Mesh-3), with and without AWT. Fig. 4.15 (a) shows the plot for the pressure coefficient along the wall of the airfoil and Fig. 4.15 (b) shows the plot of skin friction coefficient along the upper wall of the airfoil. It can be seen that for the coarse mesh both AWT (i.e., wall function) and no-AWT (i.e. no wall-function) method gives the same result for pressure. But for the skin-friction coefficient the result deteriorates without AWT. To capture the wall shear stress arising due to viscous flow near the wall would require a fully-resolved mesh at the wall or else the use of a wall treatment.

## 4.5 Closure

In this chapter, an AWT formulation is validated for the Spalart-Allmaras (SA) one-equation model. The SA model is originally a low-Re model requiring a fine grid near



(a) Surface Pressure Coefficient.



(b) Surface skin friction coefficient for the upper surface.

Figure 4.15: Case 4: Flow over the NACA 0012 airfoil with  $Ma = 0.15$  with on Mesh-3 with and without AWT.

walls. Industrial flow predictions require low sensitivity to grid spacing, as typically not all walls are well-resolved with fine grids. However, with the present AWT, the SA model can be used for wall-bounded flows with relatively coarse grids at the wall. The automatic switching of  $\mu_t$ , depending on the  $y^+$  of the first grid point, is implicit in the AWT procedure. The test cases considered in this work have been computed on different grids with the first grid point variously located in the sublayer layer region, in the buffer region, and in the log region and have always yielded near-identical results that have also matched well with benchmark reference and experimental data. The last two test-cases considered here are close to real-world simulations, for which  $y^+$  values go well beyond the traditionally accepted values to be as high as 150. However, even here, the results are good. It is also shown that the energy equation solutions can be obtained even without the use of the law of the wall, by merely using an assumed constant  $Pr_t$ . It should be noted; however while the standard SA model can capture the laminar-turbulent transition in the boundary layer, the AWT assumes the flow to be turbulent throughout. We expect, in regions of separated flows thus the AWT cannot be used.

This work has much practical significance for researchers who use turbulence models to compute complex flows in aerospace applications, as the AWT allows a near-wall grid 10–30 times as coarse as that required in the standard SA model (without wall function). Apart from this, the flexibility accruing from the freedom of not having to place the first-grid point in a narrow range of  $y^+$  (which cannot be predicted a priori during grid generation) will be very helpful to practitioners, who otherwise routinely re-grid after computations to satisfy the earlier criteria. Finally, it would interest researchers of turbulence theory, which can be so piece-meal at times, that a model developed for SST would work without modification for a completely different model like SA.

# Chapter 5

## Non-Equilibrium Boundary Conditions

### 5.1 Overview

In this chapter, we take a step forward into the flow dynamics of rarefied flows. In introduction (Sec. 1.5), we had discussed the method of replacing the commonly used no-slip boundary conditions with slip velocity and temperature jump boundary conditions for studying the rarefied gas flow in the slip regime,  $0.001 \leq Kn \leq 0.1$ . We discuss here how the boundary conditions are modified (as mentioned in Sec. 2.5.3), for the computation of these non-continuum flows in the slip regime using the Navier-Stokes equations.

We have mentioned, in Sec. 1.5, the need for a more comprehensive analysis of the recently published Le temperature jump boundary condition [62] on all relevant flow properties for different flow conditions. Here, after introducing the various non-equilibrium boundary condition, we have use the Le temperature jump condition for different inflow conditions for hypersonic rarefied gas flow over a flat plate. In the next chapter (Chapter 6) we further study different micro/nano flow cases. The results here are compared with the available experimental data and the DSMC results. Interestingly, we found an over-prediction of pressure, especially at the leading edge of the flat plate when using the Le temperature jump condition. We have proposed a correction to the anomaly by using a previously published pressure jump condition, whose use was termed by the author as “unclear” [53]. This condition does not seem to have been used in CFD studies [70], although researchers have pointed to the existence of a pressure jump at the wall [148, 149]. We begin our discussion in this

chapter with a description of the DSMC method, which is considered as a benchmark for solutions obtained from the CFD calculations.

## 5.2 Direct Simulation Monte Carlo (DSMC)

The DSMC calculation is a statistical method, originally proposed by Bird [92]. For the case of rarefied gas flows it is considered to be a reliable computational tool [92] and has been shown to converge to the solutions of Boltzmann equation [56, 57]. Unlike the molecular dynamics simulation where each molecule in the gas flow is simulated, in DSMC each particle represents many molecules in the real flow. A probabilistic method is used to solve for the intermolecular collisions and molecule-surface collisions. The commonly-used collision models are the variable hard sphere (VHS) model, hard sphere (HS) model, and the variable soft-sphere model. The DSMC method requires certain conditions which are [57] as follows:

- (a) The flow time-step should be small enough with respect to the mean time taken for the collision so that the molecular motion and intermolecular collision can be uncoupled from each other. In general, the time-step is taken to be about 1/3 of the mean collision time [57].
- (b) In the computational mesh, the cell-size should be less than the mean-free-path of the particles.
- (c) Each cell should have a sufficient number of DSMC particles so that performing a statistical average to obtain the macroscopic averaged flow quantities is meaningful. In general, 20 particles per cell is taken.

For rarefied gas flows, as experimental data are scarce, DSMC calculations are often taken as the benchmark for results obtained from the CFD calculations [63, 150]. The details of parameters chosen to perform the DSMC calculation can be found in the stated references.

## 5.3 Interactions of Gas with the Surface

The interaction between of the gas molecules with the surface is defined in terms of the collision, as determined by the chosen collision model. After, the collision of

the incoming molecules with the surface if the molecules rebound elastically, i.e., the incoming angle is equal to the reflecting angle and with the same momentum and energy, this is called specular interaction [151, 152]. Also, the value of surface shear stress and heat flux will be zero. This corresponds to the case when the surface is smooth and adiabatic.

However, if the molecule rebounds inelastically, i.e., the incoming angle is not equal to the reflecting angle and with a change of momentum and energy, then the interaction is called diffuse [151, 152]. In this case, the surface is termed rough and isothermal. The value of surface shear stress and heat flux is not equal to zero.

In reality, molecules will have both specular and diffuse interaction with the surface. This is accommodated by the (constant) accommodation coefficient which is defined as the fraction of incoming molecules which are reflected diffusely [152]. Agrawal and Prabhu [153] have conducted a survey on the value of accommodation coefficient  $\sigma_u$  which they have shown to be constant with respect to the Knudsen number for monoatomic gases at about 0.926 and decrease with increase in the Knudsen number for non-monoatomic gases. They have shown that it depends on several parameters including gaseous nature, gas pressure, surface related terms like cleanliness and roughness and, to some extent, surface temperature. We however, in this work choose the value as taken from the corresponding references for each test case. Molecule can also slip over the surface which leads to viscous heat generation, and is also known as sliding friction (or shear work). These effects are considered through the different types of non-equilibrium boundary conditions, as we shall see in the next section.

## 5.4 Different types of Boundary Conditions

The Navier-Stokes equations are generally used for flows in the continuum fluid regime. They are valid with the no-slip boundary condition upto the  $Kn \leq 0.001$ . In the continuum regime of flow, the presence of sufficient number of molecules allows them to reach local thermodynamics equilibrium, through repeated molecular collisions. This flow is then said to be in equilibrium. However, for the rarefied regime, when the molecular number density is low, the flow experiences few collisions and cannot reach local thermodynamics equilibrium. This flow is then said to be in non-equilibrium.

As the flow becomes more rarefied, at first there is an insufficient number of

collisions near the wall which causes the gas molecules to be in non-equilibrium with the wall. This leads to the flow violating the no-slip condition. This is known as the slip condition, where the velocity and temperature of the gas molecules next to the surface is not taken as equal to the surface velocity and temperature. In CFD, to accommodate this problem, it is recommended to use the velocity-slip and temperature jump condition [57, 152] in the range of  $0.001 < Kn \leq 0.1$  (slip-regime). Here, it is assumed that far from the walls, continuum condition prevail and the NS equations are valid. This helps to model the flow for a certain degree of rarefaction. In this regime, an appropriate boundary conditions are important to obtain CFD results comparable with the experimental data and the DSMC solution [152]. We explore below various non-equilibrium wall boundary conditions that are used in this work. We first explain the popular Maxwell first order velocity slip [154] and the Smoluchowski temperature jump condition [60]. Next, the new temperature jump condition [62] considering the sliding friction is discussed, followed by the pressure jump condition.

### 5.4.1 Maxwell slip boundary condition

The Maxwell slip boundary condition [59], including the effect of thermal creep<sup>1</sup>, can be written as [52]:

$$\mathbf{u} - \mathbf{u}_w = -\frac{2 - \sigma_u}{\sigma_u} \frac{\lambda \boldsymbol{\tau}}{\mu} - \frac{3}{4} Pr \frac{\gamma - 1}{\gamma p} \mathbf{q} \quad (5.1)$$

where  $\mathbf{u}$  is the flow velocity at the surface;  $\mathbf{u}_w$  is the surface velocity; the tangential shear stress is  $\boldsymbol{\tau} \equiv \mathbf{S} \cdot (\mathbf{n} \cdot \boldsymbol{\Pi})$ ;  $\mathbf{n}$  is the outward unit normal vector, and  $\mathbf{S} = \mathbf{I} - \mathbf{n}\mathbf{n}$  is a tensor (with  $\mathbf{I}$  being the identity tensor) which retains only the tangential components of any vector variable (e.g. velocity) which is dot product with it [52];  $\boldsymbol{\Pi}$  is the stress tensor at the surface; the heat flux is  $\mathbf{q} \equiv \bar{\mathbf{Q}} \cdot \mathbf{S}$  at the surface where  $\bar{\mathbf{Q}}$  is the heat flux vector;  $P$  is the gas pressure at the surface;  $\sigma_u$  is tangential momentum accommodation coefficient (which lies between 0 and 1) and  $\lambda$  is the mean free path [151] defined as

$$\lambda = \frac{\mu}{\rho} \sqrt{\frac{\pi}{2RT}} \quad (5.2)$$

---

<sup>1</sup>Thermal creep is the process in which the presence of temperature gradient at the surface creates an extra slip flow in the direction of increase in temperature. In other words, the gas slides from the colder to hotter region over the surface.



where  $\rho$  is the gas density at the surface;  $R$  is the specific gas constant; and  $\mu$  is the gas viscosity at the surface. The tangential momentum accommodation coefficient ( $\sigma_u$ ) gives the proportion of the molecules which are reflected from the surface diffusely ( $= \sigma_u$ ) or specularly ( $= 1 - \sigma_u$ ) [152].

The boundary condition (Eq. 5.1) can be expressed as a Robin (or mixed) type boundary condition [52] by substituting

$$\boldsymbol{\tau} = \mathbf{S} \cdot (\mathbf{n} \cdot \boldsymbol{\Pi})$$

and

$$\boldsymbol{\Pi} = \mu \nabla \mathbf{u} + \boldsymbol{\Pi}_{mc}$$

with

$$\boldsymbol{\Pi}_{mc} = \mu((\nabla \mathbf{u})^T - (2/3)\text{Itr}(\nabla \mathbf{u}))$$

where the superscript T denotes the transpose and tr is the trace. Also, using  $\mathbf{S} \cdot \nabla_n \phi \equiv \nabla_n(\mathbf{S} \cdot \phi)$ , Eq.5.1 becomes:

$$\mathbf{u} + \left(\frac{2 - \sigma_u}{\sigma_u}\right) \lambda \nabla_n(\mathbf{S} \cdot \mathbf{u}) = \mathbf{u}_w - \left(\frac{2 - \sigma_u}{\sigma_u}\right) \frac{\lambda}{\mu} \mathbf{S} \cdot (\mathbf{n} \cdot \boldsymbol{\Pi}_{mc}) - \frac{3}{4} \frac{\mu}{\rho} \frac{\mathbf{S} \cdot \nabla T}{T} \quad (5.3)$$

In Equation 5.3 the right hand side consist of three terms that are associated with the wall velocity, the so-called curvature effect and the thermal creep, respectively [52].

### 5.4.2 Smoluchowski temperature jump boundary condition

In rarefied conditions, the gas temperature of the surface is not equal to the surface temperature, and the corresponding difference is called the “temperature jump”. It is dependent on the heat flux normal to the surface. The Smoluchowski model [60] expressed as a Robin (or mixed) boundary condition is shown below:

$$T + \left(\frac{2 - \sigma_T}{\sigma_T}\right) \frac{2\gamma}{(\gamma + 1)} \frac{\lambda}{Pr} \nabla_n T = T_w \quad (5.4)$$

where,

$$Pr = \frac{\mu C_p}{k_L}; \quad (5.5)$$

$T$  is the surface gas temperature;  $T_w$  is the surface wall temperature;  $\sigma_T$  is thermal accommodation coefficient (which lies between 0 and 1);  $Pr$  is the Prandtl number;  $\gamma$  is specific heat ratio,  $c_p$  is specific heat capacity at constant pressure and  $k_L$  is the thermal conductivity. The thermal accommodation coefficient ( $\sigma_T$ ) is used to assign the temperature of the reflected molecules. In case of specular interaction, the reflected molecules rebound from the surface with the same energy as the incident molecules while for the case of purely diffusive interaction the reflected molecules have a temperature at thermal equilibrium with the surface. Overall,  $\sigma_T = 1$  corresponds to complete diffusive reflection, with a perfect exchange of energy between the gas and the solid surface, while  $\sigma_T = 0$  corresponds to zero energy exchange [62].

We have used, in this work, a form of the Prandtl number obtained using the kinetic theory, known as Eucken's relation [155, 57]:

$$Pr = \frac{4\gamma}{9\gamma - 5} \quad (5.6)$$

By using Eq. 5.5 we obtain the thermal conductivity as follows:

$$k_L = \frac{9\gamma - 5}{4\gamma - 4} R\mu \quad (5.7)$$

### 5.4.3 The Le Temperature Jump boundary Condition [62]

This boundary condition for temperature at the wall is a modified form of the Smoluchowski temperature jump condition which was derived considering the viscous heat generation (sliding friction) due to the presence of a slip velocity of the fluid at the wall. Following the notation used in the previous subsection, the Le temperature jump condition as proposed in [62] is:

$$T + \left( \frac{2 - \sigma_T}{\sigma_T} \right) \frac{2\gamma}{(\gamma + 1)} \frac{\lambda}{Pr} \nabla_n T = T_w - \left( \frac{2 - \sigma_T}{\sigma_T} \right) \times \frac{2\lambda(\gamma - 1)}{\mu(\gamma + 1)R} ((\mathbf{S} \cdot (\mathbf{n} \cdot \mathbf{\Pi})) \cdot (\mathbf{u} - \mathbf{u}_w)) \quad (5.8)$$

Equation 5.8 differs from the one used in [62] only in that we have replaced  $c_v$  by  $R/(\gamma - 1)$ .

It is to be noted that the velocity slip and both the temperature jump boundary condition given by Eqs. 5.3, 5.4.2 and 5.8 reduce to no-slip and constant wall temperature boundary condition as  $Kn$  assumes a smaller value, in the continuum regime. This aspect of non-equilibrium boundary condition will be studied in more depth in Chapter 7.

### 5.4.4 Pressure Jump Boundary Condition

The Maxwell-Smoluchowski boundary conditions given by Eqs. 5.3 and 5.4 are usually used with a homogeneous Neumann condition (zero normal gradient) for pressure [152, 55, 156]. Using the Le temperature jump condition given by Eq. 5.8 with a homogeneous Neumann pressure condition at the wall, however, leads to over-prediction of the pressure for various cases of hypersonic flows over the flat plate (as we shall see in Sec. 5.9). This is inconsistent with the notion that sliding friction, which is taken into account for temperature, should tend to lower the pressure and so would require consideration even in the pressure boundary condition. This observation motivates us to reconsider the pressure boundary condition at the wall.

Patterson [157] used an alternative derivation for non-equilibrium BCs using Grad's moment method [158]. It is based on the conservation laws for mass, momentum and energy for the incident and reflected molecules at a surface. Vidal et al. [148] in their study of hypersonic flow over a flat plate have used this method for velocity slip and temperature jump and have mentioned the existence of a pressure jump. Recently, Greenshields and Reese [53] have revisited those formulations and have given a derivation for the non-equilibrium BCs following Patterson's derivations. The final form of the pressure jump boundary condition, as given in [53], is presented below.

Using the analysis of mass conservation, the expression for the fluid density at the wall is obtained as

$$\frac{\rho_w}{\rho} = \sqrt{\frac{T}{T_w}}(1 + \zeta) \quad (5.9)$$

where  $\rho$  is the actual density of the fluid at the wall surface;  $\rho_w$  is the density of fluid with an equilibrium distribution at the wall temperature  $T_w$ , and

$$\zeta = -\frac{\mathbf{\Pi} : \mathbf{nn}}{2p} \quad (5.10)$$

is the ratio of the normal viscous stresses to pressure. The normal unit vector ( $\mathbf{n}$ ) is assumed to be pointing outward. Using,  $\rho_w$  we can obtain the wall pressure as  $p_w = \rho_w RT_w$ , from the ideal gas relation. A point to note here (following [53]) is the subscript  $w$  denotes the presumed properties of the fluid having an equilibrium distribution with the wall temperature  $T_w$  and those with no subscript denote the actual fluid property at the wall surface.

Using the analysis of normal-momentum conservation, the expression for the pressure

jump is obtained as follows:

$$p \left( 1 + 2\zeta + \frac{2-\sigma}{\sigma} \frac{4}{5\sqrt{2\pi}} \mathbf{a} \cdot \mathbf{n} \right) = p_w \quad (5.11)$$

or,

$$p = \frac{p_w}{\left( 1 + 2\zeta + \frac{2-\sigma}{\sigma} \frac{4}{5\sqrt{2\pi}} \mathbf{a} \cdot \mathbf{n} \right)} \quad (5.12)$$

where using  $\mathbf{q} = -k\nabla_n T$  we have:

$$\mathbf{a} \cdot \mathbf{n} = -\frac{1}{p\sqrt{RT}} \mathbf{q} \cdot \mathbf{n} = \frac{1}{p\sqrt{RT}} k\nabla_n T$$

Here,  $p$  is the pressure of the fluid at the wall and  $\mathbf{a}$  is tensor of rank 1 defined in such a way that the assumed distribution function (in terms of molecular velocity) for the incident molecule in Patterson's derivation of non-equilibrium BCs reproduces the corresponding basic variable as its moments [53]. The pressure jump BC is incorporated using this value of  $p$  as the Dirichlet condition at the wall, instead of giving it a homogeneous Neumann condition. Eq. 5.12 is usually ignored in simulations of rarefied gas flows. Greenshields and Reese [53] have written "its use is unclear" citing Gupta et al. [70]. We have however, chosen to examine the role of pressure jump condition with the Le temperature jump condition (Eq. 5.8) for various hypersonic flow situations over the flat plate cases considered in this work. In the numerical implementation, Eq. 5.10 is unphysical when  $\zeta \leq -1$  and almost impossible when  $\zeta > 1$  [53]. The value of  $|\zeta|$  is therefore assumed to be always less than 1 [157, 70], but this assumption may not hold true in the case of rarefied high speed flows [53]. To circumvent this problem researchers suggest clipping  $\zeta$  when it falls below some level. Greenshields and Reese [53] have chosen to set  $\zeta = 0$  for the cases considered in their work. We have, for our cases considered in this chapter, clipped the values of  $\zeta$  as follows:

$$\zeta = \begin{cases} 1, & \text{if } \zeta_o > 1 \\ -1, & \text{if } \zeta_o < -1 \\ \zeta_o, & \text{otherwise} \end{cases} \quad (5.13)$$

where,  $\zeta_o = \frac{-\mathbf{\Pi}:\mathbf{nn}}{2p}$ . We also analyze the influence of choosing  $\zeta = 0$  instead of using a clipping. In Eq. 5.12, based on the assumption of diffuse reflection everywhere,

the accommodation coefficient ( $\sigma$ ) is chosen as 1 [53]. In this work, we use the above formulation for the pressure jump condition with the Maxwell velocity slip and the Le temperature jump condition. Previously, Greenshields and Reese [53], as mentioned above have, used it with the velocity slip and the temperature jump condition given by Patterson [157]. For  $\zeta = -1$ , Eq. 5.9 will give,  $\rho_w$  value as zero, in such cases one may use a very small value for  $\rho_w$  ( $\sim 10^{-15}$ ) to ensure numerical stability.

## 5.5 Heat transfer in a rarefied gas flow simulations

With sliding friction being taken into the account in computing the heat transfer at the wall, Maslen [64] proposed a formulation for planar surfaces which was extended for curved surfaces by Le et al. [65, 62] as follows:

$$\mathbf{q} = -k\nabla_n T - (\mathbf{S} \cdot (\mathbf{n} \cdot \mathbf{\Pi})) \cdot (\mathbf{u} - \mathbf{u}_w) \quad (5.14)$$

where the right-hand side consists of two terms that respectively incorporate Fourier heat conduction and sliding friction (shear work per unit area).

## 5.6 Hypersonic Flat Plate Case

Several experimental and theoretical investigation has been carried out to study rarefied hypersonic flow over a flat plate with a sharp leading edge. These investigations, especially the striking experimental results obtained very near the leading edge, have generated a lot of interest in the problem [152, 156]. In this work we attempt a comprehensive analysis of different flat plate cases using the Le temperature jump condition [65] by not only studying the temperature and heat flux at the wall but also other flow properties such as pressure and slip-velocity. We compare the obtained results with DSMC results and the experimental data available in the literature [152, 53, 65, 62].

We first verify, in this section, our numerical implementation of the first order Maxwell Slip (Eq. 5.3), the Smoluchowski temperature jump (Eq. 5.4) and the Le temperature jump (Eq. 5.8) boundary condition with the results published in literature [62]. We then present our study of the different flat plate cases in the next section.

## 5.7 Boundary and initial conditions

Figure 5.1 also shows the boundaries of the flow domain for the flat plate problem. For the inlet and outlet, the characteristic boundary conditions based on Riemann invariants are used [139, 8] (Sec. 2.5). At the wall, nonequilibrium boundary conditions are applied (see Table 5.3). The uniform free-stream inflow condition is used to set the initial conditions throughout the flow-field, for the pseudo-transient solution.

## 5.8 Numerical Verification and Validations

We have implemented the non-equilibrium boundary condition in the our 3D unstructured grid solver. The first order Maxwell Slip (Eq. 5.3) and Smoluchowski temperature jump (Eq. 5.4) boundary condition have been tested for various configuration of the flow [159]. In this section, we present a numerical verification of our present code including the Le temperature jump condition (Eq. 5.8) with the results presented by Le et al. [62] for a hypersonic flow over a flat plate. The flow domain is shown in Fig. 5.1. The inlet condition is the same as that of Metcalf et al. [160] with  $T_w = 77$  K as presented in Table 5.1. The gas used is Nitrogen, and its properties are given in Table 5.2. The accommodation coefficients  $\sigma_T$  and  $\sigma_u$  used in the nonequilibrium boundary conditions are taken to be unity, as in the reference [62]. The results are compared with the DSMC results presented in [62]. Fig. 5.2(a) and Fig. 5.2(b) shows the plot of surface gas temperature and heat flux over the flat plate surface along with the results obtained by Le et al. [62]. The results show a good match with the reference study. However, the heat flux at the leading edge in the case of without sliding friction shows an over-prediction in comparison with the same reference's [62] CFD results but is close to their DSMC results. This is possible because we have implemented gradient correction for obtaining the  $\nabla_n T$  (used in heat flux computation) [8] (see Sec. 2.3.2), which hopefully gives a more accurate result in that high temperature gradient regions.

## 5.9 Results and Discussion

In this section, we investigate the behaviour of pressure and other quantities along the flat plate surface for various cases. To solve the Navier-Stokes equations at low speeds with a density-based solver we have used preconditioning with Roe flux [9] (see

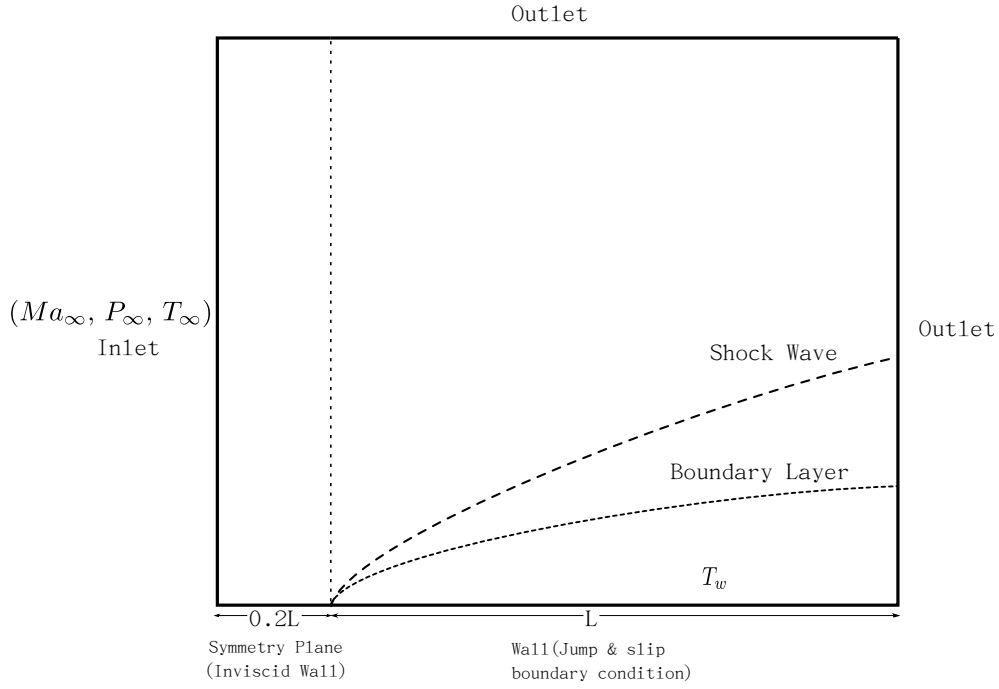
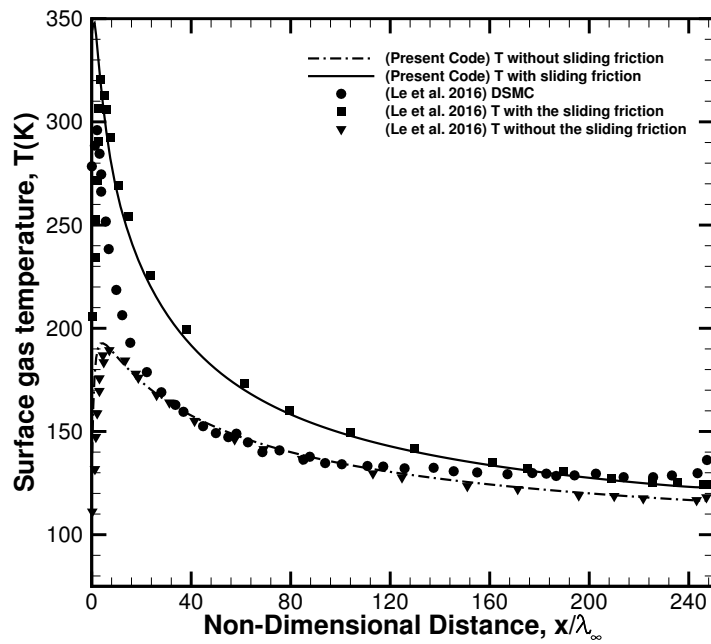
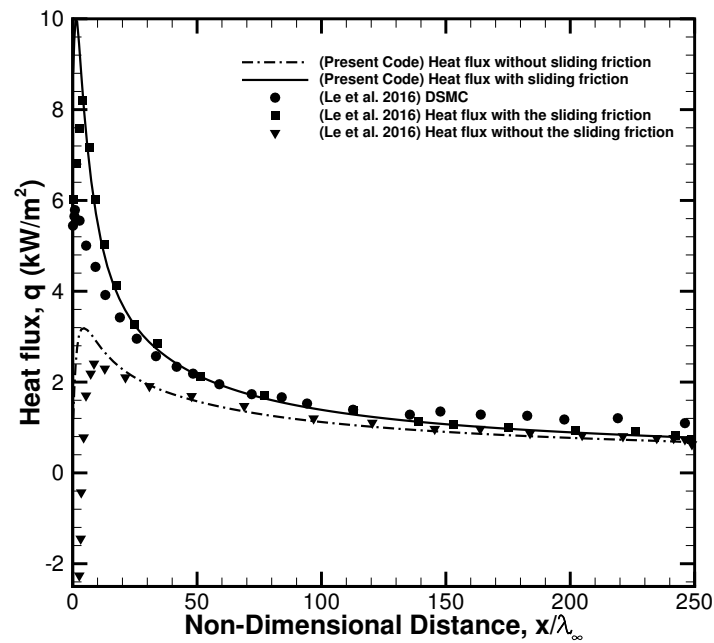


Figure 5.1: Flat plate problem.

Sec. 2.3.1.2). The time-stepping has been done implicitly using LU-SGS (Sec. 2.4.2). The CFL number for all the cases is taken as 500. We have considered the three hypersonic flat plate cases taken from Metcalf et al. [160] ( $T_w = 77$  and  $294\text{K}$ ) and Becker [161]. The flow domain is shown in Fig. 5.1. The detail inflow condition and the corresponding gas properties are listed in Table 5.1 and 5.2 respectively. The Sutherland law of viscosity (Eq. 2.9) is used for the cases considered in this chapter. In all the cases, we plot the value of surface pressure, surface gas temperature, slip velocity and heat flux at the wall against  $x/\lambda_\infty (= \frac{1}{Kn})$ . For all the cases, the value of  $\sigma_u = 0.7$  (used in Eq. 5.3) and  $\sigma_T = 1$  (used in Eq. 5.4 and 5.8) are taken, based on the study done by Le [152]. The grid spacing near the wall is taken to be the same as presented in the thesis of Le ([152]; Table 4.4, Pg. no 54). The first order Maxwell slip and Smoluchowski temperature jump along with the Le temperature jump boundary condition have been numerically verified in the previous section Sec. 5.6. Le et al. [62] have verified their temperature jump condition with the DSMC results of temperature and heat flux. In this section we attempt a more comprehensive analysis of their temperature jump boundary condition by studying the behaviour of pressure, temperature, slip velocity and heat flux along the wall. We perform studies for three different flow situations (Case 1, Case 2 and Case 3) of hypersonic flow over a flat



(a) Surface gas temperature



(b) Heat flux

Figure 5.2: Code Verification: The profile of surface temperature and heat flux over the flat-plate surface.



Table 5.1: Different experimental flow conditions for flat plate cases considered [152].

Case	Reference	$M_\infty$	$T_\infty$ (K)	$P_\infty$ (Pa)	$\lambda_\infty$ (mm)	$T_w$ (K)	Gas	$Kn$
I	Metcalf et al. [160]	6.1	83.4	2.97	0.35	77	Nitrogen	0.004
II	Metcalf et al. [160]	6.1	83.4	2.97	0.35	294	Nitrogen	0.004
III	Becker [161]	12.7	64.5	3.73	0.23	292	Argon	0.00264

Table 5.2: Coefficients of transport properties of the different gases considered [152].

Gas	$R$ ( $\text{m}^2\text{s}^{-2}\text{K}^{-1}$ )	$\gamma$	$A_s$ ( $\text{Pa}\cdot\text{sK}^{-1/2}$ )	$T_s$ (K)
Argon	208.1	1.67	$1.93 \times 10^{-6}$	142
Nitrogen	296.8	1.40	$1.41 \times 10^{-6}$	111

plate and compare them with the DSMC and the experimental results available in the literature. For each of these cases, we use three different numerical models, labelled in Table 5.3, differing in the boundary conditions used for the governing equations. It can be noted that PC1 corresponds to the ‘‘Standard’’ model [59, 60, 58, 152], PC2 to the Le temperature jump proposed in [62] and PC3 has the Le temperature jump *and* the new pressure jump condition [53]. For PC1, the heat flux is computed using only the Fourier law of heat conduction; while for PC2 and PC3, it is computed including the sliding friction component Eq. 5.14.

Table 5.3: Different studies performed based on the wall BC’s for velocity, temperature and pressure.

Label	Abbreviation	Velocity	Temperature	Pressure
(Present Code)-1	PC1	Maxwell, Eq. 5.3	Smoluchowski, Eq. 5.4	Zero Normal Gradient
(Present Code)-2	PC2	Maxwell, Eq. 5.3	Le temperature jump, Eq. 5.8	Zero Normal Gradient
(Present Code)-3	PC3	Maxwell, Eq. 5.3	Le temperature jump, Eq. 5.8	Pressure Jump, Eq. 5.12

### 5.9.1 Case 1: Metcalf *et al.*’s, $M_\infty = 6.1$ and $T_w = 77\text{K}$

In this first case of hypersonic flow over a flat plate [160], we have considered the flow of Nitrogen with the free-stream Mach number of  $M_\infty = 6.1$  and temperature  $T_\infty = 83.4$  K. The wall temperature is given as  $T_w = 77$  K. The flow condition is described in detail in Table 5.1. The corresponding DSMC and experimental results are obtained from [162, 62] and [160, 152] respectively. In this case, the Mach number is at the lower end of the hypersonic regime, and the wall temperature is close to (and less than) the free-stream temperature. The calculated surface gas temperature and surface pressure are shown in Fig. 5.3(a) and Fig. 5.3(b) respectively. We can see that the surface gas temperature in Fig. 5.3(a) using the Le temperature jump boundary

condition (PC2) comes closer to the DSMC results than the standard approach (PC1), but for the pressure (Fig. 5.3(b)) it clearly shows an over-prediction (the peak pressure being nearly 66% over-predicted w.r.t DSMC), especially at the leading edge, in comparison to both the experiment and the DSMC results. Using the Le temperature jump + the pressure jump condition (PC3) corrects this unusual rise in the pressure, showing a much closer match with the DSMC and experimental results at the leading edge (the peak pressure being merely 2.8% under-predicted w.r.t DSMC). The reason for this is probably that the calculation of pressure is based on the conservation of normal momentum which is ignored in the standard non-equilibrium BC's (i.e. Maxwell and Smoluchowski). Model PC3 also gives a somewhat closer match with the DSMC result for the surface gas temperature in comparison with PC2. Both PC2 and PC3 are closer to experiment for the temperature far from the leading edge, while at the tip both (and DSMC) over-predict the temperature. Figure 5.4(a), 5.4(b) and 5.4(c), respectively show the slip velocity, computed heat flux and the friction heating rate (wall shear stress  $\times$  slip velocity) for the three models. In these figures, only the DSMC results are used for comparison, as experimental data are unavailable. It is observed that all three models give close results, but far from the DSMC, for the slip velocity. But for the most important wall heat flux, PC2 and PC3 both give results very close to DSMC while PC1 is unexpectedly quite erroneous. All three models give close results (except at the leading edge) for the friction heating rate in Fig. 5.4(c). The region ( $x/\lambda_\infty \geq 100$ ) corresponds to  $Kn \leq 0.01$  (weakly slip regime) where CFD and DSMC are expected to give close results [53, 62]. Indeed, we see the three models better match the DSMC results in this range. Most importantly, we can clearly see the Le temperature jump + pressure jump condition (PC3) is able to model the flow in a more comprehensive way than the use of merely the temperature jump (PC2). Model PC3 ensures a good prediction of pressure at the leading edge without deterioration in the prediction of other quantities.

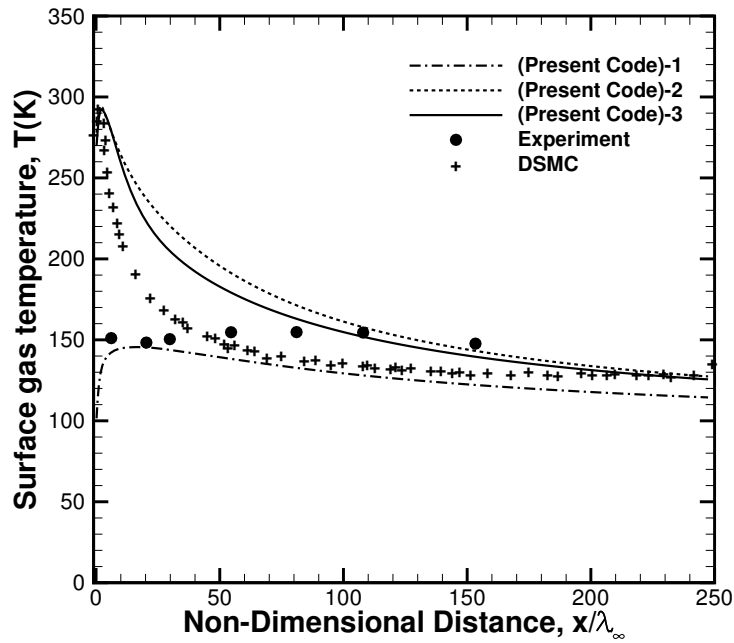
It is important to note that the slip velocity computed from PC1 to PC3 is far from the DSMC. However, despite this, the heat flux calculation, which now uses the slip velocity to find the heat gradients at the surface is accurate. This shows an inconsistency of the model which is probably due to the Maxwell velocity slip boundary model. As shown by Le (see Fig. 9 of [55]), using  $\sigma_u = 1 = \sigma_T$  gives a better match with the DSMC result for slip velocity, however the pressure and temperature along the wall are predicted better by using  $\sigma_u = 0.7$  and  $\sigma_T = 1$ . Therefore, we feel

that an additional non-equilibrium consideration, perhaps the Knudsen number, is required while modeling the boundary conditions, so as to obtain an overall numerical consistency.

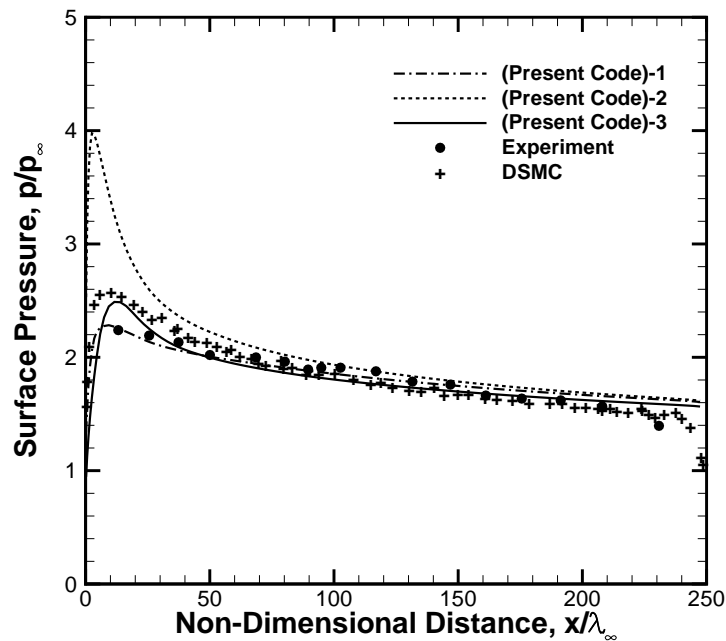
### 5.9.2 Case 2: Metcalf *et al.*'s, $M_\infty = 6.1$ and $T_w = 294\text{K}$

For the second case of hypersonic flow over a flat plate [160], we have considered Nitrogen flow with the free-stream Mach number of  $M_\infty = 6.1$  and temperature  $T_\infty = 83.4$  K. The wall temperature is  $T_w = 294$  K. The flow condition is detailed in Table 5.1. The corresponding DSMC and experimental results are obtained from [152, 65] and [160, 152] respectively. In this case, the Mach number is the same as in Case 1, but the wall temperature is high in comparison to the free-stream temperature. The calculated surface gas temperature and pressure are shown in Fig. 5.5(a) and Fig. 5.5(b) respectively. We can see that the surface gas temperature using the Le temperature jump boundary condition (PC2) comes very close to the DSMC results, especially at the leading edge. But, for the pressure, the solution clearly shows an over-prediction (the peak pressure being nearly 78.6% over-predicted w.r.t DSMC) at the leading edge, in comparison to both the experiment and the DSMC results. Using the Le temperature jump + the pressure jump condition (PC3) gives a temperature profile nearly identical to the PC2, but also shows a closer match with the DSMC results at the leading edge (the peak pressure being 21.3% over-predicted w.r.t DSMC). In comparison with the experiment, both PC2 and PC3 give better results for temperature far from the tip, while at the tip both over-predict the temperature. Paradoxically, the standard model PC1 seems to give the best results for pressure and temperature for this case.

However, for the important value of heat flux, Fig. 5.6(b), PC1 gives poor results, while PC2 and PC3 give a very close match with DSMC. For the slip velocity and friction heating rate, Fig. 5.6(a) and Fig. 5.6(c) respectively, the three models give nearly identical results. No experimental results are available for these quantities for this case as per the knowledge of the author. Overall, PC3 can be said to be as good as PC2 in predicting this case.

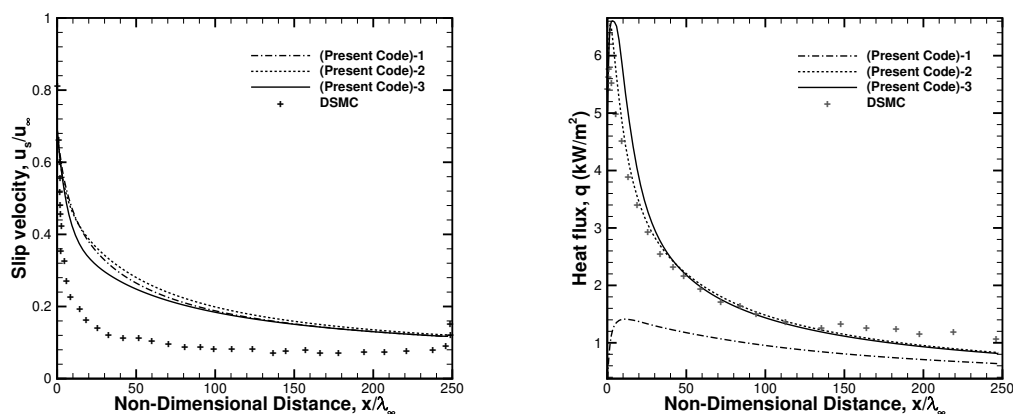


(a) Surface gas temperature.



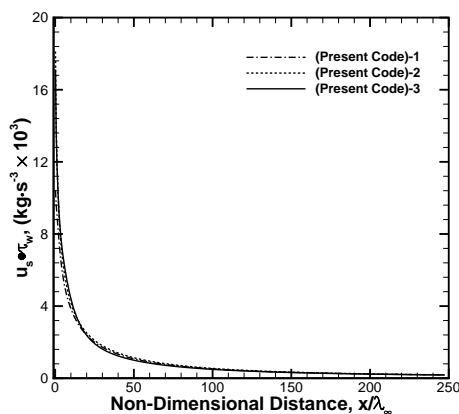
(b) Surface pressure

Figure 5.3: Metcalf et al.'s case [160]  $T_w = 77\text{K}$ . Comparison of temperature and pressure over the flat plate surface. 1 — without the sliding friction using Eq. 5.4, 2—with the sliding friction using Eq. 5.8, 3—with the sliding friction and the pressure jump BC using Eq. 5.8 and Eq. 5.12 respectively.



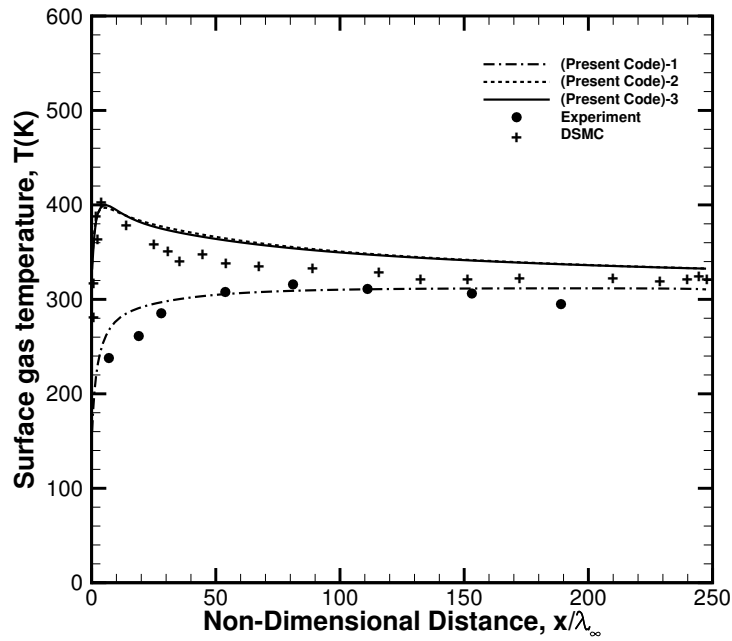
(a) Slip velocity

(b) Heat flux

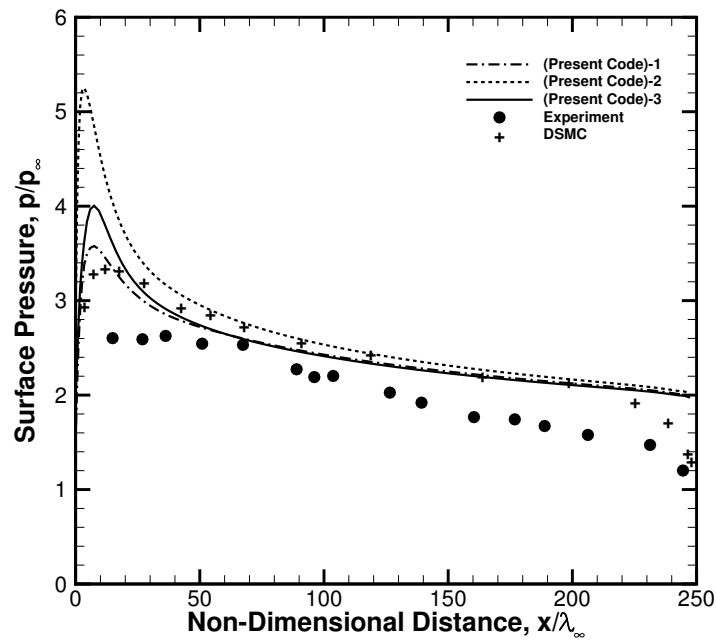


(c) Inner product of wall shear stress and slip velocity

Figure 5.4: Metcalf et al.'s case [160]  $T_w = 77\text{K}$ . Slip velocity, wall heat flux and shear work per unit area (measure of sliding friction) distribution over the flat plate surface. 1 — without the sliding friction using Eq. 5.4, 2—with the sliding friction using Eq. 5.8, 3—with the sliding friction and the pressure jump BC using Eq. 5.8 and Eq. 5.12 respectively. DSMC[162, 62]

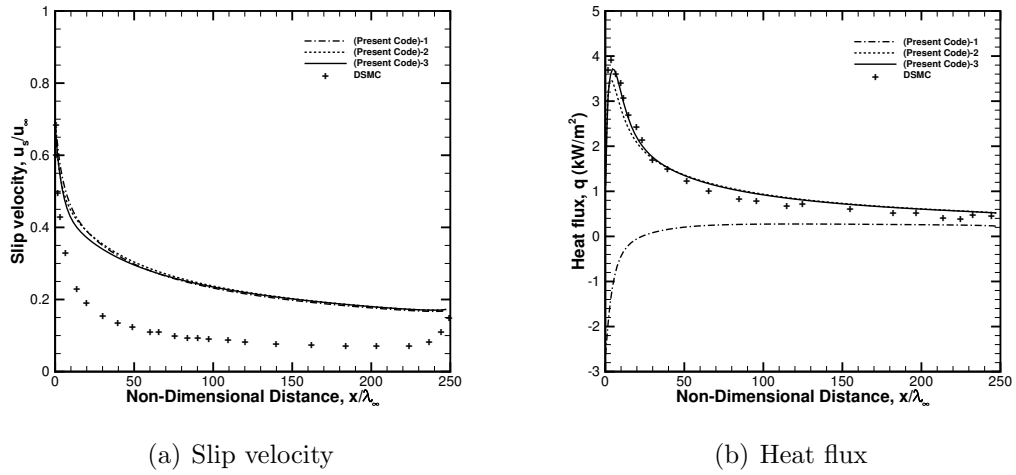


(a) Surface gas temperature.



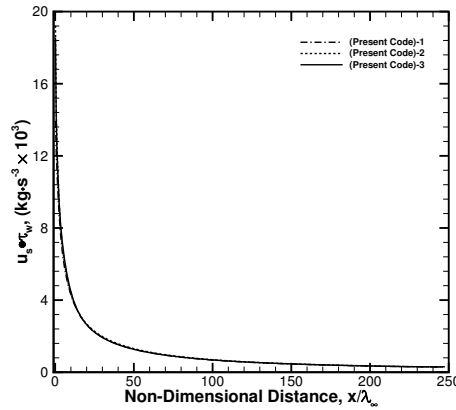
(b) Surface pressure

Figure 5.5: Metcalf et al.'s case [160]  $T_w = 294\text{K}$ . Comparison of temperature and pressure over the flat plate surface. 1 — without the sliding friction using Eq. 5.4, 2—with the sliding friction using Eq. 5.8, 3—with the sliding friction and the pressure jump BC using Eq. 5.8 and Eq. 5.12 respectively.



(a) Slip velocity

(b) Heat flux



(c) Inner product of wall shear stress and slip velocity

Figure 5.6: Metcalf et al.'s case [160]  $T_w = 294\text{K}$ . Slip velocity, wall heat flux and shear work per unit area (measure of sliding friction) distribution over the flat plate surface. 1 — without the sliding friction using Eq. 5.4, 2—with the sliding friction using Eq. 5.8, 3—with the sliding friction and the pressure jump BC using Eq. 5.8 and Eq. 5.12 respectively.

### 5.9.3 Case 3: Becker's, $M_\infty = 12.7$ and $T_w = 292$ K

For the third case of hypersonic flow over a flat plate [161], we consider Argon flow with the free-stream Mach number of  $M_\infty = 12.7$  and temperature  $T_\infty = 64.5$  K. The wall temperature is  $T_w = 292$  K. The flow condition is detailed in Table 5.1. The corresponding DSMC and experimental results are obtained from [152] and [161, 152] respectively. The significance of this case is that the Mach number is high, the wall temperature is high in comparison to the free-stream temperature and the fluid used is mono-atomic. The bulk viscosity used in the definition of stress vector in the Navier-Stokes equation is taken to be zero since the gas is mono-atomic [57]. The calculated surface gas temperature and pressure are shown in Fig. 5.7(a) and Fig. 5.7(b) respectively. We can see that the surface gas temperature using the Le temperature jump boundary condition (PC2) comes closer to the DSMC results than the standard model (PC1), especially at the leading edge. But, for the pressure, it clearly shows an over-prediction (the peak pressure being nearly 270.6% over-predicted w.r.t DSMC) at the leading edge, in comparison to both the experiment and the DSMC results. Using the Le temperature jump + the pressure jump condition (PC3) corrects this rise in the pressure with the results showing a closer match with the DSMC results at the leading edge (the peak pressure being 28.5% over-predicted w.r.t DSMC). Model PC3 also gives a closer match with the experimental result in comparison to PC1 and PC2. The results for the surface gas temperature are similar with both PC2 and PC3, i.e. the pressure jump condition does not alter the temperature prediction. But unexpectedly, we find PC2 and PC3, although predicting the temperature at the tip of the plate close to the DSMC, are clearly over-predicting the temperature downstream ( $x/\lambda_\infty \geq 20$ ) by a maximum of about 60%. As seen in first two cases, for  $x/\lambda_\infty \geq 100$ , i.e.  $Kn \leq 0.01$ , the DSMC and all the CFD results should have been closer. Here, only the results of PC1 is only close to DSMC for the specified range.

Figure 5.8(a) and 5.8(b) show the slip velocity and heat flux at the wall. For slip velocity, all the three CFD models give almost the same profile while PC1, neglecting sliding friction, under-predicts the heat flux in comparison with PC2 and PC3. The friction heating rate, Fig. 5.8(c) is almost identically predicted by all models, except at the tip where PC1 differs from PC2 and PC3.

We see in Case 3 that both jump conditions (PC2 and PC3) tend to give over-prediction of temperature in comparison with the DSMC for the region of low Kn over the flat plate while having a good agreement with the DSMC results in the



high Kn regions. The reason for this probably stems from the fact that as the free-stream Mach number is high giving rise to higher sliding friction resulting in higher temperature prediction in this region. In the region of low Knudsen number (i.e. far from the tip of the plate), in comparison to the previous two cases of lower Mach number the value of the shear work per unit area ( $u_s \cdot \tau_w$ ) is higher for this case at around  $4000 \text{ kg s}^{-3}$  (see Fig. 5.8(c)) at  $x/\lambda_\infty = 200$  compared to the previous value around  $230 \text{ kg s}^{-3}$ . This indicates we may have to consider Knudsen number effect in modeling sliding friction, i.e. the second term on the RHS of Eq. 5.8 and 5.14.

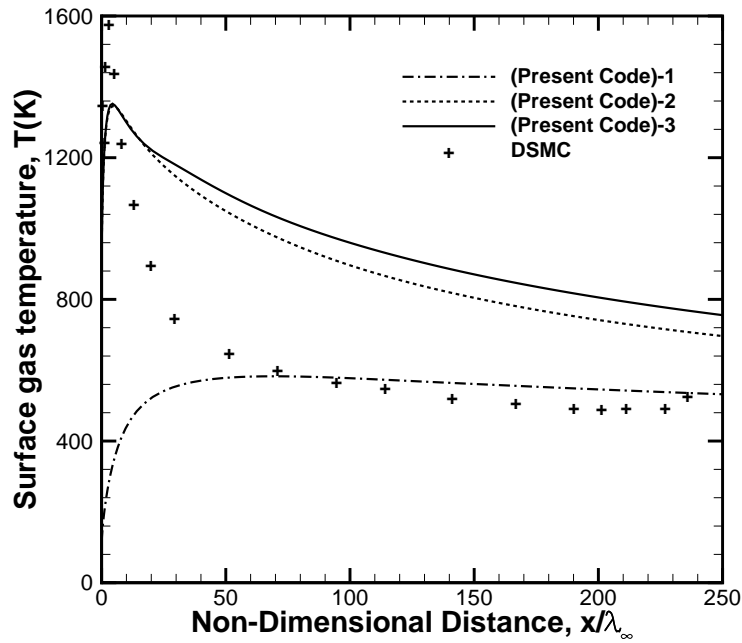
#### 5.9.4 Convergence Study

To see the effect of using the Le temperature jump condition and the pressure jump condition on the solution convergence we carry out a convergence analysis. All the cases have shown similar convergence behavior for all the flow variables. Therefore, we show here only the residual plot of pressure for the Case 1 for the three models, i.e., PC1, PC2 and PC3. The Courant number is taken as 500 for all the cases (this is acceptable for a false-transient computation of steady flow). The residual is calculated as the root-mean-square value of the differences between the old flow solution and the present flow solution over the entire flow-field, which is then normalized using the maximum root mean square averaged residual of the first five iterations.

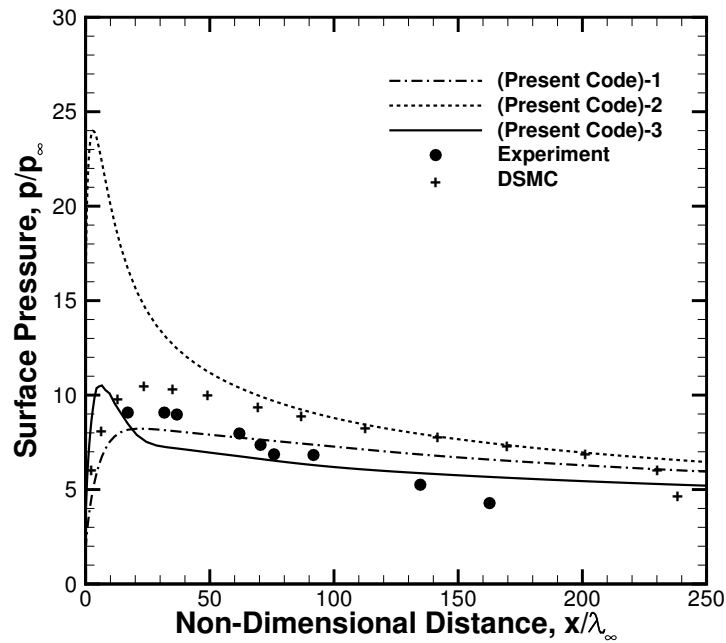
Figure 5.9 shows the normalized residual plot for the pressure for all the three studies. We see that for all the three models it follows an almost monotonic decrease pattern till they stall at the machine zero ( $\sim 10^{-12}$ ) in about 400 iterations. This shows that the Le temperature jump boundary condition and the pressure jump boundary condition do not affect the convergence rate of the computation.

#### 5.9.5 Effect of $\zeta$ used for the pressure jump wall boundary condition.

The quantity  $\zeta$  is the ratio of the normal viscous stress to pressure in Eq. 5.10. It is used in calculating the density and pressure at the wall and the corresponding pressure jump of the fluid at the wall surface. As discussed earlier, Greenshields and Reese have used  $\zeta = 0$  in their work. However, we have used a clipping for  $\zeta$  such that it always follow  $|\zeta| \leq 1$  in Eq. 5.13. We have found that clipping  $\zeta$  gives a stable solution for the hypersonic flow over a flat plate. However, it is interesting to see the

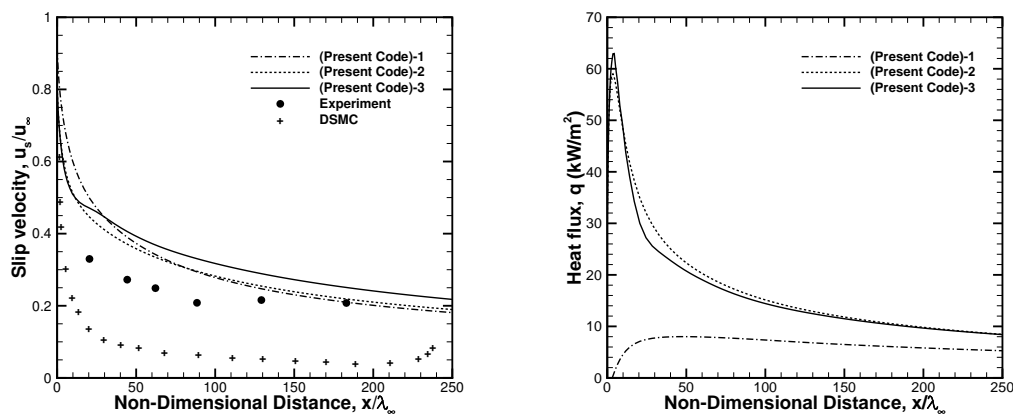


(a) Surface gas temperature.



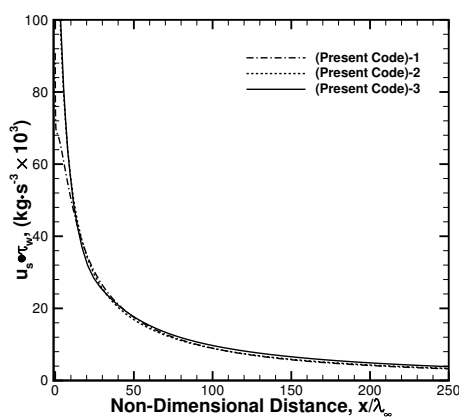
(b) Surface pressure

Figure 5.7: Becker's case [161]. Comparison of temperature and pressure over the flat plate surface. 1 — without the sliding friction using Eq. 5.4, 2—with the sliding friction using Eq. 5.8, 3—with the sliding friction and the pressure jump BC using Eq. 5.8 and Eq. 5.12 respectively.



(a) Slip velocity

(b) Heat flux



(c) Inner product of wall shear stress and slip velocity

Figure 5.8: Becker's case [161]. Slip velocity, wall heat flux and shear work per unit area (measure of sliding friction) distribution over the flat plate surface. 1 — without the sliding friction using Eq. 5.4, 2—with the sliding friction using Eq. 5.8, 3—with the sliding friction and the pressure jump BC using Eq. 5.8 and Eq. 5.12 respectively.

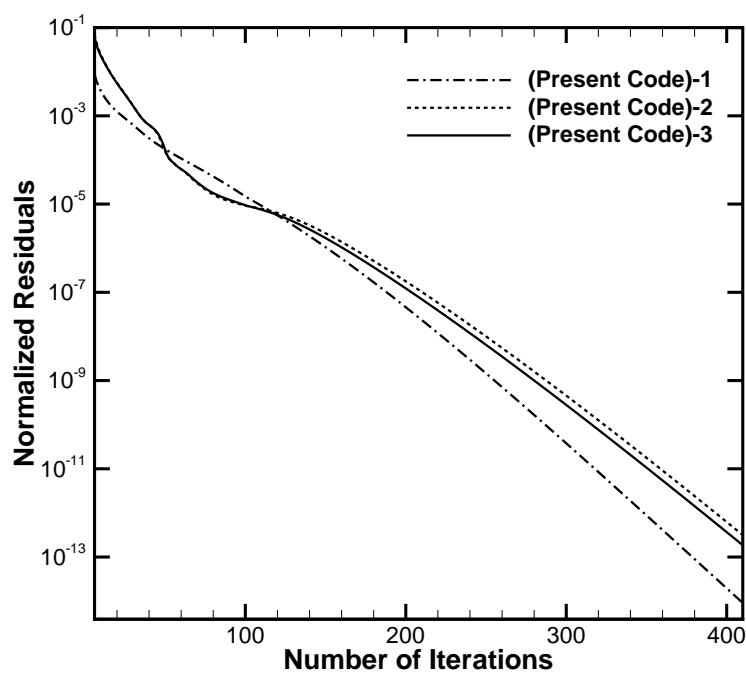
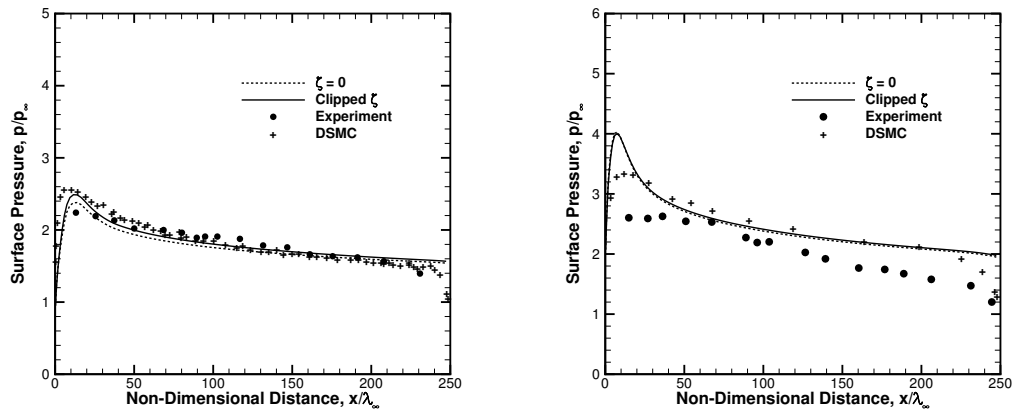


Figure 5.9: Convergence history of the scaled residue of pressure for Case-1. 1 — without the sliding friction using Eq. 5.4, 2—with the sliding friction using Eq. 5.8, 3—with the sliding friction and the pressure jump BC using Eq. 5.8 and Eq. 5.12 respectively.

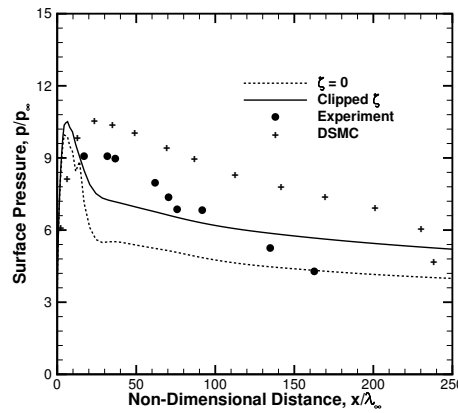
difference we get in the pressure prediction using the two models, i.e.  $\zeta = 0$  or clipped  $\zeta$ , because for other cases of rarefied high speed flows, such as flow over a cylinder, assumed values in the range of  $-20 < \zeta < -10$  have been reported [53], which may cause solution instability. For the three models studied we have found that only in the Case 3,  $\zeta$  values greater than 1 were observed, near the tip and very early in solution. Figure 5.10 shows the effect of taking  $\zeta = 0$  and clipped  $\zeta$  using Eq. 5.13 for the three cases considered in this work, for the nonequilibrium boundary condition PC3 (see Table 5.3). We see that for the first two cases, Fig. 5.10(a) and 5.10(b) of  $M_\infty = 6.1$ , there is little difference in the results for  $\zeta = 0$  and clipped  $\zeta$ . But, for the third case, Fig. 5.10(c) with  $M_\infty = 12.7$ , we see there is a marked difference in the solutions for  $\zeta = 0$  and clipped  $\zeta$ , with later one giving a more accurate result in comparison with the DSMC and experimental results. For the hypersonic flow over a flat plate, our choice of clipped  $\zeta$  seems more appropriate, as seen from these results. There is no need to assume  $\zeta = 0$  to ensure stability as done by [53] at-least for the type of cases considered in this chapter. However, we further examine whether using clipped  $\zeta$  or  $\zeta = 0$  gives more accurate and stable results in the subsequent chapters.

## 5.10 Closure

We have verified our numerical implementation of the Maxwell velocity slip, Smoluchowski and Le temperature jump condition with similar numerical implementations in the literature. A comprehensive analysis of the Le temperature jump condition has been carried out for three cases of hypersonic flow over a flat plate, and their results are compared with experiments and DSMC, wherever available. It has been found that the pressure is over-predicted in comparison with both the experiments and DSMC when using the Le temperature jump condition. The use of a pressure jump with the Le temperature jump condition is suggested as a possible remedy for the pressure over-prediction. The inclusion of the pressure jump boundary condition does not affect the prediction of other flow properties like the surface temperature, slip velocity and heat flux. We have investigated the difference obtained in the parameter  $\zeta$ , the ratio of normal viscous stress to pressure at the wall, being taken either as zero or used with a clipping. We have found that the clipping done as per the criteria described in this work gives stable and more accurate results for the hypersonic flow over flat plate cases considered here. We will further examine the choice of  $\zeta$  in the



(a) Case 1 – DSMC: [162, 62] and Experimental: [160, 152]. (b) Case 2 – DSMC: [152, 65] and Experimental: [160, 152].



(c) Case 3 – DSMC: [152] and Experimental: [161, 152].

Figure 5.10: Effect of  $\zeta = 0$  and clipped  $\zeta$  using Eq. 5.13, used for the pressure jump wall boundary condition for predicting the surface pressure. Comparison of PC3 (with the sliding friction and the pressure jump BC using Eq. 5.8 and Eq. 5.12 respectively.) with the DSMC and experiment results.

further chapters. It is also shown that the convergence is to machine zero and remains unaffected by the non-equilibrium boundary condition used.

Also, we note that the temperature jump condition considering sliding friction tends to over-predict the temperature in the region of low Kn over the flat plate in comparison with the DSMC for the case of very high Mach number ( $\sim 12$ ) flows. This suggests we may have to consider a Knudsen number effect in modelling the sliding friction part, i.e. the second term on the RHS of Eq. 5.8 and 5.14.

The most important finding of this chapter is to show that the pressure jump boundary condition, which has been largely ignored, complements the Le temperature jump condition by correcting the pressure prediction very significantly w.r.t. the DSMC results without significantly changing the prediction of the other properties. Also, we may have to reconsider the sliding friction concept in the light of more fundamental considerations of gas-wall gas interactions. In the next chapter, we shall extend the use of the Le temperature Jump and the pressure jump boundary condition to the case of micro/nano flows, wherein the rarefaction is caused by the characteristic length scale being of the order of the molecular mean free path. We will then further investigate the application of these boundary conditions.





# Chapter 6

## Investigation of non-equilibrium boundary conditions considering sliding friction for micro/nano flows

### 6.1 Overview

In the previous chapter, we used various non-equilibrium boundary conditions for the case of hypersonic flow over a flat plate with different inlet conditions. It was found that the Le temperature jump boundary condition should be complemented with a pressure jump boundary condition at the wall. It was shown that an over-prediction of pressure, especially at the leading edge of the flat plate, that is seen when the Le temperature jump condition is used alone could be corrected by the pressure jump condition. In this chapter we bring in the concept of sliding friction for the various types of boundary conditions for nano/micro flows. We investigate the proposed jump conditions for four cases: 1) a 90° bend microchannel pressure driven flow, 2) a nanochannel backward facing step with a pressure driven flow, 3) a nanoscale flat plate and 4) a NACA 0012 microairfoil. The results are compared with the available DSMC results. Also, we demonstrate the capability of our low-speed preconditioned density-based algorithm (Chapter 2) for rarefied gas flows. The algorithm captured flows of even very low Mach number of  $2.12 \times 10^{-5}$ . We now observe that the improvement in the flow prediction on including the Le temperature jump conditions is case-dependent. The use of the pressure jump condition along with

Le temperature jump has been found to be helpful in improving the flow prediction w.r.t. the DSMC results in some cases.

## 6.2 General Problem Setup

We study four different micro/nano flow test cases, which range from subsonic to supersonic regimes with varying types of flow such as internal and external flow, pressure-driven flow, flow with separation and reattachment, etc.. To solve the Navier-Stokes equations at low speeds with a density-based solver we use the preconditioning with Roe flux [9] (see Sec. 2.3.1.2). The time-stepping has been done implicitly using LU-SGS (Sec. 2.4.2). The CFL number for all the cases is taken as 500. For each of these cases, we use three different numerical models, labelled in Table 6.2, differing in the boundary conditions used for the governing equations. The variable hard sphere model (Eq. 2.10) is used for the viscosity computation, with the values of various coefficients for different gases considered in this chapter being given in Table 6.1. It can be noted that PC1 corresponds to the “Standard” model [59, 60, 58, 152], PC2 to the Le temperature jump proposed in [62] and PC3 has the Le temperature jump *and* the new pressure jump condition [53]. For PC1, the heat flux is computed using only the Fourier law of heat conduction; while for PC2 and PC3, it is computed including the sliding friction component Eq. 5.14. We evaluate if the use of the non-equilibrium boundary conditions helps to improve the accuracy of the Navier-Stokes calculation.

## 6.3 Boundary and initial conditions

For the inlet and outlet, the characteristic boundary conditions based on Riemann invariants are used [139, 8] (Sec. 2.5). At the wall, nonequilibrium boundary conditions are applied (see Table 6.2). The values of  $\sigma_u = \sigma_T = 1$  is used for all the computations presented in this work. The uniform free-stream inflow condition is used to set the initial conditions throughout the flow-field for the pseudo-transient solution.

Table 6.1: Coefficients of transport properties of the different gases considered [92, 57].

Gas	$R$ ( $\text{m}^2\text{s}^{-2}\text{K}^{-1}$ )	$\gamma$	$\bar{\omega}$	$T_{ref}$ (K)	$d_{ref}$ (m)
Argon	208.1	1.67	0.734	1000	$3.595 \times 10^{-10}$
Nitrogen	296.8	1.40	0.7	290	$4.110 \times 10^{-10}$
Air	287.0	1.40	0.77	273.0	$4.19 \times 10^{-10}$

Table 6.2: Different studies performed based on the wall BC's for velocity, temperature and pressure.

Label	Velocity	Temperature	Pressure
PC1	Maxwell, Eq. 5.3	Smoluchowski, Eq. 5.4	Zero Normal Gradient
PC2	Maxwell, Eq. 5.3	Le temperature jump, Eq. 5.8	Zero Normal Gradient
PC3	Maxwell, Eq. 5.3	Le temperature jump, Eq. 5.8	Pressure Jump, Eq. 5.12

## 6.4 Results and Discussion

The four different cases considered are: 1) a 90° bend microchannel pressure driven flow, 2) a nanochannel backward facing step with a pressure driven flow, 3) a nanoscale flat plate and 4) a NACA 0012 Microairfoil. The results and a discussion of these cases will be presented in this section.

### 6.4.1 Case 1: Pressure driven flow in a Microchannel with 90° bend

We consider here the case of a microchannel with a 90° bend, which is often encountered in MEMS gas flow. The schematic of the flow diagram is shown in the Fig. 6.2(a). The gas used is Argon. Both legs of the channel have a length of  $L = 7\mu\text{m}$  and width of  $w = 1\mu\text{m}$ . The pressure and temperature at the inlet are taken as  $2 \times 10^5$  Pa and 300 K, respectively. At the outlet, the pressure is 66666 Pa, while the temperature has a homogeneous Neumann condition. Based on the inlet values the computed inlet mean free path is  $\lambda_\infty = 3.58 \times 10^{-8}$ , using Eq. 5.2. The velocity is also given a homogeneous Neumann condition at both inlet and outlet. Non-equilibrium boundary conditions are imposed on the wall. The free-stream Kn is 0.027. In the final solution, the Reynolds number at the inlet is 5.5 which is near that of Stokes flow, a low Reynolds number flow. The mesh is chosen as hexahedral with a total of 57600 cells, as taken in the reference study [156].

The grid chosen throughout in this chapter is based on the appropriate reference. For the sake of completeness, we show here grid convergence for this case. A similar

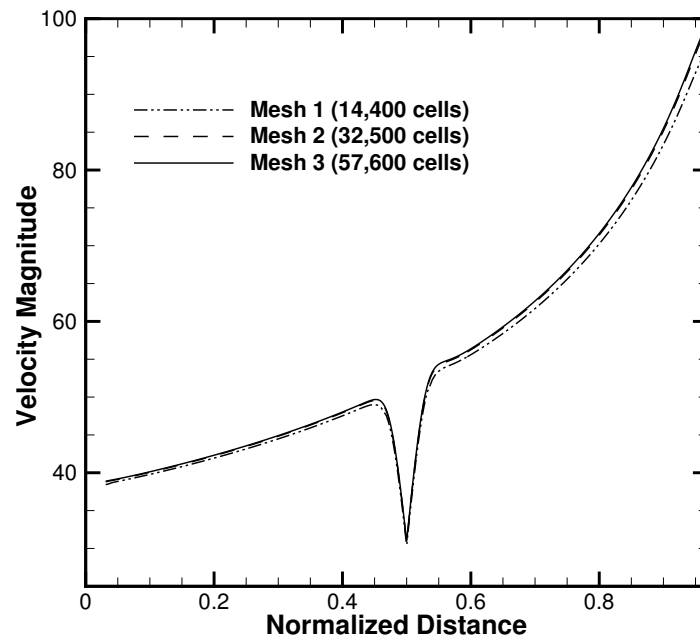
procedure is followed for other cases; but not reported here. Fig. 6.1 shows the grid independence and the convergence study for the case of pressure driven microchannel using PC1. Three meshes are considered: Mesh 1 with 14,400 cells ( $225 \times 30$ ,  $30 \times 30$  and  $225 \times 30$ ); Mesh 2 with 32,500 cells ( $300 \times 50$ ,  $50 \times 50$  and  $300 \times 50$ ) and Mesh 3 with 57,600 cells ( $450 \times 60$ ,  $60 \times 60$  and  $450 \times 60$ ). Fig. 6.1(a) shows that for Mesh 2 and Mesh 3 the results are almost grid independent. Also, all the grids show convergence up-to machine zero (see Fig. 6.1(b)). Similar convergence rates were observed with PC2 and PC3. Based on this, the grid chosen for the case of pressure driven flow in a microchannel with  $90^\circ$  bend is Mesh 3.

The corresponding DSMC results are obtained from references [163, 164, 156]. The PC3 results were run with  $\zeta = 0$  in Eq. 5.10.

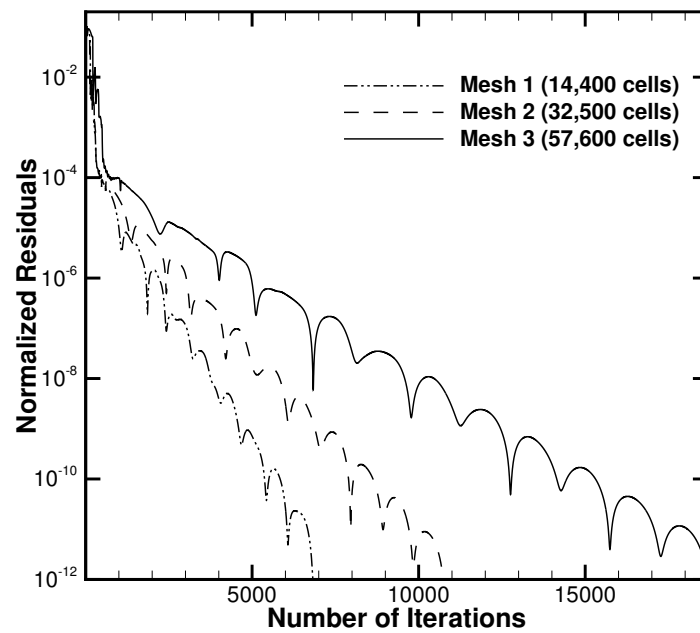
Figure 6.2(b) shows the Mach number contour (it is similar for all the three cases PC1, PC2 and PC3) with velocity streamlines. The maximum Mach number achieved by the flow is 0.313, which matches well the DSMC solution of 0.337 [164], and a minimum Mach number of  $2.12 \times 10^{-5}$  which has been captured quite efficiently. We can see that no flow separation was found at the corner, which is expected in near-Stokes flow. A similar situation was observed by a reference study [163].

Figure 6.3(a) and 6.3(b) show the Mach number and normalized pressure along the centerline of the channel. Pressure is normalized using the pressure specified at the outlet (i.e. 66666 Pa), and the x-axis shows the distance along the lower wall of the microchannel normalized with its length. The match with the DSMC [164] results are good. All the three model give the same profile, with the pressure gradually dropping from inlet to outlet and Mach number increasing with a dip at the bend. At the bend, the compressibility effects caused by a reduction of the gas velocity in the flow direction due to the sudden change of the geometry leads to a dip in Mach number which causes a jump in the pressure value. In the literature, a similar trend has been observed for the pressure and Mach number (expressed in terms of velocity) for flow through a  $90^\circ$  bend microchannel using the lattice Boltzmann method [165] and experimental results [166] for a different set of boundary conditions.

Fig. 6.4(a) and Fig. 6.4(b) shows the comparison of shear stress distribution and the slip velocity profile at the lower wall of the bend obtained from the three cases, with the DSMC results [156]. All the three boundary condition models nearly identical results with an overall good match with the DSMC results, properly capturing of the significant jump at the bend location. Figure 6.4(c) and 6.4(d) shows the computed

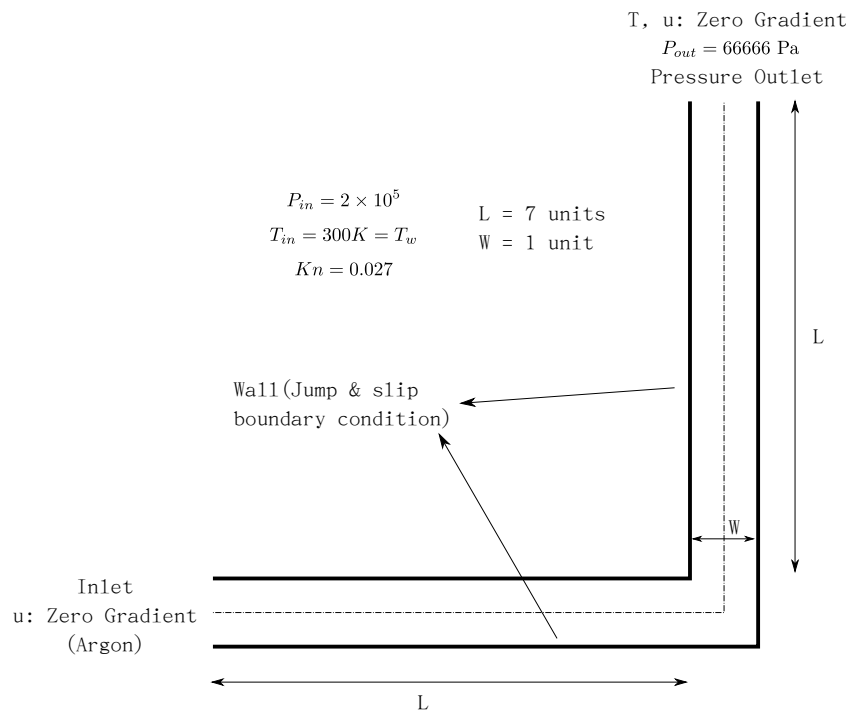


(a) Grid independence.

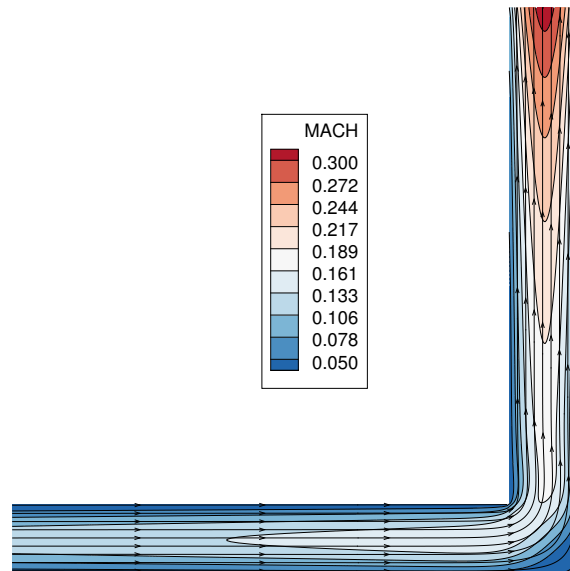


(b) Grid Convergence.

Figure 6.1: Grid Independence and Convergence study for the case of a pressure driven microchannel.

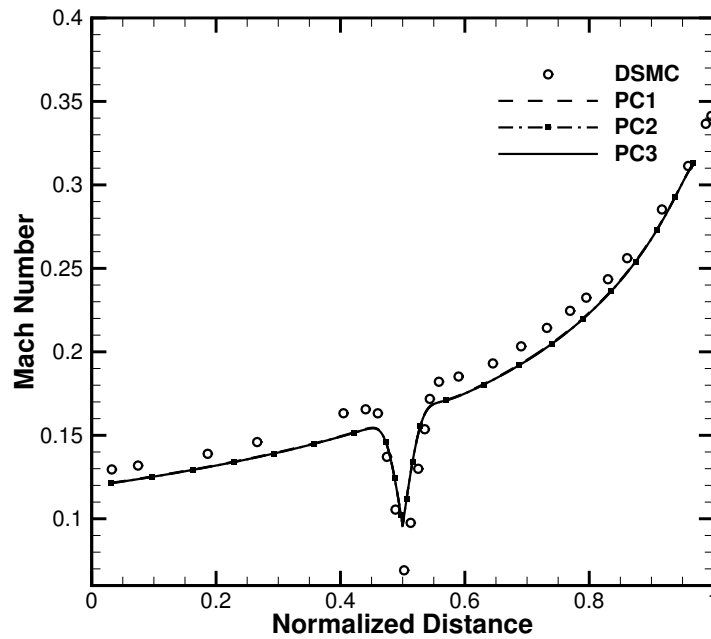


(a) Schematic of flow domain.

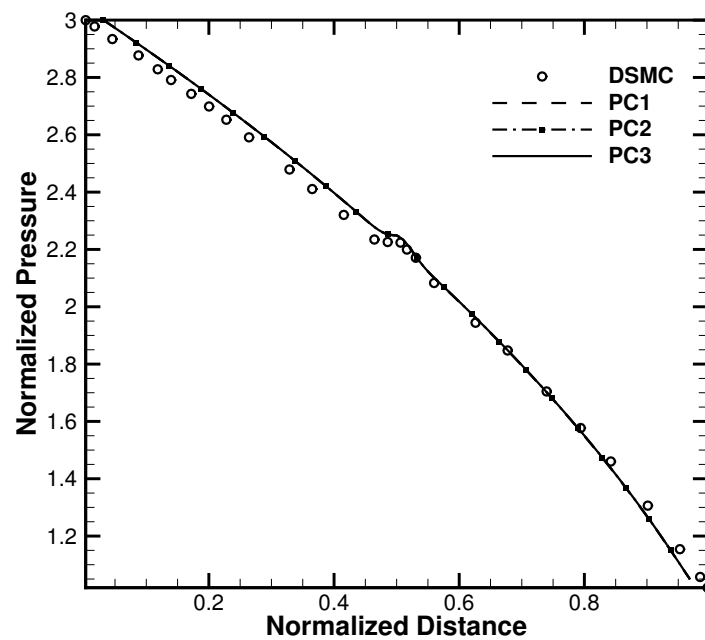


(b) Mach number Contours.

Figure 6.2: Pressure driven flow in a Microchannel with 90° bend.

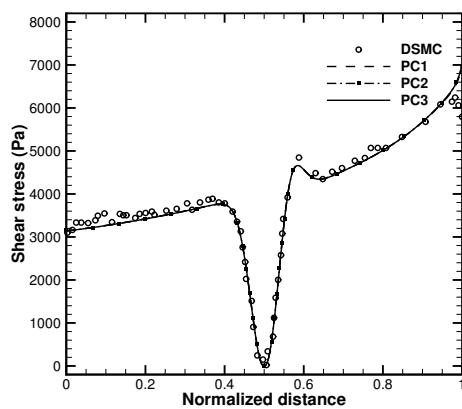


(a) Mach number.

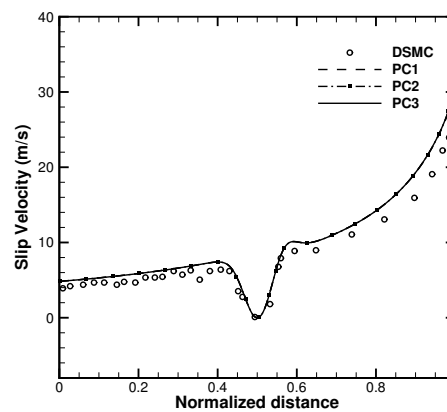


(b) Normalized Pressure.

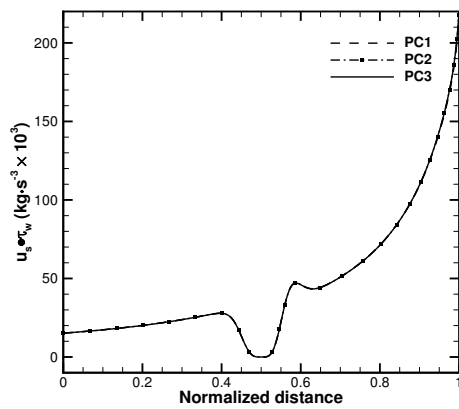
Figure 6.3: Flow distributions along the channel centerline.



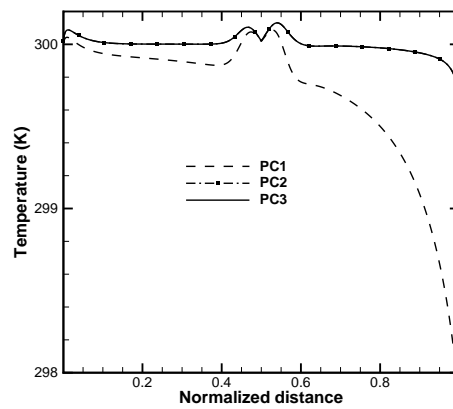
(a) Plot for Shear Stress.



(b) Plot for Slip Velocity.



(c) Inner product of wall shear stress and slip velocity (shear work per unit area).



(d) Plot for temperature.

Figure 6.4: Variation of various flow properties along the lower/right wall of  $90^\circ$  microchannel, normalised by its entire length.



shear work per unit area (wall shear stress  $\times$  slip velocity) and the temperature using the three models. We can see that with the use of Le temperature jump condition, in PC2 and PC3, the temperature predicted is higher, especially in the second leg of the microchannel. The reason being the value of friction heating rate is large ( $2 \times 10^5$ ) near the outlet. For this case, we see the all the three models, PC1, PC2 and PC3 give the same profile for all the flow variables, except temperature. The results for the temperature at the wall is not available from DSMC. But, considering the studies done earlier [62, 69], we expect that the temperature profile predicted by PC2 and PC3 will be closer to the DSMC results. Figure 6.5 shows the temperature profile, computed using the three cases, along the channel centerline. We can observe that the drop in temperature along the centerline is more compared with that along the lower/right wall (Figure 6.4(d)). Gavasane et al. [167] in their recent study of microchannels using DSMC has also obtained a similar pattern (refer Fig. 2(e) of [167]) wherein they observe a larger drop in the temperature along the channel centerline compared with that along the bottom wall for flow with inlet  $Kn = 0.0311$  (here, our inlet  $Kn = 0.027$ ).

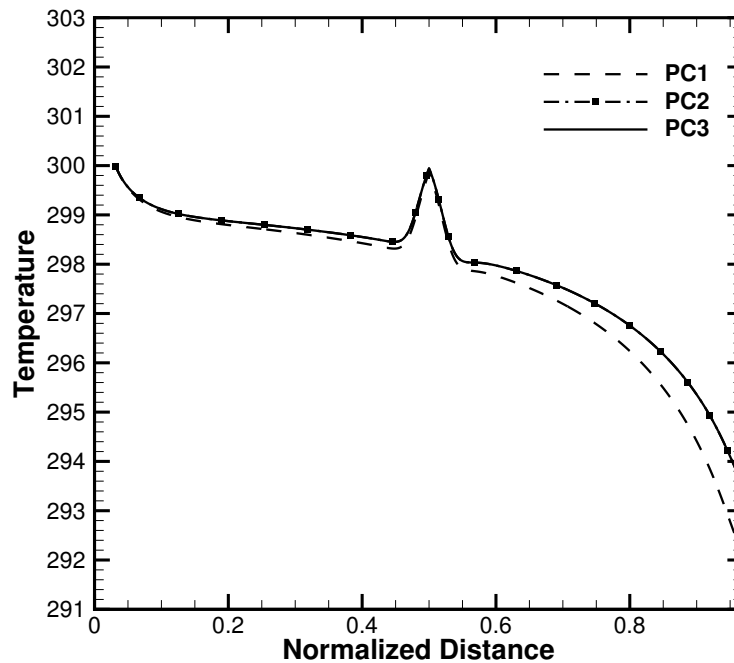


Figure 6.5: Temperature distributions along the channel centerline.

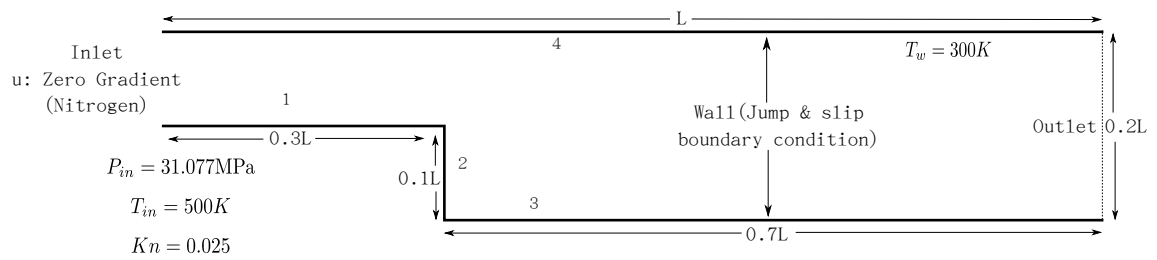
### 6.4.2 Case 2: Pressure driven flow over a backward facing step in a Nanochannel

Another case we have chosen to study is the backward facing step, which is a typical geometry utilized in nano-/micro devices [168]. The size of the channel is nanoscale, and the objective of this case is to show how the three boundary condition set (Table 6.2) affects the flow behaviour when the flow is characterized by separation and reattachment, and change of flow cross-sectional area.

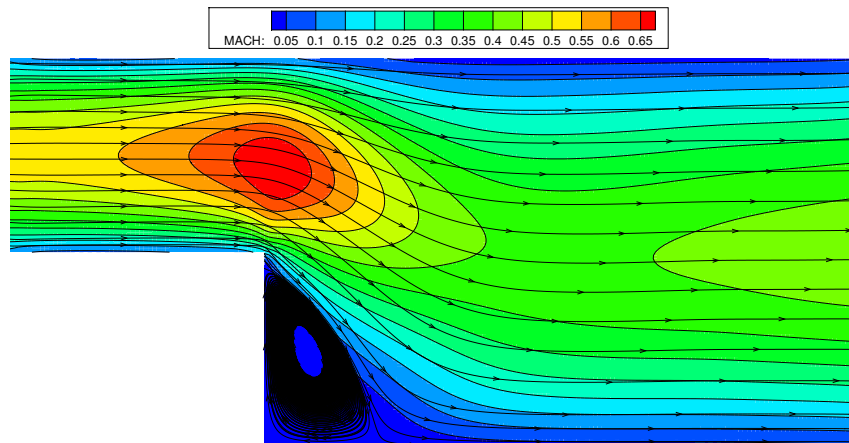
The schematic of the flow diagram is shown in Fig. 6.6(a). We have considered the flow of Nitrogen with the inlet pressure of  $P = 31.077$  MPa and temperature  $T_\infty = 500$  K. The wall temperature is given as  $T_w = 300$  K. At the outlet, the pressure is 15.53 MPa, while the temperature is given a homogeneous Neumann condition. The velocity is also given a homogeneous Neumann condition at both inlet and outlet. Based on the freestream values, the computed free-stream mean free path is  $\lambda_\infty = 3.48 \times 10^{-10}$  m, using Eq. 5.2. Non-equilibrium boundary conditions are imposed on the wall. The mesh is chosen as hexahedral with a total of 20400 cells, as in the reference [156]. The free-stream Kn is 0.025. The length of the upper wall of the channel is taken as  $L = 85.47$  nm. The corresponding DSMC results are obtained from references [168, 156]. The PC3 results were run choosing  $\zeta = 0$  in Eq. 5.10.

For all the three boundary condition (Table 6.2) we obtain nearly identical internal flow, with the Mach number contour as shown in Fig. 6.6(b). The minimum Mach number achieved is 0.0003092 which has been captured successfully by our low-speed preconditioned density-based solver. The maximum Mach number obtained is 0.65, subsonic flow.

Figure 6.7 shows the distribution of various flow properties along the surface of the lower wall after step (wall-3) with PC1, PC2 and PC3. The x-coordinate is normalized using the length of wall-3. The temperature increases in the recirculation region at the beginning of wall-3 and then gradually decreases along the wall, following an almost similar profile for all the computations, as seen in Fig. 6.7(a). The peak temperatures are 302.90 K, 302.96 K and 302.98 K respectively for PC1, PC2 and PC3, as compared to the DSMC results of 307 K. The small deviation in the results for PC1, PC2 and PC3 shows that the term of sliding friction in the Le temperature jump equation, Eq. 5.8, must have a negligible contribution. This also can be seen from the plot of computed shear work per unit area (wall shear stress  $\times$  slip velocity) as shown in Fig. 6.7(d). The value of  $u_s \cdot \tau_w$  is in the range of  $0 - 9 \times 10^6$  kg.s<sup>-3</sup> which



(a) Schematic of flow domain.



(b) Mach number Contours.

Figure 6.6: Backward facing step nanochannel with a pressure driven flow.

when multiplied with the mean-free-path (of order  $10^{-10}$  m) gives the sliding friction term in Eq. 5.8 of the order of  $10^{-1}$ . So, although the shear work per unit area is very high, it fails to contribute significantly to the temperature calculation because of the small length scales involved.

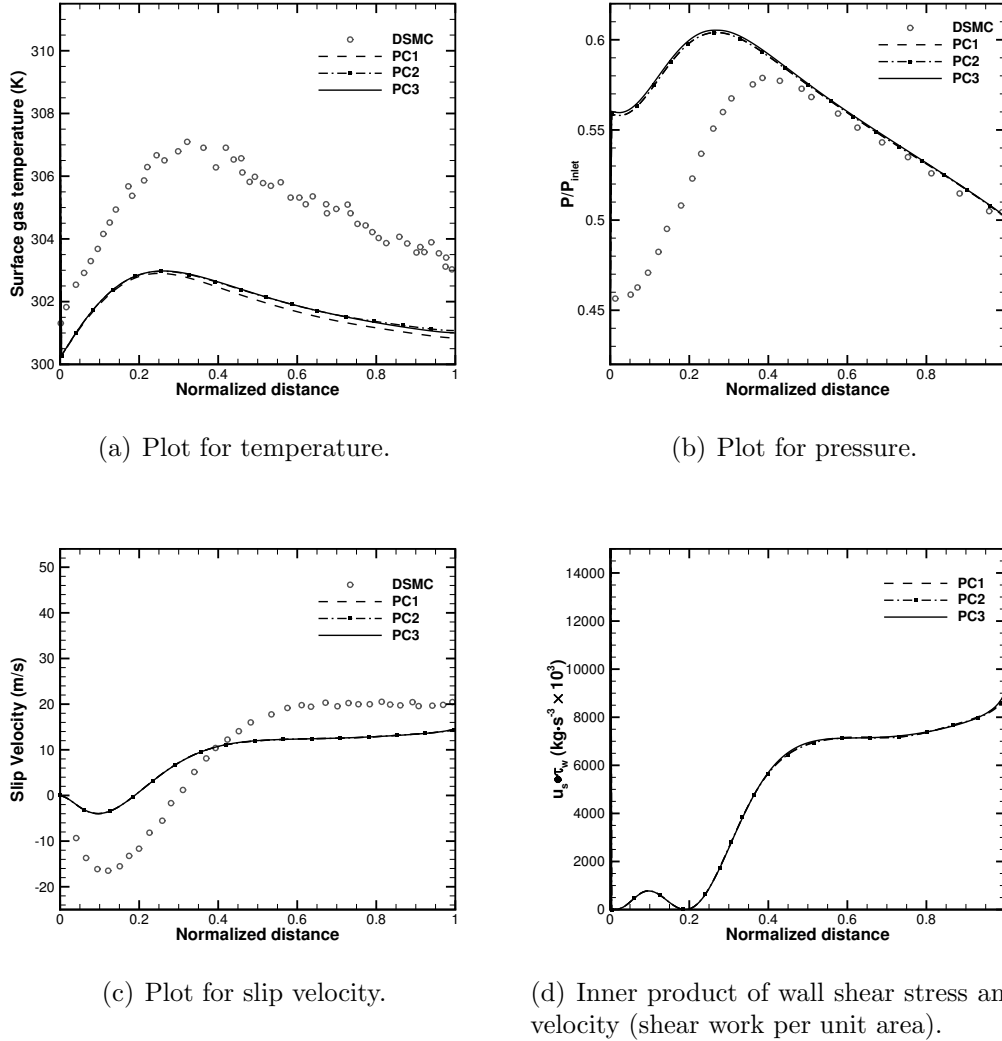


Figure 6.7: Variation of various flow properties along the wall 3 (lower wall after step).

It is also observed that all the three sets of boundary conditions give near-identical results for pressure (see Fig. 6.7(b)), with pressure being closer to the DSMC results in the region far from the recirculation zone. The same holds for the slip velocity (see Fig. 6.7(c)). The reattachment length calculated from PC1, PC2 and PC3 is around 11.30 nm, whereas from the DSMC it is 17.9 nm. The heating gas molecules

in the DSMC computation has more energy (and larger momentum) to jump over the recirculating region. This results in larger separation regions [156]. Also, for the  $Kn = 0.025$  case considered, the effect of momentum (which causes separation) is larger compared with the diffusion (which suppresses separation) due to the rarefaction effect, thus flow separation is observed in this case [167]. This can be seen by the larger magnitude of velocity for the DSMC results in the separation region (see Fig. 6.7(c)).

Overall, we may conclude that CFD does not do a very good job of predicting flow properties in recirculating nano-flows in the slip flow regime, whatever model is used.

### 6.4.3 Case 3: Nanoscale flat plate

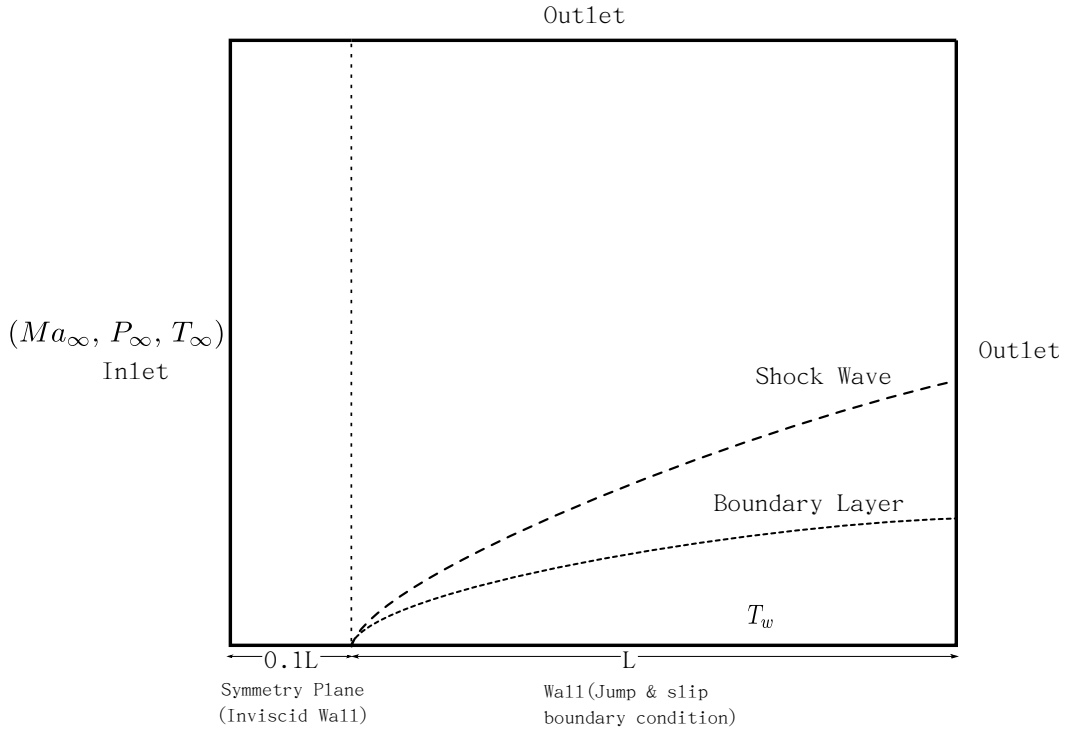


Figure 6.8: Nanoscale flat plate problem ( $L=100$  nm).

We now consider the case of the supersonic flow of Argon over a nano-scale flat plate of length  $L=100$  nm. The free stream flow conditions are  $P_\infty = 4.14 \times 10^7$  Pa,  $T_\infty = 300$  K,  $M_\infty = 4.38$  and  $Kn_\infty = 0.0013$ . The height of the flow domain is taken as 75 nm for performing the computation. The schematic of the flow domain is shown in Fig. 6.8. Based on the freestream values the computed freestream mean-free-path is  $\lambda_\infty = 1.97 \times 10^{-10}$ , using Eq. 5.2. We have considered a grid of  $113 \times 74$  cells which

is similar to the one considered in the reference [169] after a grid convergence study. The grid spacing near the wall is taken as 0.01 nm ( $\sim 0.1\lambda_\infty$ ), with an expansion coefficient of 1.016. Bi-geometric hexahedral elements are used. The corresponding DSMC results are obtained from references [169, 170].

Figure 6.9(a) and 6.9(b) shows the temperature and tangential velocity profile at  $x = 80$  nm from the plate tip. The results are in reasonable agreement with the DSMC results [169]. The three boundary conditions gave nearly identical results. A local extrema can be observed in both temperature and velocity at the distance of  $\sim 26$  nm from the wall. This is due to the diffusive shock wave formed at the leading edge of the flat plate. Figure 6.10 shows the shock formed which is diffusive due to the rarefied conditions. Because of the high Mach number, the shock wave is close to the plate surface and thus has its effect in the downstream of the flow even at  $x = 80$  nm.

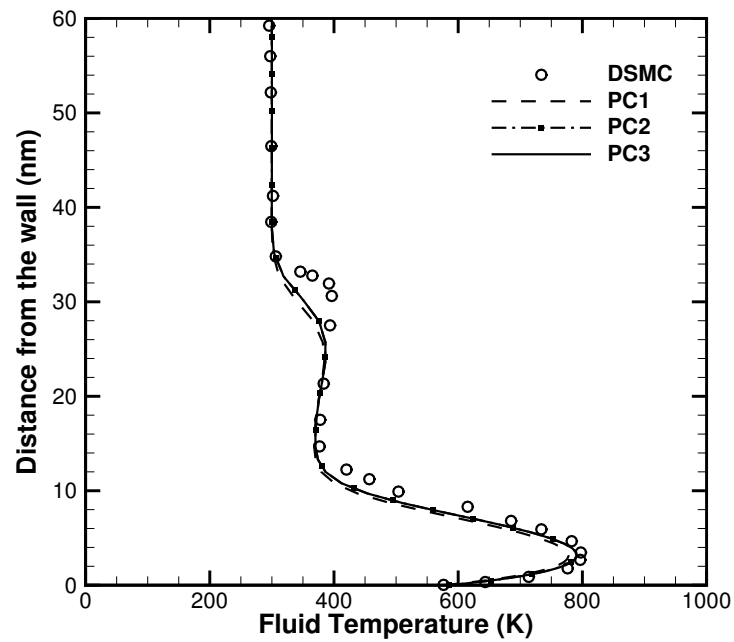
Figure 6.11 shows the distribution of various flow properties along the surface of the plate. For temperature (see Fig. 6.11(a)), PC2 and PC3 shows a close match with the DSMC results throughout the plate. But for pressure (see Fig. 6.11(b)), we see that PC2 over-predicts pressure at the tip of the plate by 72% w.r.t. the DSMC results, whereas PC3, i.e. the Le temperature jump + pressure jump boundary condition corrects this anomaly by predicting a better match (10%) for pressure at the start of the plate. However, the maximum error in pressure w.r.t. to the DSMC results away from the tip of the plate is 15%, 12.66%, 21.1% respectively.

For the slip velocity (see Fig. 6.11(c)) the results are similar for all the three cases and very close to the DSMC. Figure 6.11(d) shows the heat flux coefficient plot over the plate surface. The heat flux used for calculation includes the sliding friction component, i.e. Eq. 5.14, for PC2 and PC3. At the tip of the plate, PC2 and PC3 get a slightly closer match of  $C_h$  as compared to PC1, but significant differences exist with the DSMC results.

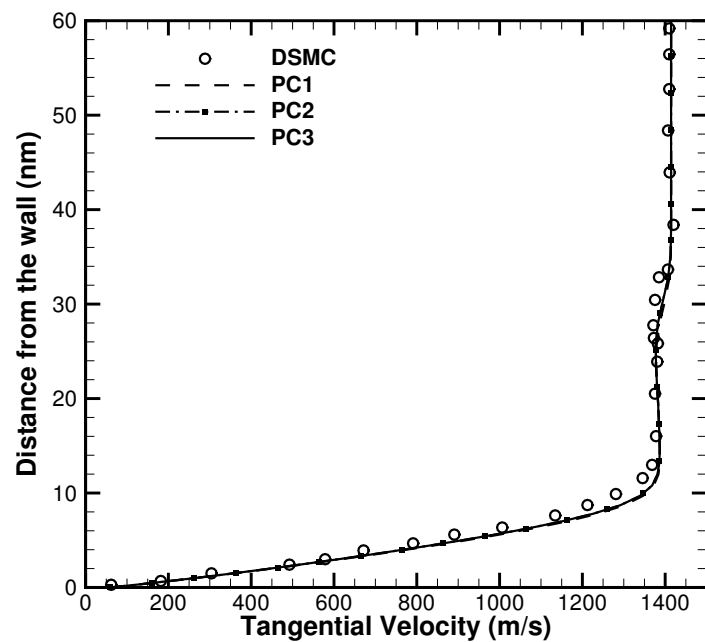
Overall, PC2 and PC3 results are closer to the DSMC results than PC1, but not by much.

#### 6.4.4 Case 4: NACA 0012 Microairfoil

The rarefied gas flows around a micro NACA 0012 is an appropriate starting point for studying the aerodynamic features of a micro vehicle [171]. The airfoil chord length,  $c'$  is taken as 4 cm and has been extensively studied previously by various researchers



(a) Temperature profile.



(b) Tangential velocity profile.

Figure 6.9: Flow profile at  $x = 80$  nm from the plate tip.

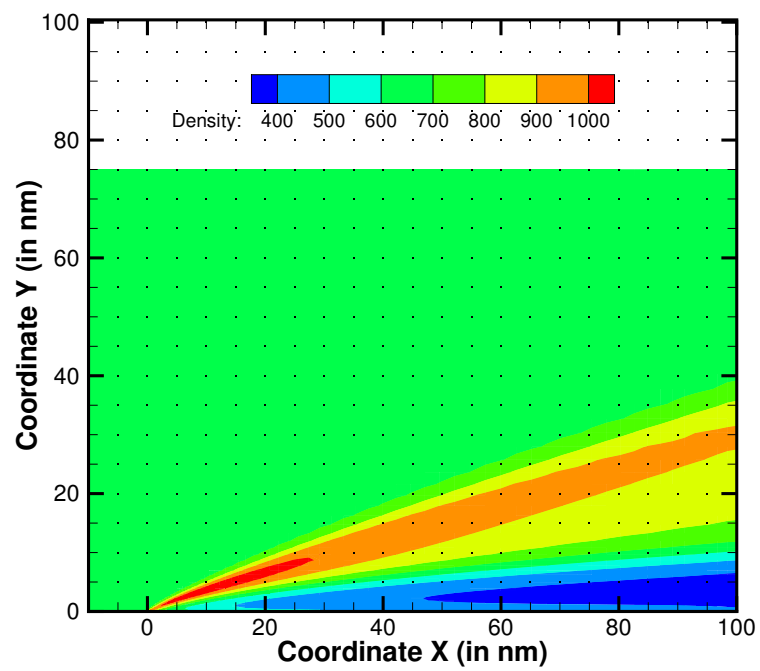
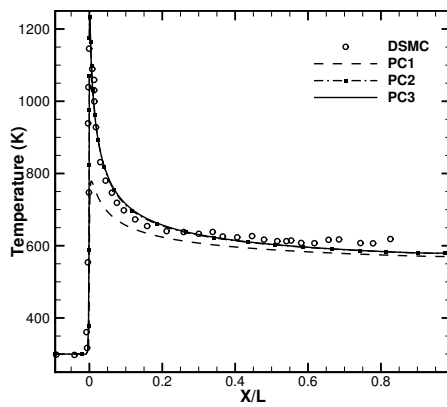
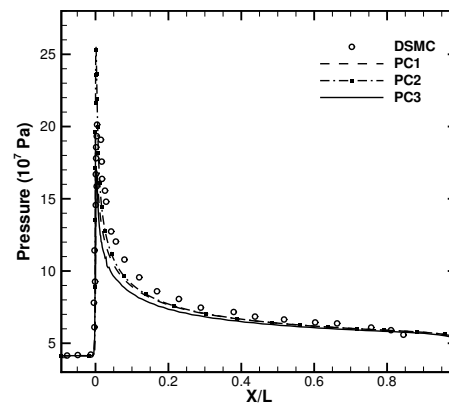


Figure 6.10: Density contour computed using PC1 for the nanoscale flat plate problem, showing the formation of boundary layer and diffusive shock at free stream Mach number of 4.38.

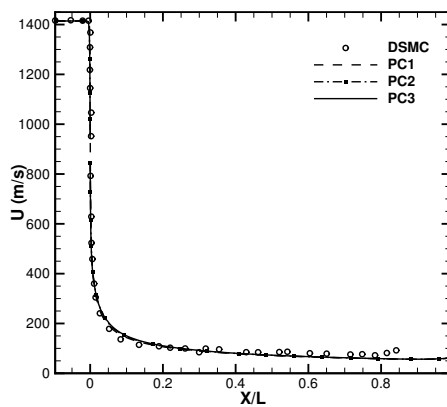




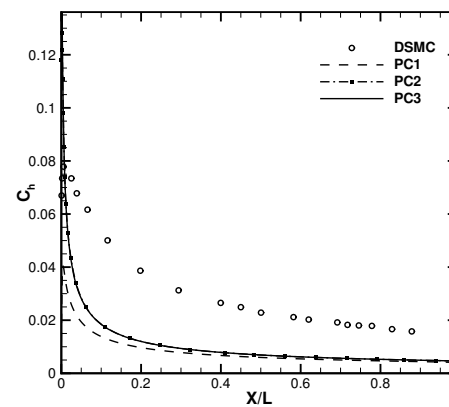
(a) Plot for temperature.



(b) Plot for pressure.



(c) Plot for slip velocity.



(d) Plot for heat flux coefficient.

Figure 6.11: Variation of various flow properties along the surface of the flat plate.

[172, 171, 173]. The NACA 0012 profile is obtained using the following expression [174]:

$$\frac{y}{c'} = 0.6 \left( 0.2969 \left( \frac{x}{c'} \right)^{0.5} - 0.126 \left( \frac{x}{c'} \right) - 0.3537 \left( \frac{x}{c'} \right)^2 + 0.2843 \left( \frac{x}{c'} \right)^3 - 0.1015 \left( \frac{x}{c'} \right)^4 \right) \quad (6.1)$$

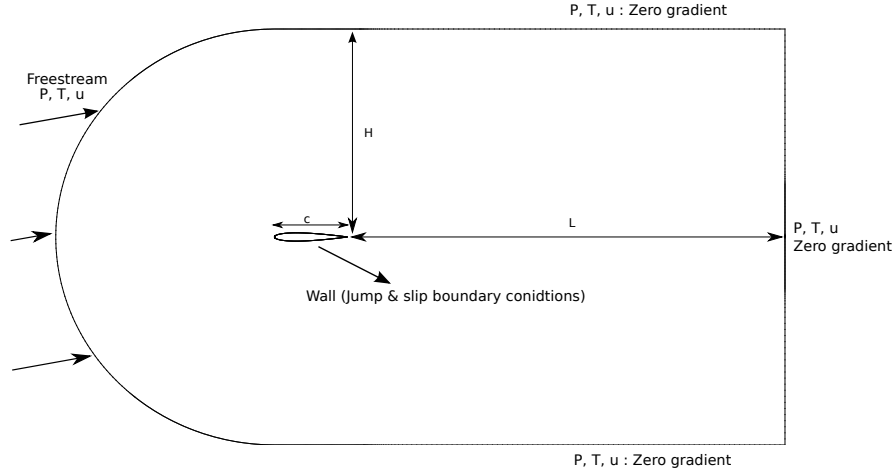


Figure 6.12: Schematic of flow domain.

where  $c$  is the chord length,  $c' = 4$  cm;  $x$  is the position along the chord ( $0 \leq x \leq c'$ ),  $y$  represents the airfoil profile at the given  $x$ . The flow domain is shown in Fig. 6.12. The mesh used is adapted from previous studies [173, 62], with 600 cells on the airfoil surface and a total of 106798 cells in the whole flow domain. The value of  $L$  and  $H$  is taken as  $6c$  and  $3c$  respectively. The freestream condition is taken as  $P_\infty = 2.78443$  Pa,  $M_\infty = 2.0$ ,  $U_\infty = 509.0$  m/s,  $T_\infty = 161$  K,  $T_w = 290$  K and  $Kn_\infty = 0.026$ . The working gas considered is air, with the flow around the airfoil taking at angle of attack of  $10^\circ$ . Based on the freestream values the computed free-stream mean free path is  $\lambda_\infty = 1 \times 10^{-3}$ , using Eq. 5.2. The corresponding DSMC results are obtained from references [173, 62].

This case was presented earlier by Le et al. [62] when they introduced the Le temperature jump condition. They ran the case with zero gradients of pressure at the wall, i.e. PC2. Here, we also run the case with pressure jump condition, i.e. PC3, and compare the results for other quantities also, apart from temperature and heat flux. The influence of three boundary conditions (Table 6.2) is studied. The PC3 results were run with choosing  $\zeta = 0$  in Eq. 5.10.

Figure 6.13, 6.14, 6.15 and 6.16 shows the comparison of temperature, surface pressure coefficient,  $C_p$ , slip velocity and heat flux distribution along the lower and

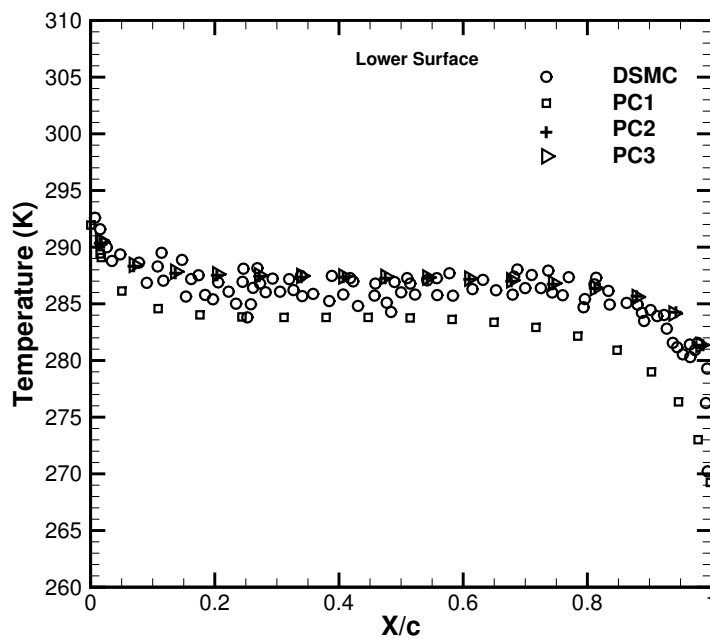
upper surface of the airfoil with the DSMC results. Figure 6.13(a) and 6.13(b) show clearly that inclusion of sliding friction term in temperature jump equation, Eq. 5.8, helps to improve the temperature prediction (PC2 and PC3) w.r.t. the DSMC results. While on the lower surface PC2 and PC3 results are almost identical, at the upper surface PC3 results are closer to the DSMC. The plot of  $C_p$  along the surface of airfoil (see Fig. 6.14(a) and 6.14(b)) give almost the same result, close to DSMC, for all the three cases.

Fig. 6.15(a) and 6.15(b) shows the plot of normalized slip velocity (the X-velocity at the surface is normalized with freestream velocity  $U_\infty$ ). For the lower surface, all the three cases give almost identical results, but for the upper surface, PC3 is closer to the DSMC results. Heat flux prediction shows that the inclusion of sliding friction component in the heat flux calculation Eq. 5.14 improves the prediction w.r.t. the DSMC results for both the upper and lower airfoil surfaces, as also reported by Le [62].

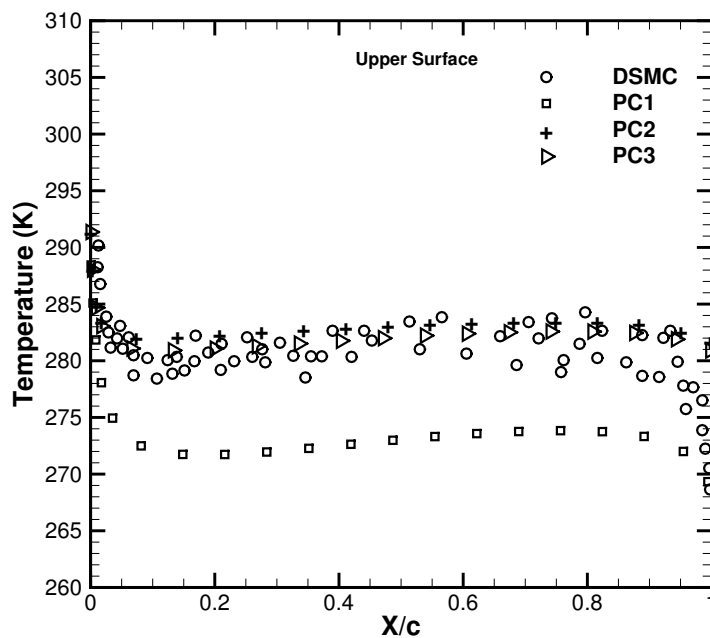
## 6.5 Closure

In this chapter, we have investigated various cases of micro/nano flows ranging from low speed to high speed using three different sets of boundary conditions respectively labelled as PC1, PC2 and PC3 (Table 6.2). Some important findings of this chapter are:

1. The inclusion of sliding friction while calculating the temperature jump at the wall helps to improve the temperature prediction of the CFD code in comparison with the DSMC results, which are considered most accurate in simulating non-equilibrium gas flows.
2. The sliding friction component contribution depends on parameters such as slip velocity at the wall and also on the mean-free path of the gas. For the case of pressure-driven flow through the 90° bent microchannel and micro-airfoil, we can see (Fig. 6.4(d), 6.13(a) and 6.13(b)) that the temperature computed using PC2 and PC3 (wherein the Le temperature jump condition is used) had marked differences to PC1 (i.e. standard temperature jump condition). But, for the case of pressure-driven backward facing step nanochannel, the overall contribution of the sliding friction component was small, as the mean free path ( $\lambda_\infty$ ) of gas was in the scale of Angstroms ( $\sim 10^{-10}m$ ). Thus, in this case, we

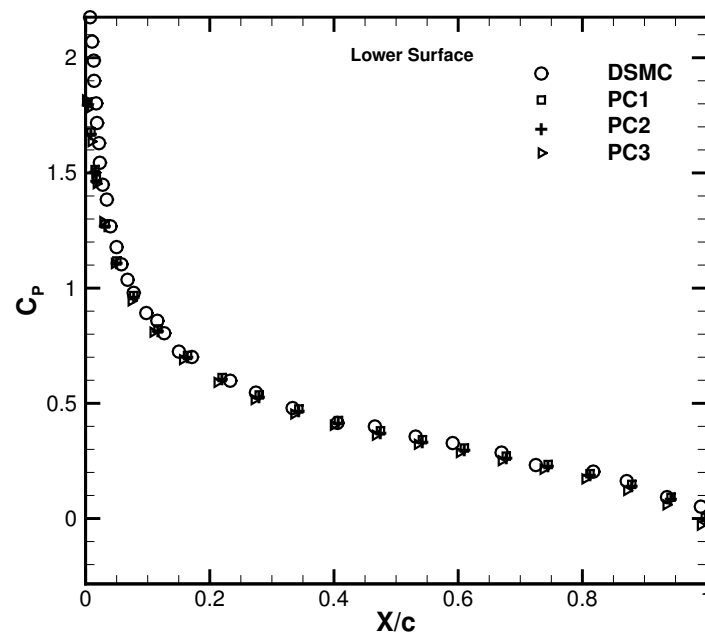


(a) Temperature along the lower surface.

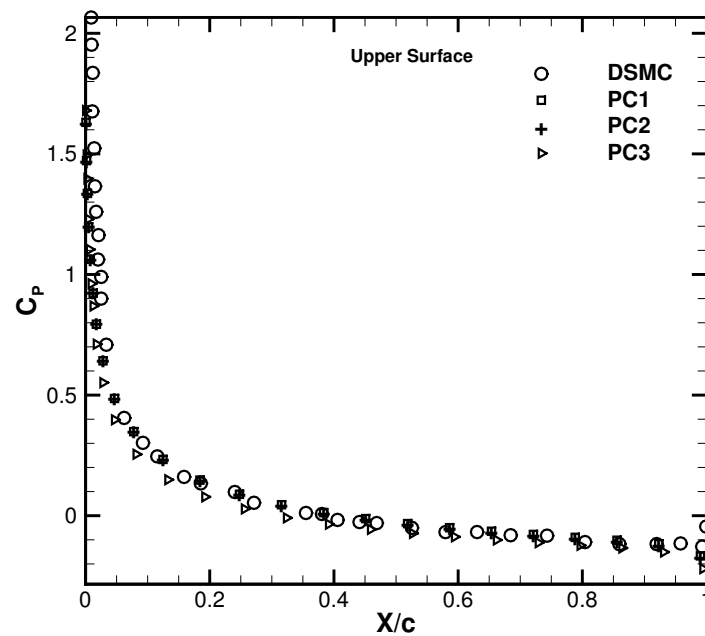


(b) Temperature along the Upper surface.

Figure 6.13: Variation of temperature along the lower and upper wall of the airfoil.

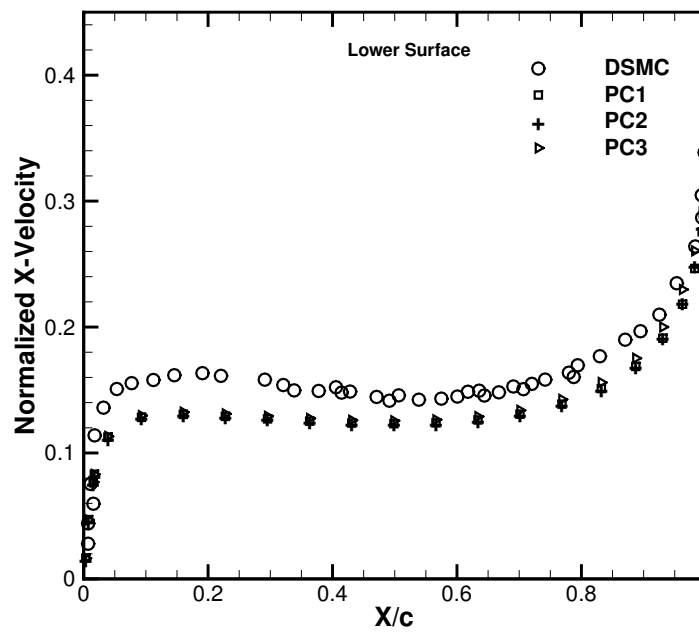


(a) Surface Pressure Coefficient along the lower surface.

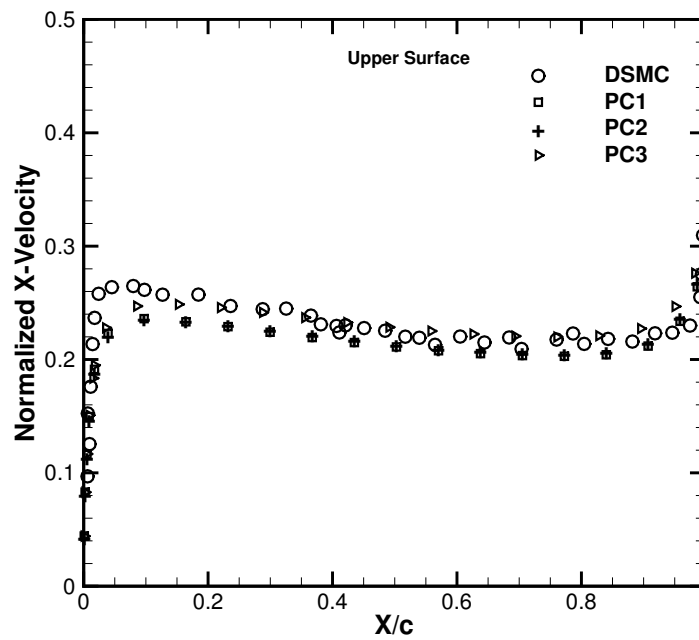


(b) Surface Pressure Coefficient along the Upper surface.

Figure 6.14: Variation of surface pressure coefficient along the lower and upper wall of the airfoil.

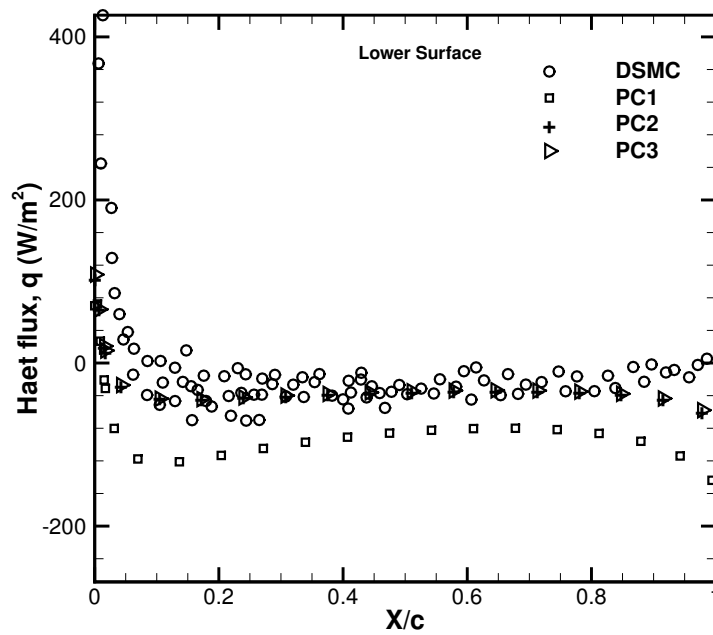


(a) Slip velocity distribution along the lower surface.

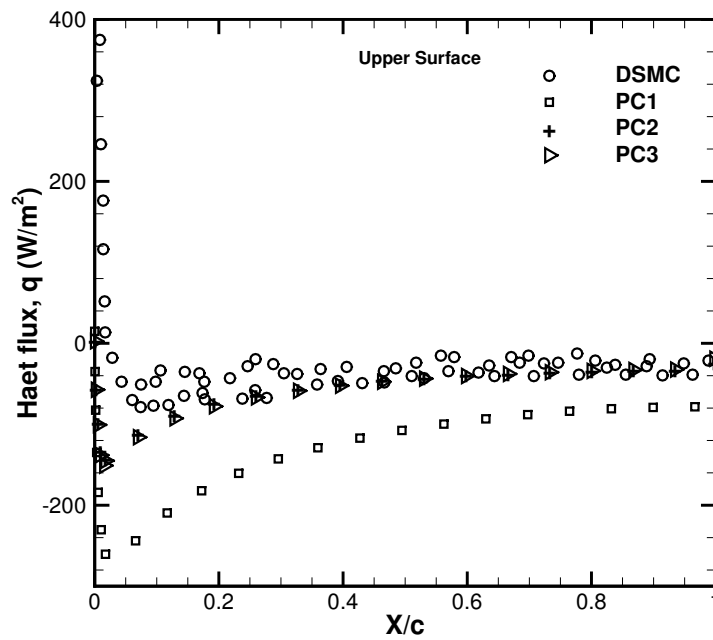


(b) Slip velocity distribution along the upper surface.

Figure 6.15: Variation of slip velocity distribution along the lower and upper wall of the airfoil.



(a) Heat transfer distribution along the lower surface.



(b) Heat transfer distribution along the upper surface.

Figure 6.16: Variation of heat transfer distribution along the lower and upper wall of the airfoil.

did not observe any significant change in the temperature predictions of PC2 and PC3 in comparison with PC1 (Fig. 6.7(a)). In the case of the nano flat-plate, although again  $\lambda_\infty \sim 10^{-10}$ , the shear stress component and slip velocity at the tip of the plate are very large, so the sliding friction caused a marked improvement at the tip of the plate both for the temperature and  $C_h$  (Fig. 6.11). Thus, the effect of the sliding friction component is dependent on the mean-free-path of the gas, shear stress and the velocity of the flow. This shows that improved prediction of the thermodynamic quantities is case-dependent. We may also need to include other non-equilibrium effects in the CFD modelling to properly capture the non-continuum phenomena.

3. We have also incorporated the pressure jump boundary condition, which is generally ignored, and have found it to complement the Le temperature jump boundary condition (PC3). It corrects the pressure, which when using the Le temperature jump condition alone, tends to be over-predicted as seen in the case of nano flat plate (Fig. 6.11(b)). In the case of the micro airfoil, it was shown to improve the prediction of temperature and slip velocity on the upper surface of the airfoil (Fig. 6.13 and 6.15). However, the PC2 (the Le temperature jump) and PC3 (the Le temperature jump + pressure jump) show no marked difference for the case of 90° bent microchannel and pressure-driven backward facing step nanochannel.



# Chapter 7

## Effect of rarefaction in hypersonic computation using two different convective schemes - Roe and modified SLAU2

### 7.1 Overview

Numerical computation of hypersonic flows over blunt bodies is challenging due to the difficulty in robust and accurate wall heat flux prediction and proper capturing of shock waves free from the “carbuncle” phenomenon. The SLAU2 convective scheme was proposed to suppress the shock anomalies found in capturing strong shocks. Still, for certain cases, it has been reported to lack accuracy. We now suggest a modification to the SLAU2 scheme based on altering the definition of the interfacial speed of sound used within the computations. Also, these convective schemes in the authors’ knowledge, have not yet been tested for the rarefied flows which we have seen in previous chapters. In this chapter, we also study how the shock anomalies found in the continuum hypersonic flows behave with the degree of rarefaction. We perform the numerical simulation of hypersonic viscous flow over a cylinder at Mach 8 and 16.34 at different Knudsen numbers. We carry out the study using the modified SLAU2 and the classical Roe schemes. It is found that the modified SLAU2 captures the shock free from the shock anomalies at all  $Kn$ , while the Roe scheme lacks robustness for  $Kn \lesssim 10^{-3}$ . The variation of different flow properties such as heat flux, wall shear stress and the Mach number is investigated. The peak heating value was observed to

decrease with the degree of rarefaction.

## 7.2 General Problem Setup

In this chapter, the convective term of Eq. 2.15 is discretized using two different schemes – modified SLAU2 (to be discussed in Sec. 7.4) and the Roe (Sec. 2.3.1.1) schemes. The Roe scheme is used with an entropy fix with tunable factor taken as  $\delta = 0.08$  (Eq. 2.31). The Venkatakrishnan limiter [116] is used. The time-stepping has been done implicitly using LU-SGS (Sec. 2.4.2). The CFL number for all the cases is taken as 200. All the simulations in this chapter are done using a parallel code based on the message passing interface (MPI) which has been developed for the present in-house solver by Nived [175]. METIS is used for the domain decomposition. The laminar perfect gas law is used throughout this work with the working gas taken as Nitrogen ( $R = 296 \text{ m}^2\text{s}^{-2}\text{K}^{-1}$  and  $\gamma = 1.4$ ). All the computations in this chapter have been performed *without* preconditioning. The reason for this is that preconditioned Roe scheme (Sec. 2.3.1.2) is known to suffer from shock instabilities at high Mach number [85]. We have observed the similar instabilities with the preconditioned Roe in our recent work [176].

## 7.3 Boundary and initial conditions

For the inlet and outlet, the characteristic boundary conditions based on Riemann invariants are used [139, 8] (Sec. 2.5). At the wall, the Maxwell velocity slip, Eq. 5.3, and Smoluchowski temperature jump, Eq. 5.4, boundary condition is applied. Pressure is given a homogeneous Neumann condition at the wall. The values of  $\sigma_u = \sigma_T = 1$  (Eqs. 5.3 and 5.4) is used for all the computations presented in this work. The uniform free-stream inflow condition is used to set the initial conditions throughout the flow-field for the pseudo-transient solution.

## 7.4 Modified SLAU2

In the SLAU2 scheme, as discussed in Sec. 2.3.1.3, the dissipation term of the pressure flux (third term in RHS of Eq. 2.40) is made proportional to the Mach number in order to feed the strong shock with adequate dissipation. This was intended to allow

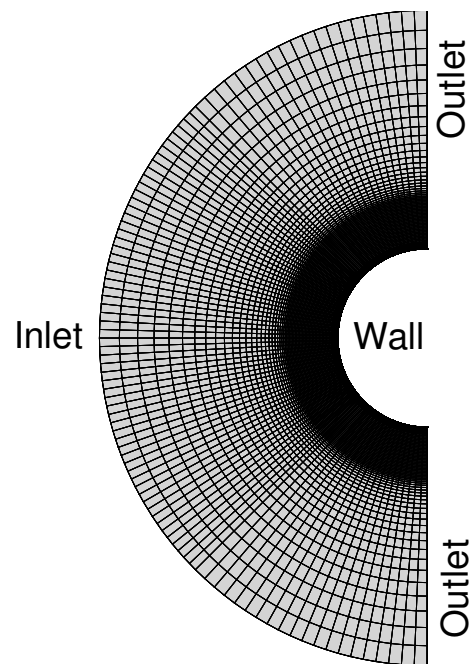


Figure 7.1: Flow domain and mesh used for the flow over the half cylinder ( $R=38.1$  mm).

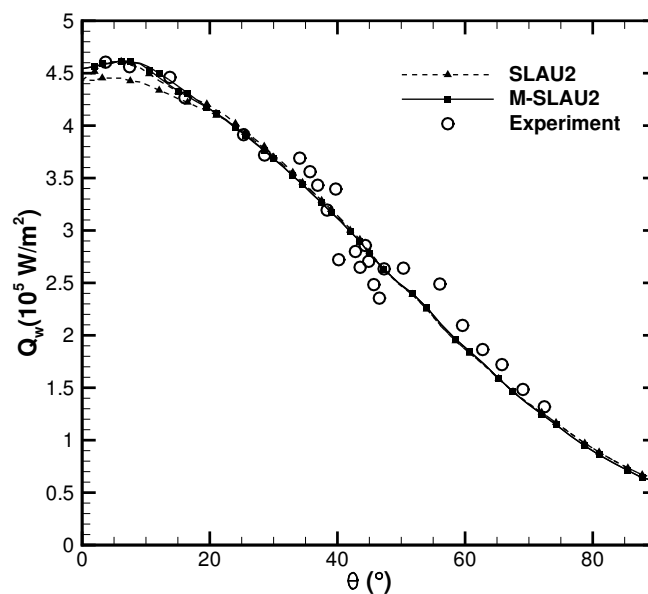
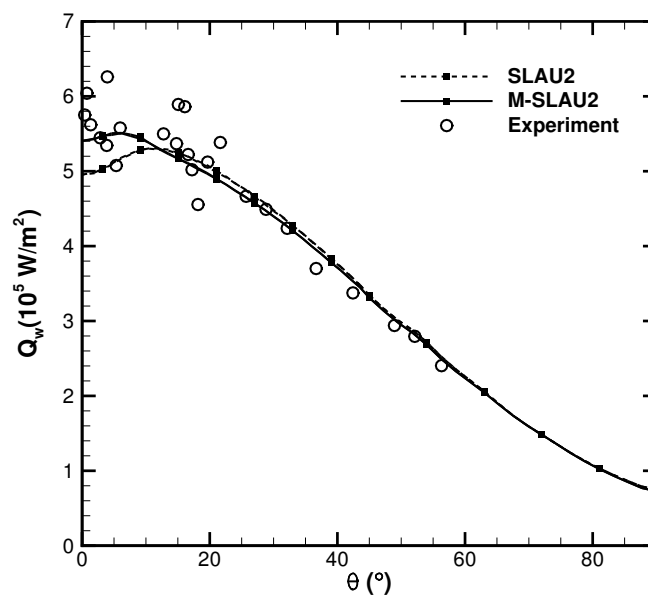
(a)  $M_\infty = 8.0$ (b)  $M_\infty = 16.34$ 

Figure 7.2: Heat flux prediction using SLAU2 and M-SLAU2 for two Mach numbers. The heat flux at the surface of wall is plotted over the whole half cylinder. We have, however, shown the variation at the top and bottom of the cylinder together in order to observe the presence of asymmetry, if present.

for the proper capture of the shock. But as noted by Kitamura et al. (see Fig. 11 of [12]) SLAU2 still showed a “wavy” pattern in the heating profile. We also observed in the hypersonic flow over a cylinder<sup>1</sup> (see Figure 7.1) discussed above, asymmetry and lack of accuracy in the heating prediction for the case of Mach number of 8.0 and 16.34 in comparison with the experimental results of Holden [177], as can be seen from the Figure 7.2. Kitamura et al. [12] have discussed the effect of various definitions of the interfacial speed of sound ( $c_{1/2}$ ) given in the literature for the accurate capturing of the normal shocks. They finally used the expression involving arithmetic average, Eq. 2.41, which we rewrite here again as Eq. 7.1:

$$c_{1/2} = \frac{c_L + c_R}{2} \quad (7.1)$$

Another definition of  $c_{1/2}$  which they had found to be robust for accurate capturing of normal shocks (in the 1D and 1.5D steady normal shock tests [12, 78]) was the one used by AUSM<sup>+</sup>-up scheme [178], given by Eq. 7.2:

$$c_{1/2} = \min(\tilde{c}_L, \tilde{c}_R), \quad \tilde{c}_{L/R} = \frac{c^{*2}}{\max(c^*, |V_n^\pm|)}, \quad c^{*2} = \frac{2(\gamma - 1)}{(\gamma + 1)} H \quad (7.2)$$

However, this too gives the same issues of inaccurate heat flux prediction. We have modified the definition of  $c_{1/2}$  given by Eq. 7.2 in the following manner:

$$c_{1/2} = \max(\tilde{c}_L, \tilde{c}_R), \quad \tilde{c}_{L/R} = \frac{c^{*2}}{\min(c^*, |V_n^\pm|)}, \quad c^{*2} = \frac{2(\gamma - 1)}{(\gamma + 1)} H \quad (7.3)$$

Using Eq. 7.3 for  $c_{1/2}$  with the SLAU2 scheme explained in Sec. 2.3.1.3, which we will now on refer to as the modified SLAU2 (M-SLAU2), we obtain a more accurate and symmetric heating profile for the case of hypersonic flow over a cylinder. The complete formulation of M-SLAU2 is also summarized in Appendix A. Figure 7.2 shows the heat flux prediction for the case of hypersonic flow over cylinder using SLAU2 and M-SLAU2 for  $Ma_\infty = 8.0$  and  $Ma_\infty = 16.34$ . It can be seen that for  $Ma_\infty = 8.0$  (Fig. 7.2(a)), while SLAU2 has shown an asymmetry in the shock prediction at the nose of the cylinder, it is nearly absent for M-SLAU2. For  $Ma_\infty = 16.34$  (Fig. 7.2(b)), SLAU2 has shown under-prediction in heating at the nose of the cylinder while M-SLAU2 has shown a more accurate prediction in comparison with the experimental data [177]. A reason for this is the Eq. 7.3 yields a larger value of

<sup>1</sup>The case is described in detail in the result and discussion section, Sec. 7.5.

$c_{1/2}$ , and thus adds a larger amount of dissipation for capturing the shock, through the RHS third term of Eq. 2.40. However, the M-SLAU2 still captures the boundary layer accurately (see Fig. A.2), which is generally a problem for the more dissipative convective schemes, like HLLE [179] as shown in the references (see Fig. 8 of [12]). In Appendix A, we have shown that with the present modification the results are same for the subsonic and transonic flows as obtained using the original SLAU2 scheme. In order to avoid the code from “blowing up” for the case of low Mach numbers, where the contravariant velocity ( $V_n$ ) may go to zero, in Eq. 7.3 we add a small term ( $= 10^{-30}$ ) in the denominator of the expression  $\tilde{c}_{L/R} = \frac{c^{*2}}{\min(c^*, |V_n^\pm|)}$ .

## 7.5 Results and Discussion

We perform the aeroheating computation using the 2D cylinder case considered by Holden et al. [177] for their experimental study. Figure 7.1 shows the flow domain and the mesh used for the computation. The cylinder radius is taken as 38.1 mm. At the inlet, the freestream Mach number, pressure, temperature and Reynolds number per unit length are taken as 8.0, 855 Pa, 125.07 K and  $4.72 \times 10^6$  to match the experiment inflow data. The wall temperature is taken as 294 K. A hexahedral mesh is used for the computation with 10000 cells. The grid is clustered near the wall where the shock occurs, with 76 nodes in the normal distance of 22 mm from the cylinder surface. The stretching factor is taken as 1.2 near the wall in the direction normal to it.

In all the computation done here, the flow variables such as heat flux at the wall are plotted over the whole half cylinder. We have, however, shown the variation at the top and bottom of the cylinder together in order to observe the presence of asymmetry, if present.

### 7.5.1 Grid Sensitivity study

A grid sensitivity study is done using four different grids (with previously described input mesh) with different first grid spacing, which is an important determinant of accuracy for hypersonic flow computations in the continuum regime. The objective is to observe how the Roe and M-SLAU2 scheme behaves and to see if we can obtain the grid which gives results free from shock instability and shock oscillations. The first grid spacing is taken as 1)  $1 \times 10^{-5}$  m, 2)  $1 \times 10^{-6}$  m, 3)  $5 \times 10^{-7}$  m and 4)  $2 \times 10^{-7}$  m, respectively. Grid spacing considered in grids 1,2 and 4 are the same as

taken by Gao et al. [77]. Figure 7.3 shows the wall heat flux computed using the Roe and M-SLAU2 scheme. We observe that the Roe scheme gives a solution which is asymmetric and inaccurate for all the four grids, with the fourth grid being most close to the experimental data. The M-SLAU2 scheme for the grid spacing of  $2 \times 10^{-7}$  m gives a solution which is symmetric over the cylinder and has the least solution oscillations. Xiang et al. [180] have suggested the use of a grid Reynolds number<sup>2</sup> of less than 10 in the heat flux simulation. The spacing of  $2 \times 10^{-7}$  m gives a grid Reynolds number of 1 for the case considered with  $M_\infty = 8.0$ . We have taken the grid with the first grid spacing of  $2 \times 10^{-7}$  m for all the cases in this work. For all the cases considered below the grid Reynolds number has always been  $\leq 1$ .

Here, the superiority of the M-SLAU2 scheme is shown based on the use of current input parameters. We further analyze on the 4th grid how with the rarefaction, two scheme behaves. We check the similarity in the obtained solution from both the schemes. The shock capturing capability without shock instabilities and oscillations is analyzed, and the numerical behavior at a different Mach number is studied for both the scheme.

## 7.5.2 Effect of Rarefaction

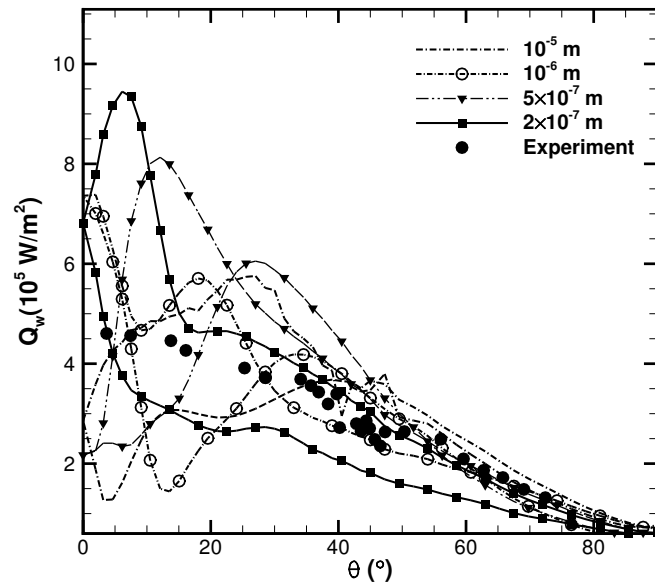
In this section, we carry out a parametric study wherein we vary the pressure which in turn changes the Knudsen number. Thus, we carry out the various simulations at different  $Kn$ . Also, we carry out the study at two different Mach numbers 8 and 16.34. The different cases considered are listed in Table 7.1. For case A1 and B1 the heat flux results are compared with the experimental results [177]. The cases A5 and B4 have  $Kn > 0.1$  where the CFD computation with the slip boundary condition is known to be inaccurate but are included to observe, at least qualitatively, the results at such high  $Kn$  [81]. We have included a separate study as Appendix B wherein we study case B using the Le temperature jump, Eq. 5.8 and the pressure jump condition, Eq. 5.12.

### 7.5.2.1 Heat Flux

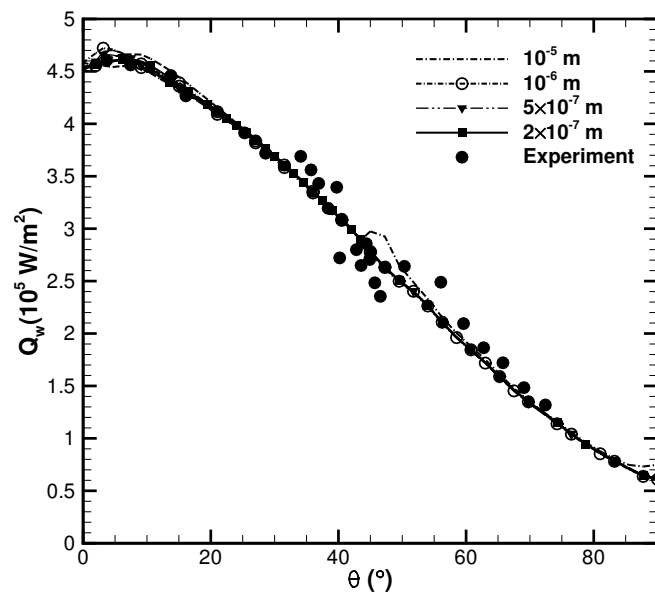
Figure 7.4 and 7.5 show the heat flux value plotted over the wall using the Roe and M-SLAU2 schemes for Mach numbers of 8 (case A) and 16.34 (case B), respectively.

---

<sup>2</sup> $Re_{cell} = \frac{\rho_\infty V_\infty \Delta l}{\mu_\infty}$



(a) Roe



(b) M-SLAU2

Figure 7.3: Grid independence study using four meshes with different first grid point spacing.



Table 7.1: Different cases considered for the parametric study.

Cases	$M_\infty$	$T_\infty$ (K)	$T_w$ (K)	$P_\infty$ (Pa)	$\lambda_\infty$ (m)	$Kn$
1				801.5	$2.51 \times 10^{-6}$	$6.60 \times 10^{-5}$
2				80.15	$2.51 \times 10^{-5}$	$6.60 \times 10^{-4}$
A 3	8	125.07	294	8.015	$2.51 \times 10^{-4}$	$6.60 \times 10^{-3}$
4				0.8015	$2.51 \times 10^{-3}$	$6.60 \times 10^{-2}$
5				0.08015	$2.51 \times 10^{-2}$	$6.60 \times 10^{-1}$
1				82	$6.15 \times 10^{-6}$	$1.62 \times 10^{-4}$
B 2	16.34	52	294.4	8.2	$6.13 \times 10^{-5}$	$1.61 \times 10^{-3}$
3				0.82	$6.13 \times 10^{-4}$	$1.61 \times 10^{-2}$
4				0.082	$6.13 \times 10^{-3}$	$1.61 \times 10^{-1}$

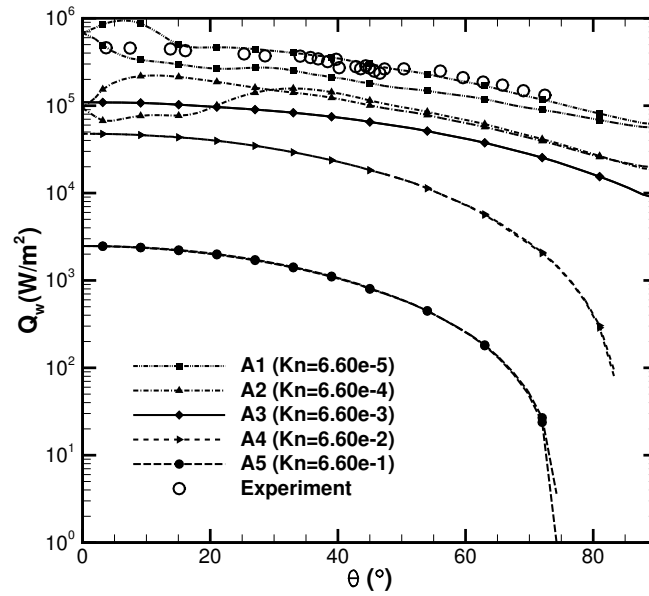
We observe that the heat flux value decreases with the increase in Knudsen number due to an increase in the degree of rarefaction. However, while the M-SLAU2 scheme shows a symmetric and no oscillatory behavior, the Roe scheme, especially at the nose of the cylinder, shows asymmetry and oscillations in the heat flux prediction for the case A1,  $Kn = 6.16E-5$  and A2,  $Kn = 6.16E-4$  (see Fig. 7.4(a)) and for the case B1  $Kn = 1.59E-4$  (see Fig. 7.5(a)). By asymmetry, it means that the solution over the cylinder should have symmetry, and the plot over the up and down wall should be symmetric. It is observed from both the cases that for free-stream  $Kn$  of the order  $10^{-3}$  and higher, both the Roe and M-SLAU2 scheme shows a stable and symmetric heat flux prediction. This Knudsen number belongs to the non-continuum regime ( $Kn > 10^{-3}$ ). In this regime, both M-SLAU2 and Roe scheme gave the same solution. However, at lower  $Kn$  they behave differently.

For the case A1 and B1 the results are also compared with the experimental data [177]. It can be seen that at both the Mach numbers, M-SLAU2 give an accurate match, while due to the shock instabilities and oscillations the Roe scheme fails to give a good match, especially, at the nose of the cylinder. It is to be noted that, at the higher Mach number (case A) the predicted heat flux is higher compared to the case of lower Mach number (case B) for all the Knudsen numbers.

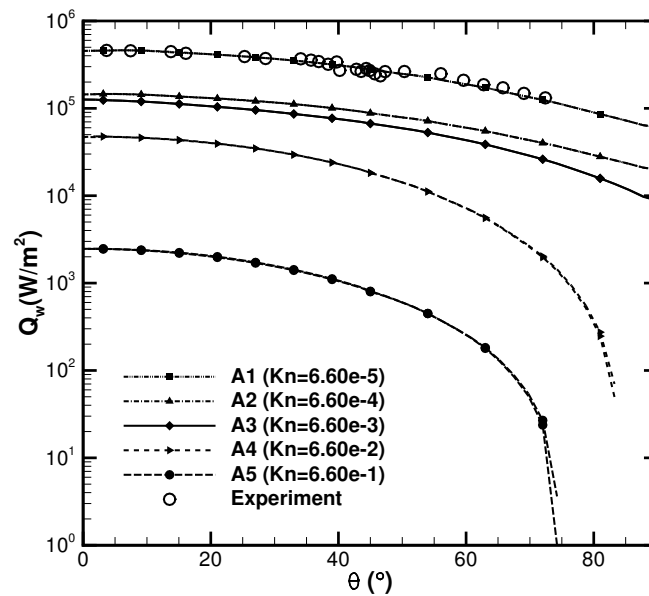
With the increase in  $Kn$ , the heat flux value decreases except where the shock instabilities are higher (see Fig. 7.4(a)). In both case A and B, we observe that the decrease in heat flux prediction with rarefaction is less from case 2 to 3, but it is large from case 3 to 4. Thus, the heat flux decreases faster with increasing order of  $Kn$ . In the case of the higher Mach number (case B), from case B2 to B3 the decrease is almost negligible for angle  $\lesssim 60^\circ$ . The reason being the shock is clearly detached and thin for angle  $\lesssim 60^\circ$  for the case B3 (see Fig. 7.9, Sec. 7.5.2.3). However, for the case, B3 for angle  $\gtrsim 60^\circ$ , the shock thickness begins to increase, and the shock tends to diffuse and stick to the surface. Thus there is a decrease in the heat flux value when compared to B2.

### 7.5.2.2 Wall Shear Stress

Figure 7.6 and 7.7 show the wall shear stress plot over the cylinder surface using the Roe and M-SLAU2 schemes, for the case A and B respectively. It is observed again that asymmetry and oscillations are found at  $Kn < 10^{-3}$  in the predicted solution when using the Roe scheme. However, M-SLAU2 gives a smooth prediction for all

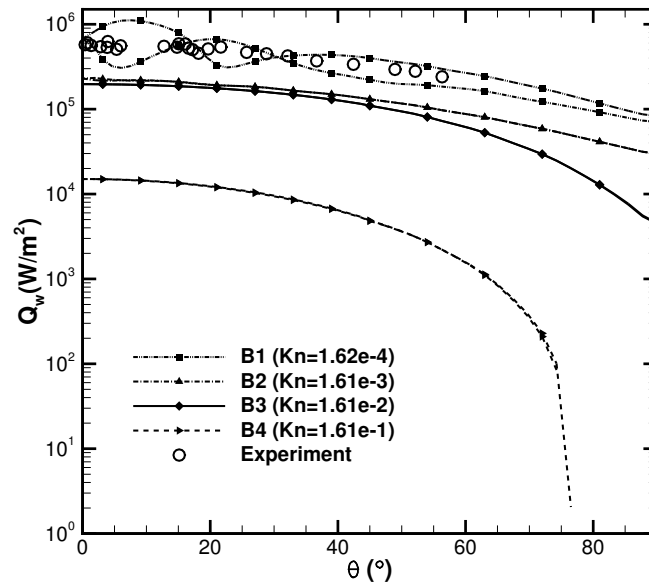


(a) Roe

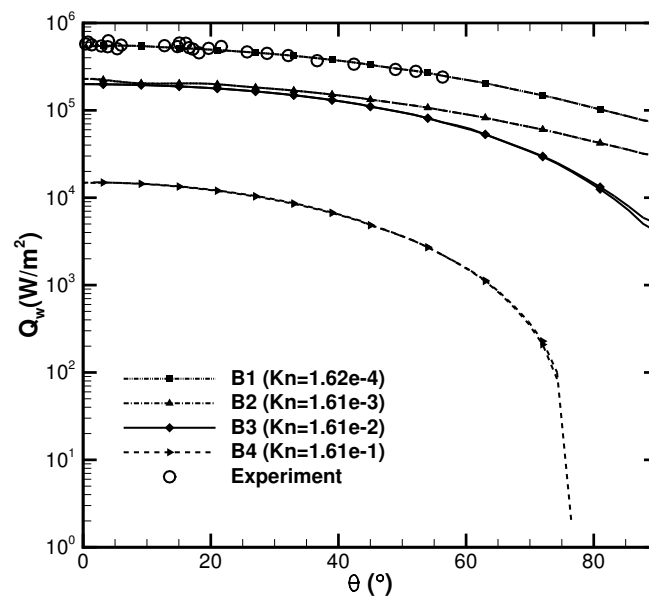


(b) M-SLAU2

Figure 7.4: Heat flux prediction at different Knudsen number for the case A ( $M_\infty = 8.0$ ).



(a) Roe



(b) M-SLAU2

Figure 7.5: Heat flux prediction at different Knudsen number for the case B ( $M_\infty = 16.34$ ).

the  $Kn$ . For  $M_\infty = 8.0$ , the overall wall shear stress predicted is higher for low  $Kn$ . Due to the increase in rarefaction (increasing  $Kn$ ), the magnitude of the wall shear stress over the cylinder reduces. For  $Kn > 10^{-3}$ , both Roe and M-SLAU2 give the same result.

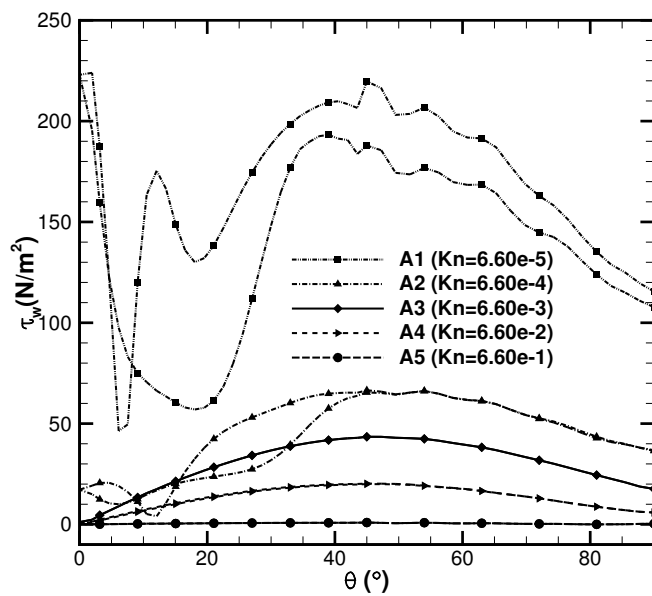
For the case B2 (lower  $Kn$ , thus less rarefaction), the predicted wall shear stress shows a higher value for  $\tau_w$  for angle  $\lesssim 60^\circ$  and a lower value for angle  $\gtrsim 60^\circ$ , when compared with the case B3 (higher  $Kn$ , thus more rarefaction). However, from B3 to B4, there is an overall and significant decrease in wall shear stress, due to increased rarefaction.

### 7.5.2.3 Contours of Mach number

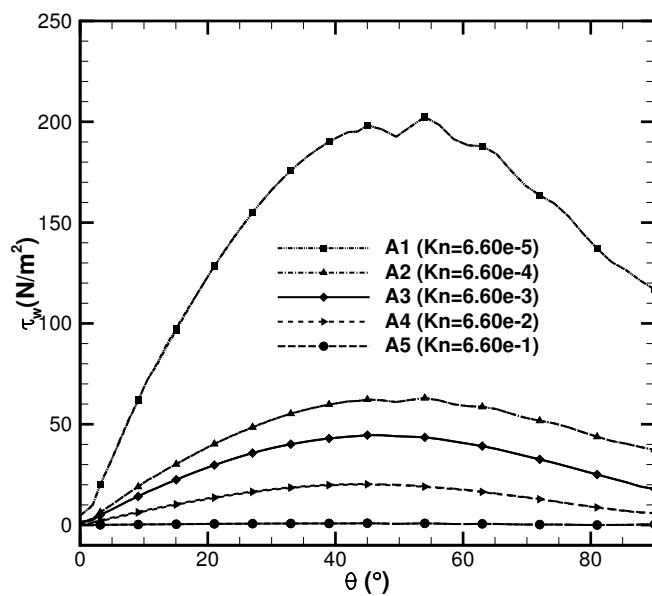
Figure 7.8 and 7.9 show the Mach number contour, using Roe and M-SLAU2 scheme, for the case A ( $M_\infty = 8.0$ ) and B ( $M_\infty = 16.34$ ), respectively. It can be seen that with the increase in rarefaction, i.e.  $Kn$ , the shock standoff distance reduces and the shock becomes attached to the surface of the cylinder. It is also noteworthy that the width of the shock increases with rarefaction. In the case A1 and A2 the shock is clearly detached and thin. However, in A3, at the nose region, the shock is detached, but the shock begins to diffuse away from the nose, finally getting attached to the surface. A similar pattern is observed in the case B, with B4 showing three phenomena – the shock is detached at the nose, the shock width tends to increase away from the nose, and the shock then gets attached to the surface. Thus, it is observed that with increasing  $Kn$  the shock becomes attached to the surface of the cylinder – to the degree that for the case A5 and B4, the shock almost diffuses completely at an angle of  $90^\circ$ .

The shock thickness in the case B for higher  $Kn$  is thinner as compared to case A. The hypersonic solution in these cases depends not only on the Knudsen number but also on the Mach number. With the increasing  $Kn$ , the shock will become more diffuse (thick) while with larger Mach number the shock becomes thin. For the same reason, we found that there is a non-uniform effect of increasing  $Kn$  on wall heat flux (Sec. 7.5.2.1) and wall shear stress (Sec. 7.5.2.2) for the case A and B.

For  $Kn \gtrsim 10^{-3}$  (A3, A4, A5, B2, B3 and B4), both Roe and M-SLAU2 scheme gives a smooth and same Mach number contours. However, for  $Kn \lesssim 10^{-3}$  (A1, A2 and B1), the Roe scheme shows shock instability and shock oscillations, especially near the nose. The M-SLAU2 scheme, for both cases A and B, for all  $Kn$  is free from

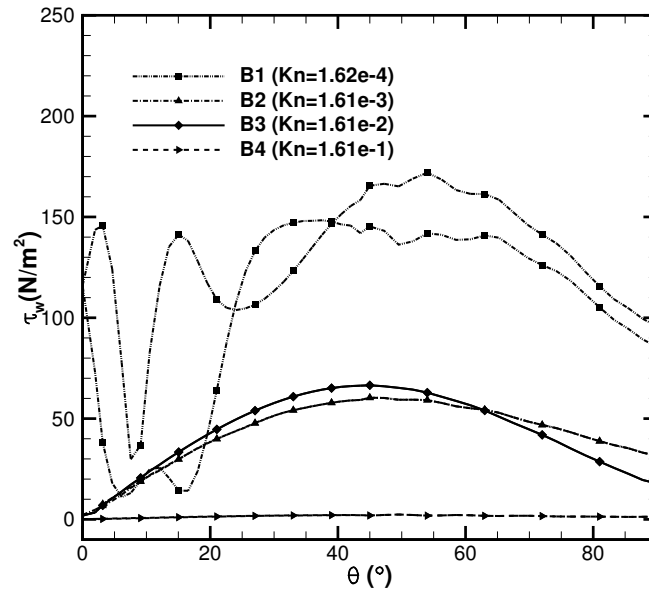


(a) Roe

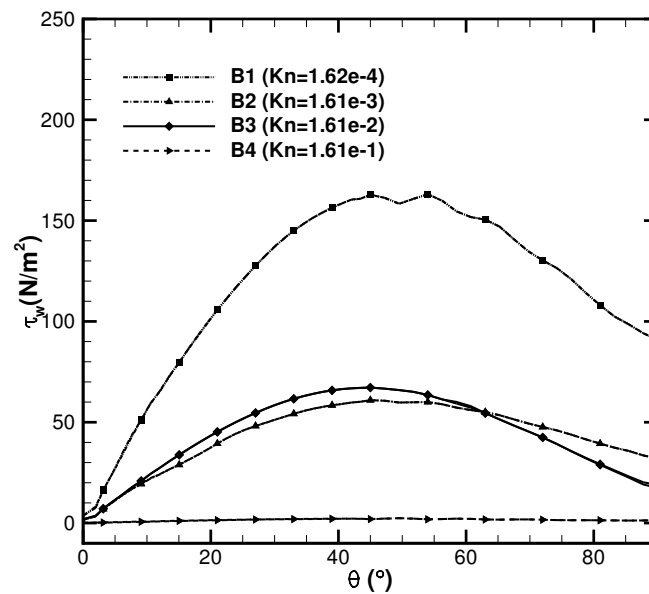


(b) M-SLAU2

Figure 7.6: Wall Shear stress prediction at different Knudsen number for the case A ( $M_\infty = 8.0$ ).



(a) Roe



(b) M-SLAU2

Figure 7.7: Wall Shear stress prediction at different Knudsen number for the case B ( $M_\infty = 16.34$ ).

shock instability and oscillations.

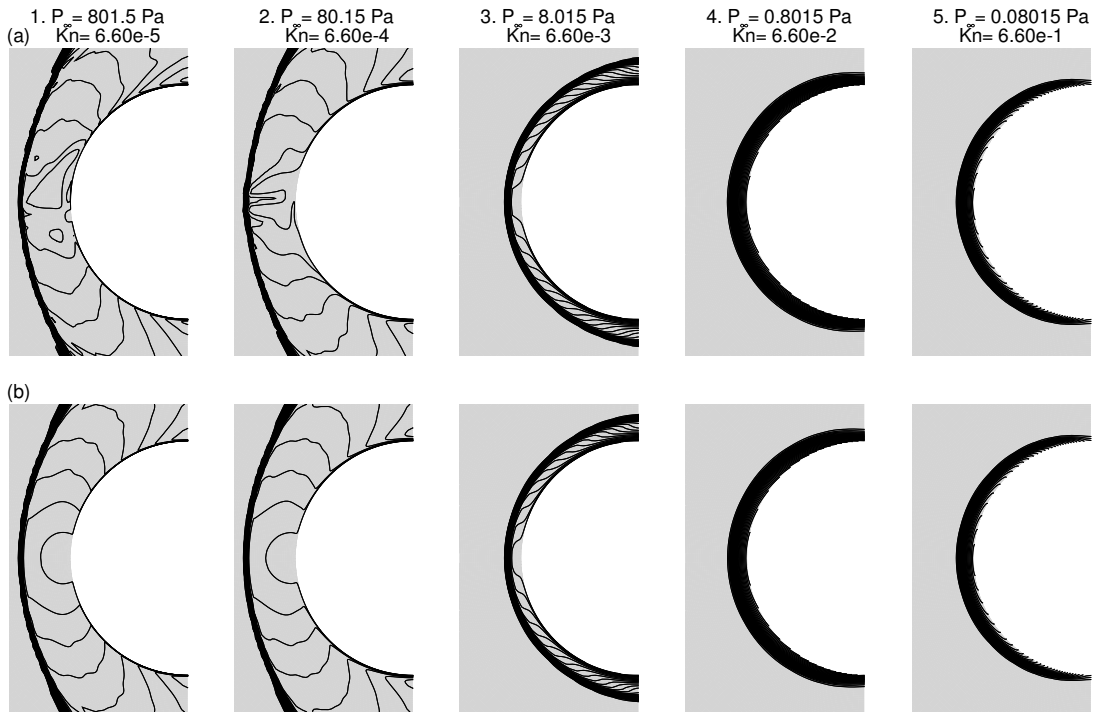


Figure 7.8: Mach number line contour using (a) Roe and (b) M-SLAU2 scheme at different Knudsen number for the case A ( $M_\infty = 8.0$ ).

#### 7.5.2.4 Peak Heating on the Surface of the Cylinder

Table 7.2 shows the peak heating value on the surface of the cylinder computed using the Roe and M-SLAU2 schemes for the cases A and B. For the cases A1 and B1 the results are also compared with the available experimental results. For the case A, the peak heating value computed using the Roe scheme is over-predicted by 105.34%, while for the M-SLAU2 scheme it is over-predicted only by 0.52%. For the case, B, the peak heating value is over-predicted by 77.99% with the Roe scheme and under-predicted by 11.8% by M-SLAU2. In both cases, M-SLAU2 gave a closer match with respect to the experimental data. The larger error with the Roe scheme is due to the generation of shock instabilities at the nose as seen from Figures 7.4(a), 7.5(a), 7.8(a) and 7.9(a). It is noted with the increase in  $Kn$ ; the peak heating value decreases due to the increase in rarefaction. Rarefaction effects decrease the amount of collision of the gas molecules with the surface, which thus reduces the amount of surface heating by the molecular collisions.



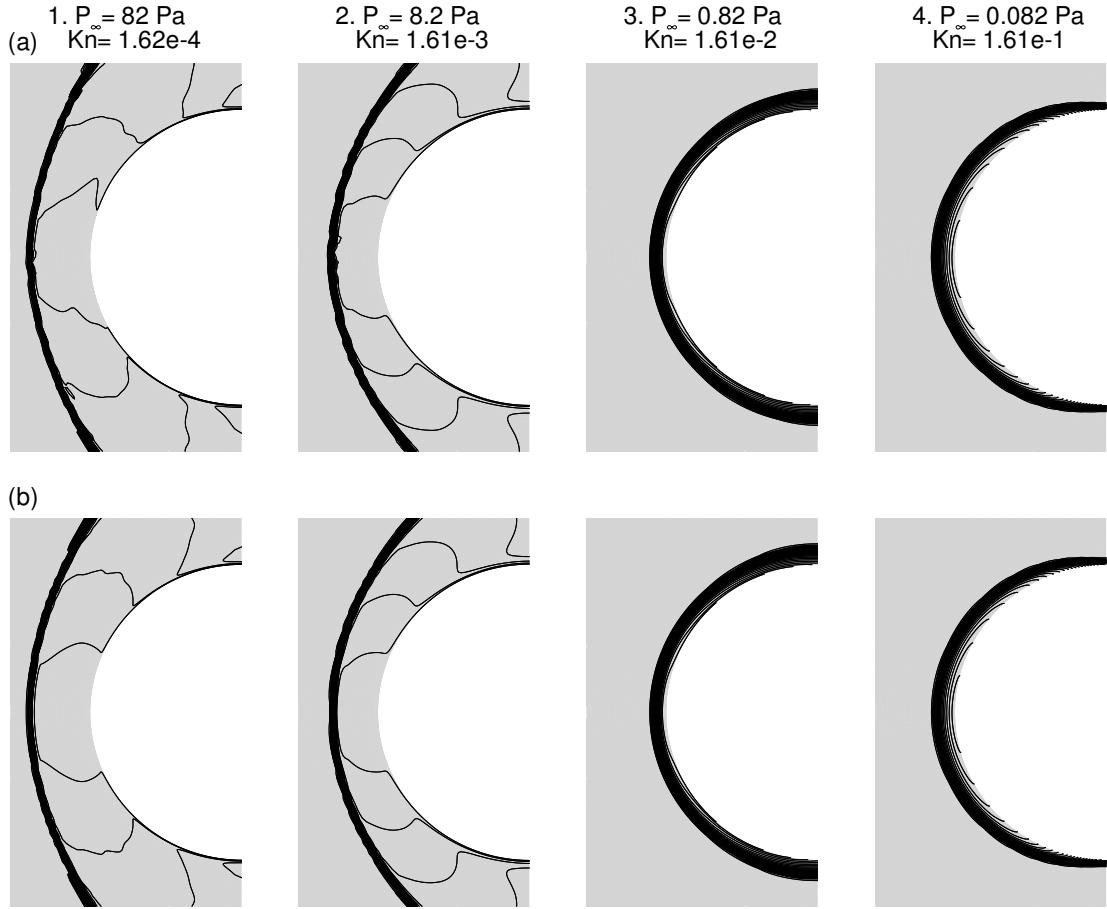


Figure 7.9: Mach number line contour using (a) Roe and (b) M-SLAU2 scheme at different Knudsen number for the case B ( $M_\infty = 16.34$ ).

Table 7.2: Peak heating computed using various cases considered. A1 and B1 experimental results [177] is also tabulated.

Case		Heat Flux ( $10^5$ W/m $^2$ )	
		Roe	M-SLAU2
A	1 (4.60e5 [177])	9.44643	4.62406
	2	2.21533	1.46182
	3	1.09442	1.2600
	4	0.47697	0.47696
	5	0.02475	0.02473
B	1 (6.26e5 [177])	11.142	5.51256
	2	2.33321	2.29541
	3	1.97081	1.99649
	4	0.15010	0.15004

It is to be noted again that at higher  $Kn$  both Roe and M-SLAU2 scheme perform almost identically.

## 7.6 Closure

In this chapter, we have proposed a modification to the SLAU2 convective scheme and have shown this to be more accurate in capturing strong shocks for the case of hypersonic flow over the cylinder. We have then further compared the solutions for viscous hypersonic flow over a cylinder using the M-SLAU2 and Roe schemes. A parametric study is carried out of the effect of rarefaction on various flow properties at the two different Mach numbers of 8.0 and 16.34. The following conclusions are drawn from this work:

1. Modified SLAU2 has given a better prediction of shock strength just by altering the interfacial speed of sound to add more dissipation as compared to the original SLAU2 scheme. And it also does not degrade the prediction at the subsonic or transonic regime. It captures the boundary-layer as well as the original SLAU2 scheme, which is generally a problem for highly dissipative convective schemes. Also, in future we hope the modification suggested here will be applied to other AUSM schemes, to test how they behave with it against shock anomalies.
2. Solutions of hypersonic flow over a cylinder are grid-sensitive.
3. The M-SLAU2 scheme provides a smooth solution free from shock instabilities and shock oscillations.
4. In the continuum regime, the shock is thin which is captured adequately by the M-SLAU2 scheme, but the Roe scheme fails to do so. However, with the increase of rarefaction ( $Kn$  of the order of  $10^{-3}$  and higher), the shock becomes diffusive and is captured adequately by both the schemes without shock instability and oscillations. This shows M-SLAU2 to yield solutions free from shock anomalies in both the continuum and rarefied regimes.
5. Mach number contours show that at high Mach number the captured shock is thinner at all  $Kn$ . It is demonstrated that the hypersonic solution does not only

depend on the  $Kn$  but also on the Mach number. The observed decrease in wall heat flux and wall shear stress with the increase in rarefaction is non-uniform.

6. That the non-equilibrium boundary conditions at the wall automatically tend to the no-slip conditions in the continuum regimes is also demonstrated. The results of the M-SLAU2 scheme for the wall heat flux (see Fig. 7.4(b) and 7.5(b)) for the case A1 and B1 are in good agreement with the available experimental results.
7. The results show M-SLAU2 to be a more robust and general convective scheme for hypersonic flows in the continuum and rarefied regimes.



# Chapter 8

## Conclusions and Future Work

### 8.1 Conclusions

A general purpose density based CFD solver for the applications of external aerodynamics and micro/nano flows has been developed and used to carry out the studies attempted in this thesis. The solver capability to handle all-speed flows has been demonstrated. Various configurations of flows with complex geometry and boundary conditions have been investigated. The solver uses a cell-centred finite volume discretization method for unstructured grids. Several convective schemes have been incorporated into the solver, such as Roe, preconditioned Roe and SLAU2. Preconditioning done using Roe method helps to have an all-speed density-based algorithm. An alternative to this is to use the SLAU2 scheme which provides an all-speed framework without the use of preconditioning. Further, various turbulence models have been incorporated into the solver following an unconditional positive convergent implicit time integration procedure.

The near wall modeling for wall-bounded turbulent flows has been a challenge for the researchers. In this work an automatic wall treatment for the one-equation Spalart-Allmaras turbulence model, a low-Reynolds-number model, has been proposed. This treatment allows an automatic switch between a low-Re formulation and the wall function approach. The wall-treatment has been validated and verified through four different cases involving adiabatic and constant temperature wall boundary conditions. The test cases considered have been computed on different grids with the first grid point variously located in the sublayer layer region, in the buffer region, and in the log region and have always yielded near-identical results that have also matched well with benchmark reference and experimental data. The case of the

NACA0012 airfoil which is close to real-world simulations had  $y^+$  value going well beyond the traditionally accepted values to be as high as 150. However, even here, the results were good. This would help the researchers who use turbulence models to compute complex flows in aerospace applications, as the AWT allows a near-wall grid 10-30 times as coarse as that required in the standard SA model (without wall function). Apart from this, the flexibility accruing from the freedom of not having to place the first-grid point in a narrow range of  $y^+$  (which cannot be predicted a priori during grid generation) will be very helpful to practitioners, who otherwise routinely re-grid after computations to satisfy the earlier criteria. Finally, from the point of view of turbulence research, which can be so piece-meal at times, it provides an interesting outcome wherein a model developed for SST works without modification for a completely different model like SA.

Further, the techniques required to solve the rarefied gas flow in the slip regime has been incorporated into the solver. Various non-equilibrium boundary conditions which replace the no-slip boundary conditions have been studied. A comprehensive analysis of the recently proposed Le temperature jump condition, which takes into account the sliding friction has been performed using three cases of hypersonic flow over a flat plate, and the results were compared with experiments and DSMC, wherever available. An over-prediction of pressure in comparison with both the experiment and DSMC results has been observed when using the Le temperature jump condition above. The additional use of pressure jump condition, which has been largely ignored in the literature, has been suggested as a possible remedy in this thesis. Further, an investigation has been carried out for the use of these boundary conditions for various cases of nano/micro flows. Therein it has been shown that the effect of the sliding friction component on the improvement of the thermodynamic prediction is case-dependent. It depends on the mean-free-path of the gas, shear stress and the velocity of the flow. A need to incorporate other non-equilibrium effects such as vibrational and chemical non-equilibrium in the CFD modeling to properly capture the non-continuum phenomena is apparent. Also, in the context of the Le temperature jump condition, we may need to reconsider the sliding friction concept in the light of more fundamental considerations of gas-wall gas interactions. Lastly, the effect of rarefaction in hypersonic computation using the Roe and modified SLAU2 scheme has been studied using the case of hypersonic flow over a cylinder. The modified SLAU2 scheme, which is proposed in this thesis, has been shown to be superior in comparison

with the original SLAU2 scheme for accuracy and imperviousness to shock anomalies. An effort is made to better understand the behaviour of shock instabilities and oscillations with the degree of rarefaction. It has been shown that the solutions of hypersonic flow are grid-sensitive. The M-SLAU2 scheme provided a smooth solution free from shock instabilities and oscillations for all  $Kn$ . The shock structure in front of the cylinder has also been studied. It has also been demonstrated that the hypersonic solution does not only depend on the  $Kn$  but also on the Mach number. In the overall sense, the results have shown M-SLAU2 scheme to be a robust and useful convective scheme for hypersonic flows in the continuum and rarefied regimes.

## 8.2 Scope for Future Work

The conclusions drawn from the present work can help to extend the applicability of the different methodologies presented for external aerothermodynamics and nano/micro flows. Some recommendations for future investigations are mentioned below:

- (a) The scope of future work in an all-speed unstructured grid density-based grid is enormous. The density-based algorithm is suited for compressible flow computations. Different modules such as combustion, multiphase can be implemented in the main code. The present work has been limited to ideal gases only. Real gas models need to be incorporated in the code.
- (b) From the computing viewpoint, many aspects can be looked upon now as the base solver is ready. Code parallelization using GPU [181], OpenMP, Intel Xeon Phi architecture can be attempted [182]. The advanced techniques of overset mesh [183] for simulating moving objects, adaptive mesh [184] refining to improve the accuracy of shock capturing, can also be done.
- (c) More compressible turbulent cases have to be simulated. The wall function at present is based on the incompressible law of wall, which can be extended to include the compressible law of wall [84]. With these, the code can be used to explore the wide area of shock-boundary layer interaction [185].
- (d) The automatic wall treatment presented in this work can be extended to newer turbulence models, like the one-equation Wray-Agarwal model [186]. A clear advantage of this model is that its recent version [187] is wall-distance free.

- (e) For the rarefied regime flows, in this thesis we have only considered thermal non-equilibrium. However, at the higher temperatures which occur in hypersonic gas flows, chemical and vibrational non-equilibrium [188, 189, 190] and ablation [191] also have to be taken into account. The suitable models for these need to be incorporated.
- (f) The non-equilibrium boundary conditions used in this work show limitations and case-dependent behavior. They need to be reconsidered from the viewpoint of more fundamental gas-wall gas interactions [192].
- (g) In the last chapter of this thesis, we have observed the challenges involved in the computation of hypersonic flows in the continuum regime and have shown M-SLAU2 convective scheme to be a possible solution. More blunt body test cases with different grid-orientations have to be tested. [193, 84]. Also, an effort can be made to improve the other convective schemes such as Roe and preconditioned Roe for hypersonic gas flows.
- (h) This thesis can be further extended into the field of hypersonic flow by including more test cases. Also, comparison can be made of the proposed M-SLAU2 scheme with the other new schemes in the literature, like Toro-Vazquez method (TVM) [194].



# Appendix A

## Modified SLAU2: Validation & Verification

### A.1 Formulation of M-SLAU2

The complete formulation of modified SLAU2 flux proposed in Sec. 7.4 is shown below:

$$\mathbf{F}_{1/2} = \frac{\dot{m} + |\dot{m}|}{2} \boldsymbol{\Psi}^+ + \frac{\dot{m} - |\dot{m}|}{2} \boldsymbol{\Psi}^- + \tilde{p} \mathbf{N} \quad (\text{A.1})$$

where,

$$\boldsymbol{\Psi} = (1, u, v, w, H)^T \quad (\text{A.2})$$

$$\mathbf{N} = (0, n_x, n_y, n_z, 0)^T \quad (\text{A.3})$$

The mass flux is written as:

$$\dot{m} = \frac{1}{2} \left\{ \rho_L (V_{nL} + |\bar{V}_n|^+) + \rho_R (V_{nR} - |V_n|^-) - \frac{\chi}{c_{1/2}} \Delta p \right\} \quad (\text{A.4})$$

where,

$$|\bar{V}_n| = \frac{\rho_L |V_{nL}| + \rho_R |V_{nR}|}{\rho_L + \rho_R} \quad (\text{A.5})$$

where,

$$|\bar{V}_n|^+ = (1 - g) |\bar{V}_n| + g |V_{nL}|$$

$$|\bar{V}_n|^- = (1 - g) |\bar{V}_n| + g |V_{nR}|$$

$$g = -\max[\min(M_L, 0), -1] \cdot \min[\max(M_R, 0), 1] \quad \in [0, 1]$$

The pressure flux is written as:

$$\begin{aligned} \tilde{p} = & \frac{p_L + p_R}{2} + \frac{f_{pL}^+ - f_{pR}^-}{2}(p_L - p_R) \\ & + \sqrt{\frac{u_L^2 + v_L^2 + w_L^2 + u_R^2 + v_R^2 + w_R^2}{2}}(f_{pL}^+ + f_{pR}^- - 1) \frac{\rho_L + \rho_R}{2} c_{1/2} \end{aligned} \quad (\text{A.6})$$

where, the **new** interfacial speed of sound, for the M-SLAU2 scheme, is given as:

$$c_{1/2} = \max(\tilde{c}_L, \tilde{c}_R), \quad \tilde{c}_{L/R} = \frac{c^{*2}}{\min(c^*, |V_n^\pm|) + \epsilon_s}, \quad c^{*2} = \frac{2(\gamma - 1)}{(\gamma + 1)} H \quad (\text{A.7})$$

where  $\epsilon_s$  is a small term taken as  $10^{-30}$  in order to avoid the denominator from taking on zero values. The other terms are defined as:

$$\chi = (1 - \hat{M})^2 \quad (\text{A.8})$$

$$\hat{M} = \min\left(1.0, \frac{1}{c_{1/2}} \sqrt{\frac{u_L^2 + v_L^2 + w_L^2 + u_R^2 + v_R^2 + w_R^2}{2}}\right) \quad (\text{A.9})$$

$$f_p^\pm = \begin{cases} \frac{1}{2}(1 \pm \text{sign}(M)), & \text{if } |M| \geq 1 \\ \frac{1}{4}(M \pm 1)^2(2 \mp M), & \text{otherwise} \end{cases} \quad (\text{A.10})$$

$$M = \frac{V_n}{c_{1/2}} = \frac{un_x + vn_y + wn_z}{c_{1/2}} \quad (\text{A.11})$$

## A.2 Validation & Verification

In this part, we will show that the M-SLAU2 does not change the results with respect to the original SLAU2, at low Mach numbers - subsonic and transonic, using two cases: (i) laminar flow over a flat plate at  $Ma_\infty = 0.2$  and (ii) transonic flow over an inviscid airfoil.

### A.2.1 Laminar flow over a flat plate ( $Ma_\infty = 0.2$ )

We consider the case of laminar flow over a flat plate with inlet  $Ma_\infty = 0.2$ . The flow domain with the mesh and boundary conditions used is shown in Fig. A.1. The flat plate starts at  $x = 0$  m and  $y = 0$  m and is of length 0.3048 m. It is given a no-slip condition. The free-stream pressure and temperature used are 97250 Pa and 297.619 K, respectively. Figure A.2 shows the comparison of computed velocity profile at  $x = 0.25$  m (corresponding to  $Re_x = 1.059 \times 10^6$ ), using SLAU2 and M-SLAU2 with the Blasius solution [89]. M-SLAU2 has the same result as obtained using SLAU2. Both matches completely with the Blasius analytical velocity profile for Mach 0.2. This test case shows that the modified SLAU2 preserved the property of original scheme to be applicable for low speed flows by allowing low dissipation at low speeds.

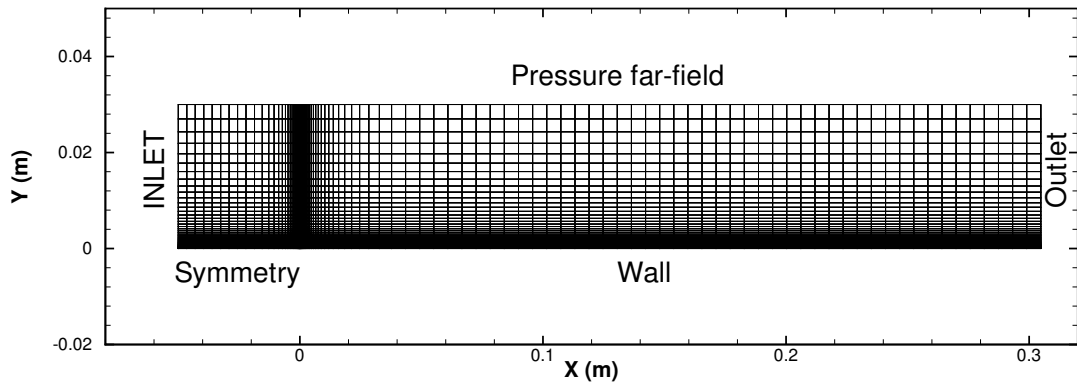


Figure A.1: Flow domain for the case of laminar flow over flat plate.

### A.2.2 Inviscid flow over airfoil with transonic free-stream condition ( $Ma_\infty = 0.8$ )

The next case considered is transonic inviscid flow over a NACA0012 airfoil with an angle of attack of  $1.25^\circ$ . The inlet Mach Number of 0.8 at 101325 Pa pressure and 273.15 K temperature is considered. The flow domain with the computational mesh and boundary condition is shown in Fig. A.3.

Figure A.4 shows the computed surface pressure coefficient,  $C_p$  at the wall of the airfoil using the SLAU2 and M-SLAU2 schemes. The results are verified with the those obtained by Arias et al. [1]. M-SLAU2 gave the exact same result as obtained using SLAU2. Both the scheme results match well with the reference result.

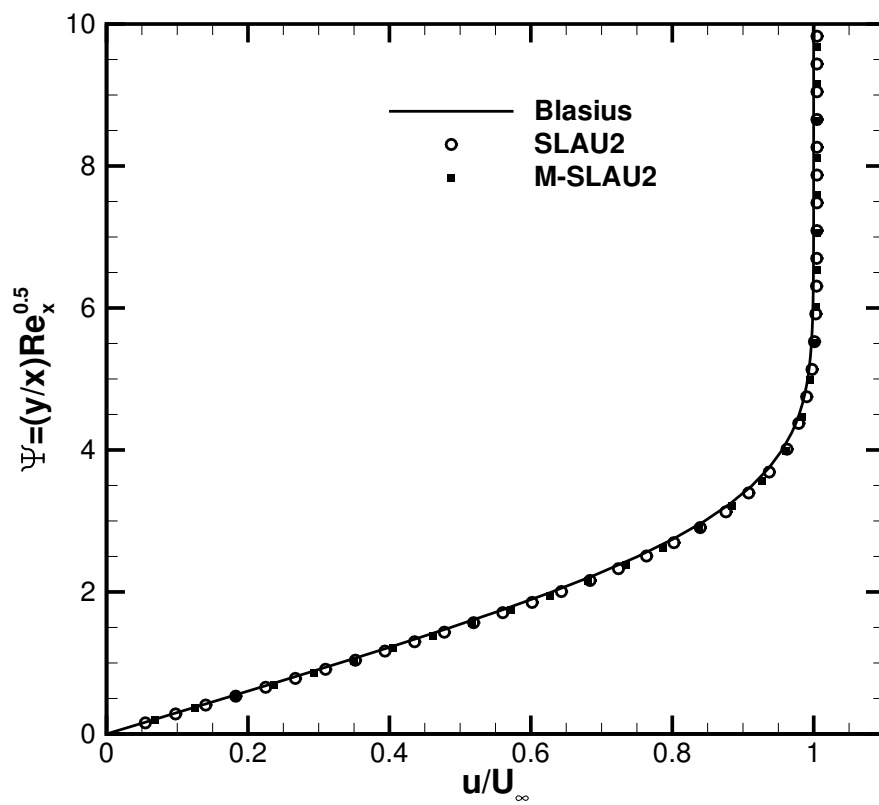


Figure A.2: Plot for the velocity profile at  $Re_x = 1.059 \times 10^6$ .

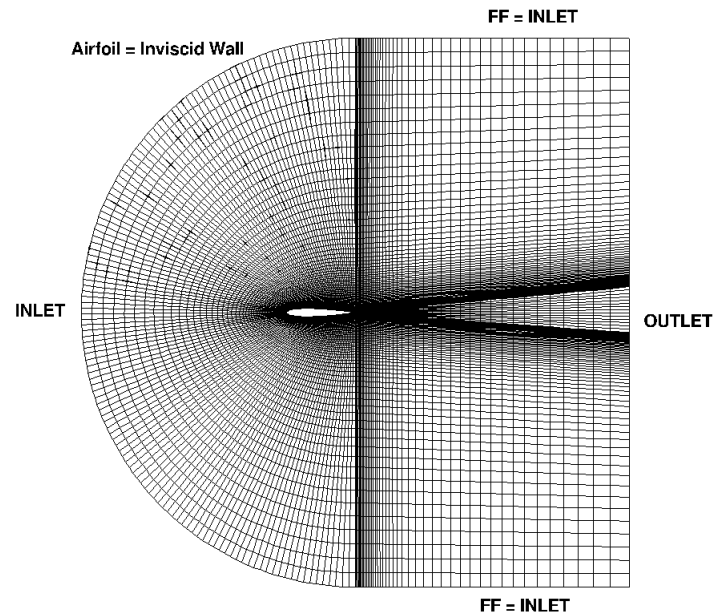


Figure A.3: Computational domain and mesh for the case of inviscid flow over airfoil.

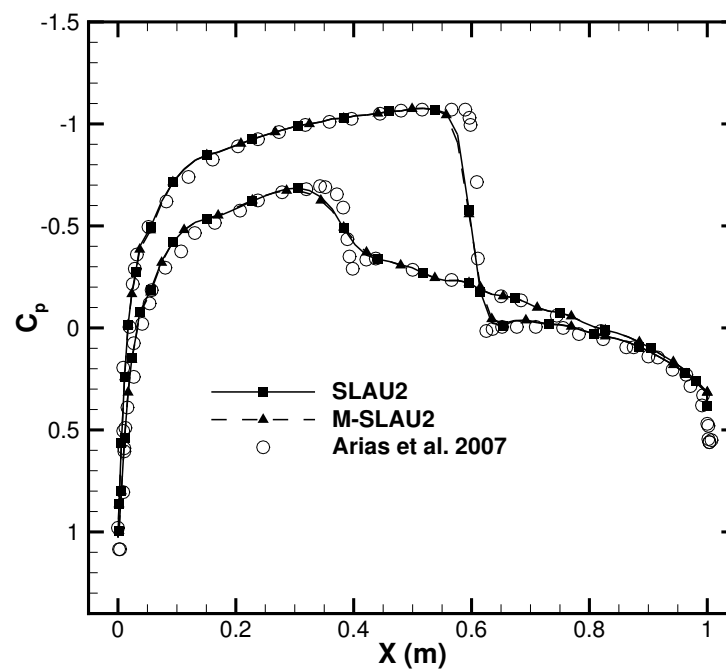


Figure A.4: Pressure Coefficient along the wall: Comparison for  $M = 0.8$  and  $\alpha = 1.25^\circ$  with the reference solution [1].



# Appendix B

## Hypersonic Flow over a cylinder: Using Pressure and Le Temperature Jump condition

In Chapter 7, we have carried out a parametric study for hypersonic flow over a cylinder at two different Mach numbers using the Roe (Sec. 2.3.1.1) and M-SLAU2 (Sec. 7.4) schemes at different  $Kn$ . We had used the standard non-equilibrium boundary condition - the first order Maxwell slip velocity, Eq. 5.3, and Smoluchowski temperature jump, Eq. 5.4. It was found that the M-SLAU2 captured the shock free from anomalies at all  $Kn$ .

In this part, we extend the study done in Chapter 7, using the other two non-equilibrium boundary conditions which have been discussed in this thesis – the Le temperature jump (Eq. 5.8) and the pressure jump condition (Eq. 5.12). The case considered is the case B ( $M_\infty = 16.34$ ) described in Table 7.1. M-SLAU2 is used as the convective scheme. Similar to the analysis we performed using three different non-equilibrium boundary conditions (Table 6.2) in Chapter 5 and Chapter 6, we perform the simulations for the case B here. It can be again noted that PC1 corresponds to the “standard” model [59, 60, 58, 152], PC2 to the Le temperature jump proposed in [62] and PC3 has the Le temperature jump *and* the new pressure jump condition [53]. For PC1, the heat flux is computed using only the Fourier law of heat conduction; while for PC2 and PC3, it is computed including the sliding friction component (Eq. 5.14). For PC3 we have clipped  $\zeta$  (Eq. 5.13) for the pressure jump boundary condition. The CFL number used for the computation is 200.

Figure B.1 shows the plot for wall heat flux and surface temperature jump and

Fig. B.2 shows the plot of pressure and slip velocity at the cylinder wall. Fig. B.1(a) also compares the results with the experimental data [177] for the case B1,  $Kn = 1.59E - 4$ . We note that for the case B1, PC1 and PC2 gave the same result as is expected. The reason being that at low Knudsen number, i.e. continuum regime the slip velocity and temperature jump boundary condition tend to become the no-slip and constant temperature jump condition. However, PC3 shows an unstable results as the pressure jump does not tend to the zero-gradient condition, which it should for the continuum regime of flow. The reason, we see, is that in the Eq. 5.12, re-written here as Eq. B.1, there is no Knudsen number (or  $\lambda_\infty$  term) effect included in the equation. This indicates we may need to revisit the steps used for the derivation<sup>1</sup> of the Eq. B.1 (or Eq. 5.12). Thus, we have only plotted the PC3 results for the case of  $Kn = 0.161$ , for which it gave a stable solution. The present computation indicates that we may need to re-derive the pressure jump condition.

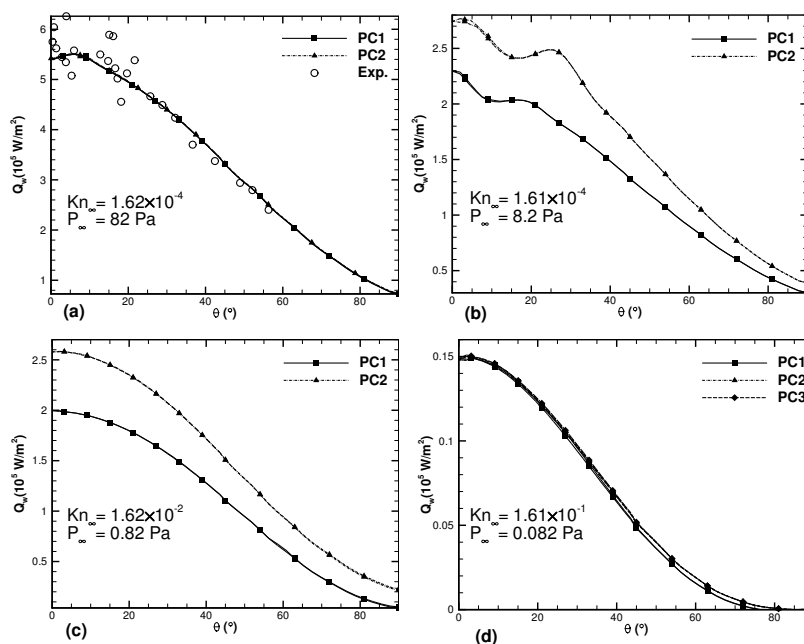
$$p = \frac{p_w}{\left(1 + 2\zeta + \frac{2-\sigma}{\sigma} \frac{4}{5\sqrt{2\pi}} \mathbf{a} \cdot \mathbf{n}\right)} \quad (\text{B.1})$$

As inclusion of  $Kn$  increases, PC2 clearly shows a higher prediction of temperature and heat flux, which is due to the inclusion of the sliding friction in the temperature jump and heat flux calculations. However, for the case of B4, heat flux, temperature jump, pressure and slip velocity all have similar results using PC1, PC2 and PC3. These results have to be examined further, and this hopefully will done in the future. At present, we conclude, following the conclusion of Chapter 6, the use of the new non-equilibrium boundary conditions are case-dependent.

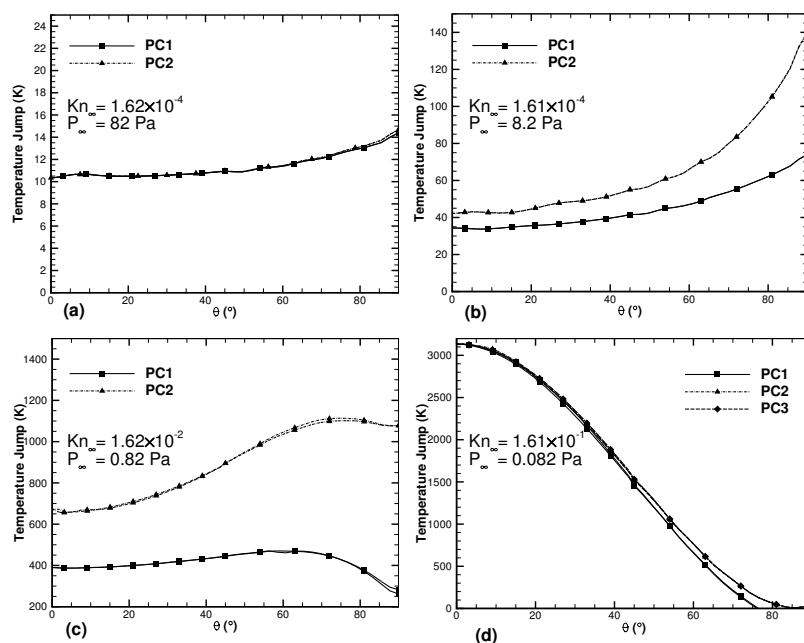
---

<sup>1</sup>Patterson derived the pressure jump equation based on the conservation of normal momentum between the incident and reflected molecules [157, 53].



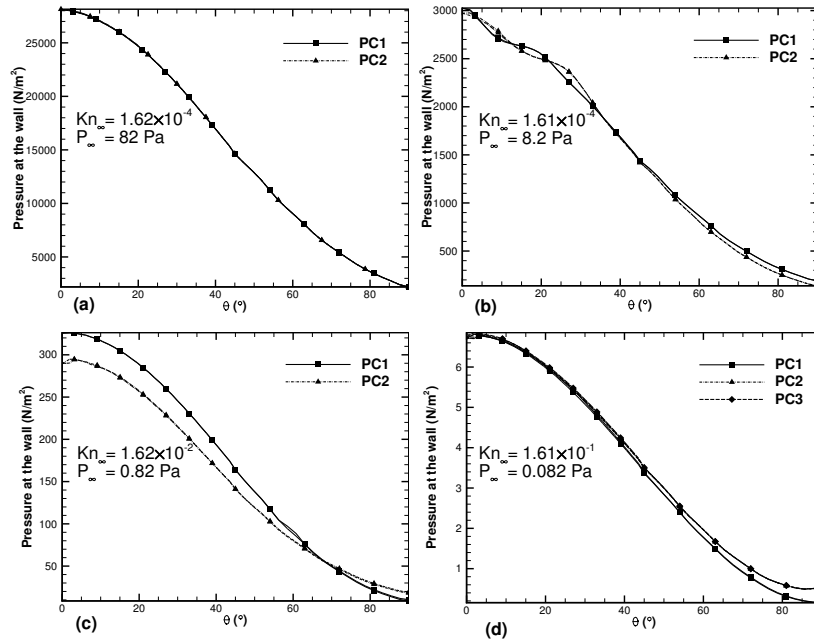


(a) Wall Heat flux

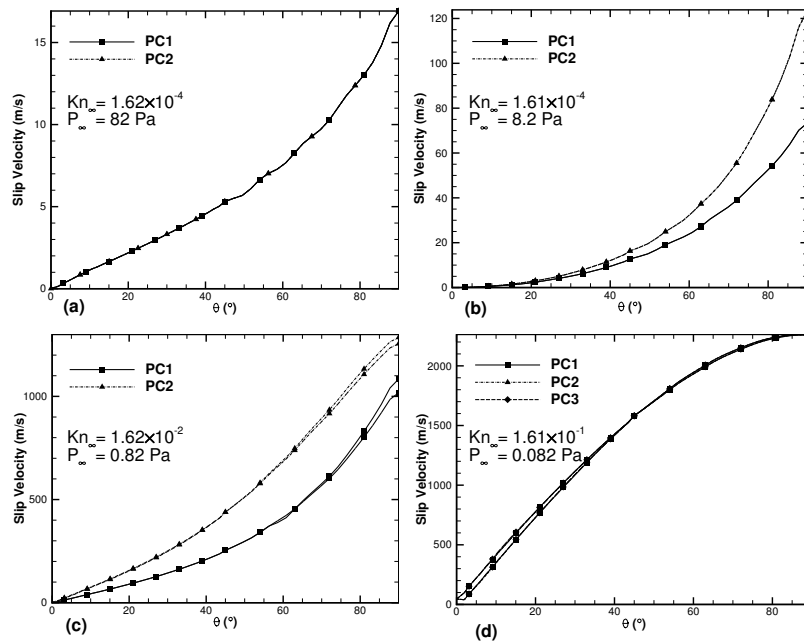


(b) Surface temperature jump

Figure B.1: Wall heat flux and temperature jump calculated for the case B ( $M_\infty = 16.34$ ) using three different boundary conditions. PC3 is not plotted for the case of (a), (b) and (c) as it leads to unstable results.



(a) Pressure



(b) Slip velocity

Figure B.2: Pressure and slip velocity at the wall calculated for the case B ( $M_\infty = 16.34$ ) using three different boundary conditions. PC3 is not plotted for the case of (a), (b) and (c) as it leads to unstable results.

---

## List of Publications

### Journals

1. **Assam A**, Narayan Kalkote N, Sharma V, Eswaran V. An Automatic Wall Treatment for SpalartAllmaras Turbulence Model. *ASME. J. Fluids Eng.* 2018; 140(6), 061403. <https://doi.org/10.1115/1.4039087>
2. **Assam A**, Kalkote N, Dongari N, Eswaran V. Comprehensive Evaluation of a New Type of Smoluchowski Temperature Jump Condition. *AIAA Journal* 2018; 56:11, 4621-4625. <https://doi.org/10.2514/1.J057385>
3. **Assam, A.**, Kalkote, N., Dongari, N. and Eswaran, V., Investigation of non-equilibrium boundary conditions considering sliding friction for micro/nano flows., *International Journal of Numerical Methods for Heat & Fluid Flow* 2018; (Accepted)
4. Kalkote, N., **Assam, A.**, and Eswaran, V., Towards developing an adaptive time stepping for compressible unsteady flows, *International Journal of Numerical Methods for Heat & Fluid Flow* 2018. <https://doi.org/10.1108/HFF-03-2018-0095>
5. Kalkote, N., **Assam, A.**, and Eswaran, V., Acceleration of Later-Convergence in a Solver using Adaptive Time-Stepping, *AIAA Journal*, Vol. 57, No. 1 (2019), pp. 352-364. <https://doi.org/10.2514/1.J057014>
6. **Assam, A.**, Nived M. R., Kalkote, N. and Eswaran, V., A numerical study of shock and heating with rarefaction for hypersonic flow over a cylinder. *Journal of Heat Transfer, ASME.* (under review)

### Conferences

1. **Assam A.**, Kalkote N., Nived M. R., Eswaran V., Performance of Various Convective Scheme for Hypersonic Flows. *7th International and 45th National Conference on Fluid Mechanics and Fluid Power (FMFP)*, Paper no. 260, IIT Bombay, Mumbai, India, December 10-12, 2018.

2. Kalkote N., **Assam A.**, Eswaran V., Application of Adaptive Time-Stepping for Steady/Unsteady Flows, *10th International Conference on Computational Fluid Dynamics (ICCFD10)*, Paper No. 148, Barcelona, Spain, July 9-13, 2018.
3. Sharma V., **Assam A.**, Eswaran V., Investigation Of Turbulent Mixing Layer With Compressibility Corrections For RANS Models, *10th International Conference on Computational Fluid Dynamics (ICCFD10)*, Paper No. 168, Barcelona, Spain, July 9-13, 2018.
4. Kalkote N., **Assam A.**, Nived M. R., Eswaran V., Investigation of All-Speed SLAU Scheme in Incompressible Limit. *5th International Conference on Computational Methods for Thermal Problems (THERMACOMP - 2018)*, Paper no. 76, Indian Institute of Science, Bangalore, INDIA, July 9-11, 2018.
5. **Assam A.**, Kalkote N., Dongari N., Eswaran V., Use of the Pressure Jump Boundary Condition in the High Speed Rarefied Gas Flows, *6th European Conference on Computational Mechanics (Solids, Structures and Coupled Problems) (ECCM 6)* and the *7th European Conference on Computational Fluid Dynamics (ECFD 7)*, ECCOMAS, Paper No. 21, Glasgow, UK, June 11-15, 2018.
6. **Assam A.**, Sharma V., and Eswaran V. Automatic Wall Treatment for Spalart-Allmaras Turbulence Model, *24th National and 2nd International ISHMT-ASTFE Heat and Mass Transfer Conference (IHMTTC-2017)*, Paper No. 479, BITS Pilani, Hyderabad Campus, India, December 27-30, 2017.
7. Athkuri S. S. C., Sharma V., **Assam A.**, Eswaran V., Performance of Convective Schemes in Density-Based Solver, *24th National and 2nd International ISHMT-ASTFE Heat and Mass Transfer Conference (IHMTTC-2017)*, Paper No. 174, BITS Pilani, Hyderabad Campus, India, December 27-30, 2017.
8. Sharma V., **Assam A.** and Eswaran V., Numerical Simulation of Turbulent High Speed Plane Jets - A Validation with Experimental Results, *24th National and 2nd International ISHMT-ASTFE Heat and Mass Transfer Conference (IHMTTC-2017)*, Paper No. 62, BITS Pilani, Hyderabad Campus, India, December 27-30, 2017.
9. **Assam A.**, Kalkote N., Dongari N., Eswaran V., Computation of Rarefied Gas Flows in Nano/micro Devices using an Indigenous developed Computational

Fluid Dynamics Solver, *International Conference on Nanotechnology: Ideas, Innovations & Initiatives (ICN:3I)*. Department of Mechanical & Industrial Engineering & Centre of Nanotechnology, Paper No. 498, Indian Institute of Technology Roorkee, India, December 6-8, 2017.

10. Sharma V., **Assam A.**, Eswaran V., Development of All Speed Three Dimensional Computational Fluid Dynamics Solver for Unstructured Grids, *6th International and 43rd National Conference on Fluid Mechanics and Fluid Power (FMFP)*, Paper No. 21, Allahabad, India, Dec. 15-17 2016.
11. Gijare H., **Assam A.**, Dongari N., Aero-Thermodynamics Optimization of Re-Entry Capsule in the Slip Flow Regime, *23rd National and 1st International ISHMT-ASTFE Heat and Mass Transfer Conference (IHMTTC-2015)*, Paper No. 487, LPSC, ISRO, Trivandrum, Kerala, India, December 17-20, 2017.



# References

- [1] O. Arias, O. Falcinelli, N. Fico Jr, and S. Elaskar. Finite volume simulation of a flow over a NACA0012 using Jameson, MacCormack, Shu and TVD schemes. *Mecánica Computacional* 26, (2007) 3097–3116. [8](#), [177](#), [179](#)
- [2] P. A. Gnoffo. A Perspective on Computational Aerothermodynamics at NASA. In 16th Australasian Fluid Mechanics Conference (AFMC). School of Engineering, The University of Queensland, 2007 24–31. [17](#)
- [3] J. M. A. Longo. Aerothermodynamics A critical review at DLR. *Aerospace Science and Technology* 7, (2003) 429–438. [17](#)
- [4] M. Dhaubhadel. CFD applications in the automotive industry. *Journal of fluids engineering* 118, (1996) 647–653. [18](#)
- [5] D. Chakraborty. Forty Years of Computational Fluid Dynamics Research in India-Achievements and Issues. *Defence Science Journal* 60, (2010) 567–576. [18](#)
- [6] M. M. A. Bhutta, N. Hayat, M. H. Bashir, A. R. Khan, K. N. Ahmad, and S. Khan. CFD applications in various heat exchangers design: A review. *Applied Thermal Engineering* 32, (2012) 1–12. [18](#)
- [7] H. Ambarita, M. Siregar, K. Kishinami, M. Daimaruya, and H. Kawai. Application of CFD in Indonesian Research: A review. In *Journal of Physics: Conference Series*, volume 1005. IOP Publishing, 2018 012014. [18](#)
- [8] J. Blazek. *Computational fluid dynamics principles and applications*. Elsevier, Amsterdam; San Diego, 2005. [18](#), [19](#), [30](#), [32](#), [33](#), [34](#), [38](#), [39](#), [40](#), [49](#), [50](#), [51](#), [52](#), [62](#), [63](#), [81](#), [108](#), [128](#), [152](#)

- [9] J. M. Weiss and W. A. Smith. Preconditioning applied to variable and constant density flows. *AIAA journal* 33, (1995) 2050–2057. [18](#), [35](#), [36](#), [40](#), [41](#), [42](#), [81](#), [108](#), [128](#)
- [10] E. Turkel and E. Turkel. Preconditioning-squared methods for multidimensional aerodynamics. In 13th Computational Fluid Dynamics Conference. 1997 2025. [18](#)
- [11] K. Kitamura and E. Shima. Improvements of simple low-dissipation AUSM against shock instabilities in consideration of interfacial speed of sound. In Proceedings of ECCOMAS CFD, 1283. 2010 Paper no. 1283. [18](#), [42](#)
- [12] K. Kitamura and E. Shima. Towards shock-stable and accurate hypersonic heating computations: A new pressure flux for AUSM-family schemes. *Journal of Computational Physics* 245, (2013) 62 – 83. [18](#), [25](#), [26](#), [36](#), [42](#), [155](#), [156](#)
- [13] P. L. Roe. Approximate Riemann solvers, parameter vectors, and difference schemes. *Journal of computational physics* 43, (1981) 357–372. [18](#), [36](#), [37](#), [38](#), [39](#)
- [14] V. Sharma, A. Assam, and V. Eswaran. Development of all speed three dimensional computational fluid dynamics solver for unstructured grids. In 6th International and 43rd National Conference on Fluid Mechanics and Fluid Power (FMFP). 2016 34. [19](#), [34](#), [35](#)
- [15] A. A. Athkuri Sai Saketha Chandra, Vatsalya Sharma and V. Eswaran. Performance of Convective Schemes in Density-Based Solver. In Proceedings of the International Heat and Mass Transfer Conference. Department of Mechanical Engineering, Bits-Pilani, Hyderabad Campus, India., 2017 01–0174. [19](#)
- [16] N. Kalkote, A. Assam, and V. Eswaran. Towards developing an adaptive time stepping for compressible unsteady flows. *International Journal of Numerical Methods for Heat & Fluid Flow* 0, (0) null. [19](#)
- [17] N. Kalkote, A. Assam, and V. Eswaran. Acceleration of Later Convergence in a Density-Based Solver Using Adaptive Time Stepping. *AIAA Journal* 1–13. [19](#), [52](#)



- [18] P. Moin and K. Mahesh. Direct numerical simulation: a tool in turbulence research. *Annual review of fluid mechanics* 30, (1998) 539–578. [19](#), [60](#)
- [19] G. Alfonsi. On Direct Numerical Simulation of Turbulent Flows. *Applied Mechanics Reviews* 64, (2011) 020,802–020,802–33. [19](#)
- [20] D. C. Wilcox et al. Turbulence modeling for CFD, volume 2. DCW industries La Canada, CA, 2003. [19](#), [61](#)
- [21] T. B. Gatski and J.-P. Bonnet. Compressibility, turbulence and high speed flow. Academic Press, 2013. [19](#)
- [22] J. Boussinesq. Essai sur la théorie des eaux courantes. Impr. nationale, Paris, France, 1877. [19](#), [62](#)
- [23] P. Spalart and S. Allmaras. A one equation turbulence model for aerodynamic flows. *AIAA Journal* 94, (1992) 439. [20](#), [21](#), [63](#), [65](#), [70](#), [77](#)
- [24] B. Launder and D. Spalding. Lectures in mathematical models of turbulence 1972. [20](#), [66](#)
- [25] F. R. Menter. Two-equation eddy-viscosity turbulence models for engineering applications. *AIAA journal* 32, (1994) 1598–1605. [20](#), [67](#)
- [26] A. J. Lew, G. C. Buscaglia, and P. M. Carrica. A note on the numerical treatment of the k-epsilon turbulence model. *International Journal of Computational Fluid Dynamics* 14, (2001) 201–209. [20](#)
- [27] T. Craft, H. Iacovides, and J. Yoon. Progress in the use of non-linear two-equation models in the computation of convective heat-transfer in impinging and separated flows. *Flow, Turbulence and Combustion* 63, (2000) 59–80. [20](#)
- [28] P. G. Tucker, Y. Liu, Y. M. Chung, and A. Jouvray. Computation of an unsteady complex geometry flow using novel non-linear turbulence models. *International journal for numerical methods in fluids* 43, (2003) 979–1001. [20](#)
- [29] Y. Moryossef and Y. Levy. Unconditionally positive implicit procedure for two-equation turbulence models: Application to k- $\omega$  turbulence models. *Journal of Computational Physics* 220, (2006) 88–108. [20](#), [70](#), [72](#), [81](#)

- [30] Y. Mor-Yossef and Y. Levy. The unconditionally positive-convergent implicit time integration scheme for two-equation turbulence models: Revisited. *Computers & Fluids* 38, (2009) 1984–1994. [20](#), [69](#), [70](#), [71](#)
- [31] J. P. A. J. v. Beeck and C. Benocci. Introduction to turbulence modeling. Rhode Saint Genese : Von Karman Institute for Fluid Dynamics, 2004. [20](#)
- [32] 15.0 User’s Manual, ANSYS Documentation / Fluent User’s Guide & Theory Guide–Release 15.0. [20](#)
- [33] J. Bredberg. On the wall boundary condition for turbulence models. Internal Report 00/4, Department of Thermo and Fluid Dynamics, Chalmers University of Technology, Goteborg, Sweden 2000. [21](#), [68](#), [80](#)
- [34] C. Gacherieu and C. Weber. Assessment of algebraic and one-equation turbulence models for the transonic turbulent flow around a full aircraft configuration. In 16th AIAA Applied Aerodynamics Conference. 1998 2737. [21](#), [77](#)
- [35] S. Rogers, K. Roth, S. Nash, M. Baker, J. Slotnick, M. Whitlock, and H. Cao. Advances in overset CFD processes applied to subsonic high-lift aircraft. In 18th Applied Aerodynamics Conference. 2000 4216. [21](#), [77](#)
- [36] S. Deck, P. Duveau, P. d’Espiney, and P. Guillen. Development and application of Spalart–Allmaras one equation turbulence model to three-dimensional supersonic complex configurations. *Aerospace Science and Technology* 6, (2002) 171–183. [21](#), [77](#)
- [37] D. K. Ota and U. C. Goldberg. Law of the wall with consistent no-slip limit. *AIAA Paper* 97–2246. [21](#)
- [38] U. Goldberg, O. Perroomian, and S. Chakravarthy. A wall-distance-free  $k-\epsilon$  model with enhanced near-wall treatment. *Journal of Fluids Engineering* 120, (1998) 457–462. [21](#)
- [39] T. Knopp, T. Alrutz, and D. Schwamborn. A grid and flow adaptive wall-function method for RANS turbulence modelling. *Journal of Computational Physics* 220, (2006) 19–40. [21](#)
- [40] G. Medic, G. Kalitzin, G. Iaccarino, and E. Van Der Weide. Adaptive wall functions with applications. *AIAA Paper* 3744, (2006) 2005. [21](#)

- [41] T. Craft, S. Gant, H. Iacovides, and B. Launder. A new wall function strategy for complex turbulent flows. *Numerical Heat Transfer, Part B: Fundamentals* 45, (2004) 301–318. [21](#)
- [42] V. M. Segunda, S. Ormiston, and M. Tachie. Numerical Analysis of Turbulent Flow Over a Wavy Wall in a Channel. In ASME 2016 Fluids Engineering Division Summer Meeting collocated with the ASME 2016 Heat Transfer Summer Conference and the ASME 2016 14th International Conference on Nanochannels, Microchannels, and Minichannels. American Society of Mechanical Engineers, 2016 V01AT03A014–V01AT03A014. [21](#)
- [43] M. J. Berger and M. J. Aftosmis. An ODE-Based Wall Model for Turbulent Flow Simulations. *AIAA Journal* 56, (2017) 700–714. [21](#), [89](#), [93](#)
- [44] M. Berger and M. Aftosmis. Progress towards a Cartesian cut-cell method for viscous compressible flow. In 50th AIAA Aerospace Sciences Meeting Including the New Horizons Forum and Aerospace Exposition. 2012 1301. [21](#)
- [45] S. R. Allmaras and F. T. Johnson. Modifications and clarifications for the implementation of the Spalart-Allmaras turbulence model. In Seventh International Conference on Computational Fluid Dynamics (ICCFD7). 2012 1–11. [21](#)
- [46] U. Goldberg and P. Batten. Rough Surface Wall Function Treatment with Single Equation Turbulence Models. *Journal of Fluids Engineering* 139, (2017) 081,204. [21](#)
- [47] F. Menter and T. Esch. Elements of industrial heat transfer predictions. In 16th Brazilian Congress of Mechanical Engineering (COBEM), volume 109. 2001 117–127. [21](#)
- [48] F. Menter, J. C. Ferreira, T. Esch, B. Konno, and A. Germany. The SST turbulence model with improved wall treatment for heat transfer predictions in gas turbines. In Proceedings of the international gas turbine congress. 2003 2–7. [21](#), [69](#), [78](#), [79](#)
- [49] F. Menter, M. Kuntz, and R. Langtry. Ten years of industrial experience with the SST turbulence model. *Turbulence, heat and mass transfer* 4, (2003) 625–632. [21](#), [67](#)

- [50] F. R. Menter. Review of the shear-stress transport turbulence model experience from an industrial perspective. *International Journal of Computational Fluid Dynamics* 23, (2009) 305–316. [21](#)
- [51] C. Cercignani. *Rarefied Gas Dynamics: From Basic Concepts to Actual Calculations*. Cambridge Texts in Applied Mathematics. Cambridge University Press, 2000. [22](#)
- [52] N. Le, C. J. Greenshields, and J. Reese. Evaluation of nonequilibrium boundary conditions for hypersonic rarefied gas flows. In *Progress in Flight Physics*, volume 3. EDP Sciences, 2012 217–230. [22](#), [102](#), [103](#)
- [53] C. J. Greenshields and J. M. Reese. Rarefied hypersonic flow simulations using the NavierStokes equations with non-equilibrium boundary conditions. *Progress in Aerospace Sciences* 52, (2012) 80 – 87. [22](#), [24](#), [99](#), [105](#), [106](#), [107](#), [111](#), [112](#), [123](#), [128](#), [181](#), [182](#)
- [54] T. Scanlon, E. Roohi, C. White, M. Darbandi, and J. Reese. An open source, parallel DSMC code for rarefied gas flows in arbitrary geometries. *Computers & Fluids* 39, (2010) 2078–2089. [22](#)
- [55] N. T. Le, C. White, J. M. Reese, and R. S. Myong. LangmuirMaxwell and LangmuirSmoluchowski boundary conditions for thermal gas flow simulations in hypersonic aerodynamics. *International Journal of Heat and Mass Transfer* 55, (2012) 5032 – 5043. [22](#), [23](#), [105](#), [112](#)
- [56] W. Wagner. A convergence proof for Bird’s direct simulation Monte Carlo method for the Boltzmann equation. *Journal of Statistical Physics* 66, (1992) 1011–1044. [22](#), [100](#)
- [57] A. J. Lofthouse. Nonequilibrium hypersonic aerothermodynamics using the direct simulation Monte Carlo and Navier-Stokes models. Ph.D. thesis, US Air Force Research Laboratory 2008. [22](#), [33](#), [100](#), [102](#), [104](#), [118](#), [129](#)
- [58] R. E. Street. Problem of slip flow in aerodynamics. Technical Report RM-57A30, NASA, NASA Washington, DC, United States 1957. [23](#), [111](#), [128](#), [181](#)
- [59] J. C. Maxwell. On stresses in rarified gases arising from inequalities of temperature. *Philosophical Transactions of the royal society of London* 231–256. [23](#), [102](#), [111](#), [128](#), [181](#)

- [60] M. Smoluchowski von Smolan. Ueber wärmeleitung in verdünnten gasen. *Annalen der Physik* 300, (1898) 101–130. [23](#), [102](#), [103](#), [111](#), [128](#), [181](#)
- [61] R. Myong. Gaseous slip models based on the Langmuir adsorption isotherm. *Physics of fluids* 16, (2004) 104–117. [23](#)
- [62] N. T. Le, N. A. Vu, and L. T. Loc. New type of Smoluchowski temperature jump condition considering the viscous heat generation. *AIAA Journal* 55, (2016) 474–483. [23](#), [24](#), [99](#), [102](#), [104](#), [107](#), [108](#), [109](#), [111](#), [112](#), [115](#), [124](#), [128](#), [135](#), [144](#), [145](#), [181](#)
- [63] G. Bird. The DSMC Method, Clarendon 2013. [23](#), [100](#)
- [64] S. H. Maslen. On Heat Transfer in Slip Flow. *Journal of the Aerospace Sciences* 25, (1958) 400–401. [23](#), [107](#)
- [65] N. T. Le, N. A. Vu, and L. T. Loc. Effect of the sliding friction on heat transfer in high-speed rarefied gas flow simulations in CFD. *International Journal of Thermal Sciences* 109, (2016) 334 – 341. [23](#), [107](#), [113](#), [124](#)
- [66] S. Mizzi, D. R. Emerson, S. K. Stefanov, R. W. Barber, and J. M. Reese. Effects of rarefaction on cavity flow in the slip regime. *Journal of computational and theoretical nanoscience* 4, (2007) 817–822. [24](#)
- [67] A. Grm, T. Grnland, and T. Rodi. Numerical analysis of a miniaturised cold gas thruster for micro and nanosatellites. *Engineering Computations* 28, (2011) 184–195. [24](#)
- [68] A. Assam, N. N. Kalkote, N. Dongari, and V. Eswaran. Use of the Pressure Jump Boundary Condition in the high speed rarefied gas flows in the Slip regime. In Proceedings of ECCOMAS CFD-CCM. 2018 968. [24](#)
- [69] A. Assam, N. Kalkote, N. Dongari, and V. Eswaran. Comprehensive Evaluation of a New Type of Smoluchowski Temperature Jump Condition. *AIAA Journal* 1–5. [24](#), [135](#)
- [70] R. N. Gupta, C. D. Scott, and J. N. Moss. Slip-boundary equations for multi-component nonequilibrium airflow. Technical Report TP-2452, NASA, NASA Johnson Space Center; Houston, TX, United States 1985. [24](#), [99](#), [106](#)

- [71] Y.-z. Yang, J.-l. Yang, and D.-n. Fang. Research progress on thermal protection materials and structures of hypersonic vehicles. *Applied Mathematics and Mechanics* 29, (2008) 51–60. [24](#)
- [72] S. Kumar and S. P. Mahulikar. Design of Thermal Protection System for Reusable Hypersonic Vehicle Using Inverse Approach. *Journal of Spacecraft and Rockets* 54, (2017) 436–446. [24](#)
- [73] V. Elling. The carbuncle phenomenon is incurable. *Acta Mathematica Scientia* 29, (2009) 1647–1656. [24](#)
- [74] R. W. MacCormack. Carbuncle computational fluid dynamics problem for blunt-body flows. *Journal of Aerospace Information Systems* 10, (2013) 229–239. [24](#)
- [75] A. Agrawal and B. Srinivasan. Stability analysis of the carbuncle phenomenon and the sonic point glitch. *Sādhanā* 42, (2017) 741–757. [24](#)
- [76] Z. Chen, X. Huang, Y.-X. Ren, Z. Xie, and M. Zhou. Mechanism Study of Shock Instability in Riemann-Solver-Based Shock-Capturing Scheme. *AIAA Journal* 1–16. [24](#)
- [77] Z.-X. Gao, H.-C. Xue, Z.-C. Zhang, H.-P. Liu, and C.-H. Lee. A hybrid numerical scheme for aeroheating computation of hypersonic reentry vehicles. *International Journal of Heat and Mass Transfer* 116, (2018) 432 – 444. [24](#), [157](#)
- [78] K. Kitamura, P. Roe, and F. Ismail. Evaluation of Euler fluxes for hypersonic flow computations. *AIAA Journal* 47, (2009) 44–53. [24](#), [155](#)
- [79] K. Hoffman, M. Siddiqui, and S. Chiang. Difficulties associated with the heat flux computations of high speed flows by the Navier-Stokes equations. *American Institute of Aeronautics and Astronautics* 0. [24](#)
- [80] R. Paciorri and A. Bonfiglioli. A shock-fitting technique for 2D unstructured grids. *Computers & Fluids* 38, (2009) 715 – 726. [25](#)
- [81] M. S. Ivanov, D. V. Khotyanovsky, A. A. Shershnev, A. N. Kudryavtsev, A. A. Shevyrin, S. Yonemura, and Y. A. Bondar. Rarefaction effects in hypersonic flow about a blunted leading edge. *Thermophysics and Aeromechanics* 18, (2011) 523–534. [25](#), [157](#)

- [82] H. S. Panda and S. G. Moulic. An analytical solution for natural convective gas microflow in a tall vertical enclosure. *Proceedings of the Institution of Mechanical Engineers, Part C: Journal of Mechanical Engineering Science* 225, (2011) 145–154. [25](#)
- [83] A. Shoja-Sani, E. Roohi, M. Kahrom, and S. Stefanov. Investigation of aerodynamic characteristics of rarefied flow around NACA 0012 airfoil using DSMC and NS solvers. *European Journal of Mechanics - B/Fluids* 48, (2014) 59 – 74. [25](#)
- [84] G. Huang and R. K. Agarwal. chapter Computation of Rarefaction Effects on a Blunt Body in Hypersonic Flow. AIAA SciTech Forum. American Institute of Aeronautics and Astronautics, 2017. 0. [25](#), [173](#), [174](#)
- [85] E. Shima and K. Kitamura. On new simple low-dissipation scheme of AUSM-family for all speeds. In 47th AIAA Aerospace Sciences Meeting Including the New Horizons Forum and Aerospace Exposition. 2009 136. [25](#), [42](#), [152](#)
- [86] K. Kitamura and E. Shima. Pressure-equation-based SLAU2 for oscillation-free, supercritical flow simulations. *Computers & Fluids* 163, (2018) 86 – 96. [25](#)
- [87] K. Chakravarthy and D. Chakraborty. Modified SLAU2 scheme with enhanced shock stability. *Computers & Fluids* 100, (2014) 176 – 184. [26](#)
- [88] S. sheng Chen, C. Yan, K. Zhong, H. chao Xue, and E. long Li. A novel flux splitting scheme with robustness and low dissipation for hypersonic heating prediction. *International Journal of Heat and Mass Transfer* 127, (2018) 126 – 137. [26](#)
- [89] F. M. White and I. Corfield. Viscous fluid flow, volume 3. McGraw-Hill New York, 2006. [30](#), [177](#)
- [90] H. W. Liepmann and A. Roshko. Elements of gasdynamics. Courier Corporation, 1957. [32](#)
- [91] W. Sutherland. LII. The viscosity of gases and molecular force. *The London, Edinburgh, and Dublin Philosophical Magazine and Journal of Science* 36, (1893) 507–531. [32](#)

- [92] G. Bird. Molecular Gas Dynamics and the Direct Simulation of Gas Flows. Number v. 1 in Molecular Gas Dynamics and the Direct Simulation of Gas Flows. Clarendon Press, 1994. [33](#), [100](#), [129](#)
- [93] S. Patankar. Numerical heat transfer and fluid flow. CRC Press, 1980. [33](#)
- [94] I. Keshtiban, F. Belblidia, and M. Webster. Compressible flow solvers for low Mach number flows a review. *Int. J. Numer. Methods Fluids* 23, (2004) 77–103. [33](#)
- [95] E. Turkel, R. Radespiel, and N. Kroll. Assessment of preconditioning methods for multidimensional aerodynamics. *Computers & Fluids* 26, (1997) 613–634. [33](#)
- [96] H. Guillard and C. Viozat. On the behaviour of upwind schemes in the low Mach number limit. *Computers & fluids* 28, (1999) 63–86. [33](#)
- [97] Y.-H. Choi and C. L. Merkle. The Application of Preconditioning in Viscous Flows. *J. Comput. Phys.* 105, (1993) 207–223. [33](#)
- [98] E. Turkel. Preconditioned Methods for Solving the Incompressible Low Speed Compressible Equations. *J. Comput. Phys.* 72, (1987) 277–298. [33](#)
- [99] J. M. Weiss and W. A. Smith. Solution of unsteady, low Mach number flow using a preconditioned multi-stage scheme on an unstructured mesh. In AIAA 11th Computational Fluid Dynamics Conference. 1993 1059. [33](#)
- [100] J. M. Weiss, J. P. Maruszewski, and W. A. Smith. Implicit Solution of Preconditioned Navier-Stokes Equations Using Algebraic Multigrid. *AIAA Journal* 37, (1999) 29–36. [33](#), [34](#), [35](#)
- [101] A. Assam, N. N. Kalkote, N. MR, , and V. Eswaran. Investigation of All-Speed SLAU Scheme in Incompressible Limit. In 5th International Conference on Computational Methods for Thermal Problems (THERMACOMP - 2018). 2018 . [36](#)
- [102] P. L. Roe. Characteristic-based schemes for the Euler equations. *Annual review of fluid mechanics* 18, (1986) 337–365. [36](#)



- [103] P. T. Karnick. Shocks, Shock-Boundary Layer Interaction, And Transonic Flutter. Ph.D. thesis, Indian Institute of Science, Bangalore, India 2017. G25863. [36](#), [37](#), [38](#)
- [104] E. F. Toro. Riemann solvers and numerical methods for fluid dynamics: A practical introduction. Springer Science & Business Media, 2013. [36](#), [37](#), [38](#)
- [105] A. Harten and J. M. Hyman. Self adjusting grid methods for one-dimensional hyperbolic conservation laws. *Journal of computational Physics* 50, (1983) 235–269. [40](#)
- [106] A. Harten, P. D. Lax, and B. v. Leer. On upstream differencing and Godunov-type schemes for hyperbolic conservation laws. *SIAM review* 25, (1983) 35–61. [40](#)
- [107] H. C. Yee, G. H. Klopfer, and J.-L. Montagne. High-resolution shock-capturing schemes for inviscid and viscous hypersonic flows. *Journal of Computational Physics* 88, (1990) 31–61. [40](#)
- [108] H. Guillard and C. Viozat. On the behaviour of upwind schemes in the low Mach number limit. *Computers & Fluids* 28, (1999) 63 – 86. [40](#)
- [109] B. VA, W.-T. LEE, and P. ROE. chapter Characteristic time-stepping or local preconditioning of the Euler equations. Fluid Dynamics and Co-located Conferences. American Institute of Aeronautics and Astronautics, 1991. 0. [40](#)
- [110] A. Haselbacher and J. Blazek. Accurate and efficient discretization of Navier-Stokes equations on mixed grids. *AIAA journal* 38, (2000) 2094–2102. [45](#)
- [111] N. Ganesh. Residual Error Estimation And Adaptive Algorithms For Fluid Flows. Ph.D. thesis, Indian Institute of Science, Bangalore, India 2011. G23588. [45](#), [47](#), [48](#), [54](#), [55](#)
- [112] T. Barth and D. Jespersen. The design and application of upwind schemes on unstructured meshes. In 27th Aerospace sciences meeting. 1989 366. [46](#)
- [113] C. Hirsch. Numerical computation of internal and external flows fundamentals of computational fluid dynamics. Elsevier, Amsterdam, 2007. [47](#), [61](#)

- [114] T. J. Barth. Recent developments in high order k-exact reconstruction on unstructured meshes. *AIAA paper* 93, (1993) 0668. [48](#)
- [115] V. Venkatakrishnan. On the accuracy of limiters and convergence to steady state solutions. In 31st Aerospace Sciences Meeting. 1993 880. [48](#)
- [116] V. Venkatakrishnan. Convergence to steady state solutions of the Euler equations on unstructured grids with limiters. *Journal of computational physics* 118, (1995) 120–130. [48](#), [152](#)
- [117] D. Mavriplis and V. Venkatakrishnan. A 3D agglomeration multigrid solver for the Reynolds-averaged Navier-Stokes equations on unstructured meshes. *International Journal for Numerical Methods in Fluids* 23, (1996) 527–544. [49](#)
- [118] M. Ivanov, P. Vashchenkov, and A. Kashkovsky. Numerical investigation of the EXPERT reentry vehicle aerothermodynamics along the descent trajectory. In 39th AIAA Thermophysics Conference. 2007 4145. [50](#)
- [119] S. Yoon and A. Jameson. Lower-upper symmetric-Gauss-Seidel method for the Euler and Navier-Stokes equations. *AIAA Journal* 26, (1988) 1025–1026. [51](#)
- [120] J. M. Weiss, J. P. Maruszewski, and W. A. Smith. Implicit solution of preconditioned Navier-Stokes equations using algebraic multigrid. *AIAA journal* 37, (1999) 29–36. [51](#)
- [121] V. P. and Y. Kallinderis. A 3D Finite-Volume Scheme for the Euler Equations on Adaptive Tetrahedral Grids. *Journal of Computational Physics* 113, (1994) 249 – 267. [52](#)
- [122] J.-R. Carlson. Inflow/outflow boundary conditions with application to FUN3D. Technical Report TM-2011-217181, NASA, NASA Langley Research Center; Hampton, VA, United States 2011. [55](#)
- [123] A. Favre. Equations des gaz turbulents compressibles. 2. methode des vitesses moyennes methode des vitesses macroscopiques ponderees par la masse volumique. *Journal de mecanique* 4, (1965) 391. [61](#)
- [124] W. M. Kays. Turbulent Prandtl number-where are we? *Journal of Heat Transfer* 116, (1994) 284–295. [63](#)

- [125] Turbulence Modeling Resource. <https://turbmodels.larc.nasa.gov/>. 63, 81, 86, 90, 92, 93
- [126] J. Dacles-Mariani, G. G. Zilliac, J. S. Chow, and P. Bradshaw. Numerical/experimental study of a wingtip vortex in the near field. *AIAA journal* 33, (1995) 1561–1568. 65
- [127] J. Dacles-Mariani, D. Kwak, and G. Zilliac. On numerical errors and turbulence modeling in tip vortex flow prediction. *International journal for numerical methods in fluids* 30, (1999) 65–82. 65
- [128] P. R. Spalart and C. L. Rumsey. Effective inflow conditions for turbulence models in aerodynamic calculations. *AIAA journal* 45, (2007) 2544. 65
- [129] D. M. Driver. Reynolds shear stress measurements in a separated boundary layer flow. *AIAA paper* 91, (1991) 5–4. 68
- [130] H.-S. Im and G.-C. Zha. Delayed Detached Eddy Simulation of Airfoil Stall Flows Using High-Order Schemes. *Journal of Fluids Engineering* 136, (2014) 111,104–111,104–12. 70
- [131] A. Berman and R. J. Plemmons. Nonnegative matrices in the mathematical sciences, volume 9. Siam, 1994. 71
- [132] M. Wasserman, Y. Mor-Yossef, I. Yavneh, and J. Greenberg. A robust implicit multigrid method for RANS equations with two-equation turbulence models. *Journal of Computational Physics* 229, (2010) 5820–5842. 71
- [133] N. V. Shende and Y. Mor-Yossef. Robust implementation of the Spalart–Allmaras turbulence model for unstructured grid. In 5th European Conference on Computational Fluid Dynamics ECCOMAS CFD. 2010 1–14. 71, 81
- [134] P. Batten, M. Leschziner, and U. Goldberg. Average-state Jacobians and implicit methods for compressible viscous and turbulent flows. *Journal of Computational Physics* 137, (1997) 38–78. 72
- [135] B. Diskin and J. L. Thomas. Introduction: Evaluation of RANS Solvers on Benchmark Aerodynamic Flows. *AIAA Journal* 54, (2016) 2561–2562. 77

- [136] B. Kader. Temperature and concentration profiles in fully turbulent boundary layers. *International Journal of Heat and Mass Transfer* 24, (1981) 1541–1544. [79](#), [86](#)
- [137] J. Bredberg, S. Peng, and L. Davidson. On the Wall Boundary Condition for Computing Turbulent Heat Transfer With K-omega Models. In ASME Heat Transfer Division, Orlando, FL, 366-5. 2000 5 – 10. [80](#)
- [138] A. Dalal. Development of a Finite Volume Based Navier-Stokes Solver on Unstructured Grids and Its Application to Analyze Transport Mechanisms in Heat Exchangers. Ph.D. thesis, Indian Institute of Technology, Kanpur 2008. [80](#)
- [139] B. Mohammad and G. Puigt. Generalized wall functions for high-speed separated flows over adiabatic and isothermal walls. *International Journal of Computational Fluid Dynamics* 14, (2001) 183–200. [81](#), [108](#), [128](#), [152](#)
- [140] Y. Zhang, J.-Q. Bai, and J.-L. Xu. A Scale-Adaptive Turbulence Model Based on the k-Equation and Recalibrated Reynolds Stress Constitutive Relation. *Journal of Fluids Engineering* 138, (2016) 061,203. [81](#)
- [141] S. L. Krist, R. T. Biedron, and C. L. Rumsey. CFL3D user’s manual (version 5.0) . [83](#), [89](#), [96](#)
- [142] K. Wieghardt and W. Tillmann. On the turbulent friction layer for rising pressure. Technical Report NACA-TM-1314, Stanford, CA United States 1951. [83](#)
- [143] S. M. Salim and S. Cheah. Wall  $y^+$  strategy for dealing with wall-bounded turbulent flows. In Proceedings of the international multiconference of engineers and computer scientists, volume 2. 2009 2165–2170. [83](#)
- [144] Forced Convection over a Flat Plate. <https://confluence.cornell.edu/display/SIMULATION/FLUENT+Learning+Modules>. [83](#)
- [145] W. C. Reynolds, W. M. Kays, and S. J. Kline. Heat Transfer in the Turbulent Incompressible Boundary Layer. 3; Arbitrary Wall Temperature and Heat Flux. Technical Report 12-3-58W, Stanford University, Stanford, CA United States 1958. [86](#)

- [146] R. Seban and D. Doughty. Heat transfer to turbulent boundary layers with variable free-stream velocity. *Trans. ASME* 78, (1956) 217–223. [86](#)
- [147] N. Gregory and C. O'reilly. Low-Speed aerodynamic characteristics of NACA 0012 aerofoil section, including the effects of upper-surface roughness simulating hoar frost. HM Stationery Office London, 1973. [96](#)
- [148] R. Vidal, T. Golian, and A. Bartz. An Experimental Study of Hypersonic Low-Density Viscous Effects on a Sharp Flat Plate. In AIAA Physics of Entry into Planetary Atmospheres Conference, Cambridge, Mass. 1963 63–435. [99](#), [105](#)
- [149] D. C. Wadsworth. Slip effects in a confined rarefied gas. I: Temperature slip. *Physics of Fluids A: Fluid Dynamics* 5, (1993) 1831–1839. [99](#)
- [150] J. M. Reese and Y. Zhang. Simulating fluid flows in micro and nano devices: the challenge of non-equilibrium behaviour. *Journal of Computational and Theoretical Nanoscience* 6, (2009) 2061–2074. [100](#)
- [151] E. H. Kennard et al. Kinetic theory of gases, with an introduction to statistical mechanics. McGraw-Hill, 1938, London, UK, 1938. [101](#), [102](#)
- [152] N. T. P. Le. Nonequilibrium boundary conditions for the Navier-Stokes-Fourier equations in hypersonic gas flow simulations. Ph.D. thesis, University of Strathclyde 2010. [101](#), [102](#), [103](#), [105](#), [107](#), [109](#), [111](#), [113](#), [118](#), [124](#), [128](#), [181](#)
- [153] A. Agrawal and S. V. Prabhu. Survey on measurement of tangential momentum accommodation coefficient. *Journal of Vacuum Science & Technology A* 26, (2008) 634–645. [101](#)
- [154] J. C. Maxwell. On Stresses in Rarefied Gases Arising from Inequalities of Temperature. *Proceedings of the Royal Society of London* 27, (1878) 304–308. [102](#)
- [155] W. Vincenti and C. Kruger. Introduction to Physical Gas Dynamics. Krieger Publishing Company, 1967. [104](#)
- [156] N. T. Le and E. Roohi. Second order temperature jump boundary condition for nano/microscale and hypersonic rarefied gas flow simulations. In AIP Conference Proceedings, volume 1628. AIP, 2014 374–381. [105](#), [107](#), [129](#), [130](#), [136](#), [139](#)

- [157] G. N. Patterson. Molecular flow of gases. John Wiley and Sons, New York, USA, 1956. [105](#), [106](#), [107](#), [182](#)
- [158] H. Grad. On the kinetic theory of rarefied gases. *Communications on pure and applied mathematics* 2, (1949) 331–407. [105](#)
- [159] A. Assam, N. N. Kalkote, N. Dongari, and V. Eswaran. Computation of Rarefied Gas Flows in Nano/micro Devices using an Indigenous developed Computational Fluid Dynamics Solver. In Proceedings of the International Conference on Nanotechnology: Ideas, Innovations & Initiatives (ICN:3I). Department of Mechanical & Industrial Engineering & Centre of Nanotechnology, Indian Institute of Technology Roorkee, India., 2017 649. [108](#)
- [160] S. Metcalf, D. Lillicrap, and C. Berry. A study of the effect of surface temperature on the shock-layer development over sharp-edged shapes in low-Reynolds-number high-speed flow. *Rarefied Gas Dynamics* 1, (1969) 619–634. [108](#), [109](#), [111](#), [113](#), [114](#), [115](#), [116](#), [117](#), [124](#)
- [161] M. Becker. Flat plate flow field and surface measurements from merged layer into transition regime. In Proceedings of the 7th International Symposium on Rarefied Gas Dynamics. Editrice tecnico scientifica, 1969 515–528. [109](#), [111](#), [118](#), [120](#), [121](#), [124](#)
- [162] N. T. Le and E. Roohi. A new form of the second-order temperature jump boundary condition for the low-speed nanoscale and hypersonic rarefied gas flow simulations. *International Journal of Thermal Sciences* 98, (2015) 51–59. [111](#), [115](#), [124](#)
- [163] M. Wang and Z. Li. Simulations for gas flows in microgeometries using the direct simulation Monte Carlo method. *International Journal of Heat and Fluid Flow* 25, (2004) 975 – 985. [130](#)
- [164] C. White, M. K. Borg, T. J. Scanlon, and J. M. Reese. A DSMC investigation of gas flows in micro-channels with bends. *Computers & Fluids* 71, (2013) 261–271. [130](#)
- [165] A. Agrawal, L. Djenidi, and A. Agrawal. Simulation of gas flow in microchannels with a single 90 bend. *Computers & Fluids* 38, (2009) 1629 – 1637. [130](#)

- [166] V. Varade, A. Agrawal, S. Prabhu, and A. Pradeep. Early onset of flow separation with rarefied gas flowing in a 90 bend tube. *Experimental Thermal and Fluid Science* 66, (2015) 221 – 234. [130](#)
- [167] A. Gavasane, A. Agrawal, and U. Bhandarkar. Study of rarefied gas flows in backward facing micro-step using Direct Simulation Monte Carlo. *Vacuum* 155, (2018) 249 – 259. [135](#), [139](#)
- [168] A.-M. Mahdavi, N. T. Le, E. Roohi, and C. White. Thermal Rarefied Gas Flow Investigations Through Micro-/Nano-Backward-Facing Step: Comparison of DSMC and CFD Subject to Hybrid Slip and Jump Boundary Conditions. *Numerical Heat Transfer, Part A: Applications* 66, (2014) 733–755. [136](#)
- [169] S. A. Rooholghdos and E. Roohi. Extension of a second order velocity slip/temperature jump boundary condition to simulate high speed micro/nanoflows. *Computers & Mathematics with Applications* 67, (2014) 2029 – 2040. [140](#)
- [170] M. Darbandi and E. Roohi. A hybrid DSMC/NavierStokes frame to solve mixed rarefied/nonrarefied hypersonic flows over nanoplateandmicrocylinder. *International Journal for Numerical Methods in Fluids* 72, (2013) 937–966. [140](#)
- [171] J. Fan, I. D. Boyd, C.-P. Cai, K. Hennighausen, and G. V. Candler. Computation of rarefied gas flows around a NACA 0012 airfoil. *AIAA journal* 39, (2001) 618–625. [140](#), [144](#)
- [172] J. Allegre, M. Raffin, and J. Lengrand. Experimental flowfields around NACA 0012 airfoils located in subsonic and supersonic rarefied air streams. In *Numerical Simulation of Compressible Navier-Stokes Flows*, 59–68. Springer, 1987. [144](#)
- [173] N. T. Le, A. Shoja-Sani, and E. Roohi. Rarefied gas flow simulations of NACA 0012 airfoil and sharp 2555-deg biconic subject to high order nonequilibrium boundary conditions in CFD. *Aerospace Science and Technology* 41, (2015) 274 – 288. [144](#)
- [174] I. H. Abbott and A. E. Von Doenhoff. *Theory of wing sections, including a summary of airfoil data*. Courier Corporation, 1959. [144](#)

- [175] M. Nived and V. Eswaran. Parallelization of a Hybrid Unstructured Grid Density-based Flow Solver. Master Thesis, Indian Institute of Technology Hyderabad, India, 2018. [152](#)
- [176] A. Assam, N. N. Kalkote, N. MR, , and V. Eswaran. Performance of Various Convective Scheme for Hypersonic Flows. In 7th International and 45th National Conference on Fluid Mechanics and Fluid Power (FMFP). Indian Institute of Science, Bangalore, INDIA, 2018 76. [152](#)
- [177] M. Holden, J. Moselle, A. Wieting, and C. Glass. chapter Studies of aerothermal loads generated in regions of shock/shock interaction in hypersonic flow. Aerospace Sciences Meetings. American Institute of Aeronautics and Astronautics, 1988. 0. [155](#), [156](#), [157](#), [160](#), [167](#), [182](#)
- [178] M.-S. Liou. A sequel to AUSM, Part II: AUSM+-up for all speeds. *Journal of computational physics* 214, (2006) 137–170. [155](#)
- [179] B. Einfeldt. On Godunov-type methods for gas dynamics. *SIAM Journal on Numerical Analysis* 25, (1988) 294–318. [156](#)
- [180] Z. Xiang, Y. Wei, and H. Haibo. Computational grid dependency in CFD simulation for heat transfer. In Mechanical and Aerospace Engineering (ICMAE), 2017 8th International Conference on. IEEE, 2017 193–197. [157](#)
- [181] G. Romanelli, L. Mangani, E. Casartelli, A. Gadda, M. Favale et al. Implementation of Explicit Density-Based Unstructured CFD Solver for Turbomachinery Applications on Graphical Processing Units. In ASME Turbo Expo 2015: Turbine Technical Conference and Exposition. ASME, 2015 1–14. [173](#)
- [182] A. Corrigan, F. F. Camelli, R. Löhner, and J. Wallin. Running unstructured grid-based CFD solvers on modern graphics hardware. *International Journal for Numerical Methods in Fluids* 66, (2011) 221–229. [173](#)
- [183] M. Jarkowski, M. Woodgate, G. Barakos, and J. Rokicki. Towards consistent hybrid overset mesh methods for rotorcraft CFD. *International Journal for Numerical Methods in Fluids* 74, (2014) 543–576. [173](#)
- [184] T. Plewa, T. Linde, and V. G. Weirs. Adaptive mesh refinement-theory and applications: proceedings of the Chicago workshop on adaptive mesh refinement



- methods, Sept. 3-5, 2003, volume 41. Springer Science & Business Media, 2005. [173](#)
- [185] A. Hadjadj and J.-P. Dussauge. Shock wave boundary layer interaction 2009. [173](#)
- [186] T. J. Wray and R. K. Agarwal. Low-Reynolds-Number One-Equation Turbulence Model Based on k- $\omega$  Closure. *AIAA Journal* 53, (2015) 2216–2227. [173](#)
- [187] X. Han, M. Rahman, and R. K. Agarwal. chapter Development and Application of Wall-Distance-Free Wray-Agarwal Turbulence Model (WA2018). AIAA SciTech Forum. American Institute of Aeronautics and Astronautics, 2018. 0. [173](#)
- [188] G. Candler. On the computation of shock shapes in nonequilibrium hypersonic flows. *AIAA Paper* . [174](#)
- [189] C. Park. Assessment of two-temperature kinetic model for ionizing air. *Journal of Thermophysics and Heat Transfer* 3, (1989) 233–244. [174](#)
- [190] P. A. Gnoffo, R. N. Gupta, and J. L. Shinn. Conservation equations and physical models for hypersonic air flows in thermal and chemical nonequilibrium. Technical Report TP-2867, NASA, NASA Langley Research Center; Hampton, VA, United States 1989. [174](#)
- [191] L. STEG and H. LEW. Chapter 32 - Hypersonic Ablation. In W. C. NELSON, ed., *The High Temperature Aspects of Hypersonic Flow*, volume 68 of *AGARDograph*, 629 – 680. Elsevier, 1964. [174](#)
- [192] G. Karniadakis, A. Beskok, and N. Aluru. *Microflows and nanoflows: Fundamentals and Simulation*, volume 29. Springer Science & Business Media, 2006. [174](#)
- [193] Y. Hu, H. Huang, and Z. Zhang. Numerical simulation of a hypersonic flow past a blunt body. *International Journal of Numerical Methods for Heat & Fluid Flow* 27, (2017) 1351–1364. [174](#)
- [194] D. Sun, F. Qu, and C. Yan. An effective flux scheme for hypersonic heating prediction of re-entry vehicles. *Computers & Fluids* 176, (2018) 109 – 116. [174](#)